UNIVERSITÀ DEGLI STUDI DI MILANO

FACOLTÀ DI SCIENZE E TECNOLOGIE

Corso di Dottorato in Chimica Industriale XXXIII Ciclo

New organic and hybrid organic/inorganic materials with intriguing solid state optoelectronic properties

Andrea PREVITALI

R12058

Tutor: Prof.ssa Elena CARIATI

Coordinatore del corso: Prof.ssa Dominique Marie ROBERTO

Anno Accademico 2019-2020

Index

1 Fluorescence and Phosphorescence: a thousand-year history

The modern perception of the photoluminescent phenomena is the product of an intensive work mostly concentrated in the 19th and 20th centuries. Actually, even before the discovery of the photoelectric effect and the wave-particle duality in quantum mechanics, the scientific community has tried to explain some exceptional phenomena observed when light and some specific materials are interacting[1].

Figure 1: Representation of Pliny the Elder

Along the centuries many proof of the observation of photoluminescent phenomena can be find. Evidences of this are present in the documents written by Pliny the Elder (*Naturalis Historia* (libri XXXVI e XXXVII)) in the ancient Rome and by Saint Albert the great (*Historia animalium* (1555)) during the Middle age. During the middle ages it is possible to date the born of the terms *phosphor* that was use to describe materials able to glow in the dark after exposure to light, this term derives from the Greek name of Venus and it literally means *the light bearer*. Only later, the name Phosphor, was given to the element discovered by Brandt in 1677, that has observed the glow from the vapors produced by this new element exposes to the atmosphere.

The most famous case of glow-in-the-dark material is the rock known as the Bolognian Phosphors (impure barium sulfate) discovered by a cobbler, Vincenzo Casciarolo, in Bologna in 1602. This rock, after calcination with coal, was able to store and re-emit the sunlight for a certain time.

Figure 2: Bolognian Phosphors

Previously, in 1565, the botanist Nicolas Monardes, noticed the bluish colour of an infuse of a plant, named *Lignum Nephriticum*, that was used by the Incas population as medicine. Matlaline is responsible for the particular coloration and is the oxidation product of the flavonoids contained in the plant. The peculiar bluish coloration of the infuse, observed under particular observation condition, is the very first case of anti-counterfeiting system, in fact, Monardes explain that another plant was sold as *Lignum Nephriticum*, but the false plant shows only a yellow infusion and no blueish emission[2-4].

Figure 3: Left: Lignum Nephriticum paint. Right: Lignum Nephriticum picture under day and UV light.

However, many famous scientists, as Newton and Boyle, have investigated the particular behaviour of this solution but its nature wasn't completely understood at that time.

In 1819, a British geologist, Edward D. Clarke, has firstly reported the discovery of a fluorite crystal in Durham describing the mineral as the most beautiful crystal he had ever seen before. Crystals of the "Durham fluor", as it was later called, show deep blue sapphire colour by reflected light and an intense emerald green by the transmitted light. Clarke offered no explanation for this behaviour but, in 1822, the French mineralogist Rene-Just Haüy, observed a similar behaviour in a fluorite crystal and it explain the phenomenon as a kind of opalescence, unfortunately for him he was wrong and many years were required to understand this uncommon behaviour.

Sir David Brewster, in 1833, describe a red dichroism in a green alcoholic extract of chlorophyll when is observed from a side. The case was considered analogous to the one of the Durham fluor, and explained through opalescence[5].

In 1845, Sir John Herschel, inventor of the term "photography", describes the blue surface colour of an inner colourless concentrate quinine sulfate solution. He named the phenomenon "epipolic dispersion" from the greek term "surface". In this case the high concentration prevents the light to be adsorbed by the inner part of the solution and the blue emission seems to be only superficial. Herschel, using a prism, demonstrated that only using the blue end of the spectrum was possible to observe the epiploic dispersion but he did not recognise that the emission had a lower energy, with a blue-green colour. He extended his theory even to fluorite crystals but, in the *Lignum Nephriticum* case, he claimed the effect was due to a tiny particles dispersion. When Brewster read about the epopilic dispersion and the intrinsic contradiction with his theory decided to further investigate this phenomenon proving the phenomenon was not superficial. For this reason, Brewster proposed that the behaviour observed was a new case of interaction between light and

some specific fluid and solid, in particular he claim that the media he studied contained minute crystals randomly oriented able to disperse the unpolarised light. Unfortunately, he was wrong[6].

Figure 4: Painting of Sir George Gabriel Stokes

A major improvement in the comprehension of the physics of light was due to the work of Professor Sir George Gabriel Stokes, that in 1852 published "On the refrangibility of light". In this work, he describes the phenomenon he called "dispersive reflection" where the dispersed light has always a longer wavelength respect the incident one. Stokes' experiment consist in the use of a tube filled with a quinine sulfate solution that is exposed to the different wavelengths using a prism. When the tube is exposed to the visible part nothing happened but when he moves the tube to the invisible section beyond the violet one the tube immediately lights up. Stokes used many different fillers for the tube and concluded that the disperse light always had a longer wavelength, this statement will be called Stokes law. Stokes also noticed that, instead of a "dispersion" of light, the tube seemed to glow itself. For this reasons he did not want to use the term "dispersive reflection" but the lack of a more proper one forced him to use this non-precise term. However, in his second work, Stokes overcomes this impasse coining the term fluorescence[7].

Figure 5: Picture of Edmon Becquerel.

Ten years before the Stokes' work publication, Edmon Becquerel, published almost the same experiments and the same conclusions but the paper was manly ignored. At the time Stokes' publication came off,

Becquerel claimed his priority over those results. The two works are effectively similar but Becquerel used calcium sulphide that is not fluorescent but phosphorescent.

However, Stokes failed in the description of the process behind the emission of light. Mainly, Stokes believed fluorescence is a scattering process that do not depend by the incident light but by the nature of the molecules, this explanation, as we know, it is false for photoluminescence but it is proper of the Raman emission (also known as Stokes and anti-Stokes).

On the other side, Becquerel argued that the term fluorescence was incorrect and it must be abandoned because the Stokes experiment was only the observation of a shorter time decay phosphorescence which was a finite process.

Becquerel and Stokes had determined very important aspects of the fluorescent and phosphorescent processes but they did not completely understand the theoretical elements behind these phenomena[8].

During the late 19th century, light radiation was intensively studied by Kirchhoff that formulated the Kirchhoff's law of radiation. In his work, Kirchhoff demonstrate that the absorption/emission power ratio is a function of temperature and wavelength for any material. Obviously, Kirchhoff law are related to the black body radiation and the incandescent phenomena, while fluorescence and phosphorescence do not follow these law, for this reason, fluorescence and phosphorescence were frequently defined as "cold light". Wiedemann proposed a mechanism based on the kinetic theory that postulated the presence of ether shells around atoms. Ether was necessary to explain the diffusion of light that was considered, as well as others waves, transmitted only through a support. In his view, collisions cause vibrations that are then transferred to ether shells which produce light whose intensity depends by the strength of vibration. This explanation brought Wiedemann to reject the term cold light and to introduce the term Luminescence for any phenomenon that produce light and does not fit the Kirchhoff's law[9].

In 1889, Wiedemann envisioned an experiment where a luminescent material emits a radiation that could be adsorbed by a body with a higher temperature violating the second low of thermodynamic. In order to overcome this problem, he introduced the concept of "luminescence temperature" that stated the temperature of an incandescent body emission necessary to match the luminescence wavelength. This approach is inconsistent because a distinction is made between a body in thermal equilibrium and a body not in equilibrium.

Wilhelm Wien get around the problem stating that the Stokes' low was just an exception of the second law of thermodynamics, unfortunately, many cases of violation of the Stokes' low were reported. In 1871, Eugen Lommel notice that, upon excitation of a solution containing naphthalene red with the yellow line of a sodium flame, was possible to observe a weak green fluorescence. The results were considered unreliable, suspecting the contamination of the source. In 1886, Franz Stenger, after a carefully check of the source, not only replicate the results obtained by Lommel but extend the investigation to eosin and fluorescein that show the same deviation[10].

Only with the proposal of the quantum theory by Plank and its application to the photoelectric effect by Einstein, the controversy was resolved.

The Stokes low respects the first principal of the thermodynamic considering the adsorbed/emitted quanta proportional to the wavelength and the bell shape of the emission suggests a statistical reason to deviation from the Stokes low.

Einstein sustained another theory, where the extra energy release during emission in an anti-Stokes emission is due to the intrinsic vibrational energy of the atoms or of the molecules and so should be greater at higher temperature. Based on this idea Joseph von Kowalski showed the agreement between the Einstein calculation and the effect of the temperature over the rhodamine emission, confirming the theory.

While the disputation over the Stokes' low was ongoing, Edmon Becquerel had focused his attention on phosphorescence. In 1858, he built his phosphorocope to run the very first time resolved photoluminescence experiment. The instrument was pretty simple but sufficiently accurate to detected decay times longer than 0.1 ms. It consists in two rotating discs with four unmatched windows with the sample inbetween. The rotation allows the incident light to reach the sample passing through the first disc while the second one is covering the passage to the detector, proceeding with the rotation, the excitation window before the sample closes while the emission window to the detector is opening. The lag time between the excitation and the measure of the emission intensity is related to the speed of the discs[8].

To Becquerel is due one of the first application of the photoluminescence, in fact, he designs the fluorescent tube which consist in the coating of the inner surface of an electric discharge tube with a luminophore to produce light. Nowadays, the modern fluorescent tubes are made in a similar way with Eu^{II}, Eu^{III} and Tb^{III} in the coating to produce withe light.

As well as Becquerel even Stokes understood the great potential behind the luminescence, theorizing the application of this phenomenon for the recognition of specific targets present in mixtures. On the same way, Victor Pierre in 1862 published an article where he was able to identify single fluorescent molecules in mixtures noting that, fluorescent bands, were characteristic of specific molecules.

Later, Göppelsröderd, firstly reported the enhancement of the emission intensity of morin due to the aluminium complexation, referring for the first time to this technique as *fluorescent analysis.*

Among the oldest application of the fluorescence, it is noteworthy the use of uranin in 1877 to monitor the flow of Danube river. Ten litres of a concentrate solution of uranin were poured in the Danube at the spring of the river. As obvious, after a long way the Danube water reach the Black sea, but after 50 hours the fluorescence was detected in the Aache river 12 Km in the south. This river flows into the Constanz lake that feed the Rhine showing that, most of the water of Danube, flows into the North sea thanks to sinks on the bed of the river[11].

1.1 References

[1] Valeur, B.; Berberan-Santos, M. r. N., A Brief History of Fluorescence and Phosphorescence before the Emergence of Quantum Theory. *Journal of Chemical Education* **2011,** *88* (6), 731-738.

[2] Muyskens, M.; Ed, V., The Fluorescence of Lignum nephriticum: A Flash Back to the Past and a Simple Demonstration of Natural Substance Fluorescence. *Journal of Chemical Education* **2006,** *83* (5), 765.

[3] Partington, J. R., Lignum nephriticum. *Annals of Science* **1955,** *11* (1), 1-26.

[4] Acuña, A. U.; Amat-Guerri, F.; Morcillo, P.; Liras, M.; Rodríguez, B., Structure and Formation of the Fluorescent Compound of Lignum nephriticum. *Organic Letters* **2009,** *11* (14), 3020-3023.

[5] Brewster, D., XIX. On the Colours of Natural Bodies. *Transactions of the Royal Society of Edinburgh* **1834,** *12* (2), 538-545.

[6] Herschel, J. F. W., V. ’Αμόρφωϒa, no. II.— on the epipölic dispersion of light, being a supplement to a paper entitled, “On a case of superficial colour presented by a homogeneous liquid internally colourless.". *Philosophical Transactions of the Royal Society of London* **1845,** *135*, 147-153.

[7] Stokes, G. G., XXX. On the change of refrangibility of light. *Philosophical Transactions of the Royal Society of London* **1852,** *142*, 463-562.

[8] Becquerel, E., *La lumière, ses causes et ses effets*. Firmin Didot frères, fils et cie: 1867.

[9] Wiedemann, E., Ueber Fluorescenz und Phosphorescenz I. Abhandlung. *Annalen der Physik* **1888,** *270* (7), 446-463.

[10] Malley, M., Thermodynamics and cold light. *Annals of Science* **1994,** *51* (3), 203-224. Lommel, E., Ueber Fluorescenz. *Annalen der Physik* **1871,** *219* (5), 26-51.

[11] Kass, W., *Tracing Technique in Geohydrology*. CRC Press: 2018.

2 Theoretical concepts

2.1 Introduction

The very first step that every system has to undergo before any transitions can take place is the absorption of a photon with the proper energy that promotes an electron from an orbital in the ground state to an unoccupied orbital generating a molecular excited state. The energy of the photon adsorbed will be equal to the "promotion jump" made by the electron implying that there must be a match between the energy transferred and the energetic gap between the ground and the excited states. The direct consequence is that not every molecule can absorb every photon but its chemical structure will define the distribution of the energetic levels thus, which portion of the electromagnetic spectrum will be absorbed[1].

It is important to remind how the orbitals are energetically distributed in order to better understand which transitions are more likely to occur. Let's take in consideration the formaldehyde:

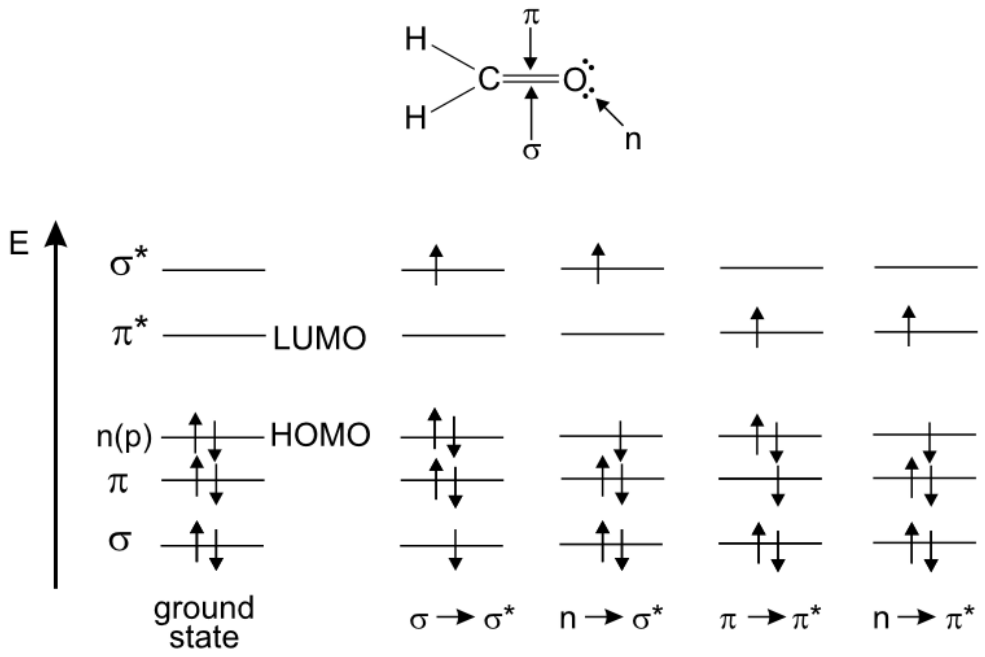

Figure 1: Chemical structure, molecular orbital and possible transition of formaldehyde. Reproduced from ref.[8] with permission Copyright © 2001, John Wiley and Sons.

As we can see 3 main kinds of molecular orbitals are present in this molecule:

- σ are bonding orbitals formed between atoms with collinear symmetry axes.
- π are bonding orbitals formed between atoms without collinear symmetry axes.
- n are non-bonding orbitals located on a single atom

It also is important to remind that for every bonding molecular orbital generated an anti-bonding orbital (π*, σ*) is generated too.

Theoretically, using a photon with the proper wavelength any electron from any occupied orbital could be promoted to any unoccupied orbital, however the lower the energy the more likely the transition. In the example taken in consideration the energy for the transition are:

$n \rightarrow \pi^* < \pi \rightarrow \pi^* < n \rightarrow \sigma^* < \pi \rightarrow \sigma^* < \sigma \rightarrow \pi^* < \sigma \rightarrow \sigma^*$

So, the most probable transition is, frequently, the one involving the frontier orbitals (HOMO and LUMO) and specifically in this case is the $n \rightarrow \pi^*$ where a non-bonding electron localized on the oxygen is promoted to a

π* anti-boning orbital, shared between oxygen and carbon, giving to this transition a charge transfer character going from the oxygen to the carbon.

When an electron is promoted to a higher energy state its spin does not change and so the total spin quantum number ($S = \sum_i s_i$ with $s_i = +\frac{1}{2}\ or\ -\frac{1}{2}$) remains unchanged and equal to 0 with a spin multiplicity ($M = 2S + 1$) equal to 1, consequently the transition occurs between states named "singlet" (S_0, S_1, S_2,…, S_n). As we will see in the next sections, in some specific cases some processes can change the spin of the electron ($S = 0$ and $M = 3$) generating "triplet states" (T_1, T_2, T_3,…, T_m) that have lower energy then single states with the same configuration (Hund's rule).

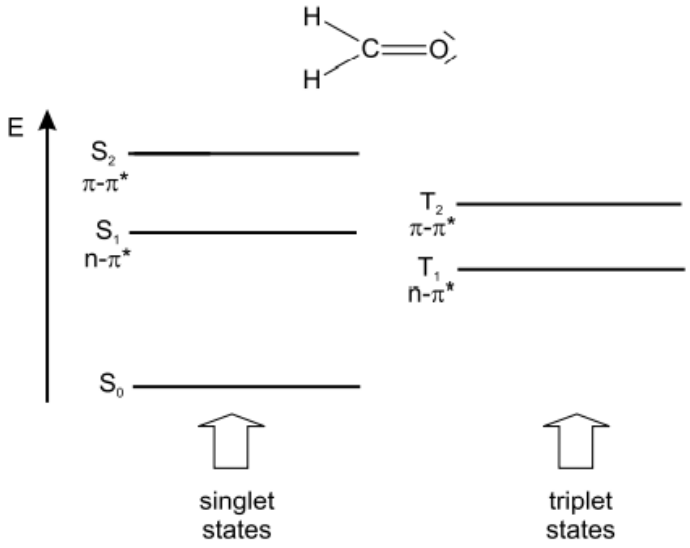

Figure 2: Jablonski diagram for formaldehyde. Reproduced from ref.[8] with permission Copyright © 2001, John Wiley and Sons.

2.2 Lambert-Beer law and oscillator strength

The probability that a molecule will absorb an incident photon with a specific wavelength is experimentally described by the molar absorption coefficient $\varepsilon(\lambda)$ that, in the Lambert-Beer law, correlates the absorbed light (I) to the concentration of a chromophore (c) when the optical path (l) is fixed.

$$A(\lambda) = \log\left(\frac{I^0}{I}\right) = \varepsilon(\lambda) l c$$

The Lambert-Beer law is valid until the concentration does not cause the formation of aggregates or micelles that have different optical properties with respect to the isolated molecule.

Classically, the absorption probability is defined through the oscillator strength f:

$$f = \frac{4\ ln10\varepsilon_0 mc}{N_a e^2} \int \varepsilon(\nu)\ d\nu = \frac{4\ ln10\varepsilon_0 mc^2}{N_a e^2 \lambda_{av}^2} \int \varepsilon(\lambda)\ d\lambda$$

The value of f can vary between 0 and 1. When $f = 0$ none of the incident photons will be absorbed oppositely when $f = 1$ all the incident photons will be adsorbed.

If we consider the absorption of a photon from a quantum mechanical point of view, the process can be described as a displacement of charges that generates a transient dipole represented by a specific transition moment for each transition. The transition dipole can be drawn as a vector whose coordinates are defined

by the nuclei positions of the atoms in the molecule. When an incident photon "hits" a molecule the probability to be absorbed depends by the angle between the transient dipole vector of the transition and the electric vector of the photon, in fact the probability is proportional to the square of the scalar product between them. This means that for every molecule with a transition dipole parallel to the electric vector of the incident photon the probability is maximum while if the two are perpendicular the probability drops to zero[2].

2.3 Selection rules

The number of the allowed transitions for a molecule in its ground state to an excited state or for a molecule that relaxes from an excited state is limited by the so called "selection rules". Particularly selective is the spin selection rule according to which a transition between states of different spin multiplicity (singlet to triplet or vice versa) is forbidden. This selection rule becomes less stringent due to spin-orbit coupling (i.e. the interaction between the magnetic field associated with the rotation of the electron around the nucleus and that associated its spin motion) which results in mixing states of different multiplicity so that the multiplicity of a specific wavefunction is no more clearly defined. The result is that the intensity integral between singlet/ triplet states in not null and the transition can occur even though with low probability.

Similarly, symmetry forbidden transitions can take place through vibronic coupling which breaks the symmetry of a molecule.

2.4 Franck-Condon principle

Since nuclei are much slower than electrons, electronic transitions occur (10^{-15} s) with nuclei freezed in their position (molecular vibrations takes 10^{-10} – 10^{-12} s). According to the Franck-Condon principle (an extension of the Born-Oppenheimer approximation): "an electronic transition is most likely to occur without changes in the positions of the nuclei in the molecular entity and its environment" (*IUPAC Compendium of Chemical Terminology, 2nd Edition (1997*). The consequent relation between the potential energy and the nuclei position allows to draw the Frank-Condon states represented by a Morse function:

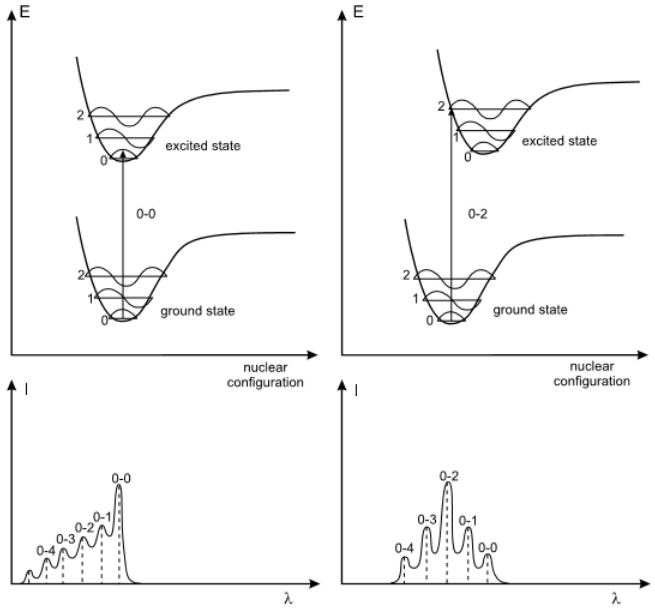

Figure 3: Potential energy diagram drawn under the Franck-Condon assumption and relative excitation spectra. Reproduced from ref.[8] with permission Copyright © 2001, John Wiley and Sons.

The Boltzmann distribution predicts that at room temperature most of the molecules are in the lowest vibration level of the ground state. However, an experimental spectrum of a generic transition only rarely displays a very sharp shape because many broadening effects are possible. Firstly, there is a continuous set of accessible vibrational sublevels for each electronic state, and secondly the fluctuation of the environment around the molecules are the main cause of the widening of the bands. The Franck-Condon principle implies that the transitions can only occur vertically. As stated by the Boltzmann distribution a molecule at room temperature is prone to be find at the lower vibrational level of the ground state but, the absorption can bring it to different vibrational levels of an excited state. After the excitation the molecules usually converge to the lower vibrational level of the excited state and only after they will relax to a vibrational level of the ground state[3]. The probability (P) to reach a certain vibrational level depends on the overlap integral of the wavefunctions involved in the transition:

$$P = \langle \psi^f \mid \boldsymbol{\mu} \mid \psi^i \rangle = \int \psi^{f*} \boldsymbol{\mu} \, \psi^i \, d\tau$$

Where the dipole operator $\boldsymbol{\mu}$ of the transition between an initial vibrational level "i" of the ground state to a final vibrational level "f" of an excited state is determined by nuclei and electrons positions ($\boldsymbol{R_n}$ and $\boldsymbol{r_m}$ respectively) and by their charges:

$$\boldsymbol{\mu} = \boldsymbol{\mu_e} + \boldsymbol{\mu_N} = -e \sum_i \boldsymbol{r_i} + e \sum_j Z_j \boldsymbol{R_j}$$

Since:

$$\psi = \psi_e \psi_v \psi_s$$

Under the Born-Oppenheimer approximation it is possible to calculate the probability for electronic, spin and vibrational contributions separately:

$$P = \langle \psi_e^f \psi_v^f \psi_s^f | \boldsymbol{\mu} | \psi_e^i \psi_v^i \psi_s^i \rangle = \int \psi_e^{f*} \psi_v^{f*} \psi_s^{f*} \, (\boldsymbol{\mu_e} + \boldsymbol{\mu_N}) \, \psi_e^i \psi_v^i \psi_s^i \, d\tau$$

$$= \int \psi_e^{f*} \psi_v^{f*} \psi_s^{f*} \, \boldsymbol{\mu_e} \, \psi_e^i \psi_v^i \psi_s^i \, d\tau + \psi_e^{f*} \psi_v^{f*} \psi_s^{f*} \, \boldsymbol{\mu_N} \, \psi_e^i \psi_v^i \psi_s^i \, d\tau$$

$$= \int \psi_v^{f*} \psi_v^i \, d\tau_v \int \psi_e^{f*} \boldsymbol{\mu_e} \psi_e^i \, d\tau_e \int \psi_s^{f*} \psi_s^i \, d\tau_s + \int \psi_e^{f*} \psi_e^i \, d\tau_e \int \psi_v^{f*} \boldsymbol{\mu_N} \psi_v^i \, d\tau_v \int \psi_s^{f*} \psi_s^i \, d\tau_s$$

The second term of this equation is null because the electronic wavefunction of different states are orthogonal thus no overlap is possible.

$$= \int \psi_v^{f*} \psi_v^i \, d\tau_v \int \psi_e^{f*} \boldsymbol{\mu_e} \psi_e^i \, d\tau_e \int \psi_s^{f*} \psi_s^i \, d\tau_s$$

The three remaining integrals represent the Frank-Condon factor (which defines the most probable vibrational transitions), the orbital selection rule and the spin selection rule, respectively. Franck-Condon factor has only a limited weigh on the intensity of a transition respect the two other selection rules.

2.5 Possible transition between electronic states

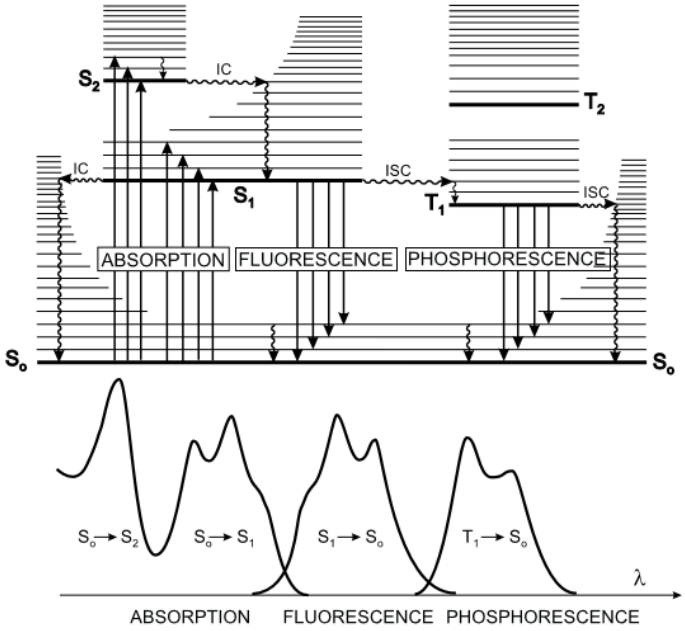

Figure 4: Perrin-Jablonski diagram for a generic chromophore. Reproduced from ref.[8] with permission Copyright © 2001, John Wiley and Sons.

2.5.1 Internal Conversion, IC

After photoexcitation, the most rapid process (10^{-13} -10^{-11} s) is the vibrational deactivation to the lower vibrational level of the electronic excited state. In this process, energy is transferred to the environment as kinetic energy. Then, radiationless deactivation through Internal Conversion allows molecules to relax to a lower electronic level of the same multiplicity. IC is accomplished through isoenergetic vibrational levels of the two electronic states followed by dissipation of the excess of energy through vibrational deactivation.

2.5.2 Fluorescence

According to the energy gap law, the efficiency of IC increases exponentially by decreasing the energy gap between the electronic states involved in the process so that only when this gap is "sufficiently" small (usually for S_1 to S_0) radiative deactivation (fluorescence) becomes competitive with IC. This is express by the Kasha's rule (which is based on the energy gap law): the emission of photon is an appreciable process only from the first excited state. A consequence of the Kasha's rule is that fluorescent emission does not depend on the excitation wavelength because the system always relaxes to S_1 before emitting.

Due to the non-radiative deactivation processes which occur in between excitation and emission, excitation is always at higher energy than the emission and this energy difference is defined as Stokes shift.

2.5.3 Intersystem Crossing, ISC

Intersystem crossing (ISC) is the non-radiative deactivation between electronic states of different multiplicity. According to the spin selection rule, ISC is a not allowed process which is however possible if favoured by specific effects such as the presence of an heavy atom on the scaffold which favours SOC, the presence of paramagnetic species and when there is a change in the nature of the states involved in the electronic

transition, in particular, the El-Sayed's rule predicts larger k_{ST} when the two states are of different orbital parentage[4].

2.5.4 Phosphorescence

Once the system is brought to a generic triplet state through ISC, it can relax to T_1 through IC. Since, according to the Hund's rule, T_1 is always lower in energy with respect to S_1, the Stokes of phosphorescence is larger than that of fluorescence. Since triplet states undergo non-radiative deactivation more easily than singlet states, phosphorescence is rarely observed, in particular in solution and at RT where collision with solvent molecules, vibrational relaxation and oxygen quenching strongly affect the phosphorescent quantum efficiency.

2.5.5 Thermally Activated Delayed Fluorescence TADF

When the lifetime of T_1 is particularly long and the energy gap between T_1 and S_1 is sufficiently small, a reverse ISC can be observed and the emission from the singlet states became much longer than normal. The energy gap between T_1 and S_1 is filled by thermal energy so this process becomes more relevant increasing the temperature.

2.5.6 Excited state lifetimes

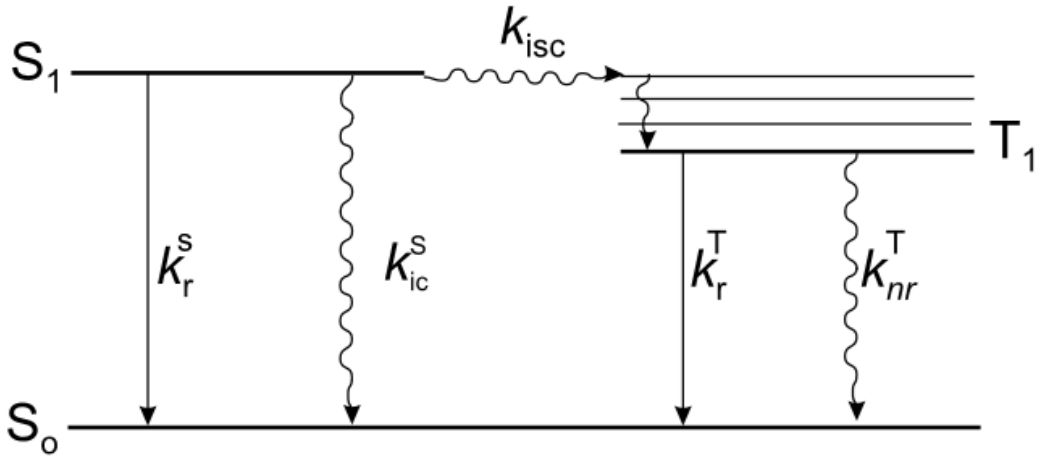

Figure 5: Jablonski diagram for a generic chromofore with the rate constants of the processes. Reproduced from ref.[8] with permission Copyright © 2001, John Wiley and Sons.

Every excited state is characterized by an intrinsic lifetime which is determined by the sum of every processes that can occur starting from the level taken into consideration (Figure 5). Every process in turn is characterized by a rate constant that is related to its probability[5].

The S_1 lifetime is determined by all the processes that can occur from it. Thus we can define the rate costant for each process:

k_F^S: rate constant for radiative deactivation (fluorescence)

k_{IC}^S: rate constant for internal conversion

k_{ISC}: rate constant for intersystem crossing

IC and ISC are the only two non-radiative deactivation channels in the absence of intermolecular interactions. Thus:

$$k_{nr}^{S} = k_{IC}^{S} + k_{ICS}$$

Let's analyse a prototypical experiment. When a diluted chromophore in solution A is excited with a short pulse of light a certain number of molecules reach the excited state S_1. The return to S_0 through radiative or non-radiative decays or the intersystem crossing can be expressed as a classical chemical kinetics:

$$\frac{-d\left[\ {}^1A^*\ \right]}{dt} = (k_r^S + k_{nr}^S)[\ {}^1A^*\ ]$$

Supposing that at time zero the amount of molecules in the excited state is $\left[\ {}^1A^*\ \right]_0$ the time integration allows to write:

$$\left[\ {}^1A^*\ \right] = [\ {}^1A^*\ ]_0 \exp\left(-\frac{t}{\tau_S}\right)$$

Where τ_S is the singlet lifetime and depends by the rate constants of the processes occurring from S_1:

$$\tau_S = \frac{1}{k_F^S + k_{nr}^S}$$

At any times during the deactivation the fluorescence intensity I_F depends by the number of molecules in the excited state. The proportionality of molecules relaxing with the emission of a photon at any time is:

$$i_F(t) = k_r^S\left[\ {}^1A^*\ \right] \ = k_r^S\left[\ {}^1A^*\ \right]_0 \exp\left(-\frac{t}{\tau_S}\right)$$

Clearly, in a real experiment the intensity is affected by many external factor and so the measured intensity is only proportional to I_F.

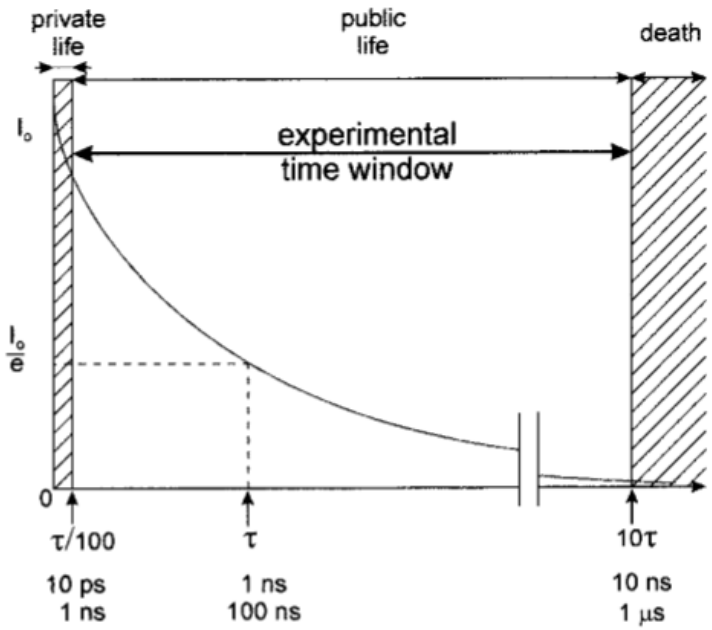

Figure 6: Graphic representation of the fluorescent decay. Reproduced from ref.[8] with permission Copyright © 2001, John Wiley and Sons.

τ_S represents the exact time at which the population of the excited state reach $1/e$ of the initial population and so it is not the total average time of the decay that is normally considered 10 times longer (Figure 6)[6].

The above discussion for singlet states on the singlet states and fluorescence lifetime is analogous for triplets and phosphorescence so that these latter will not be discussed.

2.6 Quantum efficiency

The quantum efficiency or quantum yield of a process (Φ) is defined by the amount of molecules in the excited state undergoing to a specific process with respect to the total amount of excited molecules[7][8]. If we take into consideration the fluorescent emission:

$$\Phi_F = \frac{k_F^S}{k_F^S + k_{nr}^S} = k_F^S \tau_S$$

In other words the fluorescence quantum yield is the ratio of the number of emitted photon ($i_F(t)$) to the number of adsorbed photon ($\left[\ {}^1A^*\ \right]_0$):

$$\frac{i_F(t)}{\left[\ {}^1A^*\ \right]_0} = \ k_F^S \exp(-\frac{t}{\tau_S})$$

If we integrate over an infinite time:

$$\frac{1}{\left[\ {}^1A^*\ \right]_0} \int_0^\infty i_F(t)\, dt = \ k_F^S \tau_S = \ \Phi_F$$

The fluorescent quantum yield (Φ_F) can also be written as:

$$\Phi_F = \frac{\tau_S}{\tau_r}$$

Where τ_r is the radiative lifetime if the state could only be deactivated through the emission of a photon:

$$\tau_r = \frac{1}{k_F^S}$$

From this last equation is clear that there is a direct proportionality between the decay time and the quantum efficiency. This means that variation of the environment (temperature, pressure, ecc..) will affect the two values proportionally.

2.7 References

[1] Klessinger, M., Michl, J., **1995** Excited state and photochemistry of organic molecules, Jonh Wiley and Sons, Inc., New York.

[2] Turro, N.J., Ramamurthy, V., Scaiano, J.C. **2009** Principles of molecular photochemistry, University science books, Sausalito.

[3] Birks J. B. **1970** Photophysics of Aromatic Molecules, Wiley, London.

[4] Forni, A.; Lucenti, E.; Botta, C.; Cariati, E., Metal free room temperature phosphorescence from molecular self-interactions in the solid state. *Journal of Materials Chemistry C* **2018,** *6* (17), 4603-4626.

[5] Herzberg G. **1966** Molecular Spectra and Molecular Structure. III Electronic Spectra and Electronic Structure of Polyatomic Molecules, Van Nostrand Reinhold Company, New York.

[6] Jaffe ´ H. H. and Orchin M. **1962** Theory and Applications of Ultraviolet Spectroscopy, John Wiley & Sons, New York.

[7] Lipson, R.H. **2009** Ultraviolet and visible adsorption spectroscopy, in Encyclopedia of applied spectroscopy, Wiley-VCH Verlag GmbH, Weinheim.

[8] Valeur, B., Berberan-Santos, M.N., **2012** Wiley-VCH Verlag and Co. Weinheim, Germany.

3 Aggregation Induced Emission

3.1 Introduction

Historically, in the luminescence field the formation of aggregates has always represented a big issue due to the so-called Concentration Quenching (CQ): the increase of the concentration of a luminophore in solution quenches its emission. This effect is quite common for most of aromatic hydrocarbons[1] and their derivatives that, in the classical consideration, "form aggregates[2-6]" characterized by non-emissive of poorly emissive behaviour. For this reason, this process is defined as Aggregation-Caused Quenching (ACQ).

A prototypical example of an ACQ fluorophore is fluorescein (See Figure 1 left). This chromophore displays a bright green emission in water solution which is gradually weakened by the progressive addition of a non-solvent (e.g., acetone). The low solubility of fluorescein in acetone causes a progressive increase of the local concentration of the chromophore and the CQ starts to become visible when the acetone fraction reaches 60 vol%. Further increasing of the acetone fraction causes the formation of nanoscopic aggregates and the complete quench of the fluorescein emission. The planar polycyclic structure of fluorescein makes the molecules prone to form π-π stacking interaction leading to the formation of dentrimental species, as excimers, responsible for the observed ACQ.

The ACQ phenomenon has strongly limited the number of applications of the numerous luminophores identified through dilute solution-screening in research laboratories.[7-14] In particular, luminophores are used as sensor to detect bioactive molecules in physiological media or as probe to monitor ionic species in ecological systems[8]. Although polar functionalities can be introduced into hydrophobic chromophores (polycyclic aromatic hydrocarbons PAH) to increase their polarity, and so their water solubility, the introduction can only delay or partially mitigate the aggregation process. In parallel, the ACQ effect is a thorny issue in the fabrication of OLEDs and optoelectronic devices in general, in which chromophores are frequently used as aggregates in thin films[7].

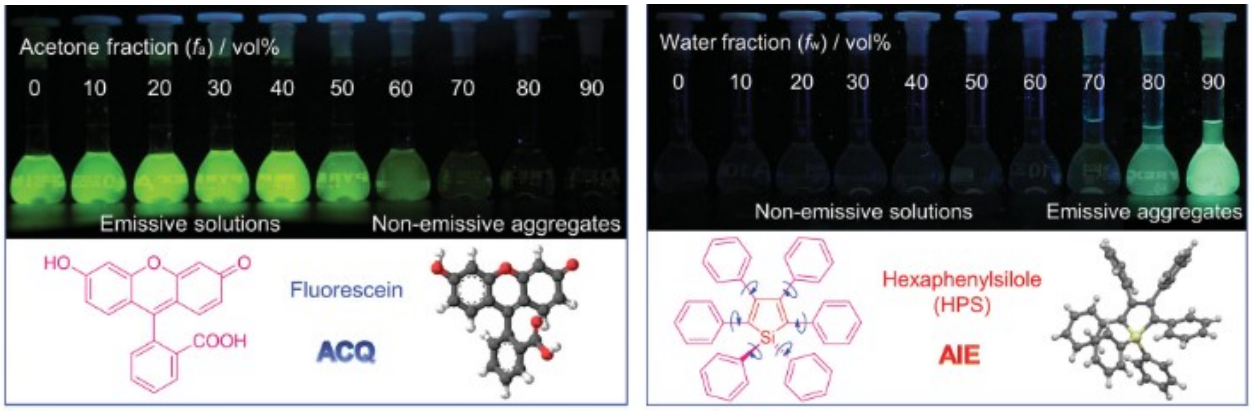

*Figure 1: Pictures of fluorescein (Left) and **HPS** (Right) with different non-solvents amount. Reproduced with permission from ref.[42]*

As elucidated before, ACQ is a harmful effect even for practical applications and almost obiquitously observed for classic chromophores.

Fortunately, almost 20 years ago an opposite behaviour, the Aggregation-Induced Emission (AIE) effect, was observed and describe by Tang and co-workers. In the AIE process, poorly emissive chromogens with propeller-shaped structures are induced to emit through aggregates formation. The very first example of chromophore displaying AIE behaviour was Hexaphenylsilole (**HPS**) (See Figure 1 Right). If **HPS** is dissolved in a good solvent, as THF, no emission is detected for the solution, while increasing the water fraction up to 80% the fluorescence is turned on and the mixture becomes highly emissive when 90% of water is reached, thanks to the heavy aggregation of **HPS** induced by water.

For a long times researchers have tried to avoid the formation of aggregates and the consequent arise of the ACQ effect through various chemical, physical and engineering approaches with the modification of the emissive core with bulky cyclic, spiral kinks and dendritic wedges.[10-14] The results of these attempts were frequently unsatisfactory and brought to the creation of new problems. In fact, most of the times the aggregation can be only temporarily prevented because the aggregate formation is a natural process for molecules in closed proximity. The AIE effects have provided a new starting point for scientists in the study of light-emissive properties of luminophores and many new strategies were developed to prepare more and more performing AIEgens since the first discovery. Moreover, AIE, oppositely to ACQ, is a constructive effect and allows to take advantage of the aggregation process instead of working against it.

The great work done along the last decades has brought to a better comprehension of the mechanism behind the AIE, to the design of many new AIEgens and to the exploration of their technological applications.

3.2 Mechanism

The understanding of AIE mechanism was crucial in order to guide the molecular engineering effort in the right direction. Mechanistically, more than one process can cooperate to the AIE effect:

- Restriction of Intramolecular Motion (RIM)[15]
- J-Aggregate Formation (JAF)[1]
- Excited-State Intramolecular Proton Transfer (ESIPT)[16]
- Twisted Intramolecular Charge Transfer (TICT)[17-18]

However, RIM is the mechanism most frequently associated to AIE phenomena.

3.2.1 RIM

In physics every movement, including molecular vibrations and rotations, consumes energy. In **HPS**, the six phenyl rings are free to rotate independently from the central silole core. Similarly, in tetraphenylethene (**TPE**, see Figure 2), that displays a configuration different from that of **HPS**, the four phenyl rings have the same freedom to rotate and twist. An isolated molecule of **TPE**, for example in a diluted solution, can dissipate the excess of energy in a non-radiative way through the active intramolecular rotations. On the contrary, the physical constriction induced by the aggregation of **TPE** molecules causes the restriction of the intramolecular rotation (RIR, see Figure 2) and blocks the radiationless relaxation channels favoring the radiative decays to the ground state.

Control experiments run on **HPS** have demonstrated that by increasing solvent viscosity, decreasing solution temperature and pressurizing solid films the **HPS** emission is enhanced verifying that RIR is the main cause of the AIE effect of this molecule.[18-20]

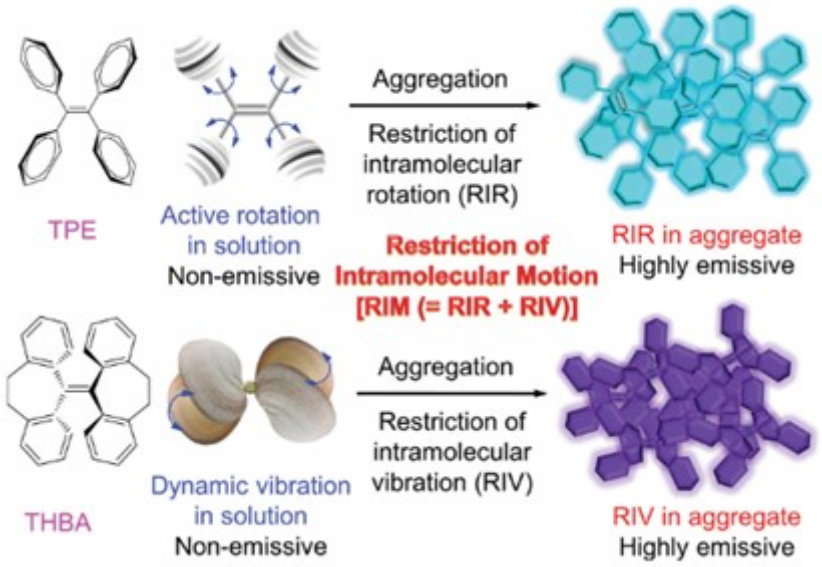

*Figure 2: Schematic representation of the AIE effect on **TPE** and **THBA**. Reproduced with permission from ref.[42] © 2014 WILEY-VCH Verlag GmbH & Co. KGaA, Weinheim.*

Even if in many cases the AIE behaviour is associated to the RIR mechanism, some AIE-systems, such 10,10',11,11'-tetrahydro-5,5'-bidibenzo[*a*,*d*][7]annulenylidene (**THBA**, see Figure 2), do not carry any rotatory elements that can dissipate the energy excess[21] so that a different explanation had to be provided. **THBA** is composed by two non-coplanar flexible parts in each of which two phenyl rings are connected by a bendable flexure. This flexibility allows isolated **THBA** molecules to bend or vibrate to relax in non-radiative ways from the excited states. Again, the physical constrain generated by the aggregation locks the vibrations opening the radiative decay channel. In conclusion, the Restriction of Molecular Rotations (RIR) or Vibrations (RIR) are the main causes of the AIE behaviour for all the propeller-shaped or shell-shaped molecules respectively.

Differently from **HPS**, **TPE**-based AIEgens can even undergo photo-induced E-Z isomerization (EZI) process to non-radiatively annihilate the excited states.[22-26] In order to clarify which mechanism plays a predominant role in the emission quenching in diluted solution Tang and co-workers have design molecule **1** whose E/Z isomers are separable and discernible with ^{1}H NMR analyses.[27]

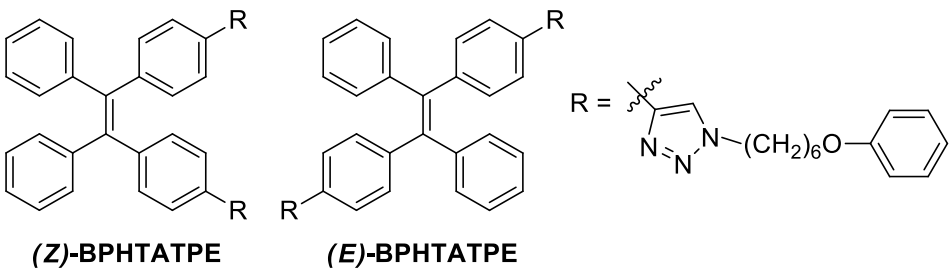

*Figure 3: Stereoisomers of a TPE derivative (**BPHTATPE**).*

The irradiation of ***(E)*-BPHTATPE** with a high power UV lamp (1.10 mW/cm^2) causes a linear increase of the *Z* isomer to 35% in the first 50 minutes of irradiation and afterwards it slow down reaching

50% in 150 minutes. Surely the EZI process can occur under these conditions but in a photoluminescence spectrum measurement a much lower power lamp (52 Mw/cm^2) is normally used. Setting the experiment to this milder conditions and exciting the sample at 322 nm for 30 min the ^{1}H NMR spectra does not show any appreciable change revealing that the EZI process has not occurred.

This previous experiment demonstrates that in the condition under which we ordinarily observe or measure the PL of a chromophore and specifically an AIEgen such as **TPE**, the alchene double bond cannot be broken. Thus, the EZI is not a competitive process in the non-radiative deactivation observed for TPE-based AIEgens in solution where the quenching effect is mostly ascribable to the active rotation of the phenyl rings.

To completely demonstrate the central role played by the RIM in the arise of the AIE behaviour, Dong at al. have convinientely lock the phenyl rings through an oxygen bridging atom through McMurry coupling (see Figure 4).[28]

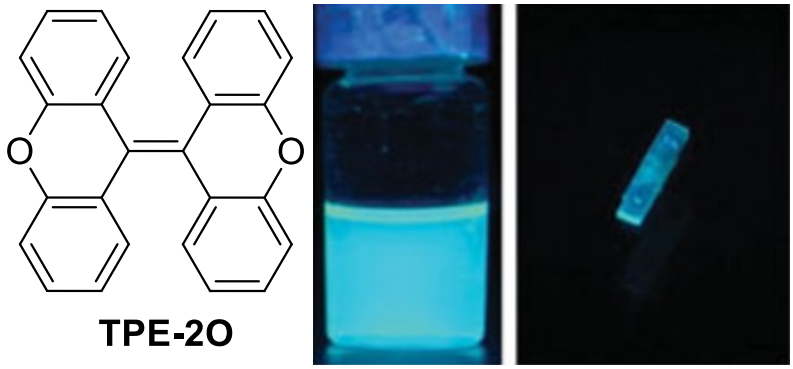

Figure 4: **TPE-2O** *structure and pictures under the UV lamp of its solution (Left) and Crystal (Right).* Reproduced with permission from [28] *©2012, Royal Society of Chemistry.*

The PL spectra of **TPE-2O** crystals and diluted solution completely overlap due to its fully locked phenyl rings. The quantum efficiency is 30.8% and 30.1% for crystals and solution respectively. This means that the molecules do not display AIE behaviour since the bridging oxygens hinder the non-radiative deactivation through intermolecular rotation. However, surprisingly, the emission is not quenched by the aggregation. This observation was explained by the twisted conformation of **TPE-2O** that prevents a close packing and the formation of harmful species such as excimers.

Theoretically, any molecule with the proper structure can undergo intramolecular rotation but not every of them will show AIE behaviour. To explain this, Tang proposed the following arguments[17].

As mentioned, an elegible AIEgen molecule should have at least a rotatable bond through which non-radiatively dissipate the energy excess in solution. This situation can be conveniently simplified by two units, A and B, linked through a single bond (see Figure 5-a). In diagram *a*, ϑ_r defines the structural flexibility of the molecule while Ψ_r describes the conformational planarity. In most of the ACQ moieties the two units A and B are arranged in a planar conformation with $\Psi_r \approx 0°$ in order to maximize the electronic conjugation and minimize the potential energy. The extension of the π-conjugation endows the connecting single bond of a pseudo-double-bond character with partial hindering of intermolecular rotation. The two chromophoric units could still swing to a small extend (ϑ_r) but this low-frequency motion is insufficient to quench the emission, on the contrary the small reorganization energy due to the rigidification of the system promote the luminescent process in

the solution state. In contrast, A' and B' (Figure 5-a) experiment a larger dihedral angle Ψ_r' in a AIEgen prototype molecule, with a lower overlap between the π-electron clouds and so a weaker conjugation posing a limited restrain to the intramolecular rotations. The low-frequency energy leads to a shallower potential energy surface, meaning that there exists a little energy barrier to a conformational change. The amount of energy dissipated through twisting becomes greater because ϑ_r can now vary in a wider range weakening the emission of the isolated chromophore in solution. According to this model the luminescent behaviour of a molecule could be predicted from Ψ_r and ϑ_r which describe the planarity of the molecule and the rotatability of the units, respectively.

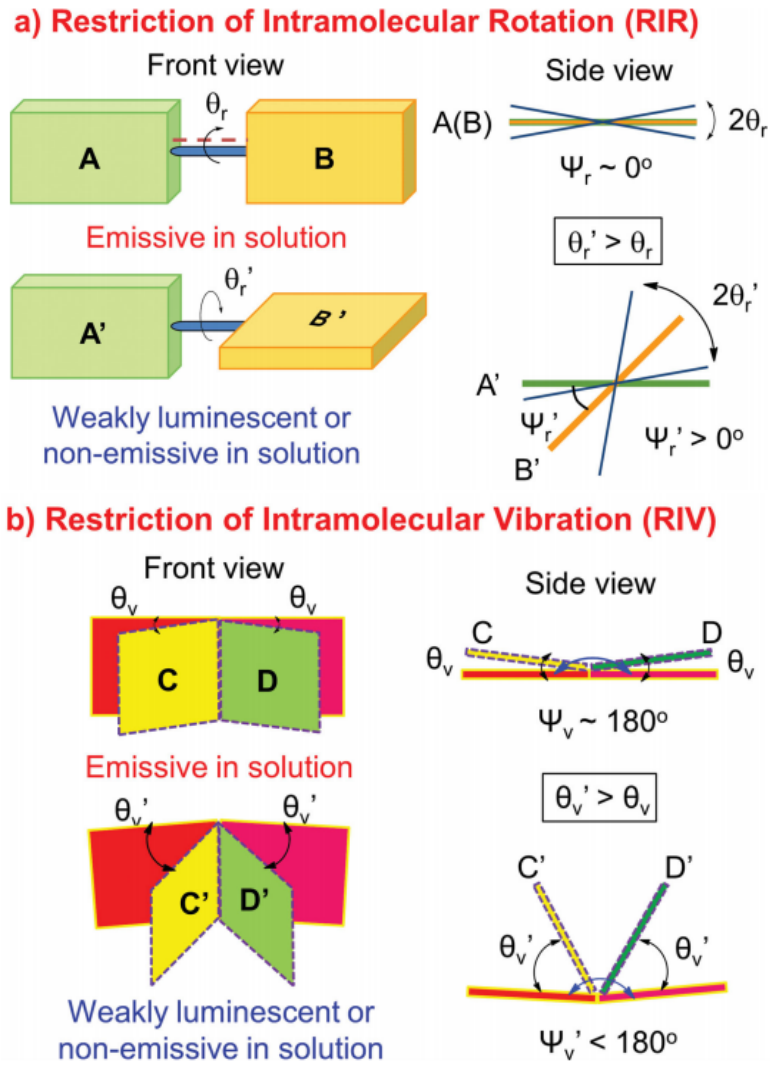

Figure 5: Illustration of the RIR (a) and RIV (b) mechanism. Reproduced with permission from [17] ©2009, Royal Society of Chemistry.

Even if the model discussed above is valid for **TPE**-based chromophores other AIE luminogens, for example **THBA**, does not show any rotatable bond and so cannot undergo to the RIR mechanism to justify its AIE behaviour. This suggest that another model must be taken in consideration in order to explain the quenching of the emission detected in diluted solution of these luminophores. Model *b* proposed by Tang and reported in Figure 5-b, graphically resumes how the AIE process depends on the molecular flexibility and the vibrational amplitude of molecules. In this case, the prototypical molecule is composed by two units, C and D, junctioned by an aromatic or alicyclic ring. Here, Ψ_v and ϑ_r define the dihedral angle between the two units and the extend of intramolecular vibration,

defining the conformational planarity and the structural stiffness of the molecules. As in case a), the planar conformation ($\Psi_v \approx 180°$) is associated to a strong π-conjugation between units, that can still oscillate in a small amplitude (ϑ_v) which is insufficient to prevent the radiative decay in diluted solutions. The conformational stiffness generates a small overall reorganization energy for the molecules and thus solutions are emissive while the aggregation can promote the instauration of strong π-π stacking interactions causing the formation of deleterious species. On the other side, if the two units, C' and D', are not coplanar due to the non-planarity of the inter-chromophore junction ($\Psi_v' < 180°$) the overlap between the π-electron clouds decreases. As in the previous case, these are the perfect conditions to observe a large vibrational amplitude (ϑ_v) that better dissipates the energy reducing the emissive intensity in solution.

3.2.2 J-Aggregate Formation (JAF)

In order to better understand the role of J-aggregation in the AIE-world it is necessary to introduce the exciton model proposed by Kasha for the description of this mechanism.

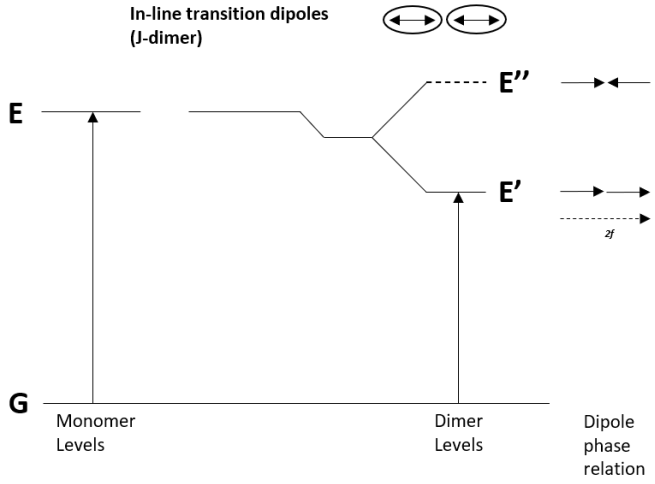

Figure 6: Modified Jablonsky diagram for a generic J-aggregate compound.

We may assume that the exciton model can be approximated with a quasi-classical vector model, thus, we have to consider the transition moment dipoles electrostatically. The molecules will be approximated as an oval with a double arrow representing the polarization axis for the electronic transition.

In a J-aggregate, typically, the transition dipoles are oriented with no overlap between adjacent molecules (see Figure 6). In a J-dimer the exciton model provides the split of the excited state due to the instauration of coulombian forces. In particular, the in-phase transition will be stabilized while the out-of-phase transition will be destabilized. The oscillator strength for the transition G → E' will be ***2f*** while for G → E'' will be virtually null, thus, the direct population of E'' is theoretically prohibited.

Usually, J-aggregated dyes show bathocromic shift, an increase of the absorption coefficient and in some cases a red-shift and an enhancement of the emission with respect to their diluted solution showing AIE or at least Aggregation Enhanced Emission (AAE) effects.[30,31] Differently from RIM mechanism, JAF dyes could be emissive already as isolated molecules because there is no

mechanism able to non-radiatively deactivate the excited state. At the same time, the enhancement of the emission intensity in the aggregate or solid state is not always observed.

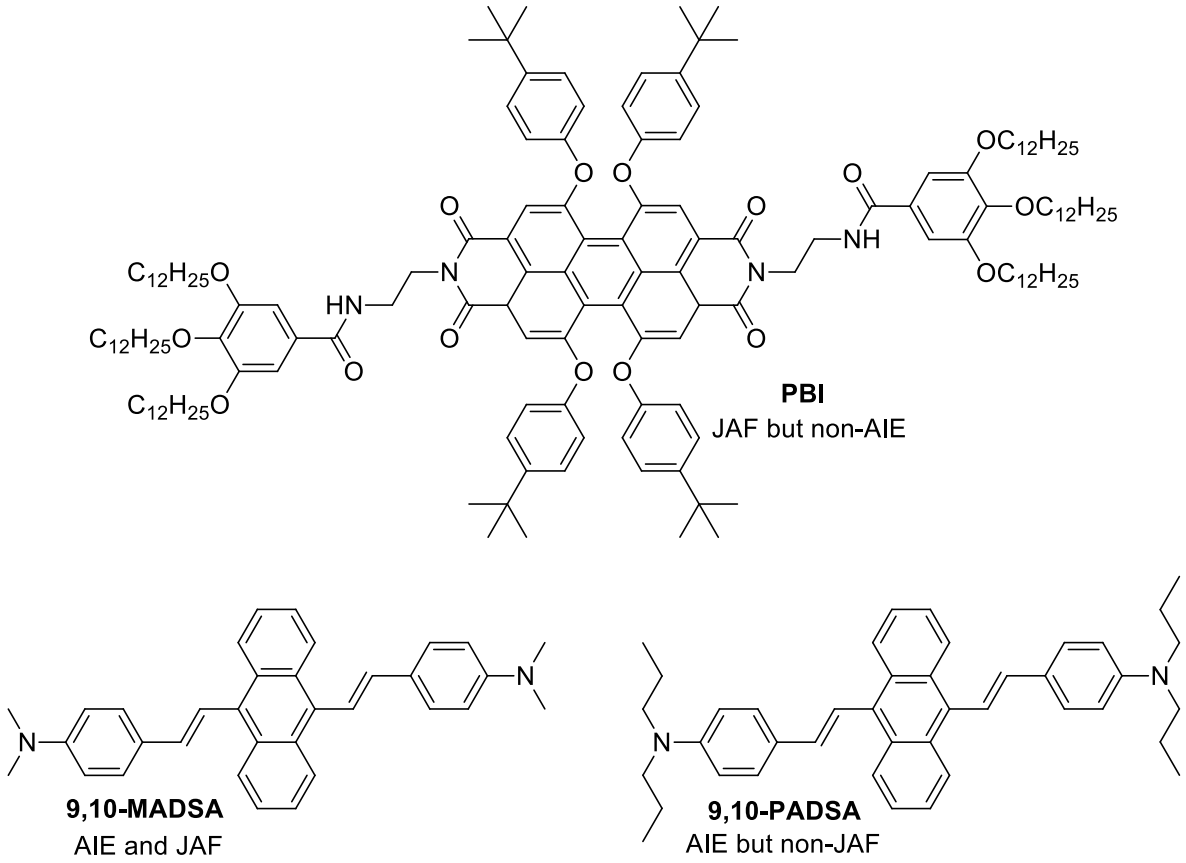

*Figure 7: Chemical structures of **PBI**, **9,10-MADSA** and **9,10-PADSA**.*

For example, the perylene bisimide derivative **PBI** forms J-aggregates in appropriated condition. In particular, in methylcyclohexane (MCH) the sharper absorption band and the bathochromic effect measured in comparison to dichloromethane diluted solution clearly indicate the formation of J-aggregates in the nonpolar solvent. However, diluted solutions of **PBI** in polar solvents display intense fluorescent emission with 100% quantum yield while in MCH, where J-aggregates are formed, is 82% and further decreases to 20% after gelification. In synthesis, the JAF in this case does not play a constructive role but in opposition the effect seems to make the **PBI** an ACQ active species.[32]

Curiously, both 9,10-Bis(*p*-dimethylaminostyryl)anthracene (**9,10-MADSA**) and 9,10-Bis(*p*-dipropylaminostyryl)anthracene (**9,10-PADSA**) display AIE effects but only **9,10-MADSA** forms J-aggregates. These two dyes share the same chemical structure with only small differences and it is obvious that the AIE mechanism should be the same, involving restriction of rotation around the connecting single bonds in the solid state.[33]

In summary, a direct correlation between JAF and AIE cannot be drawn because rigid molecules displaying JAF could still undergo quenching effects due to strong π-π interactions in the aggregate state. More flexible JAF dyes can surely display AIE but this effect has to be associated to the RIM more than to JAF, which can only partially cooperate in the rigidification of the structure in the solid state but does not provide the necessary mechanism for solution quenching.

3.2.3 ESIPT

The extremely fast photoinduced proton transfer process was extensively studied due to the great appeal of molecules displaying ESIPT as functional materials. [34] These dyes are stable as enol (E) in the ground state and as keton (K) in the excited state, in fact, when an ESPITgen is excited a four-level cycle occurs E-E*-K*-K. This process is accompanied by a large Stokes shift without self-absorption. Even if some ESIPT dyes have enhanced emission in the aggregate form this process alone does not fully explicate the observed AIE.

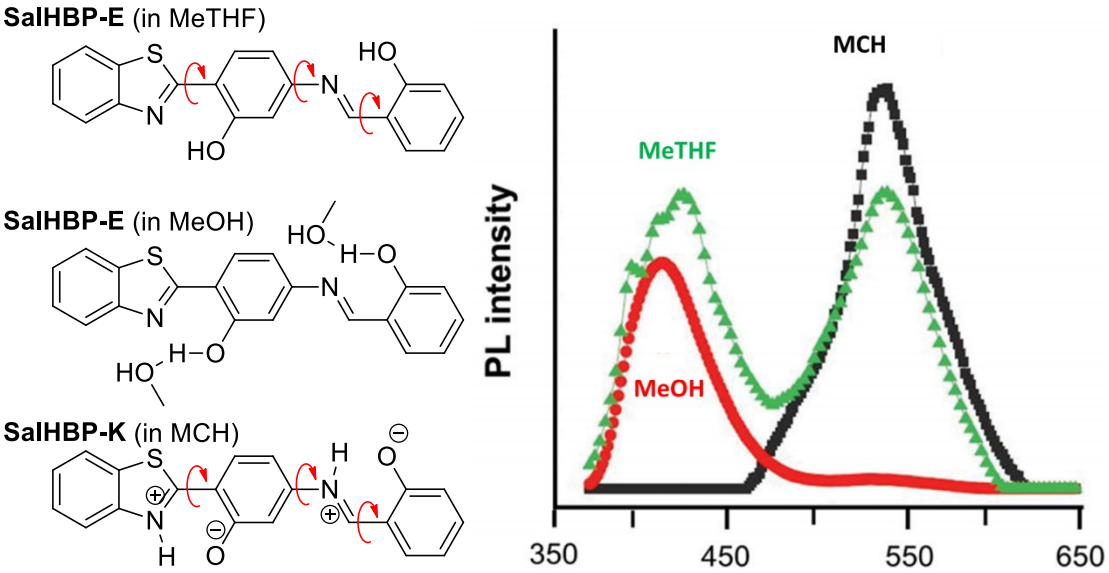

*Figure 8: Conformational changes in the **SalHBP** conformation and relative fluorescent emission. Modified with permission from ref.[35] © 2011 Académie des sciences. Published by Elsevier Masson SAS.*

In the AIE-active ESIPT luminogen **SalHBP** (see Figure 8) the proton transfer is strongly affected by solvent properties.[35] In methyltetrahydrofuran (MeTHF) two weak emissions are observed from the enol and keto forms that are in equilibrium. In this case the molecule may undergo conformational changes through rotation around the single bonds quenching the radiative decays. In a protonic solvent, such as methanol, the emission associated to the enol form completely covers the keto one. The intramolecular H-bonding is here substituded by the formation of H-bonds with the solvent that leads to a partial restriction of the intramolecular rotation thus the emission is not efficiently quenched. In methylcyclohexane (MCH), where no interaction between the solvent and the dye is possible the ESPIT process is fully active, thus only the keto emission is visible but most of the energy is dissipated through active rotation. Regardless the ESIPT process, by lowering the temperature to 140 K all the solutions show enhanced emission. This means that the enhancement of the viscosity plays a significant role in the rigidification of the environment and hinders the radiationless decays leading to a large increase of the emission.

Differently form **SalHBP** the modified salicylaldehyde azine (**MSAA**, see Figure 9) displays a greater structural flexibility but still undergoes ESIPT.[36] This feature gives to **MSAA** a larger AIE effect because in ethanol solutions the rotations around the C-C and N-N single bonds actively quench the emission while the addition of water causes the arise of the emission locking these free rotations. In this case, rather than being the main mechanism behind the AIE behaviour, ESIPT works as a tuner

of the emission in the crystalline states, by changing the emissions wavelength in the two polymorphs.

As in the case of JAF, ESIPT could have a role in the enhancement of the emission in the aggregate state but it has always to work cooperatively with RIM to result in an AIEgen.

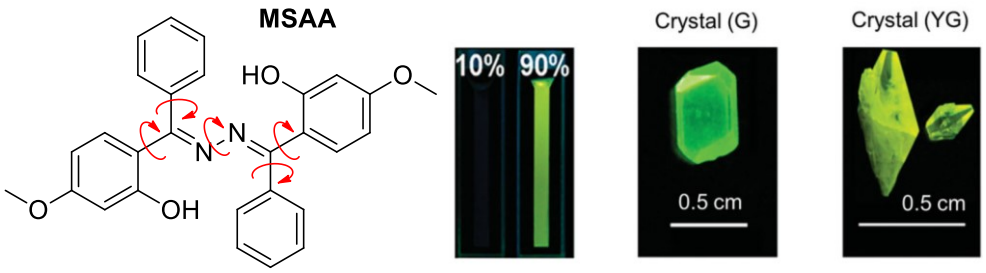

*Figure 9: Structure of **MSAA** and pictures of its solution, aggregates and crystals. Reproduced with permission from ref.[36] **© 2013 American Chemical Society.***

3.2.4 TICT

For systems with donor-acceptor (D-A) structure the AIE process can be the effect of the formation of a "dark state" with TICT character in solutions while aggregation inhibits the transformation of locally excited states (LE) into TICT states.[37,38] However, it has to be mentioned that the TICT can provide a solid explanation to AIE only in specific solvent condition.

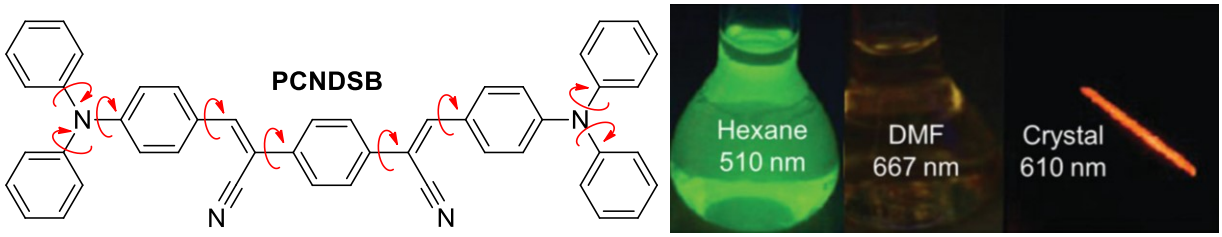

*Figure 10: **PCNDSB** chemical structure and rotatable bonds. Pictures of different **PCNDSB** solutions and crystals). Reproduced with permission from ref.[38] © 2011 Elsevier B.V.*

1,4-bis[1-cyano-2-(4-(diphenylamino)phenyl)vinyl]benzene (**PCNDSB**, see Figure 10) is composed by two D-A subunits and displays remarkable solvatochromic effect with red-shifting of the emission from green (510 nm) to red (667 nm) going from hexane to DMF. In the apolar solvent the planar conformation of **PCNDSB** is stabilized by the conjugation between the units giving rise to a sharp fluorescent emission from a locally excited (LE) state. In a polar solvent the two units are twisted and the LE state is transformed in a TICT state with complete charge separation between D and A. The TICT state is much more susceptible to quenching process and, with a quantum yield equal to 31% for the solid state (610 nm), this material clearly manifests AIE activity. The TICT inhibition can effectively explain the quenching in DMF solution but the fluorescent emission in hexane and the strong red-shifted emission of crystals can hardly be fully explained only considering the TICT[38,39].

Differently, aggregation studies on modified boron dipyrromethene (**MBODIPY**, see Figure 11) run in THF/water mixure have revealed that a small addition of water in a THF solution of **MBODIPY** strongly quenches and red-shifts the emission because it increases the polarity promoting a TICT state. However, further additions of water revitalize the emission that is now blue-shifted by the hydrophobic environment generated in the aggregates that also restricts the intramolecular

motion.[40] Similarly, **TPA-DCM** (see Figure 12) emission is weakened and red-shifted by a small addition of water in its THF solution revealing the TICT promotion.

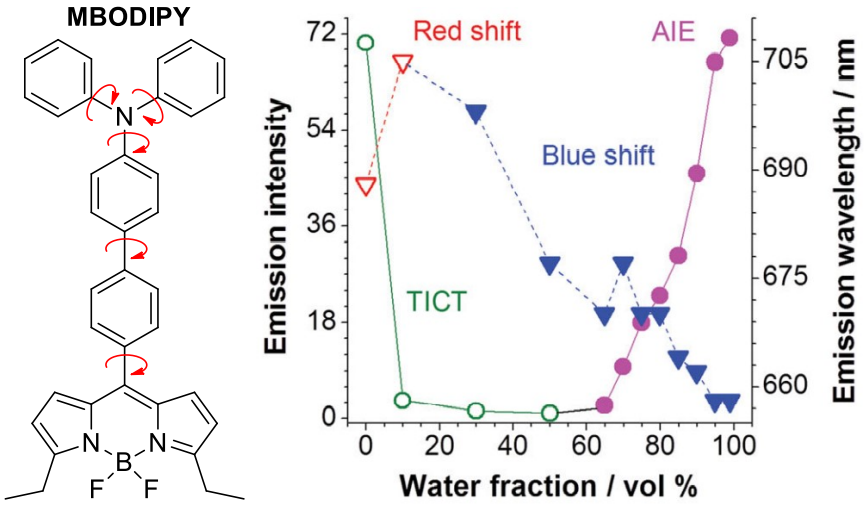

*Figure 11: **MBODIPY** chemical structure and rotatable bonds. Waterfraction (f_w) dependend behaviour. Reproduced with permission from ref.[40] ©2009 American Chemical Society.*

Differently, when aggregates are formed through addition of greater amount of water the emission is not intensified and the ACQ prevails. The hydrophobic environment generated through aggregation disfravors the TICT process that quenches the emission in polar solvent but the **TPA-DCM** core is already very rigid and the aggregation cannot restrict any rotational motion thus, the molecule does not exhibit AIE effects.[41] This behaviour indicates that not all the TICT molecules are AIE because the amplitude of the rotations involved in the TICT are not necessarily enough energetic to be the main reason of the observed quench and so the AIE activity of a molecule undergoing TICT depends by its flexibility and rotational motion.

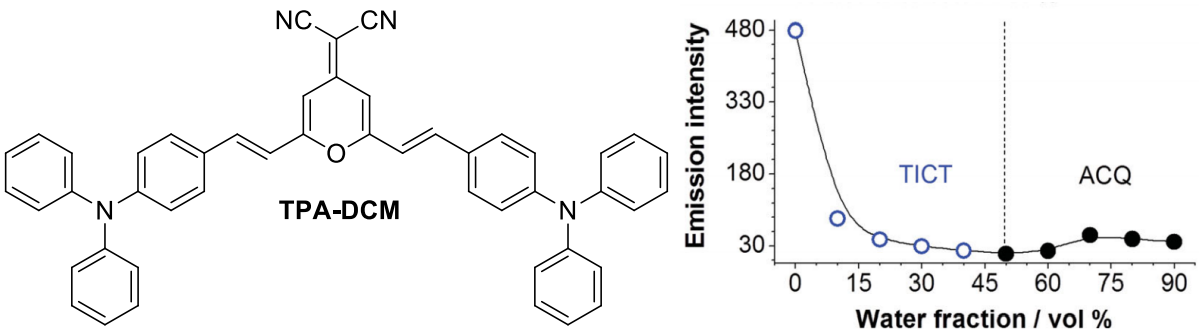

*Figure 12: **TPA-DCM** chemical structure and rotatable bonds. Waterfraction (f_w) dependend behaviour). Reproduced with permission from ref. [41] © 2012 WILEY-VCH Verlag GmbH & Co.*

3.3 Conclusion

Based on the above reported examples of the literature it was concluded that RIM, whose essence is the structural rigidification or conformational stiffening, is the only mechanism through which a dye can develop a pure AIE behaviour even if a partial overlap with others mechanism such JAF, ESIPT and TICT is always possible.

3.4 References

[1] Bünau, G., J. B. Birks: Photophysics of Aromatic Molecules. Wiley-Interscience, London 1970. 704 Seiten. Preis: 210s. *Berichte der Bunsengesellschaft für physikalische Chemie* **1970,** *74* (12), 1294-1295.

[2] a) Zhang, X.; Görl, D.; Stepanenko, V.; Würthner, F., Hierarchical Growth of Fluorescent Dye Aggregates in Water by Fusion of Segmented Nanostructures. *Angewandte Chemie International Edition* **2014,** *53* (5), 1270-1274.

b) Thomas, S. W.; Joly, G. D.; Swager, T. M., Chemical Sensors Based on Amplifying Fluorescent Conjugated Polymers. *Chemical Reviews* **2007,** *107* (4), 1339-1386.

[3] Hoeben, F. J. M.; Jonkheijm, P.; Meijer, E. W.; Schenning, A. P. H. J., About Supramolecular Assemblies of π-Conjugated Systems. *Chemical Reviews* **2005,** *105* (4), 1491-1546.

[4] Bunz, U. H. F., Poly(aryleneethynylene)s: Syntheses, Properties, Structures, and Applications. *Chemical Reviews* **2000,** *100* (4), 1605-1644.

[5] Hide, F.; DÍaz-GarcÍa, M. A.; Schwartz, B. J.; Heeger, A. J., New Developments in the Photonic Applications of Conjugated Polymers. *Accounts of Chemical Research* **1997,** *30* (10), 430-436.

[6] Borisov, S. M.; Wolfbeis, O. S., Optical Biosensors. *Chemical Reviews* **2008,** *108* (2), 423-461.

[7] Tang, C. W.; VanSlyke, S. A., Organic electroluminescent diodes. *Applied Physics Letters* **1987,** *51* (12), 913-915.

[8] Jares-Erijman, E. A.; Jovin, T. M., FRET imaging. *Nature Biotechnology* **2003,** *21* (11), 1387-1395.

[9] Saigusa, H.; Lim, E. C., Excimer Formation in van der Waals Dimers and Clusters of Aromatic Molecules. *Accounts of Chemical Research* **1996,** *29* (4), 171-178.

[10] Wang, J.; Zhao, Y.; Dou, C.; Sun, H.; Xu, P.; Ye, K.; Zhang, J.; Jiang, S.; Li, F.; Wang, Y., Alkyl and Dendron Substituted Quinacridones: Synthesis, Structures, and Luminescent Properties. *The Journal of Physical Chemistry B* **2007,** *111* (19), 5082-5089.

[11] Hecht, S.; Fréchet, J. M. J., Dendritic Encapsulation of Function: Applying Nature's Site Isolation Principle from Biomimetics to Materials Science. *Angewandte Chemie International Edition* **2001,** *40* (1), 74-91.

[12] Nguyen, B. T.; Gautrot, J. E.; Ji, C.; Brunner, P.-L.; Nguyen, M. T.; Zhu, X. X., Enhancing the Photoluminescence Intensity of Conjugated Polycationic Polymers by Using Quantum Dots as Antiaggregation Reagents. *Langmuir* **2006,** *22* (10), 4799-4803.

[13] Chen, L.; Xu, S.; McBranch, D.; Whitten, D., Tuning the Properties of Conjugated Polyelectrolytes through Surfactant Complexation. *Journal of the American Chemical Society* **2000,** *122* (38), 9302-9303.

[14] Taylor, P. N.; O'Connell, M. J.; McNeill, L. A.; Hall, M. J.; Aplin, R. T.; Anderson, H. L., Insulated Molecular Wires: Synthesis of Conjugated Polyrotaxanes by Suzuki Coupling in Water. *Angewandte Chemie International Edition* **2000,** *39* (19), 3456-3460.

[15] Chen, J.; Law, C. C. W.; Lam, J. W. Y.; Dong, Y.; Lo, S. M. F.; Williams, I. D.; Zhu, D.; Tang, B. Z., Synthesis, Light Emission, Nanoaggregation, and Restricted Intramolecular Rotation of 1,1-Substituted 2,3,4,5-Tetraphenylsiloles. *Chemistry of Materials* **2003,** *15* (7), 1535-1546.

[16] Li, H.; Zhang, X.; Zhang, X.; Yang, B.; Yang, Y.; Wei, Y., Ultra-stable biocompatible cross-linked fluorescent polymeric nanoparticles using AIE chain transfer agent. *Polymer Chemistry* **2014,** *5* (12), 3758-3762.

[17] Hong, Y.; Lam, J. W. Y.; Tang, B. Z., Aggregation-induced emission: phenomenon, mechanism and applications. *Chemical Communications* **2009,** (29), 4332-4353.

[18] Hu, R.; Leung, N. L. C.; Tang, B. Z., AIE macromolecules: syntheses, structures and functionalities. *Chemical Society Reviews* **2014,** *43* (13), 4494-4562.

[19] Fan, X.; Sun, J.; Wang, F.; Chu, Z.; Wang, P.; Dong, Y.; Hu, R.; Tang, B. Z.; Zou, D., Photoluminescence and electroluminescence of hexaphenylsilole are enhanced by pressurization in the solid state. *Chemical Communications* **2008,** (26), 2989-2991.

[20] Li, S.; Wang, Q.; Qian, Y.; Wang, S.; Li, Y.; Yang, G., Understanding the Pressure-Induced Emission Enhancement for Triple Fluorescent Compound with Excited-State Intramolecular Proton Transfer. *The Journal of Physical Chemistry A* **2007,** *111* (46), 11793-11800..

[21] a) Luo, J.; Song, K.; Gu, F. l.; Miao, Q., Switching of non-helical overcrowded tetrabenzoheptafulvalene derivatives. *Chemical Science* **2011,** *2* (10), 2029-2034.

b) Li, Z.; Qin, A., Diverge from the norm. *National Science Review* **2014,** *1* (1), 22-24.

[22] Schilling, C. L.; Hilinski, E. F., Dependence of the lifetime of the twisted excited singlet state of tetraphenylethylene on solvent polarity. *Journal of the American Chemical Society* **1988,** *110* (7), 2296-2298.

[23] Shultz, D. A.; Fox, M. A., Effect of phenyl ring torsional rigidity on the photophysical behavior of tetraphenylethylenes. *Journal of the American Chemical Society* **1989,** *111* (16), 6311-6320.

[24] Simeonov, A.; Matsushita, M.; Juban, E. A.; Thompson, E. H. Z.; Hoffman, T. Z.; Beuscher Iv, A. E.; Taylor, M. J.; Wirsching, P.; Rettig, W.; McCusker, J. K.; Stevens, R. C.; Millar, D. P.; Schultz, P. G.; Lerner, R. A.; Janda, K. D., Blue-Fluorescent Antibodies. *Science* **2000,** *290* (5490), 307.

[25] Waldeck, D. H., Photoisomerization dynamics of stilbenes. *Chemical Reviews* **1991,** *91* (3), 415-436.

[26] Saltiel, J.; D'Agostino, J. T., Separation of viscosity and temperature effects on the singlet pathway to stilbene photoisomerization. *Journal of the American Chemical Society* **1972,** *94* (18), 6445-6456.

[27] Wang, J.; Mei, J.; Hu, R.; Sun, J. Z.; Qin, A.; Tang, B. Z., Click Synthesis, Aggregation-Induced Emission, E/Z Isomerization, Self-Organization, and Multiple Chromisms of Pure Stereoisomers of a Tetraphenylethene-Cored Luminogen. *Journal of the American Chemical Society* **2012,** *134* (24), 9956-9966.

[28] Shi, J.; Chang, N.; Li, C.; Mei, J.; Deng, C.; Luo, X.; Liu, Z.; Bo, Z.; Dong, Y. Q.; Tang, B. Z., Locking the phenyl rings of tetraphenylethene step by step: understanding the mechanism of aggregation-induced emission. *Chemical Communications* **2012,** *48* (86), 10675-10677.

[29] Herman, M.; Perry, D. S., Molecular spectroscopy and dynamics: a polyad-based perspective. *Physical Chemistry Chemical Physics* **2013,** *15* (25), 9970-9993.

b) Klaumünzer, B.; Kröner, D.; Lischka, H.; Saalfrank, P., Non-adiabatic excited state dynamics of riboflavin after photoexcitation. *Physical Chemistry Chemical Physics* **2012,** *14* (24), 8693-8702.

[30] a) Jelley, E. E., Spectral Absorption and Fluorescence of Dyes in the Molecular State. *Nature* **1936,** *138* (3502), 1009-1010.b) Möbius, D., Scheibe Aggregates. *Advanced Materials* **1995,** *7* (5), 437-444.

[31] Würthner, F.; Kaiser, T. E.; Saha-Möller, C. R., J-Aggregates: From Serendipitous Discovery to Supramolecular Engineering of Functional Dye Materials. *Angewandte Chemie International Edition* **2011,** *50* (15), 3376-3410.

[32] Li, X.-Q.; Zhang, X.; Ghosh, S.; Würthner, F., Highly Fluorescent Lyotropic Mesophases and Organogels Based on J-Aggregates of Core-Twisted Perylene Bisimide Dyes. *Chemistry – A European Journal* **2008,** *14* (27), 8074-8078.

[33] Wang, Y.; Liu, T.; Bu, L.; Li, J.; Yang, C.; Li, X.; Tao, Y.; Yang, W., Aqueous Nanoaggregation-Enhanced One- and Two-Photon Fluorescence, Crystalline J-Aggregation-Induced Red Shift, and Amplified Spontaneous Emission of 9,10-Bis(p-dimethylaminostyryl)anthracene. *The Journal of Physical Chemistry C* **2012,** *116* (29), 15576-15583.

[34] Goodman, J.; Brus, L. E., Proton transfer and tautomerism in an excited state of methyl salicylate. *Journal of the American Chemical Society* **1978,** *100* (24), 7472-7474.

[35]. Yang, G.; Li, S.; Wang, S.; Li, Y., Emissive properties and aggregation-induced emission enhancement of excited-state intramolecular proton-transfer compounds. *Comptes Rendus Chimie* **2011,** *14* (9), 789-798.

[36] Wei, R.; Song, P.; Tong, A., Reversible Thermochromism of Aggregation-Induced Emission-Active Benzophenone Azine Based on Polymorph-Dependent Excited-State Intramolecular Proton Transfer Fluorescence. *The Journal of Physical Chemistry C* **2013,** *117* (7), 3467-3474.

[37] Gao, B.-R.; Wang, H.-Y.; Yang, Z.-Y.; Wang, H.; Wang, L.; Jiang, Y.; Hao, Y.-W.; Chen, Q.-D.; Li, Y.-P.; Ma, Y.-G.; Sun, H.-B., Comparative Time-Resolved Study of Two Aggregation-Induced Emissive Molecules. *The Journal of Physical Chemistry C* **2011,** *115* (32), 16150-16154.

[38] Yan, Z.-Q.; Yang, Z.-Y.; Wang, H.; Li, A.-W.; Wang, L.-P.; Yang, H.; Gao, B.-R., Study of aggregation induced emission of cyano-substituted oligo (p-phenylenevinylene) by femtosecond time resolved fluorescence. *Spectrochimica Acta Part A: Molecular and Biomolecular Spectroscopy* **2011,** *78* (5), 1640-1645.

[39] Fang, H.-H.; Chen, Q.-D.; Yang, J.; Xia, H.; Gao, B.-R.; Feng, J.; Ma, Y.-G.; Sun, H.-B., Two-Photon Pumped Amplified Spontaneous Emission from Cyano-Substituted Oligo(p-phenylenevinylene) Crystals with Aggregation-Induced Emission Enhancement. *The Journal of Physical Chemistry C* **2010,** *114* (27), 11958-11961.

[40] Hu, R.; Lager, E.; Aguilar-Aguilar, A.; Liu, J.; Lam, J. W. Y.; Sung, H. H. Y.; Williams, I. D.; Zhong, Y.; Wong, K. S.; Peña-Cabrera, E.; Tang, B. Z., Twisted Intramolecular Charge Transfer and Aggregation-Induced Emission of BODIPY Derivatives. *The Journal of Physical Chemistry C* **2009,** *113* (36), 15845-15853.

[41] Qin, W.; Ding, D.; Liu, J.; Yuan, W. Z.; Hu, Y.; Liu, B.; Tang, B. Z., Biocompatible Nanoparticles with Aggregation-Induced Emission Characteristics as Far-Red/Near-Infrared Fluorescent Bioprobes for In Vitro and In Vivo Imaging Applications. *Advanced Functional Materials* **2012,** *22* (4), 771-779 .

[42] Mei, J.; Hong, Y.; Lam, J. W. Y.; Qin, A.; Tang, Y.; Tang, B. Z., Aggregation-Induced Emission: The Whole Is More Brilliant than the Parts. *Advanced Materials* **2014,** *26* (31), 5429-5479.

4 Room Temperature Phosphorescence

4.1 Introduction

Room Temperature Phosphorescence or RTP has been for a long time considered the realm of inorganic compounds due to the low Spin-Orbit Coupling (SOC) observed in pure organic materials that prevents the population of accessible triplet states and their high sensitivity to atmospheric oxygen[1][2]. Only in recent times the scientific community started to deeply investigate purely organic materials displaying phosphorescent emission. A Major boost in this research field was given by the large number of application for these materials such as the fabrication of OLEDs, digital security, sensors, bioimaging and in general in the fields of optoelectronic and bioelectronic.

Big efforts were done in order to raise SOC in organic compounds in particular through the introduction of aromatic carbonyl groups, halogen bonding, formation of charge transfer states and radical anion pairs. Another crucial point in the development of efficient organic phosphors has been the stabilization of the triplet state once it is selectively populated. The emission of a photon from a triplet state is just one of the possible processes and, most of the time, thermal deactivation through molecular vibration or rotation and oxygen quenching strongly overcome the phosphorescent emission. This drawback can be efficiently solved by crystallization, host-guest doping, inclusion in metal-organic frameworks MOFs, ionic bonding or molecular assembly.

The preparation of good emitters displaying long RTP is furtherly complicated by the obvious consideration that, most of the times, there is an inverse proportionality between the decay time $\boldsymbol{\tau_P}$ and the quantum efficiency $\boldsymbol{\Phi_P}$[3][4].

4.2 Organic phosphorescence

By its definition phosphorescence is the radiative deactivation from an upper excited state to a lower state characterized by a different multiplicity. Transferred to the organic realm this means that all the relevant processes labelled as phosphorescence involve a triplet excited state that relax to a singlet ground state.

The necessary step to observe any photophysical process is the excitation of the system that brings the molecule from the ground state $\mathbf{S_0}$ to a generic excited state $\mathbf{S_n}$ ($n \geq 1$). Usually more than one absorption is possible but excitation to high energy levels is often accompanied by photodegradation of the material. The most common process that will occur after bringing the system to a generic single excited state is Internal Conversion (IC) to the $\mathbf{S_1}$ level through vibrational deactivation. As postulated by Kasha's rule, IC is related to the overlap between energetic levels with different vibrational and electronic quantum numbers as expressed by the Franck-Condon factors, the greater is the overlap the faster is the transition. IC is commonly most rapid than all the other possible processes and leads to the selective population of $\mathbf{S_1}$. IC from $\mathbf{S_1}$ to $\mathbf{S_0}$ is usually less efficient than from upper $\mathbf{S_n}$ levels to $\mathbf{S_1}$ due to the small overlap between the vibronic levels of $\mathbf{S_1}$ and $\mathbf{S_0}$. This allows radiative deactivation from $\mathbf{S_1}$ (fluorescence) to be competitive with IC. It is also possible that Intersystem Crossing (ISC) occurs from $\mathbf{S_1}$ to populate a triplet level $\mathbf{T_m}$. ISC is generally difficult in purely organic molecules due to a small SOC. Population of $\mathbf{T_m}$ is usually very efficiently followed by a rapid IC to $\mathbf{T_1}$, from which the system can non radiatively or radiatively relax to S_0 (phosphorescence) (See Figure 1). A less common process can occur from $\mathbf{T_1}$ that is the re-population of $\mathbf{S_1}$, this is possible only when the two levels have a small energy gap that can be filled by the thermal energy. This phenomenon leads to a delayed fluorescence defined as TADF (Thermally Activated Delayed Fluorescence).

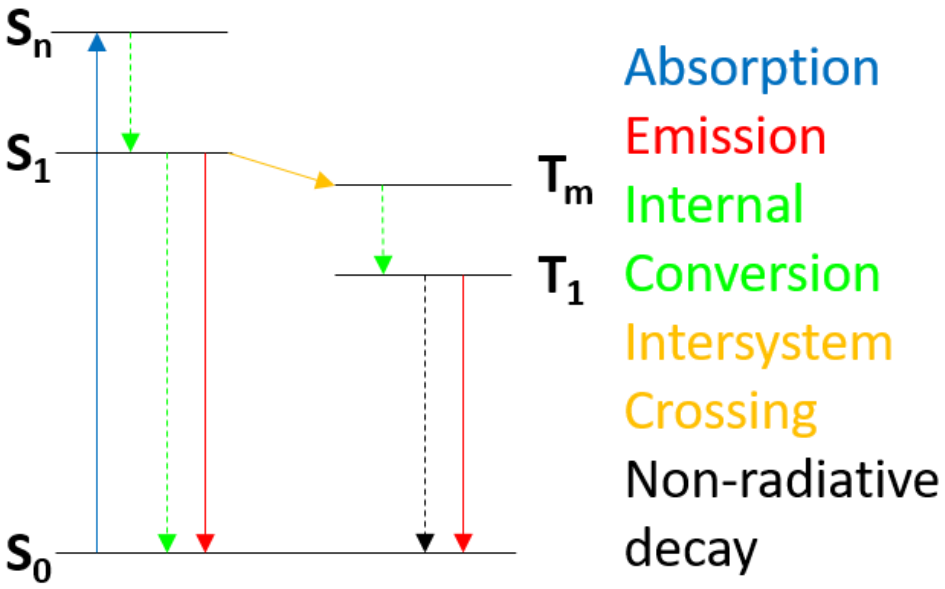

Figure 1: Jablonski diagram and possible processes.

Based on these considerations we can define the phosphorescent quantum efficiency Φ_P, the ISC quantum efficiency Φ_{ISC} and the phosphorescent life time τ_P according to the following equations:

$$\Phi_P = \Phi_{ISC}\tau_P k_P$$

$$\Phi_{ISC} = \frac{k_{ISC}}{k_F + k_{IC} + k_{ISC}}$$

$$\tau_P = \frac{1}{k_P + k_{nr}}$$

Where k_X are the rate constants of specific processes.

To better understand the related factors that allow the arise of the phosphorescence we have to approach this phenomenon from a theoretical point of view through the quantum mechanics theory.

The rate constant k for a process based on Fermi's golden rule is here defined:

$$k = \frac{2\pi}{h} |H'|^2 \delta (E_i - E_f)$$

Where H' is the matrix element of the perturbed Hamiltonian, $(E_i - E_f)$ is the adiabatic energy gap between the initial and the final state and δ is the function that ensure the energy conservation for the non-radiative transition.

For singlet to singlet transitions the implementation of a non-adiabatic coupling between the two states leads to IC rate k_{IC} while, turning to singlet to triplet transitions, SOC breaks the spin-forbidden transition and opens to ISC with rate k_{ISC}. There are two mainly consistent ISC processes that can occur in an organic molecule: $S_1 \rightarrow T_m$ ISC, that is the main process to populate the triplet levels, and $T_1 \rightarrow S_0$ ISC, that dominates the triplet deactivation.

Assuming the high temperature approximation and the short time approximation:

$$k_{ISC} = \frac{2\pi}{h} \left|\langle S|\hat{H}_{SOC}|T\rangle\right|^2 \sqrt{\frac{\pi}{\lambda k_B T}}\, e^{-\frac{(\Delta E_{ST}-\lambda)^2}{4\lambda k_B T}}$$

$\left|\langle S|\hat{H}_{SOC}|T\rangle\right|$ is the SOC matrix element between the two levels and λ is the reorganization energy, sum of the normal mode components with $\lambda_k = \frac{1}{2}\,\omega_k^2 \Delta Q_k^2$ (ΔQ_k^2 represents the difference their equilibrium geometry) that describes the nuclear change during the transition.

k_{ISC} is promoted by a magnification of SOC, that is the reason why, based on the El-Sayed's rule, the ISC process is favoured by a change in the molecular orbital type. In fact, the SOC matrix element of a transition involving a transition from $^1(\pi, \pi^*)$ to $^3(n, \pi^*)$ is two times larger than a transition from $^1(\pi, \pi^*)$ to $^3(\pi, \pi^*)$. The SOC operator is the product of the orbital and spin angular moment. It is evident that the orbital angular moment operator rotates the atoms and changes their symmetry, this leads to a greater spatial integral between states of different orbital symmetry with respect to the molecular plane reflection.

The significance of the vibronic component is not considered in the El-Sayed's rule but it can be evaluated by the Frank-Condon Integral. The vibronic term is determined by two parameters: ΔE_{ST} and λ. In a rigid environment the displacement between the electronic state is small and the direct consequence is a weak coupling limit ($\Delta E_{ST} \gg \lambda$). In order to accelerate the ISC process, it is necessary to increase λ and in parallel decrease ΔE_{ST}, however, this relationship is true till the ISC has a small structural change.

The k_P radiative rate determine the spontaneous radiative emission of a photon from the lowest triplet level. This rate can be calculated by the Einstein coefficient:

$$k_P = \frac{64\pi^4}{3h^4c^2}\, \Delta E_{T1\to S0}^3 |\mu_{T1\to S0}|^2$$

$$\mu_{T1\to S0} = \sum_k \frac{\langle T_1|\hat{H}_{SOC}|S_k\rangle}{^3E_1 - {}^1E_k} \text{ x } \mu_{Sk\to S0} + \sum_m \frac{\langle T_m|\hat{H}_{SOC}|S_0\rangle}{^3E_m - {}^1E_0} \text{ x } \mu_{Tm\to T1}$$

$\mu_{T1\to S0}$ is directly proportional to the SOC between triplet and singlet state but it is inversely proportional to the energy gap. While, the rate k_P is directly proportional to the gap between the emissive triplet state and the singlet ground state.

To summarize, the various strategies enhance phosphorescence quantum yield, Φ_P:

- Promote ISC by enhancing $\langle S_1|\hat{H}_{SOC}|T_m\rangle$ and λ, decreasing the energy gap $\Delta E_{S1\to Tm}$ or disadvantaging the other competitive processes.
- Decrease the non-radiative decay from the T_1 state through the decrease of the $\langle T_1|\hat{H}_{SOC}|S_0\rangle$ and the relative λ, or the increase of the gap $\Delta E_{T1\to S0}$.
- Enhance k_P by increasing $\Delta E_{T1\to S0}$ and $\mu_{T1\to S0}$

When the enhancement of the phosphorescent lifetime τ_P is taken into account we have to consider that the stabilization of the triplet state is achievable only through the reduction of the decay processes allowed from this state, the non-radiative decay and the phosphorescence. Obviously, the population of the triplet state is the key process to observe phosphorescent emission but the increase of the SOC $\langle S_1|\hat{H}_{SOC}|T_1\rangle$, the decrease of the gap between them, not only favours ISC but it results in an increase of the k_P leading to a shorter τ_P. On the contrary, the increase of the SOC $\langle S_1|\hat{H}_{SOC}|T_m\rangle$ (m>1) leads to a selective increase of the k_{ISC} and it does not affect the k_P. The raise of the gap $\Delta E_{T1\to S0}$ can result in a reduction of the non-radiative decay and also in an acceleration of the phosphorescence that it is not suitable for the achievement of a long lifetime, that is the reason why it is rather difficult to find red or blue phosphorescence with long lifetime but

it is common to observe longer decay time for green or yellows emission, where k_P and k_{nr} are balanced. The decrease of the SOC $\langle T_1|\hat{H}_{SOC}|S_0\rangle$ and λ, that is controlled by the rigidity of the environment and by the deuteration, that controls ω, allowing the achievement of high Φ_P and long k_P even if this process suppresses the λ for the transition $S_1 \rightarrow T_m$ reducing the k_{ISC}.

All these considerations allow to claim that the achievement of both great Φ_P and long τ_P is feasible even if it is an arduous challenge due to the contribution of many factors.

Finally, the Reverse Intersystem Crossing (RISC) must by mentioned. This process is not very common but it can be present and competes with phosphorescence when $\mathbf{S_1} \rightarrow \mathbf{T_1}$ gap is smaller than 0.37 eV. This is a necessary condition to observe the Thermally activated Delay Fluorescence (TADF). This uncommon emission is frequently observed in copresence with RTP generating a dual emissive behaviour.

Two of the different strategies pursued in order to isolate organic RTP dyes are reported in the following.

4.2.1 Halogen bonding induced RTP

The introduction of heavy atoms in a purely organic chromophore can effectively increase the Spin-Orbit Coupling thus enhancing ISC from singlets to triplets. Obviously, choosing a transition metal all the benefits deriving by the purely organic structure, such as low prize, high processability and low toxicity will be lost. In this regard, the introduction of heavy halogen atoms can have the same impact on the photophysic of the system without all the drawbacks associated with the heavy metal. Moreover, the presence of halogens in some cases has allowed the formation of intermolecular interactions through halogen bonds that rigidify of the environment and positively contribute to the arise of the RTP. In addition, cocrystallization of a chromophore with halogen bond donor species has been reported to induce intermolecular electronic coupling (IEC) that promotes the ISC[4].

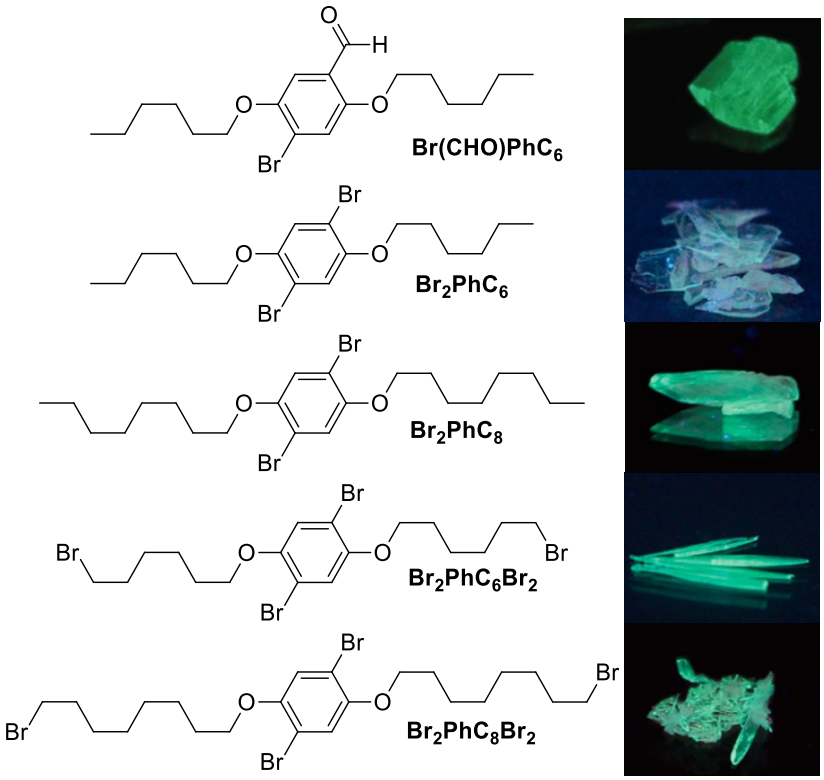

Figure 2: Bromobenzene derivatives structure displaying RTP and relative pictures. Adapted with permission from ref.[5] © 2011, Nature Publishing Group, and from ref.[6]© 2016, American Chemical Society.

As an example bromobenzene derivatives reported in figure 2 are here reported as bromine atoms induced RTP behaviour [5;6]. All the species presented are poorly or completely non emissive in diluted solution while crystals display intense green phosphorescences. To understand the role played by the presence of bromine atoms the crystal structures are fundamental. **Br(CHO)PhC$_6$** has a weak fluorescence in solution which is followed by a phosphorescence in the solid state (Φ_P = 2.9%). The relative intensities of these two emissions depend by the quality of the crystals, where strong C-Br···O=C interactions were detected ($r_{Br\cdots O}$= 2.86 Å) that allow an efficient SOC and thus an efficient ISC.

The four others compounds **Br$_2$PhC$_6$**, **Br$_2$PhC$_8$**, **Br$_2$PhC$_6$Br$_2$** and **Br$_2$PhC$_6$Br$_8$** display similar features. In their crystal structures close Br···Br interactions can be found, moreover **Br$_2$PhC$_6$Br$_2$** and **Br$_2$PhC$_6$Br$_8$** form multiple halogen bonds. The differences between the phosphorescence quantum yields detected (**Br$_2$PhC$_6$**; Φ_P = 3.4%, **Br$_2$PhC$_8$**; Φ_P = 8.9%, **Br$_2$PhC$_6$Br$_2$**; Φ_P = 21.9%, **Br$_2$PhC$_6$Br$_8$**; Φ_P = 13.1%) are ascribable to the different number of XB that, not only provides a rigidification of the environment and promotes SOC, but even prevents triplet-triplet annihilation.

4.2.2 Strong π-π interaction induced RTP

Since the introduction of the exciton model by Kasha at the end of the '50s[7], the formation of strong π-π stacking interaction in a chromophore aggregate was considered to be the main cause of the emission quenching.

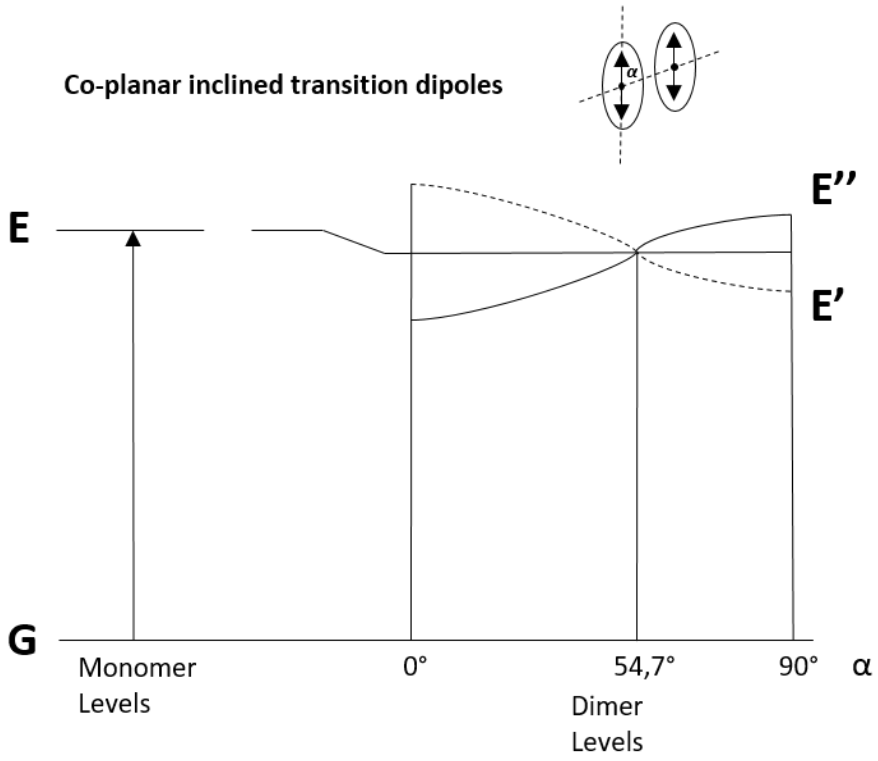

Figure 3: Modified Jablonski diagram for dimer formation for the Kasha's exciton model.

In fact, when two molecules (represented by an oval with a double arrow which is the transition moment, see Figure 3) form a dimer an exciton split is observed for singlet and triplet states but the latter one is almost negligible. When more than two molecules are considered the splitting results in the formation of bands instead of discrete levels. The angle formed between the axis connecting the molecular centroids and the molecular plane defines the magnitude of the splitting (Figure 3). At 54.7° the splitting is null as well as the dipole-dipole interaction. Larger angles are associated with the formation of H-dimers (or aggregates if *N*

molecules are taken in consideration; figure 4 right) while smaller angles generate J-dimers (or aggregates; Figure 4 left).

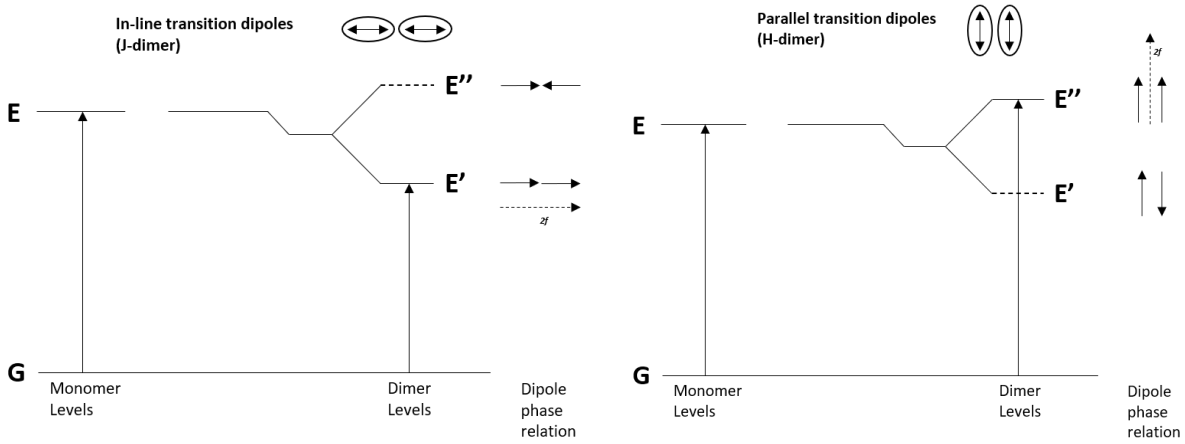

Figure 4: Modified Jablonski diagram for J-dimer (Left) and H-dimer (Right) for the Kasha's exciton model.

In a H-dimer the lower exciton level (or the bottom of the bands considering an N-fold aggregate) is not directly accessible from the ground state because the stabilized out-of-phase transition generates a null variation of the transition moment while in a J-dimer (or aggregate) the opposite is true. The probabilities to observe a transition from or to a specific level are identical thus, the emission from the lowest level is theoretically prohibited in a H-aggregate while it could be enhanced in a J-aggregate. For this reason, after excitation on the top of the band, an H-aggregate undergoes rapid IC to the lowest level where the exciton is trapped since the transition to the ground state is prohibited. Now, the energy split induced by the aggregation, that causes a decrease of the gap between the singlet levels and the triplet state, together with the trapping effect allow ISC to became competitive with respect to fluorescent emission[8;9] (Figure 5).

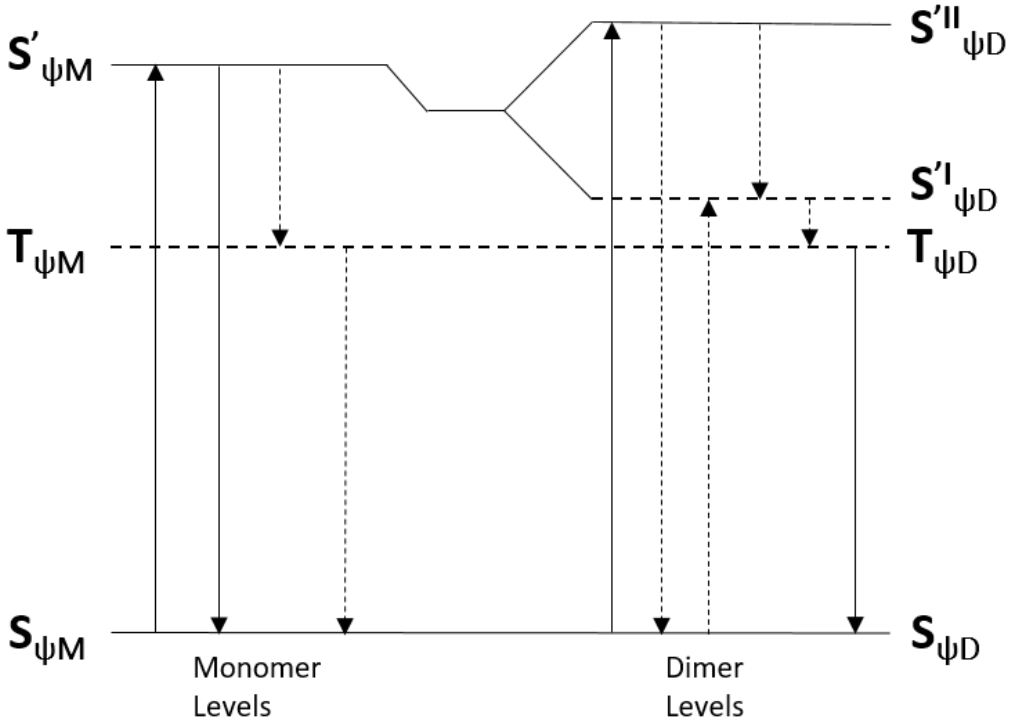

Figure 5: Modified Jablonski diagram for H-dimer formation for the Kasha's exciton model comprehensive of the triplet states and the possible transition.

For this reason, H-aggregation can be considered a good strategy in order to obtain efficient organic RTP.

Examples of organic phosphors with H-aggregate generated RTP are carbazole (**Cz**) and iminodibenzyl (**Ib**)[10].

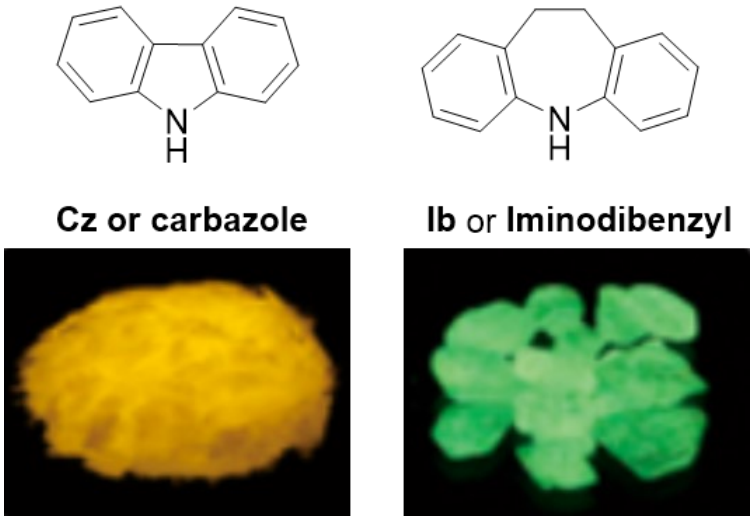

*Figure 6: **Cz** and **Ib** structure and pictures of the RTP in crystals. Adapted with permission from ref.[10] © 2018, American Chemical Society.*

Cz and **Ib** crystals display at RT an ultralong phosphorescence (RTUP) with τ_{av}= 910 ms at 560 nm and τ_{av}= 402 ms at 520 nm respectively (Figure 6). According to the authors, the RTUP is due to H-aggregates that effectively promote ISC and stabilize the triplet exciton, together with other multiple intermolecular interactions (N-H···π; C-H···π; N-H···H-C) which provide an additional rigidification of the systems. The relatively shorter decay time of **Ib** has been attributed to the presence of the unconjugated central ring which allows a partial bending of the molecule that, in the solid state, avoids the perfect planarity and the consequent thinner packing experienced by **Cz**. As known, a more rigid environment prevents the non-radiative decay of triplet states elongating the triplet lifetime.

4.3 References

[1] Forni, A.; Lucenti, E.; Botta, C.; Cariati, E., Metal free room temperature phosphorescence from molecular self-interactions in the solid state. *Journal of Materials Chemistry C* **2018,** *6* (17), 4603-4626.

[2] Ma, H.; Lv, A.; Fu, L.; Wang, S.; An, Z.; Shi, H.; Huang, W., Room-Temperature Phosphorescence in Metal-Free Organic Materials. *Annalen der Physik* **2019,** *531* (7), 1800482.

[3] An, Z.; Zheng, C.; Tao, Y.; Chen, R.; Shi, H.; Chen, T.; Wang, Z.; Li, H.; Deng, R.; Liu, X.; Huang, W., Stabilizing triplet excited states for ultralong organic phosphorescence. *Nature Materials* **2015,** *14* (7), 685-690.

[4] X. Pang and W. J. Jin, in *Halogen Bonding II. Topics in Current Chemistry*, ed. P. Metrangolo and G. Resnati, Springer International Publishing, Cham, **2014**, vol. 359, pp. 115–146.

[5] Bolton, O.; Lee, K.; Kim, H.-J.; Lin, K. Y.; Kim, J., Activating efficient phosphorescence from purely organic materials by crystal design. *Nature Chemistry* **2011,** *3* (3), 205-210.

[6] Shi, H.; An, Z.; Li, P.-Z.; Yin, J.; Xing, G.; He, T.; Chen, H.; Wang, J.; Sun, H.; Huang, W.; Zhao, Y., Enhancing Organic Phosphorescence by Manipulating Heavy-Atom Interaction. *Crystal Growth & Design* **2016,** *16* (2), 808-813.

[7] McRae, E. G.; Kasha, M., Enhancement of Phosphorescence Ability upon Aggregation of Dye Molecules. *The Journal of Chemical Physics* **1958,** *28* (4), 721-722.

[8] Kasha, M.; Rawls, H. R.; El-Bayoumi, M. A., The exciton model in molecular spectroscopy. *Pure and Applied Chemistry* **1965,** *11* (3-4), 371-392.

[9] Levinson, G. S.; Simpson, W. T.; Curtis, W., Electronic Spectra of Pyridocyanine Dyes with Assignments of Transitions[1]. *Journal of the American Chemical Society* **1957,** *79* (16), 4314-4320.

[10] Sun, C.; Ran, X.; Wang, X.; Cheng, Z.; Wu, Q.; Cai, S.; Gu, L.; Gan, N.; Shi, H.; An, Z.; Shi, H.; Huang, W., Twisted Molecular Structure on Tuning Ultralong Organic Phosphorescence. *The Journal of Physical Chemistry Letters* **2018,** *9* (2), 335-339.

5 Cyclic Triimidazole

5.1 Introduction

Great efforts have been made along the last decades in order to the develop purely organic RTP or RTUP moieties. Even if phosphorescence is usually considered the realm of organometallic species many architectures have been explored to enhance the phosphorescence quantum efficency of organic compounds. In particular, the formation of large interchromophoric interaction in the solid state has been successfully applied. For example, the formation of supramolecular halogen bonded motifs as well as strong π-π interaction have allowed to obtain positive results in the promotion of ISC to populate triplet states and in the protection of exciton from atmospheric oxygen.

In this regard, triimidazo[1,2-*a*:1',2'-*c*:1'',2''-*e*][1,3,5]triazine, hereafter triimidazole or **TT,** is a very simple organic molecule with a peculiar emissive behaviour[1]. Crystals of **TT** show an intense blueish fluorescent emission and a green phosphorescence while diluted solution of this dye shows a very weak emission.

Cyclic triimidazole was firstly reported in the early 1970[2][3] as the product of the auto-condensation of 2-fluoroimidazole. However, due to the multi-step and tedious procedures for the synthesis of the 2-fluoro-imidazole precursor, the properties and reactivity of **TT** remained mainly unexplored until 2011, when Schubert and coworkers reported a simple procedure for its preparation on multigram scale (Scheme 1).[4] The authors developed a straightforward synthesis exploiting the thermolysis at temperatures above 240°C of the blue polymorph of copper(II) diimidazolate $Cu(C_3H_3N_2)_2$, which is easily obtained by reaction of $CuSO_4$ with imidazole in the presence of Na_2CO_3 [5]. The easy availability of low cost starting materials such as copper sulfate and imidazole, together with the possibility of recycling the imidazole which co-sublimes with **TT**, make this new synthetic route quite appealing for the preparation of the cyclic trimer. The authors also described the formation in about 1 to 5 ratio, with respect to **TT**, of a minor isomer (**ISO-A**) which was later confirmed as the product showing a 1,5- instead of 1,2-annelation in one imidazole ring [6].

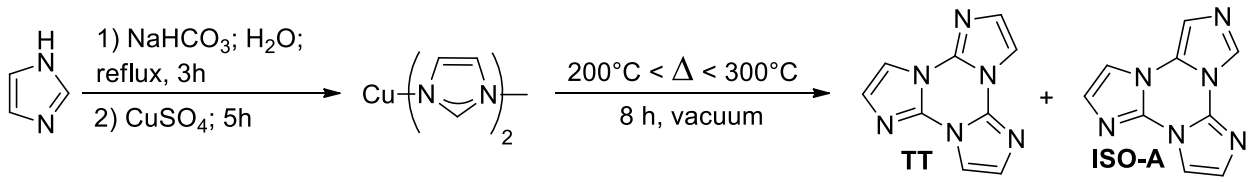

Scheme 1: TT synthetic pathway.

5.2 Photophysical characterization

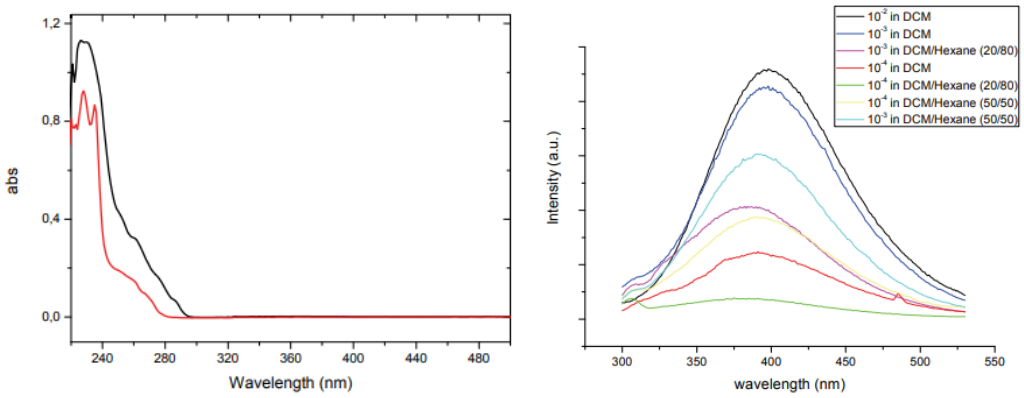

*Figure 1: Left: Absorption spectra of 2.5 x 10^{-5} M DCM solutions of **TT** (Black line) and **ISO-A** (Red line) at RT. **Right:** Emission spectra of **TT** in DCM-DCM/hexane (different volumes) at 298 K. Reproduced with permission from ref.[1] © 2017 American Chemical Society.*

TT shows an absorption band at 230 nm (Figure 1 left) and a weak emission at 390 nm in solution (10^{-4}- 10^{-5} M DCM) with Φ equal to only 2% (Figure 1 right). Only forcing the aggregation with the addition of a non-solvent (hexane or pentane 50/50 v/v) it is possible to observe a slightly intensification of the emission (Figure 1 right).

Similarly, increasing the concentration of the DCM solution to 10^{-2} M, the emission (400 nm; τ_{av}= 7.09 ns) is intensified and an additional weak absorption band appears at 345 nm.

Surprisingly, by lowering the temperature to 77 K, the 10^{-2} M DCM solution of **TT** shows an additional broader band centered at 435 nm that is the result of the overlap of the fast component observed even at RT at 400 nm (τ_{av}= 14.31 ns) with an ultralong component centered at 500 nm (τ_{av}= 926.76 ms) (Figure 2).

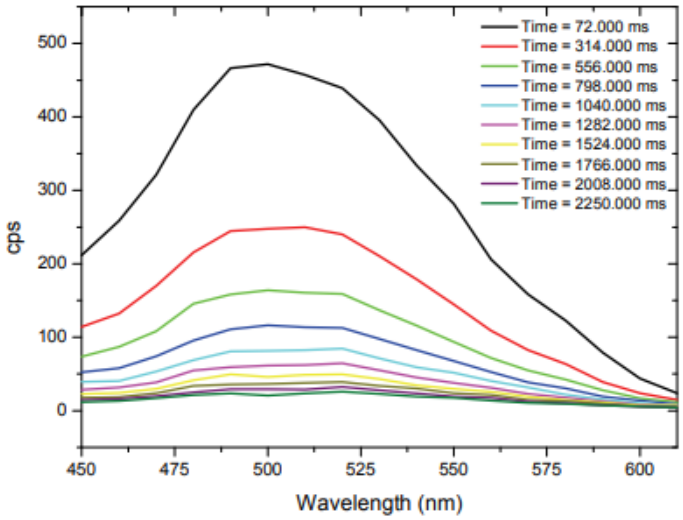

*Figure 2: Emission spectra of **TT** in DCM (10^{-2} M) at 77 K recorded at different time delays (λ_{exc}=350 nm). Reproduced with permission from ref.[1] © 2017 American Chemical Society.*

The remarkably long luminescence visible for highly concentrated solution at 77 K is also present in **TT** powders that show an intense blue emission under the UV lamp that switches to a fading green when the lamp is turned off.

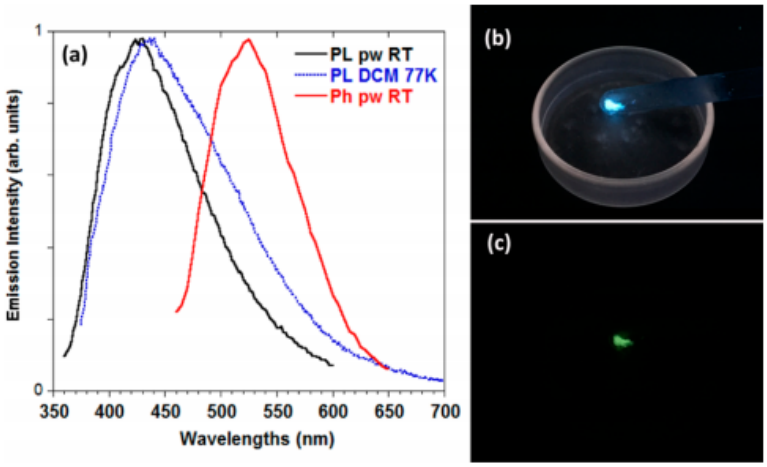

Figure 3: (a) Photoluminescence of the DCM solution (10^{-2} M, λ_{exc} = 350 nm) at 77 K (blue dotted line). Photoluminescence (black line, λ_{exc} = 330 nm) and phosphorescence (red line, time delay = 172 ms, λ_{exc} = 374 nm) of powders at 298 K. Pictures of powders at 77 K with UV on (b) and off (c). Reproduced with permission from ref.[1] © 2017 American Chemical Society.

Powders of **TT** obtained through rapid evaporation of a DCM solution show a broad band centered at 425 (τ_{av}= 9.88 ns) nm at RT (Φ = 18%) when excited at 350 nm (Figure 3). Time-resolved experiment revealed the

presence of a prompt component overlaying to a ultralong emission centered at 520 nm (τ_{av}= 555.10 ms) (Figure 4).

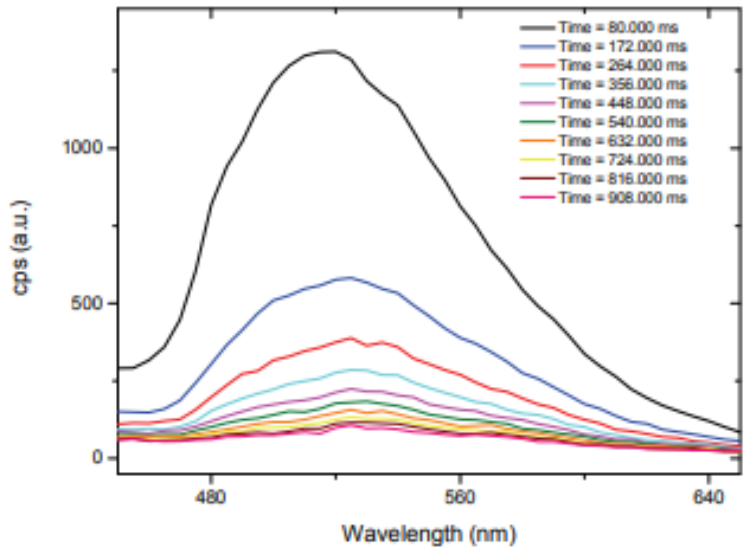

*Figure 4: Emission spectra of **TT** (powder) at 298 K recorded at different time delays (λ_{exc}=374 nm). Reproduced with permission from ref.[1]* ***© 2017 American Chemical Society.***

At 77 K no additional emissions are detected, with the prompt component at 430 nm (τ_{av}= 12.31 ns) and the green component, which is strongly intensified and elongated lasting for almost 3.6 s, at 525 nm (τ_{av}= 963.15 ms) (Figure 5). Moreover, no significant differences are noticed when the sample is exposed to nitrogen indicating an inertness of the triplet to oxygen.

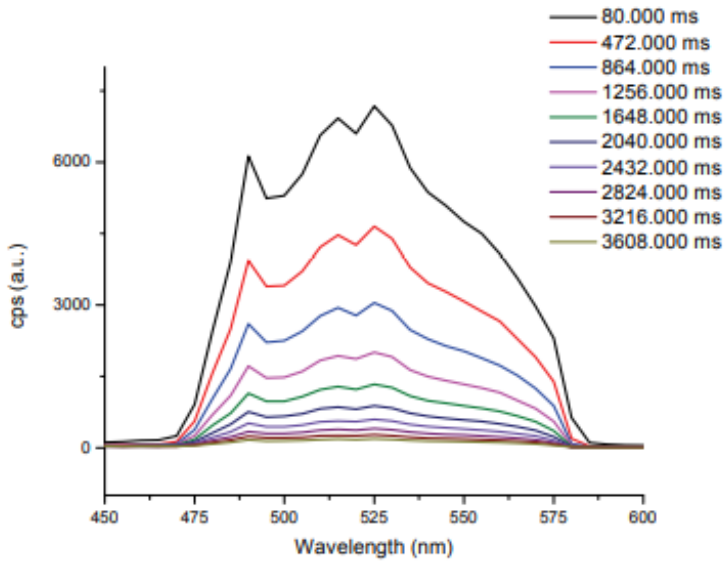

*Figure 5: Emission spectra of **TT** (powder) at 77 K recorded at different time delays (λ_{exc} = 374 nm). Reproduced with permission from ref.[1]* ***© 2017 American Chemical Society.***

However, the photophysical behaviour seems to be sensitive to the crystallinity grade of the sample. Crystals of **TT** (obtained by slow evaporation of a DCM solution, Φ = 30%) display vibronic components in both the prompt (400 and 424 nm) and the delayed (525 and 570 nm) emissions. The vibronic components of these

two emissions are lost when the sample is ground and in parallel the Φ decreases to 22% revealing a mechanochromic behaviour[7][8][9].

The exposure to unpolarised UV light of a single crystal of **TT** determines an emission polarized orthogonally to the long axis of the crystal indicating that the transition dipole is orthogonal to this axis. The crystal surfaces display bright emission due to wave-guiding effects (Figure 6).

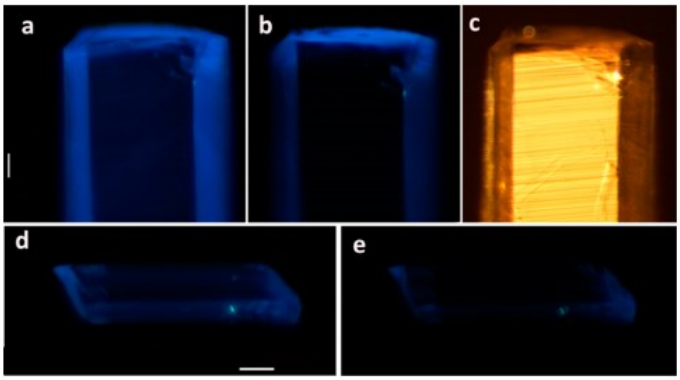

*Figure 6: Microscopy images of a part of a **TT** crystal under unpolarized UV light taken with an analyzer with the transmission axis horizontal (a), vertical (b), and under white light (c). Images of a smaller crystal under unpolarized UV light taken with the analyzer with the transmission axis vertical (d) and horizontal (e). White bars are 30 µm long. Reproduced with permission from ref.[1]*

5.3 Crystalline structure-emission relation

The X-ray crystal structure evidences that **TT** molecules are slightly distorted with respect to an ideal D_{3h} symmetry. Weak C-H··N hydrogen bonds connect molecules along planar rows, connected through other C-H··N hydrogen bonds to form approximated sheets. Along the third axis molecules of **TT** stack in face-to-face antiparallel-packed zigzag columns with distances between average molecular planes alternately equal to 3.204 and 3.290 Å and corresponding distances between centroids of the central rings equal to 3.95 and 3.73 Å, respectively (Figure 7).

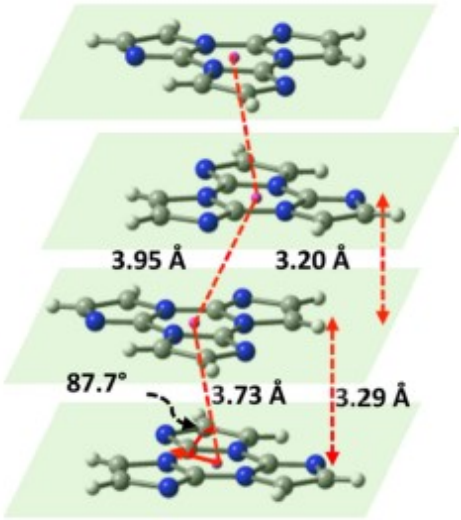

*Figure 7: Fragment of crystal packing of **TT** showing the key intermolecular distances and the angles between the transition moment dipoles (red arrows) and the axis through the centroids of the triazinic rings (purple circles). Reproduced with permission from ref.[1]*

The small distance between molecules is indicative of a strong π-π interaction in the ground state associated with a large π-stacking area and formation of H-aggregates.

DFT and TDDFT calculations on isolated **TT** molecules provide a minimum when the perfect C_{3h} symmetry is respected. On the contrary, optimization of the stacked aggregates leads to a minimum when the molecules lose their perfect symmetry, thus the π-π interactions are responsible for the observed molecular distortion.

The simulated absorption spectrum for the monomer consists of mainly two transitions, $S_0 \rightarrow S_3$ and $S_0 \rightarrow S_4$, both computed at 203 nm with oscillator strength $f = 0.56$ and described as $\pi \rightarrow \pi^*$ transition with the frontier orbitals delocalized over the whole molecule. These transitions correspond to the band observed at 230 nm in DCM. The $S_0 \rightarrow S_1$ transition, that has the same $\pi \rightarrow \pi^*$character, is computed at 228 nm with virtually zero oscillator strength.

Similarly, dimer and tetramer show strong transitions at 200-203 nm and only weak degenerated transitions at 228-230 nm with a small increase of the oscillator strength ($f = 0.0007$ for the dimer; $f = 0.0011$ for the tetramer) proportionally to the increase of the dimension of the aggregate. This trend perfectly agrees with the weak absorption band observed in concentrated DCM solutions. The low absorption intensity can be associated to a symmetry-forbidden transition due to the high symmetry of the **TT** that is preserved in diluted solution but disrupted in the aggregate allowing the intensification of the $S_0 \rightarrow S_1$ transition. The corresponding transition dipole moment lies in the molecular plane and forms almost a perfect square angle (87.7°) with the axis passing through the centroids of the triazinc ring confirming the H-type nature of the crystalline aggregates[10]. The increase of the fluorescence intensity in the solid state is again associated to the aggregation. In fact, going from the monomer to the dimer, a non-vanishing enhancement of the oscillator strength (from 0 to 0.086) is provided for the optimized S_1 excited state computed at 249 nm for the monomer and at 276 nm for the dimer (Figure 8).

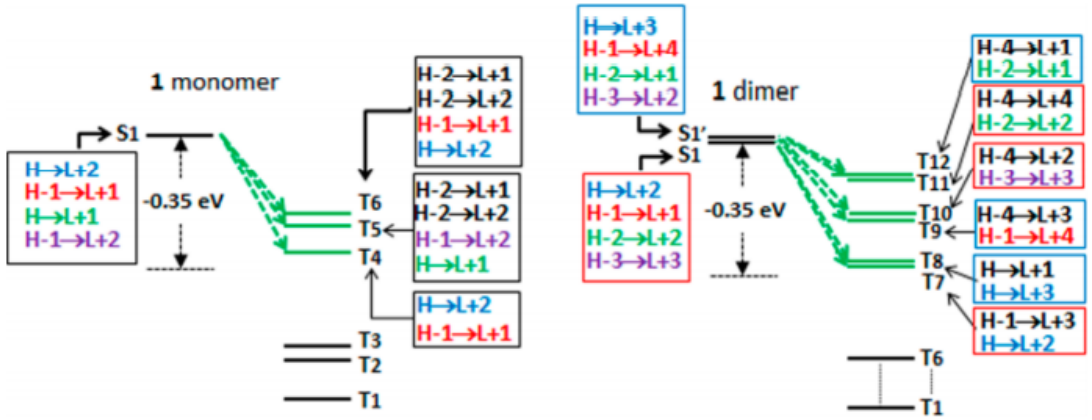

*Figure 8: Schematic diagram of singlet and triplet TD-ωB97X/6-311++G(d,p) energy levels and main orbital configurations of a monomer (left) and dimer (right) of **TT**. The green dashed arrows correspond to the ISC processes probably occurring from the S_1 state to the closest lower-lying triplet states (T_n). Reproduced with permission from ref.[1] © 2017 American Chemical Society.*

A deep investigation on the nature of the excited emissive states of **TT** has been performed in order to explain the uncommon behaviour of this chromophore and in particular the ultralong phosphorescence displayed by its crystals.

The simulation of the first set of excited triplet states for the monomer has shown the presence of six triples (T_1-T_6) below S_1. In particular, T_4, T_5 and T_6 have a similar transition configuration as that of S_1 and lying within 0.35 eV of it. Moving to the dimer, we have observed an increase of the number of the low lying triplet states (T_1-T_{12}), six of which has similar transition configuration as those of S_1 and S_1' and close to them within 0.35 eV[11]. Obviously this indicate a smaller energy gap between the singlets and the first accessible triplet states in the dimer respect to the monomer (Figure 8).

As previously explained in Chapter 4, the reduction of the S-T energy gap promotes the ISC allowing an efficient population of the triplet states. In parallel, the (π;π*) nature of the emitting triplet state, which has a poor spin-orbit coupling, provides an efficient stabilization of the triplet exciton elongating the decay time.

5.4 Conclusion

In conclusion, this very simple organic molecule, **TT**, displays crystallization-induced and mechanochromic emissive behavior, together with visible ultralong luminescence (1 s) at ambient conditions associated with H-aggregation. The **TT** uncommon features open up even to an intensive study of the possible structural modification of this scaffold in view of tuning its properties and deeply explore its potentiality as smart or functional material.

5.5 References

[1] Lucenti, E.; Forni, A.; Botta, C.; Carlucci, L.; Giannini, C.; Marinotto, D.; Previtali, A.; Righetto, S.; Cariati, E., H-Aggregates Granting Crystallization-Induced Emissive Behavior and Ultralong Phosphorescence from a Pure Organic Molecule. *The Journal of Physical Chemistry Letters* **2017,** *8* (8), 1894-1898.

[2] Kirk, K. L.; Nagai, W.; Cohen, L. A., Photochemistry of diazonium salts. II. Synthesis of 2-fluoro-L-histidine and 2-fluorohistamine, and the halogen lability of 2-fluoroimidazoles. *Journal of the American Chemical Society* **1973,** *95* (25), 8389-8392.

[3] Takeuchi, Y.; Kirk, K. L.; Cohen, L. A., Imidazole cyclotrimers (trimidazoles), a novel heteroannular series. *The Journal of Organic Chemistry* **1979,** *44* (24), 4243-4246.

[4] Schubert, D. M.; Natan, D. T.; Wilson, D. C.; Hardcastle, K. I., Facile Synthesis and Structures of Cyclic Triimidazole and Its Boric Acid Adduct. *Crystal Growth & Design* **2011,** *11* (3), 843-850.

[5] Masciocchi, N.; Bruni, S.; Cariati, E.; Cariati, F.; Galli, S.; Sironi, A., Extended Polymorphism in Copper(II) Imidazolate Polymers: A Spectroscopic and XRPD Structural Study. *Inorganic Chemistry* **2001,** *40* (23), 5897-5905

[6] Buck, D. M.; Kunz, D., Triazine Annelated NHC Featuring Unprecedented Coordination Versatility. *Organometallics* **2015,** *34* (21), 5335-5340.

[7] Cariati, E.; Lanzeni, V.; Tordin, E.; Ugo, R.; Botta, C.; Giacometti Schieroni, A.; Sironi, A.; Pasini, D., Efficient crystallization induced emissive materials based on a simple push–pull molecular structure. *Physical Chemistry Chemical Physics* **2011,** *13* (40), 18005-18014.

[8] Botta, C.; Benedini, S.; Carlucci, L.; Forni, A.; Marinotto, D.; Nitti, A.; Pasini, D.; Righetto, S.; Cariati, E., Polymorphism-dependent aggregation induced emission of a push–pull dye and its multi-stimuli responsive behavior. *Journal of Materials Chemistry C* **2016,** *4* (14), 2979-2989.

[9] Li, C.; Tang, X.; Zhang, L.; Li, C.; Liu, Z.; Bo, Z.; Dong, Y. Q.; Tian, Y.-H.; Dong, Y.; Tang, B. Z., Reversible Luminescence Switching of an Organic Solid: Controllable On–Off Persistent Room Temperature Phosphorescence and Stimulated Multiple Fluorescence Conversion. *Advanced Optical Materials* **2015,** *3* (9), 1184-1190.

[10] Kasha, M.; Rawls, H. R.; El-Bayoumi, M. A., The exciton model in molecular spectroscopy. *Pure and Applied Chemistry* **1965,** *11* (3-4), 371-392.

[11] Englman, R.; Jortner, J., The energy gap law for radiationless transitions in large molecules. *Molecular Physics* **1970,** *18* (2), 145-164.

6 The effect of Bromo Substituents on Cyclic Triimidazole

6.1 Introduction

As it was demonstrated in the previous chapter, **TT** shows RTP features associated with the formation in its crystal structure of H-aggregates that reduce the singlet-triplet gap, promoting ISC, stabilize the triplet, prolonging the decay time, and protect the inner layers from oxygen inhibiting quenching effects.

In general, the organization of emitting dyes in the solid state plays a central role in activating/favouring RTP in purely organic materials. In this regard, halogen or hydrogen bonds as well as H-aggregation have been reported to lead to structural rigidification minimizing the non-radiative deactivation processes of triplet excitons[1].

In order to investigate the effect of substituents on the emissive properties of **TT** we decided to functionalize the scaffold with bromine atoms[2][3]. In principle, heavy bromine atoms are expected to improve **TT** RTP performances due to their positive effects on ISC associated with high spin-orbit coupling. Moreover, the bromination of an aromatic compound is easily achieved at RT and can be considered as a first step for further functionalization.

Brominated derivatives of triimidazole can be easily obtained under mild conditions with *N*-bromosuccinimmide (NBS). In particular, different NBS/**TT** ratios lead to the formation of different amounts of: 3-bromotriimidazo[1,2-*a*:1',2'-*c*:1'',2''-*e*][1,3,5]triazine, 3,7-dibromotriimidazo[1,2-*a*:1',2'-*c*:1'',2''-*e*][1,3,5]triazine, 3,7,11-tribromotriimidazo[1,2-*a*:1',2'-*c*:1'',2''-*e*][1,3,5]triazine, hereafter **TT1Br**, **TT2Br** and **TT3Br** respectively (See Scheme 1). The products are then isolated and purified through flash column with DCM/MeOH, crystallized from hot acetonitrile/water mixture and characterized by NMR and mass spectrometry.

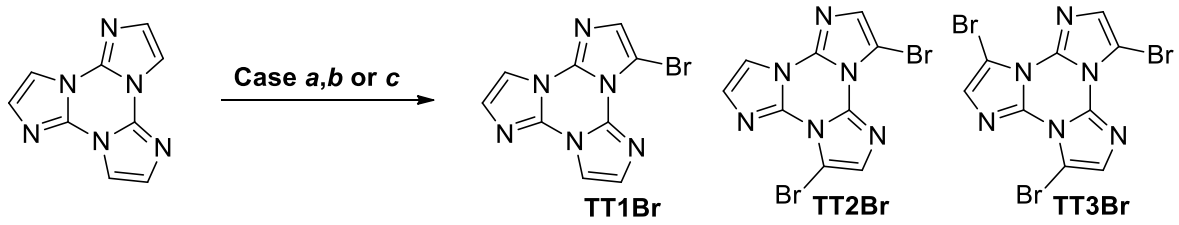

*Scheme 1: Synthetic patways for the synthesis of the brominated derivatives of **TT** and relative yields.*

	Description	**TT1Br %**	**TT2Br %**	**TT3Br %**
Case *a*	1 eq. NBS; 12h; CH_3CN, rt	85	5	Null
Case *b*	2 eq. NBS; 12h; CH_3CN, rt	57%	40%	Trace
Case *c*	3.3 eq. NBS; 12h; CH_3CN/CH_2Cl_2, rt, Cat. TFA	Null	Null	90%

*Table 1: Conditions and yields for the synthesis of the brominated derivatives of **TT**.*

Interestingly, despite an extensive NMR investigation including 1D (^1H and ^{13}C) and 2D (COSY, ^1H-^{13}C HSQC, ^1H-^{13}C HMBC, ^1H-^{15}N HMBC) experiments, the NMR structural assignment of all proton and carbon resonances for **TT1Br** and **TT2Br** has been hampered by the lack of crucial and diagnostic long-range correlations between quaternary carbon and proton signals. The experimental results have been implemented by quantum mechanical calculations of chemical shifts and heteronuclear coupling constants, the latter highlighting $^4J_{C\text{-}H}$ correlations about twice in value than $^3J_{C\text{-}H}$ ones, which have allowed the correct chemical shift assignments for both derivatives [4].

Moreover, an electrochemical investigation of the brominated derivatives on glassy carbon has revealed a shift of the reduction peak toward more positive potentials with respect to **TT**, with the carbon-halogen bond undergoing dissociative electron transfer with concerted mechanism. This result is quite interesting since such pathway is usually observed in alkyl derivatives (for which the injection of an electron leads to a purely dissociative state) while aromatic halides follow a stepwise mechanism (due to the presence of low lying LUMO orbitals that stabilize the incoming electron). In addition, the electrocleavage of the C–X bond is only slightly influenced by increasing the number of halogens when going from **TT1Br** to **TT3Br**. These findings support the hypothesis that each imidazole unit in the cyclic trimer acts as an almost independent redox site, with very poor heteroannular aromaticity [4].

6.2 Photophysical characterization and discussion

6.2.1 TT1Br

Dilute solutions of **TT1Br** (2.5 X 10^{-5} - 5 X 10^{-6} M) in DCM display a very sharp and intense absorption band at 230 nm, with a shoulder at approximately 237 nm and a low-energy tail at about 250- 280 nm. A structured emission was observed at 328 and 342 nm (τ_{av} = 0.38 ns, Φ = 3%) (See Figure 1b). At 77 K, upon excitation at wavelengths > 300 nm, a very weak emission is observed at approximately 460 nm. However, a very intense and broad Molecular Phosphorescence (MP) centered at 580 nm (τ_{av} = 256 µs) dominates the spectrum obtained upon excitation below 280 nm. The lifetime of this phosphorescence is unaffected by the presence/absence of O_2 (See Figure 1b).

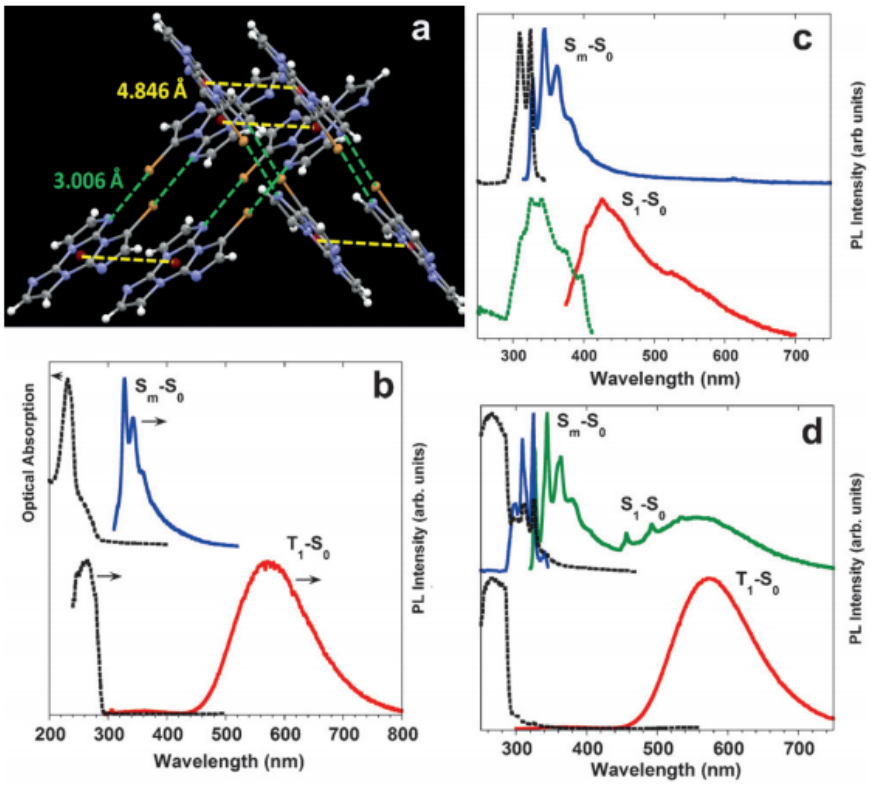

*Figure 1: **TT1Br** a) Crystal packing: π-π stacking interactions and Br···N XB shown as yellow and green dotted lines, respectively. b) In DCM (2.5 X 10^{-5} - 5 X 10^{-6} M): top: absorption and emission (λ_{exc}=280 nm) at RT; bottom: excitation (black dotted line, λ_{em} =580 nm) and emission (red line, λ_{exc} =280 nm) at 77 K. c) Powders at RT: top: excitation (black dotted line, λ_{em} =363 nm) and emission (blue line, λ_{exc} =300 nm); bottom: excitation (green dashed line, λ_{em} =429 nm) and emission (red line, λ_{exc} =360 nm). d) Powders at 77 K: top: emission (green line, λ_{exc} =300 nm) and excitation (blue line, λ_{em} =363 nm; black dashed line, λ_{em} =492 nm); bottom: excitation (black dashed line, λ_{em} =580 nm) and emission (red line, λ_{exc} =280 nm). Reproduced with permission from ref.[2] © 2017 Wiley-VCH Verlag GmbH & Co.*

Crystals of **TT1Br,** prepared from a hot CH_3CN/H_2O solution and manually selected using a microscope, when excited at 300 nm at room temperature are characterized, similarly to its diluted solution, by a structured emission at 326, 345, and 365 nm (τ < 1 ns, with Φ below the instrumental sensitivity). Moreover, an additional fluorescence centered at approximately 426 nm is activated by exciting at 360 nm (τ_{av} = 4 ns) (See Figure 1c). Upon lowering the temperature, similar features are observed for excitation above 300 nm, while upon excitation at 280 nm, the spectrum is dominated by the MP at 575 nm (τ_{av} = 274 µs) (See Figure 1d).

TD-DFT calculations on **TT1Br** monomer provide an allowed $S_0 \rightarrow S_1$ transition with $\pi \rightarrow \pi^*$ character at 231 nm (*f*= 0.024) owing to the introduction of bromine which disrupts the perfect symmetry of the triimidazolic scaffold. Stronger transitions are computed at 214, 208 and 204 nm ($S_0 \rightarrow S_3$ *f*= 0.203; $S_0 \rightarrow S_4$ *f*= 0.400; $S_0 \rightarrow S_5$ *f*= 0.524) in perfect agreement with the experimental spectrum. Calculations also provide an explanation to the observed dual emission, in fact, the fluorescence detected at 326 nm in solution is an anti-Kasha process $S_m \rightarrow S_0$ while the weak emission detected at 426 nm is a fluorescence $S_1 \rightarrow S_0$ that is accessible only when the S_1 level is selectively populated. The origin of the 580 nm phosphorescence observed at 77 K both in solution and in the solid state when exciting at high energy, below 280 nm, was disclosed through theoretical calculations. An efficient ISC is expected to occur from a high energy S_n to a close T_n level with $\sigma \rightarrow \sigma^*$ symmetry where the σ orbital is mainly delocalized on the bromine. No other phosphorescence is detected, in particular, no ultralong component is present in the solid sample at RT or at 77 K. H-aggregates are absent in the crystal structure of **TT1Br** where dimers with large distances between centroids (4.846 Å) self-assembled through cyclic Br···N halogen-bonded motifs, interact through C-H···N hydrogen bonds along the molecular plane and through C-H···π hydrogen bonds perpendicularly to the plane (See Figure 1a).

6.2.2 TT2Br

Diluted DCM solution (2.5 x 10^{-5} M) of **TT2Br** displays an intense adsorption at 235 nm with a low-energy tail at 250-280 nm and a hardly discernible emission at 380 nm with short decay time (τ_{av} = 3.48 ns) (See Figure 2b). At 77 K, similarly to **TT1Br**, a strong phosphorescence at 580 nm (τ_{av} = 265 µs) is observed by exciting at high energy (See Figure 2b).

Crystals of **TT2Br,** prepared from a hot CH_3CN/H_2O solution and manually selected using a microscope, at RT display a structured fluorescence with peaks at 395 nm, 419 nm and 443 nm (τ_{av} = 0.71 ns), a broad long-lived component at 470 nm (τ_{av} = 1.25 ms), visible only in the delayed spectrum, and a structured RTUP at 553, 600 nm (τ_{av} = 49 ms) that is strongly affected by the crystallinity of the sample (See Figure 2c). At 77 K, the molecular phosphorescence dominates the spectrum when the sample is irradiated at high energy (below 280 nm) while at lower energy a long lived component at 461, 484 nm (τ_{av} = 3.59 ms) and a structured fluorescence at 409, 434 and 462 nm (τ_{av} = 4.51 ns) are overlapped (See Figure 2d). Unlike RTUP, the two additional phosphorescent components are insensitive to the degree of crystallinity. To better understand this aspect the analysis of high concentrated PMMA films (10% w/w) was performed. **TT2Br**/PMMA thin film does not show any RTUP component while the long lived component at 480 nm is still visible in absence of oxygen The molecular phosphorescent appears only at 200 K, overcoming the other component under 180 K. The analysis of the photophysical behaviour clearly indicates the presence of three different phosphorescences whose attribution has required the support of theoretical calculations.

TD-DFT calculations provide two allowed transition ($S_0 \rightarrow S_1$ *f*= 0.016 at 233 nm and $S_0 \rightarrow S_4$ *f*= 0.067 at 215 nm) and two symmetry-forbidden transition ($S_0 \rightarrow S_2$; $S_0 \rightarrow S_3$) all with $\pi \rightarrow \pi^*$ character. As in the case of **TT1Br**, the 570 nm phosphorescence detected at 77 K in both solutions and powders is activated through excitation below 280 nm for the presence of a T_n level with $\sigma \rightarrow \sigma^*$ symmetry and Br character. Unlike **TT1Br**, **TT2Br** display RTUP ($T_1^H \rightarrow S_0$) due to the presence of H-aggregates clearly visible from single crystal X-ray diffraction analysis. Moreover, the crystal structure shows the presence of tetrameric structure bonded

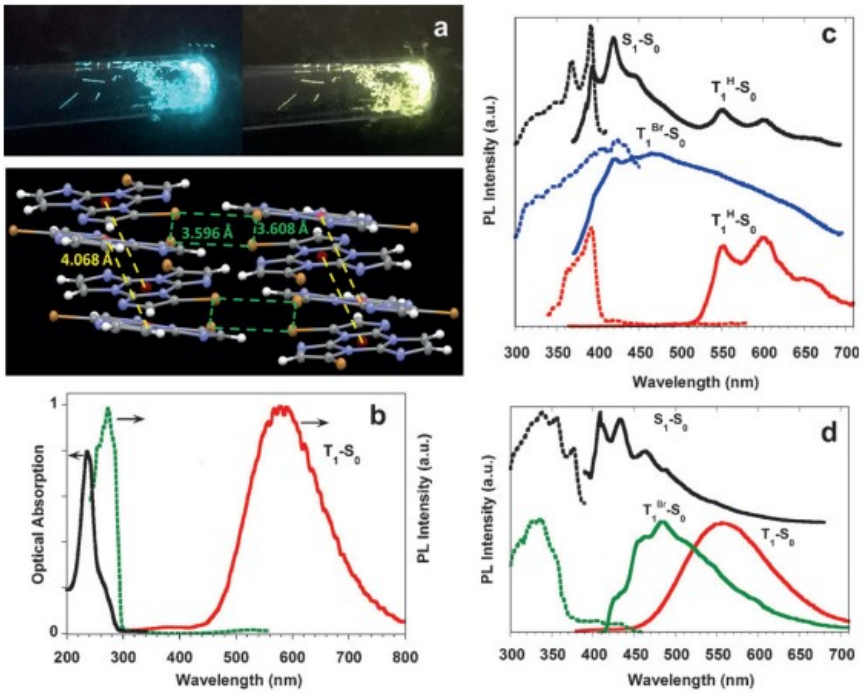

*Figure 2: **TT2Br** a) Top: powders at 77 K under a 360 nm (left) and 254 nm lamp (right); bottom: crystal packing: π-π stacking interactions and Br···Br XB shown as yellow and green dotted lines, respectively. b) In DCM (2.5 x 10^{-5} M): absorption at RT (black line); excitation (green dashed line, λ_{em} =580 nm) and emission (red line, λ_{exc} =280 nm) at 77 K. c) Powders at RT: top: excitation (black dotted line, λ_{em} =418 nm) and emission (black line, lex=355 nm); middle: excitation and phosphorescence emission (blue dashed line, λ_{em} =475 nm; blue line, λ_{exc} =355 nm, 5 ms delay, window 0.1 ms); bottom: excitation and phosphorescence emission (red dashed line, λ_{em} =600 nm; red line, λ_{exc} =355 nm, 0.5 ms delay, window 30 ms). d) Powders at 77 K: top: excitation (black dotted line, λ_{em} =410 nm) and emission (black line, λ_{exc} =375 nm); bottom: excitation (green dashed line, λ_{em} =475 nm), phosphorescence emission (green line, λ_{exc} =355 nm, 0.5 ms delay, window 30 ms), and delayed emission (red line, λ_{exc} =265 nm, 5 ms delay, window 100 ms). Reproduced with permission from ref.[2] © 2017 Wiley-VCH Verlag GmbH & Co.*

through Br···Br (Br_4-synthons)[5][6] that stacks along the *a* axis with a small lateral shift (the distance between the centroids of the triazinic rings is 4.068 Å). The Br···Br supramolecular units are responsible for the third phosphorescent component ($T_1^{Br} \rightarrow S_0$) which is sensitive to thermal vibration and oxygen at RT but becomes predominant at 77 K[7]. Structural studies demonstrate that at 120 K the cell volume is reduced of 2.6%, so that Br···Br distances are reduced as well as the distances between triazinic rings (See Figure 2a).

6.2.3 TT3Br

TT3Br diluted DCM solutions (10^{-4}M) show features similar to the other brominated derivatives with absorption at 245 nm and an onset at 300 nm. At RT a hardly discernible emission is detected at 370 nm (τ_{av} = 10.91 ns) and a very broad molecular phosphorescence at 585 nm (τ_{av} = 263 μs) when the temperature is lowered at 77 K (See Figure 3a). TDDFT calculation provides, as in the **TT1Br** and **TT2Br** cases, a vanishing $S_0 \rightarrow S_1$ transition with $^1(\pi,\pi^*)$ character due to the high symmetry of the molecule in diluted solution. Moreover, a forbidden transition with $^1(\pi,\sigma^*)$ character is computed, in which the σ orbitals are localized on the bromine atoms and on C-Br bonds. At higher energy a series of $^1(\pi,\pi^*)$ transition are expected, as well as, T_n levels with $^3(\sigma,\sigma^*)$ and $^3(\sigma,\pi^*)$ characters.

TT3Br absorption spectrum consists of two close intense peaks followed by two shoulders at low energy that are due to high energy $^1(\pi,\pi^*)$ states which are responsible for the RT emission in solution (S_n). The shoulders observed at lower energies correspond to the weak $^1(\pi,\pi^*)$ excitations to low-lying singlet states. The presence of the $^3(\sigma,\sigma^*)$ and $^3(\sigma,\pi^*)$ T_n levels justifies the efficient ISC from the closest S_n and the resulting S_1 molecular phosphorescence selectively excited below 280 nm.

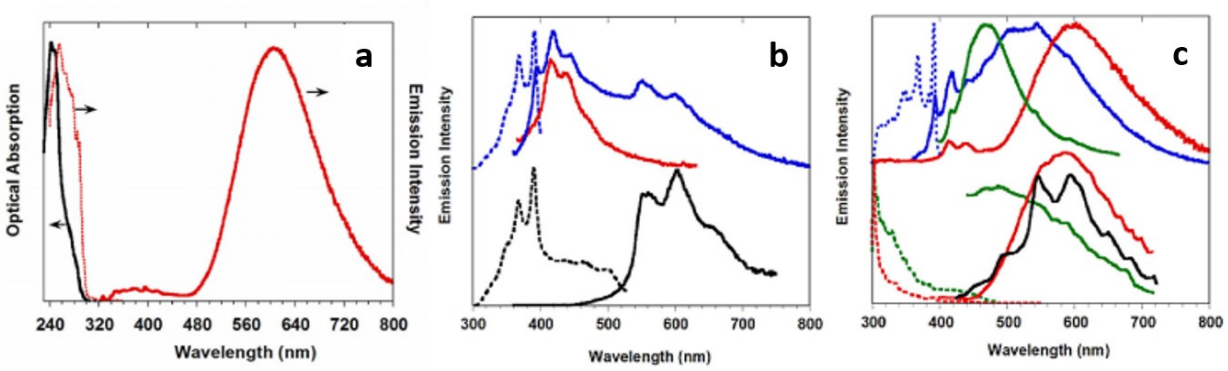

*Figure 3: **TT3Br** a)Absorption (black line) of **TT3Br** in DCM (10^{-4} M) at RT. Emission (λ_{exc} =280 nm; red solid line) and excitation profile at 77 K (λ_{em} =580 nm; red dotted line). b) Powders at RT. Top: Prompt emission (λ_{exc} =280 nm, red solid line; λ_{exc} =340 nm, blue solid line) and excitation profile (λ_{em} =420 nm, dashed blue line). Bottom: Delayed emission (λ_{exc} =340 nm, 1 ms delay, window 50 ms; black solid line) and excitation profile (λ_{em} =550 nm, dotted black line). c) Powders at 77 K. Top: Prompt emission (λ_{exc} =280 nm, red solid line; λ_{exc} =340 nm, blue solid line; λ_{exc} =385 nm, green solid line) and excitation profile (λ_{em} =420 nm, dotted blue line). Bottom: Delayed emission (λ_{exc} =360 nm, 100 ms delay, window 500 ms, red solid line; λ_{exc} =385 nm, 100 ms delay, window 500 ms, green solid line; λ_{exc} =385 nm, 5 ms delay, window 10 ms, black solid line) and excitation profiles (λ_{em}=523 nm, dotted green line; λ_{em} =600 nm, dotted red line). Reproduced with permission from ref.[3] © 2018 Wiley-VCH Verlag GmbH & Co.*

Crystals of **TT3Br,** obtained by slow cooling of a hot CH_3CN solution and manually selected using a microscope, at RT display a structured fluorescence at 415 nm and 437 nm (τ_{av} = 1.02 ns) when excited at 280 nm. At longer wavelength excitation an additional peak appears at 394 nm together with a lower energy phosphorescence at 555, 605 and 656 nm (τ_{av} = 18.42 ms) (See Figure 3b). At 77 K the emission becomes even more intricate. As in the frozen solution, the molecular phosphorescence (590 nm; τ_{av} = 200 µs) dominates the spectrum exciting at 280 nm, while the blue structured fluorescence at 414 and 440 nm is still present. When exciting at 340 nm the structured fluorescence at 392, 417, 440 nm (τ_{av} = 1.51 ns) is superimposed to a broad phosphorescence (τ_{av} = 18.11 ms) which becomes sharper exciting at 385 nm (See Figure 3c). As for **TT2Br**, the presence of three different long-lasting emission requires additional investigation to better understand the behaviour. Time gated experiments have revealed that with short delay times (100-600 µs) the broad molecular phosphorescence is easily recognizable exciting at 360 nm, while exciting at 385 nm a broad phosphorescence at 490 nm is observed. When longer delay times (>5 ms) are used it is possible to isolate the structured phosphorescence already observed at RT.

TT3Br crystallizes with two independent molecules in the asymmetric unit. The crystal packing of the flat and symmetric molecules is sustained by different intermolecular interactions Br···Br and Br···N, weak C-H···N, π-π stacking and many van der Waals contacts. Two different orientations are recognizable so that alternating layers of parallel molecules extend in the *ab* directions and perpendicular to *c*. Molecules belonging to each layer are involved in columnar π-π interactions characterized by triazinic centroids distances of 4.427, 4.759 and 4.838 Å.

Br···Br and Br···N XB interactions significantly shorter than the sum of vdW radii involve non-coplanar molecules, except for two short Br···N interactions between coplanar adjacent molecules that give XB chain motifs. The Br···N XB chains run along [1,1,0] and [1,1,0] directions with a relative inclination of about 50°. Furthermore, adjacent 1D chains are bonded by short Br···Br XBs to give layered motifs that pack along *c* with an *ABAB* sequence. Considering the additional relatively long Br···Br contact, such layered motif evidences the presence of a trimeric Br_3 XB unit with C-Br···Br angles from 154.8 to 171.5°, in agreement with a type II X···X geometrical arrangement of the X atoms. These layers are further connected by short Br···N interactions to give a 3D supramolecular array. Additional Br···Br (3.77–4.20 Å range) and Br···N (3.42–3.57 Å range) interactions longer than the sum of VdW radii are also present (See Figure 4).

DFT optimization of π-π dimeric units of **TT3Br** results in a geometry quite similar to the X-ray one with distances between triazinic centroids equal to 4.254 Å (calculated) and 4.4266 Å (measured), associated with

strong π-π interactions that are also responsible for the red shift observed between the fluorescence observed in solution and in the solid state. The dual fluorescence observed in the solid state should be ascribed to the high energy gap between the strong high energy singlet excitation and the weak S_0-S_1. The latter is intensified in the solid state owning to the distortion caused by the packing forces.

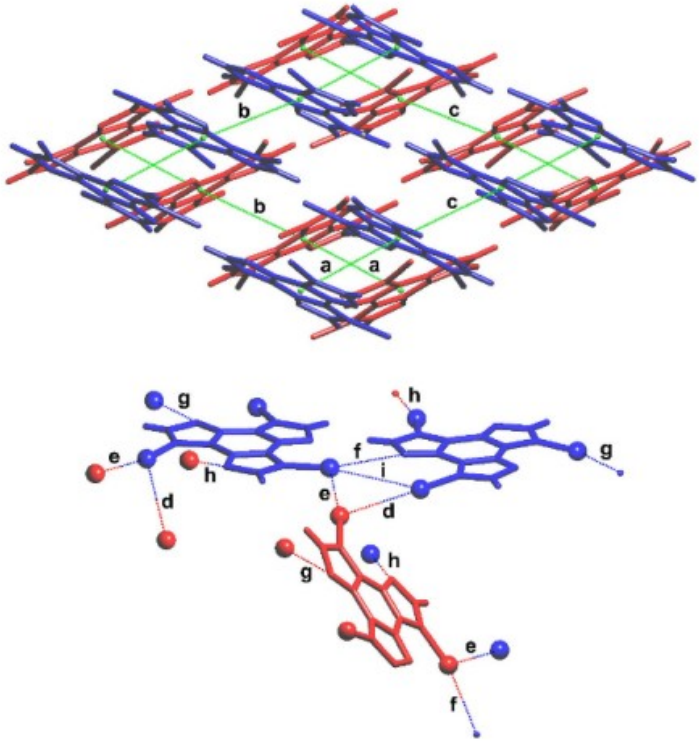

*Figure 4: Top: view of the packing along the c-axis in **TT3Br**. Two adjacent molecular layers extending parallel to ab are shown in red and blue. π -π interactions appear as green lines connecting triazine centroids: 4.4266(4) (**a**), 4.7591(5) (**b**) and 4.8385(5) A˚ (**c**). Bottom: The trimeric unit assembled through Br···Br and Br···N XBs. Br···N interactions **f** and **g**, 3.1344(3) and 3.1545(3) A˚ respectively, give 1D chains; Br···Br interactions **d** and **e**, 3.5405(3) and 3.6746(3) A˚ respectively, give layers; Br···N XB **h**, 3.0099(3) A˚, extend to 3D; Br···Br contact **i**, 4.1963(14) A˚. Reproduced with permission from ref.[2] © 2018 Wiley-VCH Verlag GmbH & Co.*

On the other side, geometry optimization of the Br_3 unit leads to a coplanar structure with two short (3.702 and 3.751 Å) and one long (3.990 Å) Br···Br distances. The TDDFT computed levels include a ^{3}(π, σ*) state close in energy to a ^{1}(π,π*) one suggesting that efficient spin-orbit coupling may occur between the two states allowing T_1^{Br} phosphorescence. This triplet is the only one involving excitation towards σ* orbitals mainly delocalized on the three Br atoms supporting the role of the Br_3 unit in the intermolecular electronic coupling[8]. However, the planarity of the optimized fragment suggests reduced stability associated with the Br_3 motif in the crystal. This could justify the lack of emission from T_1^{Br} at RT and the fact that the ultralong phosphorescence due to H-aggregation is observed also at 77 K.

6.3 Conclusion

In conclusion, a comprehensive investigation on the photophysical behaviour of **TT** brominated derivatives has deepen the knowledge on the heavy halogen effect. Multiple radiative deactivation processes have been disclosed for these new three excitation-dependent dyes. Unfortunately, the low quantum yields showed by **TT1Br** and **TT3Br** could negatively affect their possible use in the development of new optoelectronic devices. However, as it will be shown in the following chapters, the introduction of halogen has opened up to further modification and to the preparation of even more interesting dyes.

6.4 References

[1] Forni, A.; Lucenti, E.; Botta, C.; Cariati, E., Metal free room temperature phosphorescence from molecular self-interactions in the solid state. *Journal of Materials Chemistry C* **2018,** *6* (17), 4603-4626.

[2] Lucenti, E.; Forni, A.; Botta, C.; Carlucci, L.; Giannini, C.; Marinotto, D.; Pavanello, A.; Previtali, A.; Righetto, S.; Cariati, E., Cyclic Triimidazole Derivatives: Intriguing Examples of Multiple Emissions and Ultralong Phosphorescence at Room Temperature. *Angewandte Chemie International Edition* **2017**, *56* (51), 16302-16307.

[3] Lucenti, E.; Forni, A.; Botta, C.; Carlucci, L.; Colombo, A.; Giannini, C.; Marinotto, D.; Previtali, A.; Righetto, S.; Cariati, E., The Effect of Bromo Substituents on the Multifaceted Emissive and Crystal-Packing Features of Cyclic Triimidazole Derivatives. *ChemPhotoChem* **2018**, *2* (9), 801-805.

[4] Di Micco, S.; Giannini, C.; Previtali, A.; Lucenti, E.; Bifulco, G., Chemical shift assignment of mono- and di-bromo triimidazo[1,2-a:1′,2′-c:1″,2″-e][1,3,5]triazine derivatives by DFT/NMR integrated approach. *Magnetic Resonance in Chemistry* **2019,** *57* (2-3), 82-92.

[5] Clark, T.; Hennemann, M.; Murray, J. S.; Politzer, P., Halogen bonding: the σ-hole. *Journal of Molecular Modeling* **2007**, *13* (2), 291-296.

[6] Shi, H.; An, Z.; Li, P.-Z.; Yin, J.; Xing, G.; He, T.; Chen, H.; Wang, J.; Sun, H.; Huang, W.; Zhao, Y., Enhancing Organic Phosphorescence by Manipulating Heavy-Atom Interaction. *Crystal Growth & Design* **2016**, *16* (2), 808-813.

[7] Mukherjee, A.; Tothadi, S.; Desiraju, G. R., Halogen Bonds in Crystal Engineering: Like Hydrogen Bonds yet Different. *Accounts of Chemical Research* **2014**, *47* (8), 2514-2524.

[8] Yang, Z.; Mao, Z.; Zhang, X.; Ou, D.; Mu, Y.; Zhang, Y.; Zhao, C.; Liu, S.; Chi, Z.; Xu, J.; Wu, Y.-C.; Lu, P.-Y.; Lien, A.; Bryce, M. R., Intermolecular Electronic Coupling of Organic Units for Efficient Persistent Room-Temperature Phosphorescence. *Angewandte Chemie International Edition* **2016**, *55* (6), 2181-2185.

7 Iodine introduction on the triimidazole scaffold: Intrinsic *vs* Extrinsic effect.

7.1 Introduction

The introduction of heavy halogen atoms (like Br or I)[1] in the molecular structure (intrinsic effect) or the formation of intramolecular interactions based on halogen bonding (extrinsic effect) [2][3][4], with molecules of the same type (one component)[5][6][7][8] or with molecules of a different type (two components)[9][10][11][12], can effectively modulate the emissive properties of a chromophore providing an efficient strategy for the preparation of functional materials.

The wide range of possible halogen bonds (XB) patterns can produce various effects either on fluorescence and phosphorescence, as previously demonstrated by the brominated derivatives of **TT**, which displays an extrinsic one-component effect combined with an intrinsic one[13][14][15]. For example, **TT2Br** forms strong and rigid Br_4 XB intramolecular units that induces a long lived RTP which is absent in **TT3Br** where only weaker and non-planar Br_3 XB units are formed.

In order to better understand the extrinsic/intrinsic effects on the **TT** scaffold, the structural and emissive properties of 3-iodiotriimidazo[1,2-*a*:1',2'-*c*:1'',2''-*e*][1,3,5]triazine (**TT1I**), 3,7-diiodiotriimidazo[1,2-*a*:1',2'-*c*:1'',2''-*e*][1,3,5]triazine (**TT2I**) and **TTCo**, the 1:1 co-crystal self-assembled through I···N XB between two acceptor nitrogen atoms of **TT** and the two iodine atoms of 1,4-diiodotetrafluorobenzene (DITFB) to form a 1D infinite chain structure, have been investigated. **TT1I** is an archetypal molecule to evaluate the intrinsic halogen-atom effect and to run a comparative study with its brominated analogue (**TT1Br**). In parallel, **TTCo** allows to isolate the extrinsic two-component effect and so, through a comparison with **TT1I** and **TT**, to draw a complete picture of the heavy halogen role in the modulation of the photophysical properties. The iodinated derivatives of triimidazole, similarly to the brominated ones, were prepared using N-iodosuccinimmide (NIS) as iodinating agent in the presence of catalytic amount of TFA. By using different **TT**/NIS ratios, different amounts of **TT1I** and **TT2I** were obtained. The crude products were purified through flash chromatography using DCM/MeOH and crystallized from hot acetonitrile/water mixture.

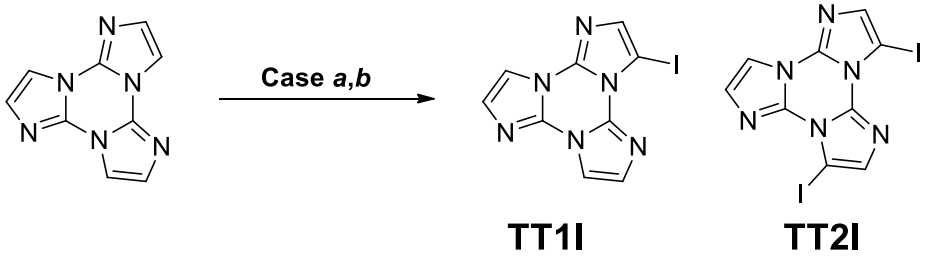

*Scheme 1: Synthetic pathways for the synthesis of the iodinated derivatives of **TT**.*

	Description	**TT1I %**	**TT2I %**
Case *a*	1 eq. NIS; 12h; CH_3CN; Cat. TFA, rt	55%	15%
Case *b*	2 eq. NIS; 12h; CH_3CN; Cat. TFA, rt	62%	27%

*Table 1: Conditions and yields for the synthesis of the iodinated derivatives of **TT**.*

7.2 Photophysical characterization and discussion

7.2.1 TT1I

Solutions of **TT1I** in DCM (10^{-4} M) show an absorption band at about 240 nm but no emission is detected at RT (Figure 1b). Only lowering the temperature to 77 K and exciting at 340 nm an unresolved emission is detected at about 420 nm. When exciting at higher energy (below 300 nm) the spectrum is dominated by a phosphorescence at 630 nm (τ_{av}= 27.27 ms)(Figure 1b). From a comparison between **TT1I** and the brominated derivatives solutions some statements can be made. 1) The fluorescent emission of **TT1I** in diluted solutions appears only at low temperature and it is compatible with an emission from S_1, while in the bromo-derivatives a fluorescent emission is observed even at RT and associated to an emission from high energy singlet. 2) The molecular phosphorescence (MP) detected for **TT1I** is red shifted (almost 50 nm) compared to the brominated derivatives ones. 3) The **TT1I** MP lifetime is 10 times shorter than the brominated derivatives ones 4) Only **TT1Br** solutions display a non-null quantum yield while **TT1I**, **TT2Br** and **TT3Br** quantum yields are under the instrument detection limit. Points 3) and 4) are reasonably explained by the enhanced heavy atom effects of the iodine that increases the spin-orbit coupling promoting the ISC. The results of these two processes are the quenching of the fluorescence and the speed up of the MP and so points number 1) and 2). Computational DFT (TDDFT) calculations provide a solid explanation for the MP. As for the bromo-analogues, the presence of an high energy triplet state (T_5) with $^3(\sigma,\sigma^*)$ close to a $^1(\pi,\pi^*)$ singlet state allows an efficient SOC on this high energy levels. The $^3(\sigma,\sigma^*)$ level of **TT1I** is at lower energy with respect to **TT1Br**, with a red-shifted emission as direct consequence.

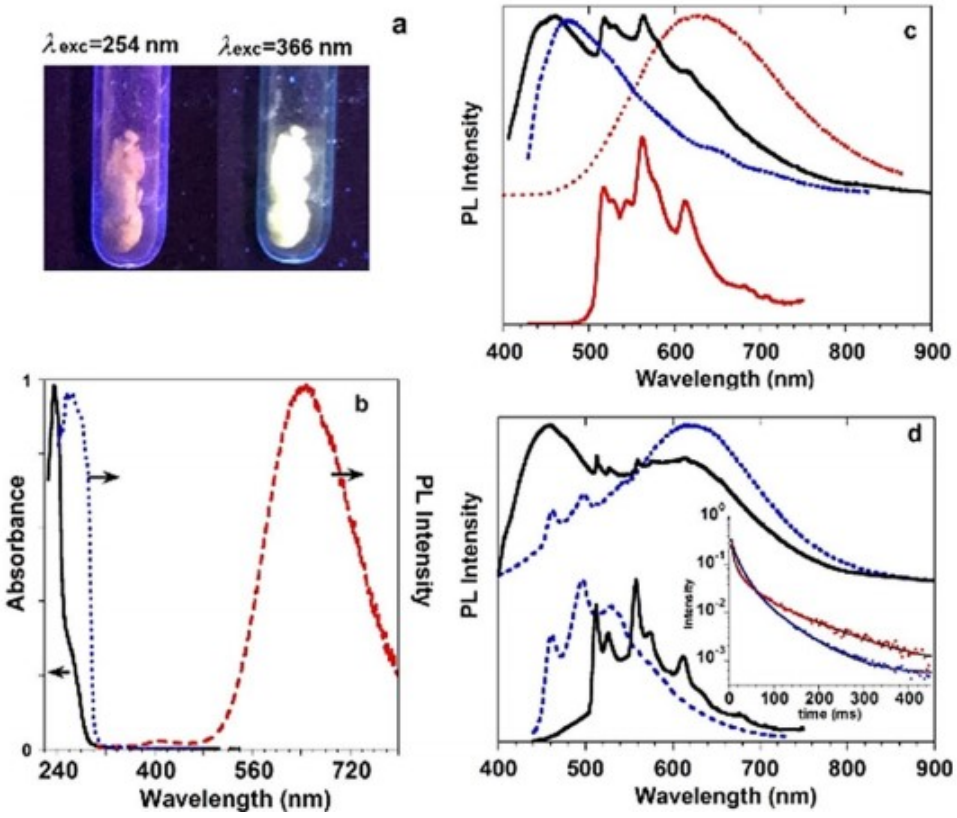

*Figure 1: a) Pictures of **TT1I** crystals under UV-light illumination at 298 K. b) **TT1I** in DCM (10^{-4} M): absorption spectrum at 298 K (black solid line); emission and excitation spectra at 77 K (λ_{exc}=280 nm, red dashed line; λ_{em} =648 nm, blue dotted line). c) Emission spectra of **TT1I** crystals at 298 K. Top: PL at λ_{exc} =300 nm (red dotted line), λ_{exc} =370 nm (black solid line), λ_{exc} =415 nm (blue dashed line); bottom: phosphorescence spectrum (λ_{exc} =370 nm, delay 50 ms, window 200 ms, red solid line). d) Emission spectra of **TT1I** crystals at 77 K. Top: PL at λ_{exc} =320 nm (blue dotted line), λ_{exc} =370 nm (black solid line); bottom: phosphorescence spectra at λ_{exc} =320 nm (delay 10 ms, window 50 ms, blue dotted line) and λ_{exc} =370 nm (delay 50 ms, window 200 ms, black solid line). Phosphorescence decays at λ_{em} =460 nm (λ_{exc} =320 nm, blue points) and λ_{em} =558 nm (λ_{exc} =370 nm, red points) with their three-exponential fits (black lines) shown in the inset. Reproduced with permission from ref.[1] © 2019 Wiley-VCH Verlag GmbH & Co.*

At 298 K, exciting at 415 nm crystals of **TT1I** (Φ< 0.1%), manually selected using a microscope, display a broad fluorescence is measured at 476 nm (τ_{av}=1.37 ns). As for its solution, **TT1I** is prone to emit from the S_1 level while, **TT1Br** and **TT3Br** in the same condition display dual fluorescence from S_1 and S_m and **TT2Br** only displays fluorescence from S_m. When exciting at 370 nm, the **TT1I** fluorescent emission is superimposed to an ultralong phosphorescence (τ_{av} = 63.69 ms) peaked at 517, 563 and 612 nm, which is clearly visible in the delayed spectrum (Figure 1c). With shorter wavelengths (<300 nm) the MP at about 630 nm is observed (τ_{av} = 0.53 ms) (Figure 1c). Lowering the temperature to 77 K the behaviour becomes more intricate. When the sample is excited at 370 nm an overlap between the fluorescence at 458 nm (τ_{av} = 2.77 ns), the vibrational resolved ultralong phosphorescence and the MP makes the situation hardly discernible. Thankfully, exciting at high energy (320 nm) the situation is simplified with the MP superimposed to a new phosphorescence peaked at 460 and 495 nm Integration of the phosphorescence at different delays times allows to define the two components (Figure 1d bottom). The longer component, with τ_{av} = 66.47 ms, displays narrow peaks at 511, 526, 558, 573 and 610 nm, while the shorter one is peaked at 460 nm and 530 nm (τ_{av} = 34.85 ms).

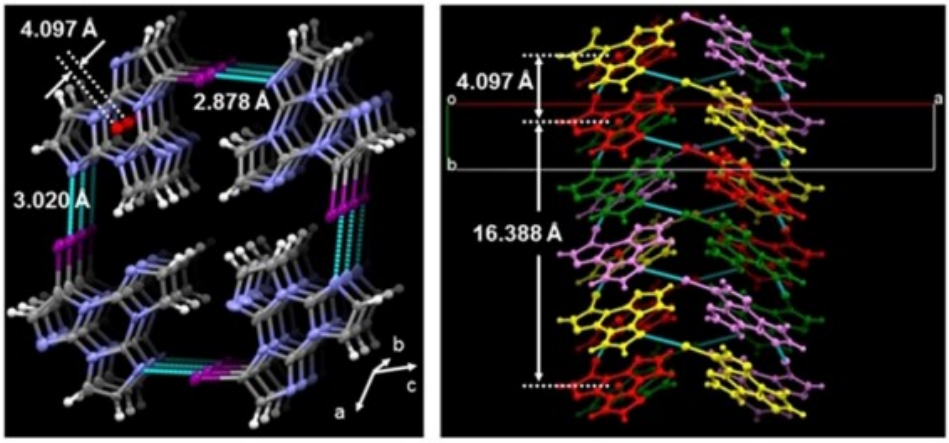

*Figure 2: Partial views along b (left) and c axes (right) of the **TT1I** crystal. Reproduced with permission from ref.[1] © 2019 Wiley-VCH Verlag GmbH & Co.*

Single crystal X-ray diffraction analysis has revealed a C2/*c* space group for **TT1I** with the presence of two molecules in the asymmetric unit. The molecules form helicoidal chains through non-equivalent I···N halogen bonds along the *b* direction. The shortest bond is 18% smaller than the Van der Waals radii sum ($r_{I2\cdots N5}$=2.878 Å) and connects two almost co-planar molecules, while the longer one is 14% smaller than the rVdW ($r_{N11\cdots I2}$=3.020 Å) and connects two twisted molecules (the dihedral angles between the l.s. planes through the triazinic rings of the interacting pair are 14.6 and 69.28°, respectively;Figure 2). Along the helix axis, where every pitch is formed by four molecules (16.388 Å pitch length), small interplanar distances (3.309 Å) and reduced slippage (2.3 Å) are measured between adjacent **TT1I** molecules. The distance between centroids of the triazinic rings (4.097 Å), the angle between the connecting axes and its projection on the molecular plane (55°) are indicative of the formation of H-aggregate even for this molecule. Different helices are connected though strong C-H···N ($r_{N7\cdots H17}$=2.38 Å and $r_{N1\cdots H16}$=2.50 Å) and weak C-H···I hydrogen bonds

In order to better understand the intrinsic heavy atom effect on the **TT, TT2I** has been prepared. **TT2I**, which is isostructural to its brominated analogue **TT2Br**, shows slightly corrugated planes with molecules forming tetrameric I···I XB cyclic units stacking along the *a* axis with a small lateral shift and longer centroid-centroid distance with respect to **TT2Br** (4.304 Å vs 4.068 Å). Similarly to **TT1I**, **TT2I** crystals (Φ = 7%) display a fluorescence (443 nm, τ_{av} = 1.23 ns), a RTUP (625 nm, τ_{av} = 9.47 ms) and a MP (680 nm, τ_{av} = 3.47 ms) at RT.

The comparison between these **TT** derivatives allows to define that: 1) The ultralong RTP is ascribable to H-aggregates formation even in **TT1I** and **TT2I**. 2) The strong N···I XBs, detected in **TT1I** crystals, generate a more rigid environment that favours the vibrational resolution observed for its RTUP. 3) The decrease of the

RTUP decay time (**TT** (970 ms)>**TT1I** (64 ms)>**TT2Br** (29 ms)> **TT3Br** (18 ms)>**TT2I** (9 ms)) is a consequence of the different strength of the H-aggregates and the presence of heavy atoms. 4) The formation of XB generates a ms order phosphorescence that, differently from **TT2Br** and **TT3Br**, is present even at RT. Interestingly, a similar phosphorescent emission is absent in **TT1Br**, showing in its structure only weaker Br···N XB ($r_{Br\cdots N}$ = 3.006 Å, 12% shorter than the sum of van der Waals radii). 5) In agreement with the presence of the heavier iodine atom on the molecule, the iodinated derivatives display at RT a MP which is much more intense than the one observed for the brominated analogues that appears only at 77K. In addition, high energy wavelengths are not required to observe the MP of **TT1I** that can be activated even populating S_1 in the solid sample.

7.2.2 TTCo

Crystals of **TTCo** at 298 K (Φ = 5%) excited below 340 nm show a broad fluorescence with maximum at about 410 nm (τ_{av} = 2.56 ns) and phosphorescence bands at 496, 528 and 566 nm (τ_{av} = 21.48 ms). With higher excitation wavelength even a structured long lasting component becomes visible and can be isolated with a time gated experiment (Figure 3c). Lowering the temperature to 77K an additional phosphorescence appears at 720 nm (τ = 6.83 ms) exciting at 300 nm. This latter emission is associate to the extrinsic heavy-atom effect due to the presence of the iodine atom in the **TT·DITFB** dimer. In fact, DFT/TDDFT calculations provide $^3(\sigma,\sigma^*)$ and $^3(\pi,\sigma^*)$ levels that, similarly to what observed for **TT1I**, promote the SOC from close singlet states of different character. The lower efficiency of this process respect to **TT1I** allows to observe this "extrinsic MP" only at low temperature. Exciting at lower energy a fluorescent emission at 440 nm (τ_{av} =3.41 ns) is superimposed to two different phosphorescences, at 490, 527, 560 nm (τ_{av} =20.01 ms) and at 463, 497, 537 nm (τ_{av} = 14.65 ms), that are distinguishable using time-gated experiments (Figure 3e).

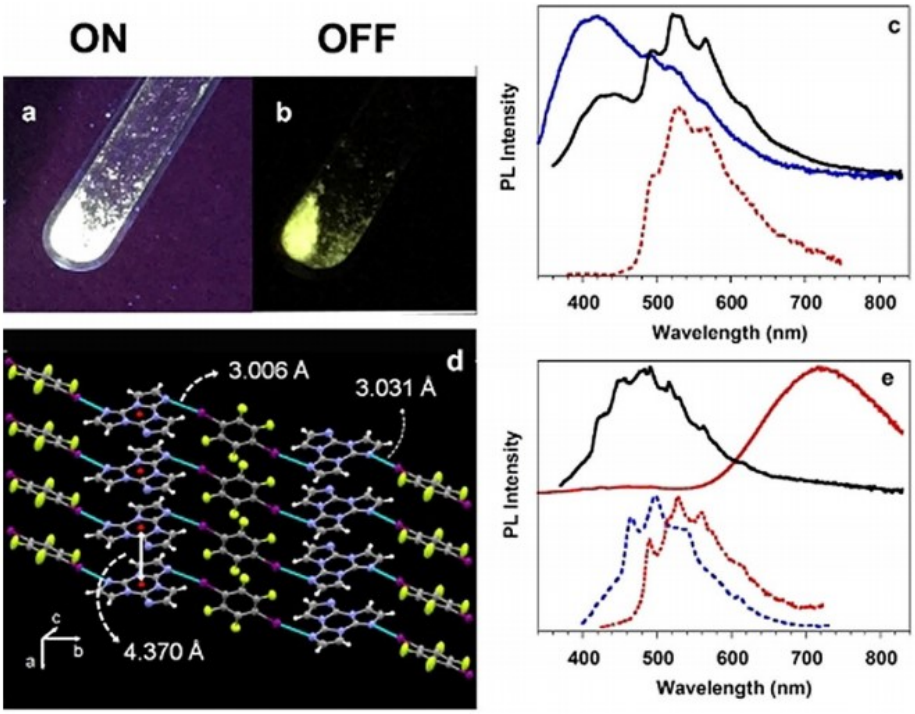

*Figure 3: a,b) Images of **TTCo** crystals at 298 K with UV-light illumination on and off. c) Emission spectra of **TTCo** at 298 K. Top: PL at λ_{exc}=300 nm (blue line) and λ_{exc} =350 nm (black solid line); bottom: phosphorescence spectrum (λ_{exc} =350 nm, delay 0.5 ms, window 1 ms, red dashed line). d) Partial view of the crystal structure of **TTCo** showing columnar H-aggregates of **TT** along the a direction (centroids of the triazinic rings shown as red circles) interconnected through I···N XB (light-blue dashed lines) with **DITFB** to form infinite 1D zigzag chains. e) Emission spectra of **TTCo** crystals at 77 K. Top: PL at λ_{exc} =340 nm (black line), λ_{exc} =300 nm (red solid line); bottom: phosphorescence spectra at λ_{exc} =320 nm (delay 10 ms, window 50 ms, blue dashed line) and λ_{exc} =370 nm (delay 10 ms, window 50 ms, red dotted line). Reproduced with permission from ref.[1] © 2019 Wiley-VCH Verlag GmbH & Co.*

TTCo crystallize in a P21/*n* space group, with an asymmetric unit containing two half molecules of **DITFB** and one molecule of **TT** (Figure 3d). In the crystal structure **TT** molecules act as double XB acceptor and **DITFB** as double XB donor forming a theoretically infinite mono-dimensional zigzag chain through I···N XB. Antiguous chains form weak C-H···N and C-H···F hydrogen bonds. The I···N distances are, alternatively, shorter by 14% and 15% than the rVdW ($r_{I1\cdots N1}$=3.031 Å (XB_1) and $r_{I2\cdots N5}$=3.006 a (XB_2)). No co-planarity between **TT** and **DITFB** units is detected along the chains where the dihedral angles formed by the l.s. planes through the triazinic ring and the **DITFB** units are 31.51° (XB_1) and 77.36° (XB_2). **TT** molecules belonging to different chains are connected through strong π– π stacking interactions along the *a* axis forming columns with interplanar distances equal to 3.332, 3.488 and 3.777 Å. The larger slippage (2.8 Å) and the longer distance (4.370 Å) between triazinic centroids in addition to the lower value of θ (50°) respect to **TT1I**, are indicative of a less efficient H-aggregation. In agreement with this structural feature, the long-lived component visible at RT has to be associated to the H-aggregation while the shorter one visible only at 77K is probably due to the I···N XB formation.

The comparison between **TT1I** and **TTCo** allows to make some consideration about the introduction of iodine on the triimidazolic scaffold and about the difference between the intrinsic and extrinsic introduction of the heavy atom. As for the brominated counterparts, the introduction of Iodine generates two new emissive deactivation processes. In general, the introduction of Iodine has the same "overall" effect on **TT**. In particular, three different phosphorescences can be recognised for both our species: the RTUP ($T_1^H \rightarrow S_0$), which is activated at 370 nm at RT, the I···N XB induced phosphorescence ($T_1^I \rightarrow S_0$), that is active only at 77K exciting at 320 nm and the extrinsic or the intrinsic MP ($T^1 \rightarrow S_0$) which requires an high-energy excitation.

For what concern the extrinsic/intrinsic heavy-atom effect: 1) The quantum yields are <0.1, 5 and 7% for **TT1I**, **TTCo** and **TT2I**, respectively. This means that the increase of Φ has to be associated to a more rigid environment in the crystal structure (the same conclusion was drawn for **TT1Br** and **TT2Br**). 2) The observation of the MP at RT for **TT1I** and **TT2I** agrees with a stronger intrinsic heavy-atom effect. 3) The strong red shift of the "extrinsic MP" of **TTCo** and its faster decay can be explain through the greater distortion of the $^3(\sigma,\sigma^*)$ triplet state due to the non-bonded interaction. 4) The intensity of the I···N XB induced phosphorescence depends by the strength of the intramolecular bond regardless its one- or two-component origin because it is observed in both **TT1I** and **TTCo.** 5) The shorter average lifetimes of $T_1^H \rightarrow S_0$ and $T_1^I \rightarrow S_0$ of **TTCo** respect to **TT1I** agree with its weaker XB and H-aggregate motives.

7.3 Conclusion

This comparative study has allowed to better understand the heavy halogen effects on the triimidazolic scaffold and the difference between the intrinsic and extrinsic role played by the iodine in **TT1I** and **TTCo**. In particular, the possibility to tune the emission through the cocrystallization with an XB donor is surely an appealing strategy to develop functional materials without dealing with challenging synthetic and purification steps.

7.4 References

[1] Lucenti, E.; Forni, A.; Botta, C.; Giannini, C.; Malpicci, D.; Marinotto, D.; Previtali, A.; Righetto, S.; Cariati, E., Intrinsic and Extrinsic Heavy-Atom Effects on the Multifaceted Emissive Behavior of Cyclic Triimidazole. *Chemistry – A European Journal* **2019,** *25* (10), 2452-2456.

[2] Sarkar, S.; Hendrickson, H. P.; Lee, D.; DeVine, F.; Jung, J.; Geva, E.; Kim, J.; Dunietz, B. D., Phosphorescence in Bromobenzaldehyde Can Be Enhanced through Intramolecular Heavy Atom Effect. *The Journal of Physical Chemistry C* **2017,** *121* (7), 3771-3777.

[3] Yuan, W. Z.; Shen, X. Y.; Zhao, H.; Lam, J. W. Y.; Tang, L.; Lu, P.; Wang, C.; Liu, Y.; Wang, Z.; Zheng, Q.; Sun, J. Z.; Ma, Y.; Tang, B. Z., Crystallization-Induced Phosphorescence of Pure Organic Luminogens at Room Temperature. *The Journal of Physical Chemistry C* **2010,** *114* (13), 6090-6099.

[4] Pan, S.; Chen, Z.; Zheng, X.; Wu, D.; Chen, G.; Xu, J.; Feng, H.; Qian, Z., Ultralong Room-Temperature Phosphorescence from Supramolecular Behavior via Intermolecular Electronic Coupling in Pure Organic Crystals. *The Journal of Physical Chemistry Letters* **2018,** *9* (14), 3939-3945.

[5] Bolton, O.; Lee, K.; Kim, H.-J.; Lin, K. Y.; Kim, J., Activating efficient phosphorescence from purely organic materials by crystal design. *Nature Chemistry* **2011,** *3* (5), 415-415.

[6] Maity, S. K.; Bera, S.; Paikar, A.; Pramanik, A.; Haldar, D., Halogen bond induced phosphorescence of capped γ-amino acid in the solid state. *Chemical Communications* **2013,** *49* (79), 9051-9053.

[7] Shi, H.; An, Z.; Li, P.-Z.; Yin, J.; Xing, G.; He, T.; Chen, H.; Wang, J.; Sun, H.; Huang, W.; Zhao, Y., Enhancing Organic Phosphorescence by Manipulating Heavy-Atom Interaction. *Crystal Growth & Design* **2016,** *16* (2), 808-813.

[8] Sun, X.; Zhang, B.; Li, X.; Trindle, C. O.; Zhang, G., External Heavy-Atom Effect via Orbital Interactions Revealed by Single-Crystal X-ray Diffraction. *The Journal of Physical Chemistry A* **2016,** *120* (29), 5791-5797.

[9] Bolton, O.; Lee, D.; Jung, J.; Kim, J., Tuning the Photophysical Properties of Metal-Free Room Temperature Organic Phosphors via Compositional Variations in Bromobenzaldehyde/Dibromobenzene Mixed Crystals. *Chemistry of Materials* **2014,** *26* (22), 6644-6649.

[10] Pang, X.; Wang, H.; Wang, W.; Jin, W. J., Phosphorescent π-Hole···π Bonding Cocrystals of Pyrene with Halo-perfluorobenzenes (F, Cl, Br, I). *Crystal Growth & Design* **2015,** *15* (10), 4938-4945.

[11] d'Agostino, S.; Spinelli, F.; Taddei, P.; Ventura, B.; Grepioni, F., Ultralong Organic Phosphorescence in the Solid State: The Case of Triphenylene Cocrystals with Halo- and Dihalo-penta/tetrafluorobenzene. *Crystal Growth & Design* **2019,** *19* (1), 336-346.

[12] Li, C.; Tang, X.; Zhang, L.; Li, C.; Liu, Z.; Bo, Z.; Dong, Y. Q.; Tian, Y.-H.; Dong, Y.; Tang, B. Z., Reversible Luminescence Switching of an Organic Solid: Controllable On–Off Persistent Room Temperature Phosphorescence and Stimulated Multiple Fluorescence Conversion. *Advanced Optical Materials* **2015,** *3* (9), 1184-1190.

[13] Lucenti, E.; Forni, A.; Botta, C.; Carlucci, L.; Colombo, A.; Giannini, C.; Marinotto, D.; Previtali, A.; Righetto, S.; Cariati, E., The Effect of Bromo Substituents on the Multifaceted Emissive and Crystal-Packing Features of Cyclic Triimidazole Derivatives. *ChemPhotoChem* **2018,** *2* (9), 801-805.

[14] Lucenti, E.; Forni, A.; Botta, C.; Carlucci, L.; Giannini, C.; Marinotto, D.; Pavanello, A.; Previtali, A.; Righetto, S.; Cariati, E., Cyclic Triimidazole Derivatives: Intriguing Examples of Multiple Emissions and Ultralong Phosphorescence at Room Temperature. *Angewandte Chemie International Edition* **2017,** *56* (51), 16302-16307.

[15] Lucenti, E.; Forni, A.; Botta, C.; Carlucci, L.; Giannini, C.; Marinotto, D.; Previtali, A.; Righetto, S.; Cariati, E., H-Aggregates Granting Crystallization-Induced Emissive Behavior and Ultralong Phosphorescence from a Pure Organic Molecule. *The Journal of Physical Chemistry Letters* **2017,** *8* (8), 1894-1898.

8 Pyridinyl fragment conjugation: (2-fluoropyridin-4-yl)

8.1 Introduction

The greater attention gained by molecules with prolonged solid state emission[1,2], that can find various applications in the development of new technologies, makes the development of these materials an hot-topic today[3-7].

As reported in the previous chapters, the introduction of Br and I atoms on the trimidazolic scaffold strongly affects its photophysical behaviour that comprises dual fluorescence, molecular phosphorescence, supramolecular room temperature phosphorescence (RTP) and RTUP[8–10]. Unfortunately, the Φ of these compounds dramatically drops in comparison with the PLQY measured for **TT**, probably because of the introduction of heavy atoms that promotes new non-radiative deactivation processes in addition to the emissive ones, reducing their potential applications.

To solve this drawback, a step forward in the chemistry and photophysics of **TT**-derivatives has been accomplished by insertion of a chromophoric fragment (2-fluoropyridine) on the trimidazolic scaffold. Organic substituents are expected to modify the emissive properties at both molecular and, through different packing arrangement, solid-state levels[11–15]. These effects were not predictable, so that any new member of the **TT**-family represents a building block worth studying to get information on this new and very intriguing class of emitters.

The halo-derivatization of the **TT** scaffold open up to a greater reactivity towards coupling reaction giving the opportunity to introduce others organic fragment.

3-(2-fluoropyridin-4-yl)triimidazo[1,2-*a*:1′,2′-*c*:1″,2″-*e*][1,3,5]triazine, **TTFPy**, containing the 2-fluoropyridine moiety, has been synthetized by Suzuki-Miyaura coupling between **TT1Br** and 2-fluoropyridine-4-boronic acid pinacol ester (See Scheme 1) [16].

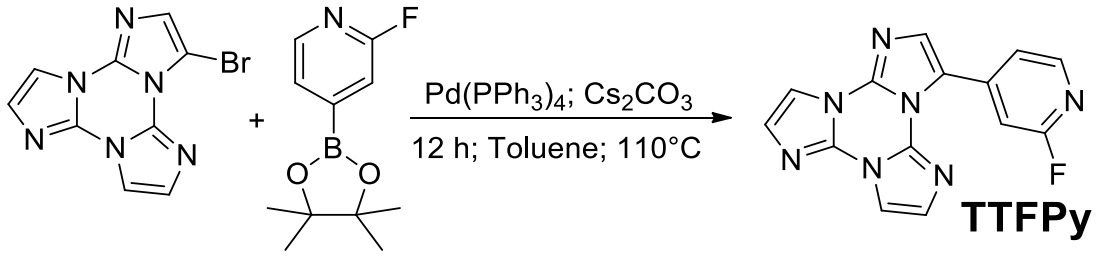

*Scheme 1: Synthesis of **TTFPy**.*

The compound's photophysical behavior is markedly different from that of parent **TT** being, already as a molecule, quite fluorescent at room temperature and showing additional molecular phosphorescence at 77 K.

8.2 Photophysical characterization

Solutions of **TTFPy** in CH_3CN (10^{-5} M) display at 298 K absorption maxima at 227 and 291 nm, and an emission band at 358 nm (Φ = 50 %), corresponding to radiative S_1-S_0 deactivation (τ = 4.26 ns) (See Figure 1). Absorption and emission spectra in solvents of different polarity reveal a weak positive solvatochromism for the low energy band and a negative one for the high energy band ($\Delta\lambda$ = 3 and 17 nm, respectively, from $CHCl_3$ to CH_3CN).

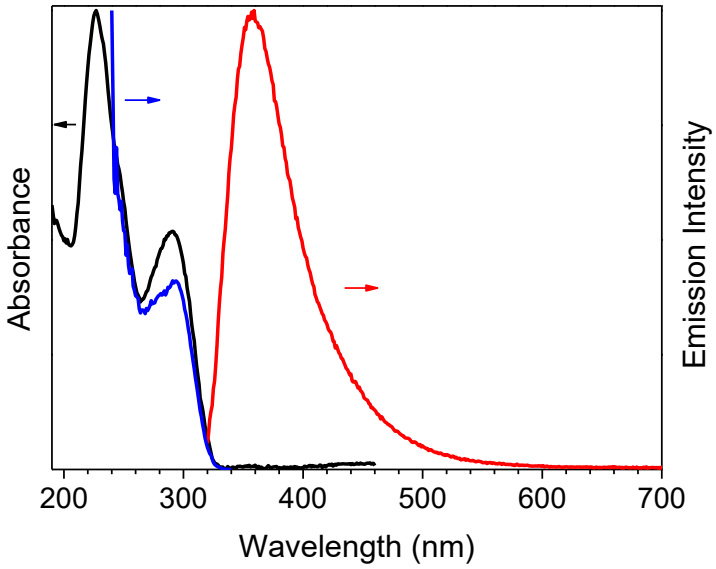

*Figure 1: Solution of **TTFPy** in CH_3CN (10^{-5} M) at 298 K: normalized absorption (black line), emission (λ_{exc} = 300 nm, red line) and excitation spectra (λ_{em} = 358 nm, blue line). Reproduced from ref.[16] free of charge; https://www.mdpi.com.*

At 77 K, a slight blue shift (344 nm, τ_{av} = 4.05 ns) of the fluorescent emission is observed by exciting at 300 nm. Interestingly, at this low temperature, a weak phosphorescent low energy tail appears in the PL spectrum and can be isolated (454 nm, τ_{av} = 1.63 s) from the fluorescent component by selectively populating the T_1 level (λ_{exc} = 350 nm) (See Figure 2). In this regard, the importance of direct S_0-T_1 excitation of organic phosphorescent compounds has been highlighted by Huang and coworkers[17].

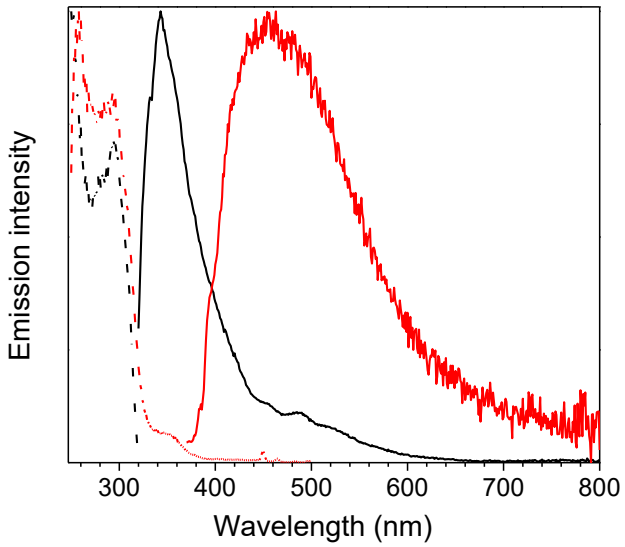

*Figure 2: Solution of **TTFPy** in CH_3CN (10^{-5} M) at 77 K: normalized emission (λ_{exc} = 300 nm, black line; λ_{exc} = 350 nm, red line) and excitation (λ_{em} = 343 nm, black dashed line; λ_{em} = 450 nm, red dashed line) spectra. Reproduced from ref.[16] free of charge; https://www.mdpi.com.*

To deepen the knowledge of the photophysic of **TTFPy**, spin coated thin films dispersed in polymethylmethacrylate (PMMA) (6% w/w) have been prepared. The thin films display at 298 K an intense fluorescent emission at 348 nm (τ_{av} = 1.89 ns) together with a weak phosphorescent component which can

be isolated (415, 436 nm, τ_{av} = 3.09 ms) from the fast emission by exciting at low energy (λ_{exc} = 360 nm) (See Figure 3).

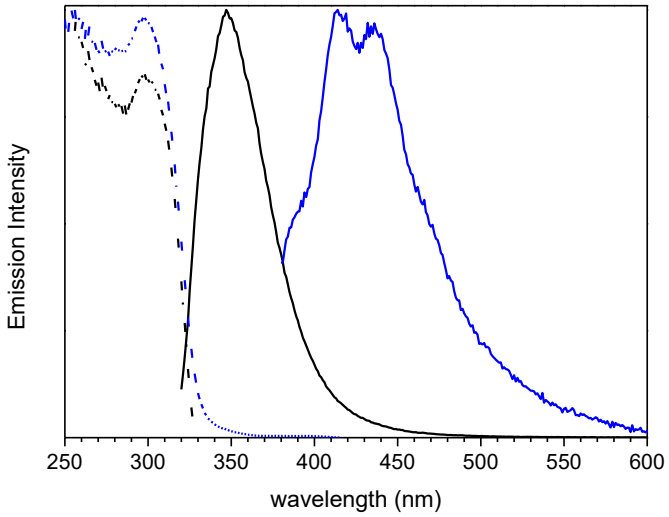

*Figure 3: **TTFPy**:PMMA film (6% w/w loading) at 298 K: normalized emission (λ_{exc} = 300 nm, black line; λ_{exc} = 360 nm, blue line) and excitation (λ_{em} = 348nm, black dashed line; λ_{em} = 436 nm, blue dashed line) spectra. Reproduced from ref.[16] free of charge; https://www.mdpi.com.*

Crystals of **TTFPy**, manually selected using a microscope, are characterized by multiple emissions. In particular, at 298 K, a fluorescent (373 nm, τ_{av} = 4.77 ns) and two phosphorescent (403, 424 and 446 nm, τ_{av} = 11.64 ms; 547 nm, τ_{av} = 417.78 ms) bands, with overall quantum efficiency equal to 25%, are observed in the PL spectrum by exciting at 300, 360 and 480 nm respectively. The two phosphorescences can be separated from the prompt emission in the delayed spectra where the longest-lived component displays peaks at 546 and 592nm (See Figure 4).

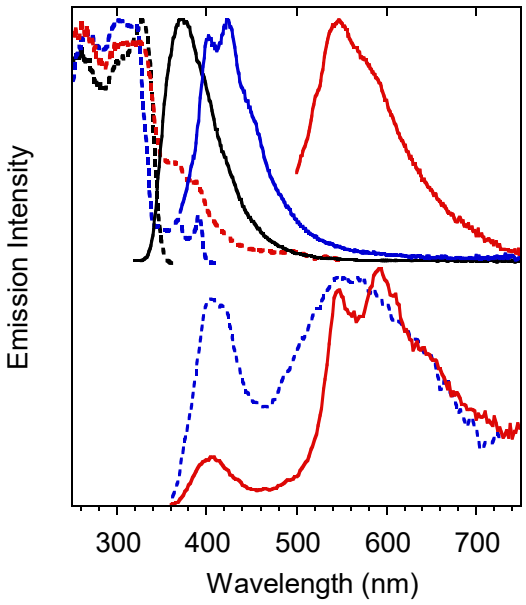

*Figure 4: Crystals of **TTFPy** at 298 K. Upper panel: normalized emission (λ_{exc} = 300 nm, black solid line; λ_{exc} = 360 nm, blue solid line; λ_{exc} = 480 nm, red solid line) and excitation (λ_{em} = 373 nm, black dashed line; λ_{em} = 425 nm, blue dashed line; λ_{em} = 570 nm, red dashed line) spectra. Bottom panel: normalized phosphorescence spectra (λ_{exc} = 300 nm; delay 200 µs, window 1 ms, blue dashed line; delay 5 ms, window 20 ms, red solid line). Reproduced from ref.[16] free of charge; https://www.mdpi.com.*

At 77 K the three emissions are still visible in almost the same position, but, for the lower energy phosphorescent band, much longer lifetimes (up to 2s) are measured (See figure 5).

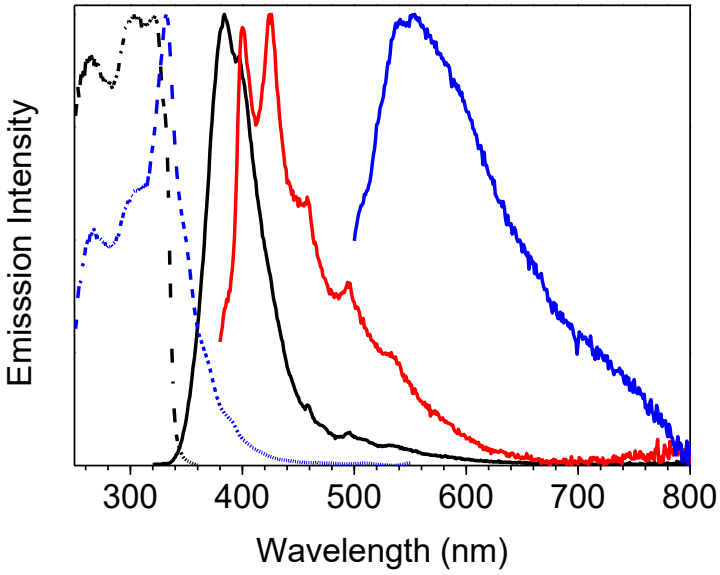

*Figure 5: Crystals of **TTFPy** at 77 K: normalized emission (λ_{exc} = 300 nm, black line; λ_{exc} = 360 nm, red line; λ_{exc} = 480 nm, blue line) and excitation (λ_{em} = 375 nm, black dashed line; λ_{em} = 570 nm, blue dashed line line) spectra. Reproduced from ref.[16] free of charge; https://www.mdpi.com.*

Both phosphorescent emissions display vibronic replicas with energy separation (about 180 meV) that can be associated to a vibronic progression involving the imidazole ring modes[18].

8.3 Discussion

Theoretical calculations and single-crystal X-ray diffraction analysis have been performed on **TTFPy** in order to interpret its photophysical behaviour. Starting from its X-ray analysis, molecular structure DFT geometry optimization was firstly performed to investigate the behavior of the luminophor in solution. The rotability of the C-C bond connecting the **TT** and the pyridinic moiety requires to calculate the presence of local minima besides that observed in the crystal. The asymmetry due to the presence of the fluorine atom generates two independent almost isoenergetic minima in the potential energy surface besides the symmetric ones with respect to the **TT** least squares (l.s.) plane. The two conformations are similar, the one derived from the X-ray geometry forms a dihedral angle of 47° between the l.s planes through **TT** and the 2-fluoropyridine while the one corresponding to additional minimum forms a 43° angle, the major difference consists in the fluorine position. The twisted conformation suggests a reduced conjugation between the two aromatic moieties within the molecule. Moreover, the presence of the fluorine atom grants some degree of polarity to the molecule (μ_g = 4.03 and 3.75 D in the two conformations, respectively).

Similar results are provided by TDDFT calculations of the two optimized conformations of **TTFPy**. For the most stable they give a strong $\pi\rightarrow\pi^*$ transition ($S_0\rightarrow S_1$ at 245 nm, f = 0.353), dominated by the HOMO→LUMO contribution with charge transfer (CT) character (from **TT** to 2-fluoropyridine) in the same direction as the ground state dipole moment, followed by a weak one ($S_0\rightarrow S_2$ at 234 nm, f=0.043) of mixed $\sigma/\pi\rightarrow\pi^*$ character. One of the occupied MOs involved in the latter (HOMO-5) is, in fact, a π orbital except for a σ contribution localized on a **TT** nitrogen atom (Figure 6).

The other computed π→π* transitions well reproduce the observed absorption band at high energy. The HOMO→LUMO+1 contribution is the strongest one($S_0 \rightarrow S_6$ at 205 nm, f = 0.421) with a CT character from the 2-fluoropyridine to the **TT** with opposite direction with respect to the $S_0 \rightarrow S_1$. Consequently, the difference between different state dipole moment ($\Delta\mu_{eg} = \mu_e - \mu_g$) for $S_0 \rightarrow S_6$ (0.24 D) is almost null while for $S_0 \rightarrow S_1$ (2.88 D) is high. An even bigger difference between these transitions is computed with IEFPCM (TD)DFT in acetonitrile and chloroform with a dipole moment equal to 4.75 and 5.03 D, $S_0 \rightarrow S_1$ equal to 4.68 and 5.47 D and $S_0 \rightarrow S_6$ equal to −1.74 and −2.32 D. The results completely agree with the solvatochromism observed for the low and high energy absorption bands in different solvents, even if the IEFPCM method can only reproduce the positive solvatochromism observed for the low energy band. The high energy band does not undergo any particular change probably because $S_0 \rightarrow S_6$ is not the only transition contained in the band so its weight is limited.

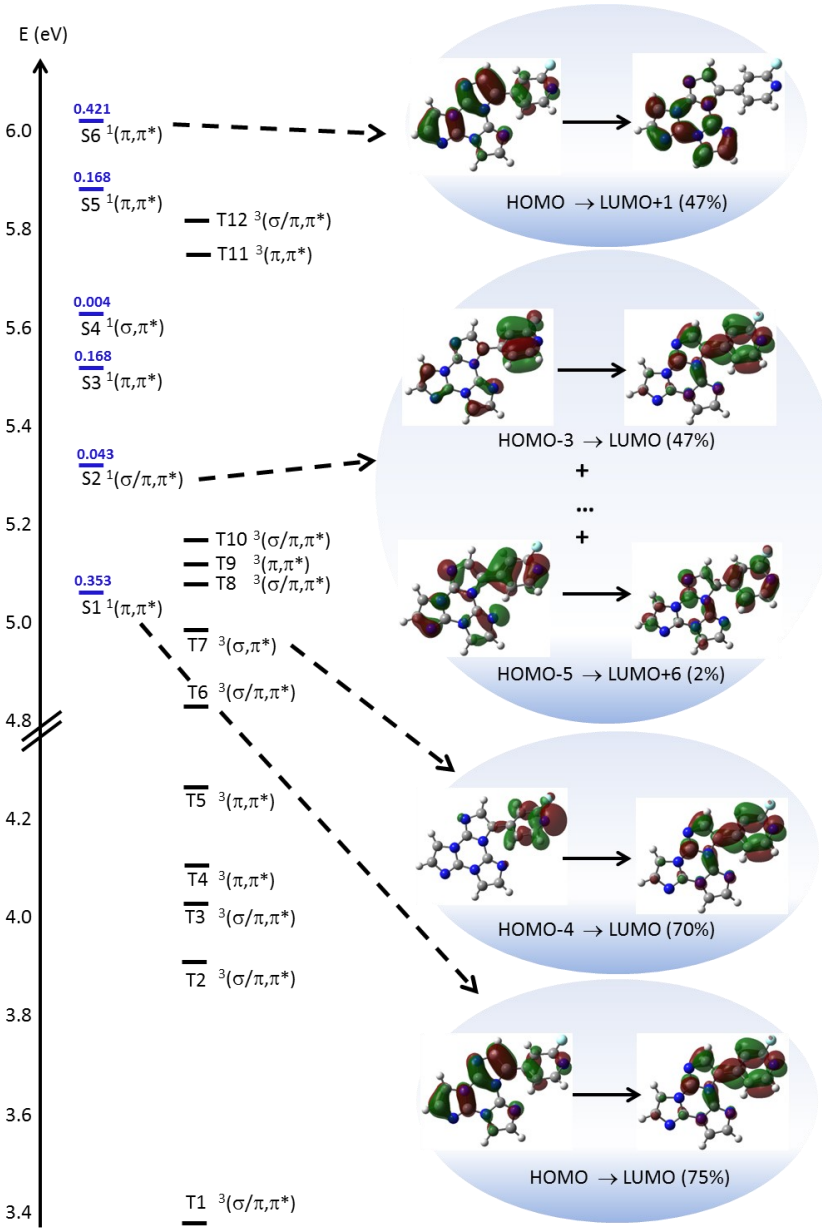

*Figure 6: Electronic levels computed for **TTFPy** (left) and selected MO involved in the transitions (right) at molecular level. In blue are reported the singlet levels with the corresponding oscillator strengths f. Reproduced from ref.[16] free of charge; https://www.mdpi.com.*

Regarding the emission at 450 nm observed in solution at 77 K, the calculation computed a T_n level (T_7 at 250 nm) with (σ,π*) symmetry that can be responsible for a fast ISC from the close S_1 (π,π*) level (computed at 245 nm) and the consequent relaxation through IC to T_1 from where the phosphorescence is observed. This explanation is furtherly confirmed by the presence of a similar component at 430 nm in the PMMA film at RT.

In opposition to the fluorescent emission and the high energy phosphorescence, which can be assigned to radiative deactivation from molecular S_1 and T_1 even in the crystal, the nature of the additional phosphorescence is not clear and cannot be associated with a simple molecular contribution. To disclose the origin of this radiative process, single-crystal structure must be analysed.

TTFPy crystallizes in the P-1 space group with equidistant face-to-face stacking along the crystallographic axis forming infinite columns. Taking into consideration a single axis, molecules of **TTFPy** lie iso-oriented on planes with distances of 3.366 Å and a rather small slippage (1.9 Å), with a distance between triazinic centroids equal to (3.831 Å) and high angle θ (61°) between the centroid axis and the molecular plane (Figure 7). This disposition suggests the formation of H-aggregate even for this molecule even if some differences with the stacking pattern of **TT** is evident. In the case of triimidazole, an infinite ABAB alternate sequence is formed by the molecules in which every molecule is rotate of 180° respect the adjacent one with alternate distances equal to 3.204 and 3.290 Å and centroid-centroid distances of 3.733 and 3.949 Å. The **TTFPy** packing mode is much more similar to that of the **TT1I**[10] where the molecules are iso-oriented and disposed face-to-face with larger slippage (2.3 Å, θ = 55°) and longer distance between centroids of triazinic rings (4.097 Å).

Molecules of **TTFPy** are laterally connected through several C-H···N and C-H···F close contacts (the shorter one being C8-H8···N1, H···N = 2.52 Å, C-H···N = 170.5°) forming slightly corrugated planes. The dihedral angle between l.s. planes through **TT** and pyridine moieties measures 49.80°. This value, close to that computed for the isolated molecule (47.00°), suggests minor conformational rearrangement from solution to the solid state.

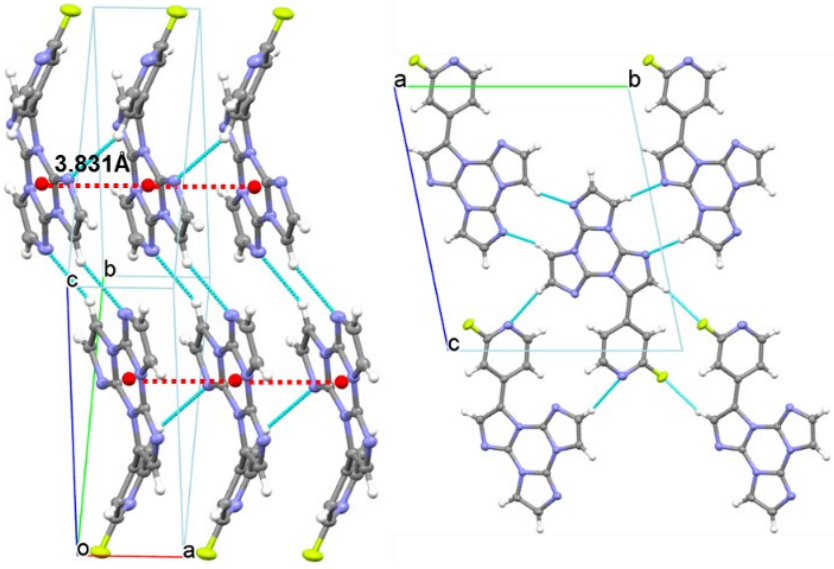

*Figure 7: Partial views along bc (left) and a directions (right) of **TTFPy** crystal structure showing columnar H-aggregates (centroids of the triazinic rings shown as red circles) and hydrogen bonds (light blue dashed lines). Reproduced from ref.[16] free of charge; https://www.mdpi.com.*

The disposition of **TTFPy** molecules in the crystal structure justifies the observed long-last component in the solid state together with the observation that H-aggregates, as well as in the others case regarding the **TT**-family[8-10, 12], efficiently trap the triplet exciton. Moreover, the rigidification and oxygen protection associated with intramolecular interactions allow the arise of the high energy phosphorescence in the solid state even

at RT. In perfect agreement, the same effect is observed in the PMMA blend where the rigidification provided by the polymeric matric allows the arise of the high energy component, while the low energy one is absent due to the lack of H-aggregates.

8.4 Conclusion

The **TTFPy** derivative represents the first attempt to conjugate **TT** with another aromatic structure in order to tune its photophysical behaviour. Despite the presence of an additional 2-fluoropyridinic fragment the formation of H-aggregates motifs is not prevented but the strength of the interchromophoric π-π interactions is decreased and consequently the associated phosphorescence decay time becomes shorter. However, the presence of the fluoropyridinyl moiety strongly enhances the solution emissive properties and contributes in the arise of an additional molecular phosphorescence. These promising results obtained with this first conjugation attempt open up to further modification with different fragments.

8.5 References

[1] Gu, L.; Shi, H.; Bian, L.; Gu, M.; Ling, K.; Wang, X.; Ma, H.; Cai, S.; Ning, W.; Fu, L.; Wang, H.; Wang, S.; Gao, Y.; Yao, W.; Huo, F.; Tao, Y.; An, Z.; Liu, X.; Huang, W., Colour-tunable ultra-long organic phosphorescence of a single-component molecular crystal. *Nature Photonics* **2019,** *13* (6), 406-411.

[2] Zhao, W.; Cheung, T. S.; Jiang, N.; Huang, W.; Lam, J. W. Y.; Zhang, X.; He, Z.; Tang, B. Z., Boosting the efficiency of organic persistent room-temperature phosphorescence by intramolecular triplet-triplet energy transfer. *Nature Communications* **2019,** *10* (1), 1595.

[3] Jiang, K.; Wang, Y.; Cai, C.; Lin, H., Conversion of Carbon Dots from Fluorescence to Ultralong Room-Temperature Phosphorescence by Heating for Security Applications. *Advanced Materials* **2018,** *30* (26), 7.

[4] Sun, H.; Liu, S.; Lin, W.; Zhang, K. Y.; Lv, W.; Huang, X.; Huo, F.; Yang, H.; Jenkins, G.; Zhao, Q.; Huang, W., Smart responsive phosphorescent materials for data recording and security protection. *Nature Communications* **2014,** *5* (1), 3601.

[5] Wang, X.-F.; Xiao, H.; Chen, P.-Z.; Yang, Q.-Z.; Chen, B.; Tung, C.-H.; Chen, Y.-Z.; Wu, L.-Z., Pure Organic Room Temperature Phosphorescence from Excited Dimers in Self-Assembled Nanoparticles under Visible and Near-Infrared Irradiation in Water. *Journal of the American Chemical Society* **2019,** *141* (12), 5045-5050.

[6] Zhen, X.; Xie, C.; Pu, K., Temperature-Correlated Afterglow of a Semiconducting Polymer Nanococktail for Imaging-Guided Photothermal Therapy. *Angewandte Chemie International Edition* **2018,** *57* (15), 3938-3942.

[7] Kabe, R.; Notsuka, N.; Yoshida, K.; Adachi, C., Afterglow Organic Light-Emitting Diode. *Advanced Materials* **2016,** *28* (4), 655-660.

[8] Lucenti, E.; Forni, A.; Botta, C.; Carlucci, L.; Colombo, A.; Giannini, C.; Marinotto, D.; Previtali, A.; Righetto, S.; Cariati, E., The Effect of Bromo Substituents on the Multifaceted Emissive and Crystal-Packing Features of Cyclic Triimidazole Derivatives. *ChemPhotoChem* **2018,** *2* (9), 801-805.

[9] Lucenti, E.; Forni, A.; Botta, C.; Carlucci, L.; Giannini, C.; Marinotto, D.; Pavanello, A.; Previtali, A.; Righetto, S.; Cariati, E., Cyclic Triimidazole Derivatives: Intriguing Examples of Multiple Emissions and Ultralong Phosphorescence at Room Temperature. *Angewandte Chemie International Edition* **2017,** *56* (51), 16302-16307.

[10] Lucenti, E.; Forni, A.; Botta, C.; Giannini, C.; Malpicci, D.; Marinotto, D.; Previtali, A.; Righetto, S.; Cariati, E., Intrinsic and Extrinsic Heavy-Atom Effects on the Multifaceted Emissive Behavior of Cyclic Triimidazole. *Chemistry – A European Journal* **2019,** *25* (10), 2452-2456.

[11] Xiao, L.; Fu, H., Enhanced Room-Temperature Phosphorescence through Intermolecular Halogen/Hydrogen Bonding. *Chemistry – A European Journal* **2019,** *25* (3), 714-723.

[12] Lucenti, E.; Forni, A.; Botta, C.; Carlucci, L.; Giannini, C.; Marinotto, D.; Previtali, A.; Righetto, S.; Cariati, E., H-Aggregates Granting Crystallization-Induced Emissive Behavior and Ultralong Phosphorescence from a Pure Organic Molecule. *The Journal of Physical Chemistry Letters* **2017,** *8* (8), 1894-1898.

[13] An, Z.; Zheng, C.; Tao, Y.; Chen, R.; Shi, H.; Chen, T.; Wang, Z.; Li, H.; Deng, R.; Liu, X.; Huang, W., Stabilizing triplet excited states for ultralong organic phosphorescence. *Nature Materials* **2015,** *14* (7), 685-90.

[14] Pan, S.; Chen, Z.; Zheng, X.; Wu, D.; Chen, G.; Xu, J.; Feng, H.; Qian, Z., Ultralong Room-Temperature Phosphorescence from Supramolecular Behavior via Intermolecular Electronic Coupling in Pure Organic Crystals. *The Journal of Physical Chemistry Letters* **2018,** *9* (14), 3939-3945.

[15] Wang, S.; Ma, L.; Wang, Q.; Shao, P.; Ma, D.; Yuan, S.; Lei, P.; Li, P.; Feng, X.; Wang, B., Covalent organic frameworks: a platform for the experimental establishment of the influence of intermolecular distance on phosphorescence. *Journal of Materials Chemistry C* **2018,** *6* (20), 5369-5374.

[16] Previtali, A.; Lucenti, E.; Forni, A.; Mauri, L.; Botta, C.; Giannini, C.; Malpicci, D.; Marinotto, D.; Righetto, S.; Cariati, E., Solid State Room Temperature Dual Phosphorescence from 3-(2-Fluoropyridin-4-yl)triimidazo[1,2-a:1′,2′-c:1″,2″-e][1,3,5]triazine. *Molecules* **2019,** *24* (14), 2552.

[17] Yuan, J.; Chen, R.; Tang, X.; Tao, Y.; Xu, S.; Jin, L.; Chen, C.; Zhou, X.; Zheng, C.; Huang, W., Direct population of triplet excited states through singlet–triplet transition for visible-light excitable organic afterglow. *Chemical Science* **2019,** *10* (19), 5031-5038.

[18] Majoube, M.; Henry, M.; Chinsky, L.; Turpin, P. Y., Preresonance Raman spectra for imidazole and imidazolium ion: interpretation of the intensity enhancement from a precise assignment of normal modes. *Chemical Physics* **1993,** *169* (2), 231-241.

9 Pyridinyl fragment conjugation: (pyridin-2-yl)

9.1 Introduction

The intriguing results obtained with the insertion of the 2-fluoropyridine fragment[1] on the **TT** scaffold have demonstrated that modification of the central trimidazolic ring not only preserves the formation of H-aggregates and so the RTUP but it can even furtherly introduce new radiative deactivation processes leading to more complex and fascinating materials. Even if it is still not possible to forecast how the introduction of a fragment can modify the photophysical behaviour of cyclic triimidazole, due to the huge number of factors that have to be taken into account in the solid state emission, some considerations about which is the best kind of pendant attachable to **TT** can be made. On this regard, heteroaromatic substituents should be considered as suitable chromophores in shifting the emission of **TT** towards the red while preserving the long lifetime of its triplet state.

The introduction on cyclic triimidazole of a pyridine moiety, with the nitrogen atom in the ortho position, is expected to generate a material similar to **TTFPy**, and to also lead to a potential candidate, as ligand, for the formation of chelated complexes.

3-(pyridin-2-yl)triimidazotriazine **(TT2Py**) has been prepared by Stille coupling between **TT1Br** and 2-(tributylstannyl)pyridine (See Scheme 1) and characterized by NMR spectroscopy, mass spectrometry and X-ray analysis[2]. The compound was recrystallized three times before photophysical characterization in order to avoid signals due to impurities.

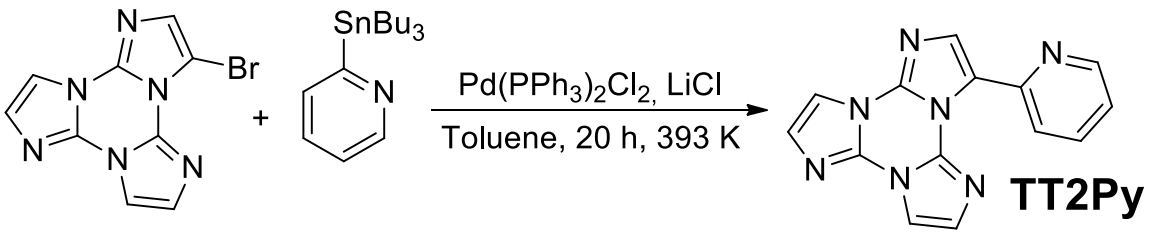

*Scheme 1: Synthesis of **TT2Py**.*

9.2 Photophysical characterization

Diluted solutions of **TT2Py** (10^{-5} M) in acetonitrile (CH_3CN) and dichloromethane (CH_2Cl_2) in air at 298 K display absorption bands at about 235 and 290 nm and emission around 350 nm ($\Phi \cong 17$ %) (Figure 1). Exciting the sample at 355 nm two bands appear in the spectrum: one with short lifetime (ns) and one with long lifetime (ms). Surprisingly, while no other bands are visible in the PL spectrum long live components are detected in both solvents when the lifetimes are monitored at 400 and 500 nm. To better understand the processes behind these emission steady state and time resolved studies of the deareated solutions have been performed.

Two bands are detected in the time gated spectra of the deareated DCM solution, at about 420 nm a medium energy phosphorescence **MEP** (τ_{av}= 40 μs) and a structured band at lower energy, defined low energy phosphorescence **LEP1**, with peaks at 520 and 562 nm (τ_{av}= 441 μs), both these emissions are quenched by oxygen diffusion inside the cell (Figure 1 top). In CH_3CN, similarly to CH_2Cl_2 solution, a blue shifted **LEP2** component is observed with peaks at 488, 521 and 560 nm when the sample is excited at 390 nm while no other higher energy phosphorescences have been detected (Figure 1 bottom).

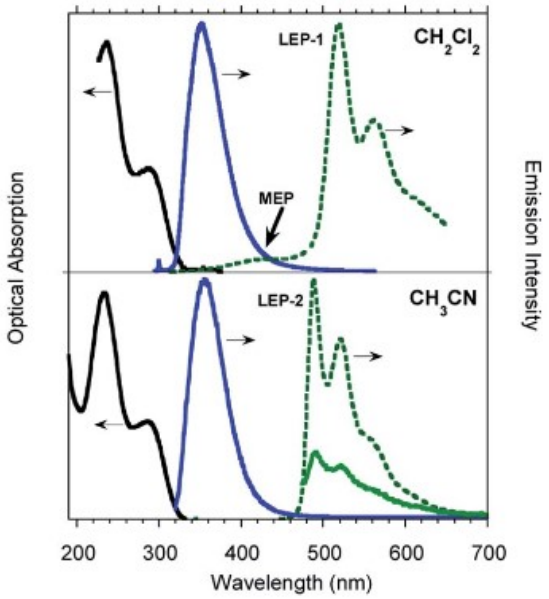

*Figure 1: Normalized optical absorption (black solid line) and PL spectra of 10^{-5} M deareated solutions of **TT2Py** in DCM (top) and CH_3CN (bottom) at 298 K. Top: λ_{exc}= 270 nm, (blue solid line); Bottom: λ_{exc} = 300nm, (blue solid line); λ_{exc} = 390 nm, (green solid line). Phosphorescence spectra of CH_2Cl_2 (top) (dotted green line, delay 50 µs, window 100 µs) and CH_3CN (bottom) (dotted green line, delay 200 µs, window 500 µs) λ_{exc} = 300 nm. Reproduced from ref.[2] free of charge, https://pubs.rsc.org/en.*

Forcing the aggregation through the addition of water (CH_3CN/H_2O 1:1), while maintaining the deareated condition, the **LEP2** spectral shape is detected even in the steady state experiment (λ_{exc}= 390 nm). In parallel, no absorption is detected at 390 nm but a weak band appears in the excitation profile of the emission. The time gated spectra show features similar to the CH_2Cl_2 solution with the structured **LEP1** and an additional emission at 345 nm, a high energy phosphorescence **HEP**, with shorter decay time with respect to the **MEP** centered at 380-420 nm. The presence of the two **LEPs** in the CH_3CN/H_2O solution could be associated with the presence of different aggregates (Figure 2).

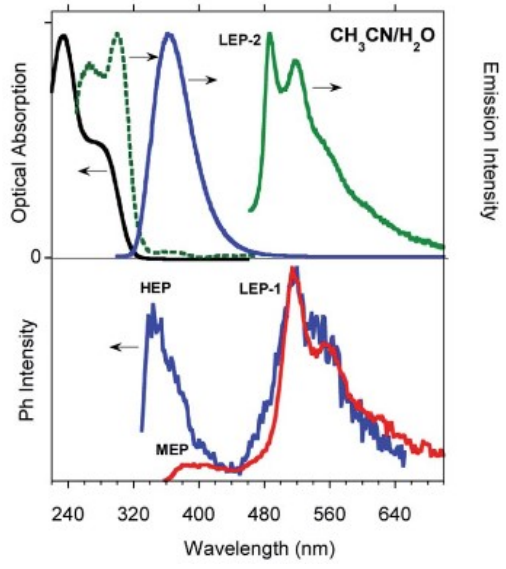

*Figure 2: Photophysical properties of deareated solutions of **TT2Py** in 10^{-4} M CH_3CN/H_2O (v/v=50/50) solution at 298 K. Top: Absorption (black solid line), PLE (green dashed line, λ_{em} = 488 nm) and PL spectra (blue solid line, λ_{exc} = 270 nm, green solid line, λ_{exc} = 390 nm). Bottom: Phosphorescence spectra (blue line, delay 100 µs, window 200 µs; red line, delay 0.5 ms, window 1 ms, λ_{exc} = 300 nm). Reproduced from ref.[2] free of charge, https://pubs.rsc.org/en.*

Shortly, the two long lived component **HEP** and **MEP** are molecular components while the **LEPs** arise from different aggregates.

At 77 K an excitation dependent PL spectrum is observed. A high energy fluorescence **HEF** at 340 nm is detected in the CH_2Cl_2 frozen solution (τ_{av}= 2.32 ns) together with the **HEP** at 375 nm when the sample is excited at 280 nm. At lower excitation energy (λ_{exc}=350 nm) the **MEP** at 393 nm (τ_{av}= 13.16 ms) dominates the spectrum. Time gated experiments reveal at 405 nm the **MEP** and the relative excitation band at 350 nm and at 485, 520 and 555 nm a long lived component (τ_{av}= 1.31 s) similar to **LEP2**. Exciting with shorter wavelength the spectra become broader (Figure 3). Lowering the temperature of other solutions (CH_3CN, CH_3OH/CH_3CH_2OH 2:8) similar results are observed.

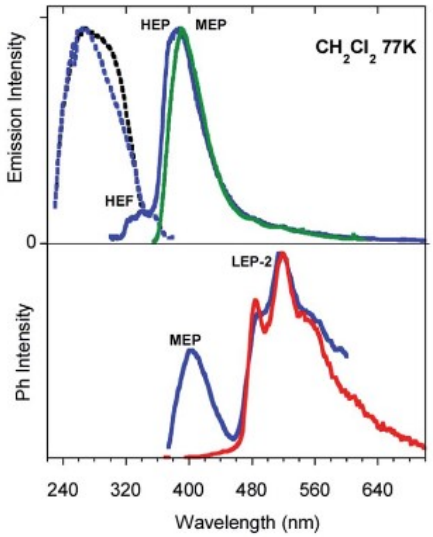

*Figure 3: Photophysical properties of 10^{-5} M DCM solution of **TT2Py** at 77 K. Top: PL and PLE spectra (λ_{em} = 350 nm, black dotted line; λ_{em} = 400 nm, blue dotted line; λ_{exc} = 280 nm, blue solid line, λ_{exc} = 350 nm, green solid line). Bottom: Phosphorescence spectra λ_{exc} = 350 nm (delay 200 µs, window 400 µs, blue line; delay 10 ms, window 20 ms, red line). Reproduced from ref.[2] free of charge, https://pubs.rsc.org/en.*

To furtherly extend the photophysical characterization of the **TT2Py** and to explore its potential application in the field of organic light emitting diodes (OLED), blended thin films in PMMA have been prepared (w/w **TT2Py**/PMMA 10% and 5%). Independently from the film concentration, the photophysical behaviour becomes even more complicated with four different emissions covering a large area of the PL spectrum (Figure 4). However, the emissions can be selectively activated choosing different excitation wavelengths.

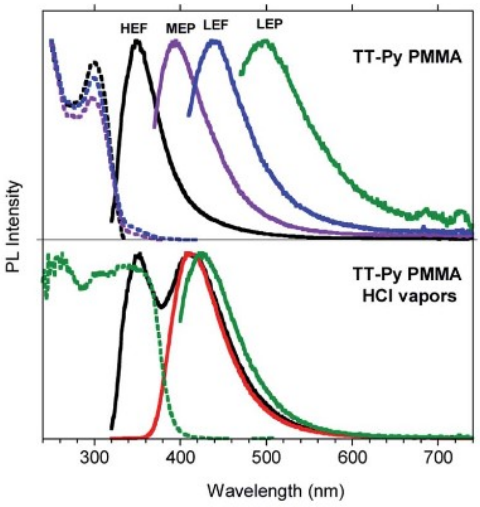

*Figure 4: Top: Photophysical properties of **TT2Py** in PMMA (w/w **TT2Py**/PMMA 10%). λ_{exc} = 300 nm (black line), λ_{exc} = 350 nm (violet line), λ_{exc} = 390 nm (blue line), λ_{exc} = 450 nm (green line) and excitation spectra λ_{em} = 352 nm (black dotted line), λ_{em} = 400 nm (violet dotted line), λ_{em} = 440 nm (blue dotted line). Bottom: Film exposed to HCl vapors (λ_{exc} = 300 nm; black line, 30 min; red line, 45 min; λ_{exc} = 390 nm, green line, 45 min; λ_{em} = 527 nm, green dotted line, 45 min). Reproduced from ref.[2] free of charge, https://pubs.rsc.org/en.*

With high energy excitations (below 300 nm) the spectrum is dominated by an intense fluorescence **HEF** (τ = 1.18 ns) at 350 nm. The **MEP** is observed at 395 nm (τ_{av} = 13.73 ms) when the sample is excited at 350 nm while, at 390 nm, a second fluorescence band appears at 440 nm (τ_{av} = 3.47 ns, low energy fluorescence, **LEF**). Unresolved **LEPs** at 530 nm, already observed in solution, are activated by exciting at 450 nm (Figure 4).

To better understand the articulated behaviour of **TT2Py** (w/w **TT2Py**/PMMA 10%) films, ultrafast pump-probe experiments have been performed.

The measured signal is:

$$\frac{\Delta T(\lambda_{PR},\tau)}{T} = \frac{T_{ON}(\lambda_{PR},\tau) - T_{OFF}(\lambda_{PR},\tau)}{T_{OFF}(\lambda_{PR},\tau)}$$

where T_{ON} and T_{OFF} are the probe transmission intensities with and without pump excitation at a given λ_{PR} and τ probe delay. A positive $\Delta T/T$ signal corresponds to the bleaching of the ground state or stimulated emission (SE) from excited states, while a negative signal indicates the presence of a photoinduced absorption (PIA) band [3].

The $\Delta T/T$ spectra at different probe delays after excitation at the first absorption peak (290 nm) with 20 fs time resolution [4] are reported in the left panel of Figure 5.

The spectra show an initial SE band at around 350 nm and two PIA bands, peaked at 450 nm and 550 nm, PIA_1 and PIA_2 respectively. The temporal evolutions indicate that SE and PIA_2 bands are instantaneously formed, while PIA_1 signal is delayed by about 100 fs with respect to the other two. Based on this observation, SE and PIA_2 bands can be assigned to the temporal evolution of the photo-generated excitons which give origin to the **HEF** stimulated emission (S_1-S_0) or to the photoinduced absorption band PIA_2 (S_1-S_n), while the band at 450 nm is associated to the generation of charged states [5]. This result shows the presence of intermolecular interaction between the different molecules. To investigate the origin of the **LEF** emission, $\Delta T/T$ spectra at different probe delays after excitation at 390 nm (with 100 fs temporal resolution) [5] have been collected. The spectra show an initial PIA band all over the visible spectral region; moreover, at long probe delays, a positive signal appears in the region between 420 nm and 550 nm, indicating emission (supposedly **LEF**) from a newly formed state. This formation is evident looking at the temporal evolution of the $\Delta T/T$ signal at 450 nm which clearly indicates an initial negative signal which becomes positive in around 700 ps. Moreover, after 1 ns the signal is still growing indicating that the excitation comes from a long living initial excited state and it is likely that this emission will present a long-lived emission tail.

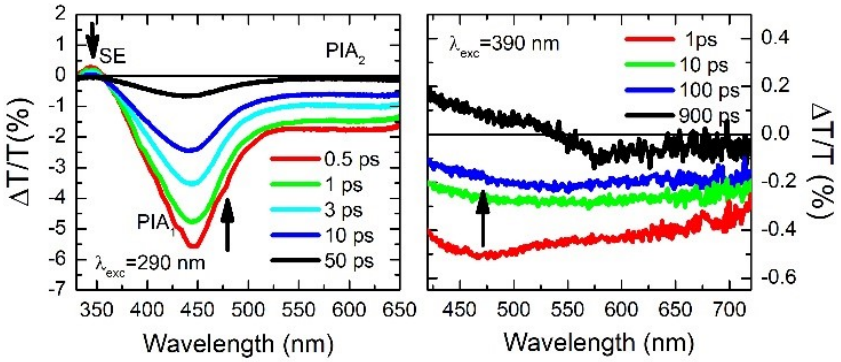

*Figure 5: Ultrafast spectroscopy measurements on **TT2Py** in PMMA (w/w **TT2Py**/PMMA 10%). Pump-probe spectra selected at different probe delays after 290 nm (left panel) and 390 nm (right panel) excitations. Reproduced from ref.[2] free of charge, https://pubs.rsc.org/en.*

Three different polymorphs have been isolated for **TT2Py**: **TT2Py-A** as laminae from CH_2Cl_2/CH_3OH, **TT2Py-H** as needles from CH_3CN/H_2O, which includes disordered cocrystallized water molecules and **TT2Py-X** from

CH_3CN. All the three polymorphs show the typical π···π stacking already observed in cyclic triimidazole and its already investigated derivatives[1, 7-10] (Figure 6). Before any photophysical measurements crystals of each phase were manually selected using a microscope in order to avoid the presence of more than one phase.

TT2Py-A shows largely shifted triimidazole units one with respect to the other with distance of 5.358 Å between triazinic centroids. However, short C···C distances (3.234, 3.301 Å to cite the shorter ones) are measured, indicating strong π···π stacking interactions. Adjacent molecules along the stacks are rotated in the plane of **TT**.

Shorter distances between triazinc centroids (3.736 Å) are detected in **TT2Py-H**, the molecules do not display any rotation along the stacks but longer C···C distances (3.309, 3.328 Å), respect to **TT2Py-A**, are measured.

In **TT2Py-X**, two molecules are contained in the asymmetric unit, the triazinic centroids of adjacent **TT** units are alternately separated by 4.756 and 4.917 Å and the shorter C···C contacts measure 3.373 and 3.416 Å. Along the stacks, the molecules are slightly rotated in the **TT**'s plane, similarly to what observed in **TT2Py-A**.

It should be evidenced that in all polymorphs, the **TT** moieties are strongly anchored to each other by not only π···π stacking interactions but also several short C–H···N hydrogen bonds (HBs) in the plane roughly perpendicular to the stacking axis (the shortest ones measuring 2.44, 2.50 and 2.29 Å in **TT2Py-A**, **TT2Py-H**, and **TT2Py-X**, respectively). On the contrary, the pyridinic functions of **TT2Py-A** and **TT2Py-X** are involved only in weak C–H···π HBs and N···C close contacts while, in **TT2Py-H**, the pyridinic nitrogen atom is hydrogen bonded with the disordered cocrystallized water molecules, the high mobility of the latter could not support a rigid environment for the pyridinic ring.

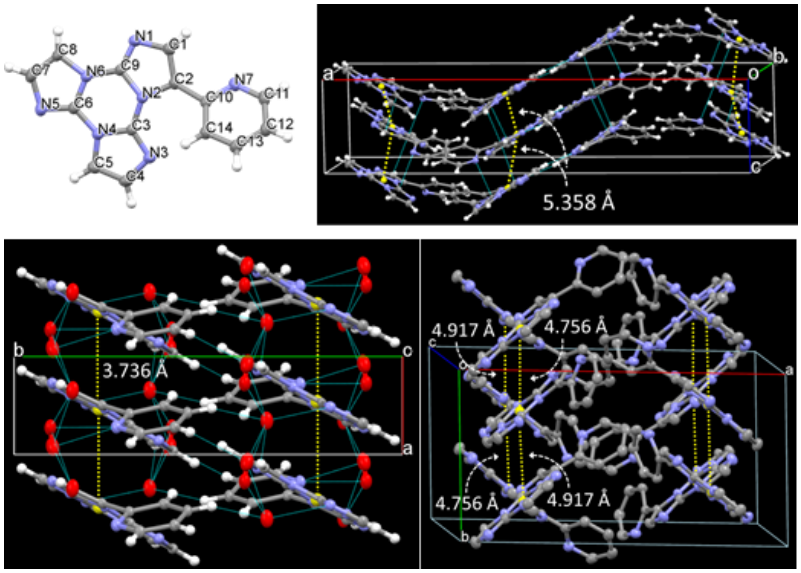

*Figure 6: Top: Asymmetric unit of **TT2Py-A** and its crystal packing. Bottom: Crystal packing of **TT2Py-H** (left) and **TT2Py-X** (right). The centroids of triazinic rings, together with their separation, are shown in yellow. Ellipsoids at 30% probability. Reproduced from ref.[2] free of charge, https://pubs.rsc.org/en.*

It is clear that the tilting between **TT** and pyridine is slightly different in the three polymorphs, the dihedral angles between the two fragments measure 41.47°, 43.7° and 37.6/39.6° in **TT2Py-A**, **-H** and **-X** while the DFT optimized value in vacuo is 36.70°. In addition, the pyridine displays a different relative orientation with respect to **TT** in **TT2Py-A** compared to **TT2Py-H** and **TT2Py-X** as evidenced by the N7-C10-C2-C1 torsion angle that measures -35.18° in the former and 41.51 and 34.16/34.64° in the latter structures, respectively.

The photophysical studies on the three polymorphs were performed separately on crystals manually selected using a microscope.

At 298 K in air, crystals of **TT2Py-A** show an intense high energy ultralong emission at 370 nm **HEP** (τ_{av}= 0.7 s) with an impressive quantum efficiency equal to 52% when exciting between 270 nm and 380 nm. Exciting at longer wavelength broad emissions peaked at 450 nm (λ_{exc}= 390 nm) and 524 nm (λ_{exc}= 460 nm) are observed as the results of **LEF** and **LEP**, respectively. Time-gated experiments allow to resolve different phosphorescent contributions by changing the delay times. With delays longer than 1 ms, the **HEP** peaked at 370 nm decreases in intensity and the spectral shape evolves revealing a contribution at about 420 nm (**MEP**; τ_{av} = 0.29 ms) and a longer-lived broad **LEP** at 575-615 nm (τ_{av} = 2.09 ms) (Figure 7).

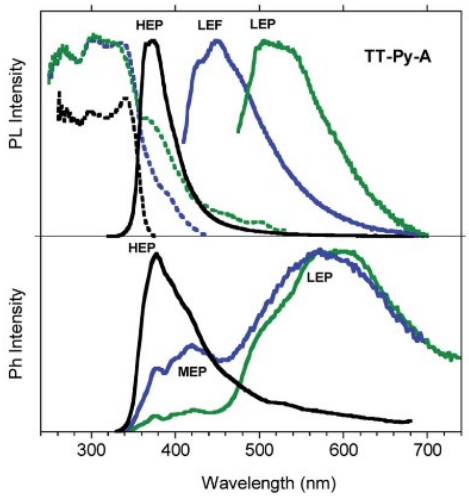

*Figure 7: PL (top) and phosphorescence (bottom) spectra of crystals of **TT2Py-A** at 298 K. Top: Emission spectra (solid lines, λ_{exc} = 300 nm, black line; λ_{exc} = 390 nm, blue line, λ_{exc} = 460 nm, green line) and excitation spectra dotted lines λ_{em} = 390 nm, black line; λ_{em} = 460 nm, blue line; λ_{em} = 550 nm, green line) . Bottom: Phosphorescence spectra (λ_{exc} = 290 nm; delay 200 µs, window 500 µs, black line; delay 1 ms, window 3 ms, blue line; delay 5 ms, window 10 ms, green line). Reproduced from ref.[2] free of charge, https://pubs.rsc.org/en.*

Similarly, **TT2Py-H** crystals show **HEP**, **LEF** and **LEP** at 374, 450 and 520 nm (20.38 ms, 1.91 ns and 18.25 ms, respectively). Time-gated spectra have revealed that the **HEP**, peaked at 375 nm, evolves into **MEP** (τ_{av} = 0.47 ms) and the structured **LEP-1** at delays longer than 1 ms (λ_{exc} = 320 nm, 535, 570 and 625 nm; τ_{av} = 5.98 ms) (Figure 8). When crystals of **TT2Py-H** are analysed at 77 K **HEF**, **HEP**, **LEF** and **LEP-2** (345, 373, 392, 420 and 493 nm) are resolved. In time gated spectra **MEP** and **HEP** emissions overlap, while, as previously observed in CH_2Cl_2, the spectral profile of **LEP-1** is selectively activated by exciting at 400 nm (Figure 9).

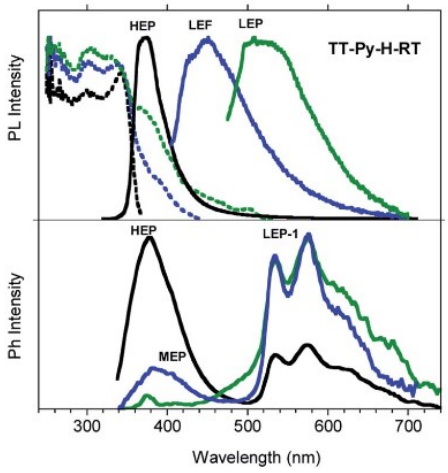

*Figure 8: PL (top) and phosphorescence (bottom) spectra of crystals of **TT2Py-H** at 298 K. Top: Emission spectra: λ_{exc} = 300 nm (black line), λ_{exc} = 390 nm (blue line), λ_{exc} = 460 nm (green line) and excitation spectra λ_{em} = 390 nm (black line), λ_{em} = 460 nm (blue line), λ_{em} = 550 nm (green line). Bottom: Phosphorescence spectra (λ_{exc} = 320 nm; delay 50 µs, window 200 µs, black line; delay 100 µs, window 200 µs, blue line; delay 1 ms, window 10 ms, green line). Reproduced from ref.[2] free of charge, https://pubs.rsc.org/en.*

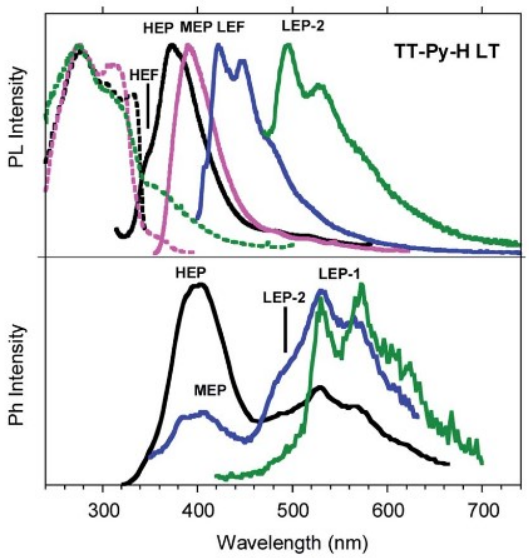

*Figure 9: PL (top) and phosphorescence (bottom) spectra of crystals of **TT2Py-H** at 77 K. Top: Emission spectra λ_{exc} = 300 nm (black line), λ_{exc} = 350 nm (pink line), λ_{exc} = 380 nm (blue line), λ_{exc} = 450 nm (green line) and excitation spectra λ_{em} = 356 nm (black dashed line), λ_{em} = 410 nm (pink dashed line), λ_{em} = 520 nm (green dashed line). Bottom: Phosphorescence spectra at delay 100 µs, window 500 µs (λ_{exc} = 300 nm, black line; λ_{exc} = 330 nm, blue line; λ_{exc} = 400 nm, green line). Reproduced from ref.[2] free of charge, https://pubs.rsc.org/en.*

Steady state emission spectra of crystals of **TT2Py-X** at 298 K in air display **HEP**, **LEF** and **LEPs** (at 362, 466 and 524 nm, τ_{av} = 91.83 ms, 4.13 ns and 9.38 ms, respectively), similar to the previous phases while their phosphorescence appears more complex. Time-gated spectra (Fig. 10 bottom) show a structured long-lived deep red phosphorescence (**DRP** at 636, 695 and 767 nm, τ_{av} = 111.07 ms) dominating the spectrum at delays longer than 0.1 ms. The **HEP** is observed only at short delays (0.1 ms) while longer lived **MEP** at 400 nm and **LEP** at about 530 nm (τ_{av} = 1.31 ms and 22.60 ms, respectively) are observed, the latter revealing vibronic replicas similar to those observed for **TT2Py-H** crystals (Figure 10).

To sum up, **TT2Py** shows two fluorescences (**HEF** and **LEF**), four phosphorescences (**HEP**, **MEP**, **LEPs** and **DRP**) differently distributed on three different polymorphs and the isolated molecule in solution or in PMMA film.

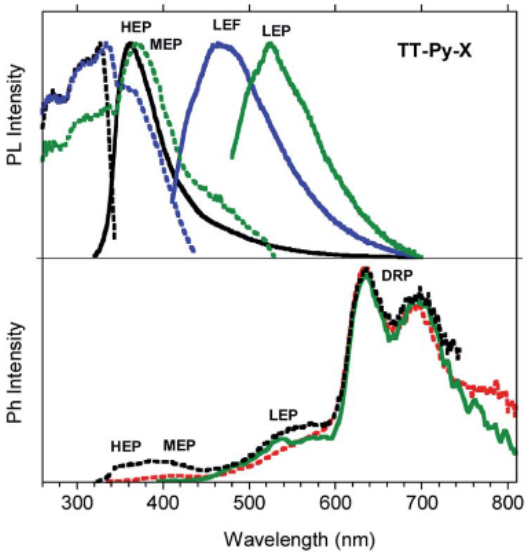

*Figure 10: PL (top) and phosphorescence (bottom) spectra of crystals of **TT2Py-X** at 298 K. Top: Emission spectra λ_{exc} = 300 nm (black line), λ_{exc} = 390 nm (blue line), λ_{exc} = 460 nm (green line) and excitation spectra λ_{em} = 360 nm (black dashed line), λ_{em} = 390 nm (blue dashed line), λ_{exc} = 460 nm (blue dashed line), λ_{em} = 550 nm (green dashed line). Bottom: Phosphorescence spectra (λ_{exc} = 300 nm; delay 100 µs, window 500µs, (black dashed line); delay 0.5 ms, window 10 ms, (red dashed line); λ_{exc} = 370 nm, delay 200 µs, window 500 µs, (green line). Reproduced from ref.[2] free of charge, https://pubs.rsc.org/en.*

9.3 Discussion

As previously reported in literature[1, 7-10], **LEPs** and **DRP** can be reasonably associated to dimeric or supramolecular columnar π-π interactions among **TT** units, even if the **LEP** components have been detected in diluted (10^{-5} M) CH_2Cl_2 and CH_3CN solutions where the presence of aggregated species cannot be completely excluded[11]. The geometrical optimization of dimeric units extracted from the three crystal structure converges in three different but almost isoenergetic stationary states with large interaction energies (11.92 kcal/mol BSSE-corrected, for the most stable one). **LEP1** and **LEP2**, which are present in all the structures, may derive from **TT2Py** units interacting in different conformations or/and relative orientations [12], as supported by the polymorphism shown by this molecule. On the contrary, **DRP** is observed only for **TT2Py-X** so, it is to be related to a specific interchromoforic interaction. The X-ray structures point out that **TT2Py-X** and **TT2Py-H** have a high H-aggregated character but the water contained in the **TT2Py-H** may acts as a vibrational quencher for this low energy emission [13].

The other emissions **HEF**, **HEP**, **MEP** and **LEF**, seem to be generated from molecular electronic states. In fact, even if **LEF** is not visible in solutions, it is present in the blended films (and in all polymorphs), probably the rigidification of the environment is necessary to activate this emission.

The comparison with the **TTFPy** analogue allows to clarify the behaviour[1]. This latter derivative shows a fluorescent deactivation from S_1 at 370 nm, a molecular phosphorescence from T_1 at 420 nm and a long lived component arising from the presence of H-aggregates at 560 nm. In the same way, the **HEF** band observed for **TT2Py** can be associated with a deactivation from S_1, as well as the **MEP** can be originated from T_1.

The nature of **LEF** and **HEP** is more complex and requires the support of DFT and TDDFT calculations on the optimized molecular geometry of **TT2Py** (Figure 11). Two almost isoenergetic minima, separated by a small barrier(B), were provided through energy scan calculations around the single bond connecting the **TT** to the pyridine. In the two minima the pyridinic nitrogen atom lies below (polymorph A) or above (polymorph H, X) the plane of cyclic triimidazole. Another local minimum (D), higher by only ~1 kcal/mol than the absolute one, corresponds to the conformation with the pyridinic N atom close to the **TT** one, none of the isolated polymorphs display this conformation which however might be taken in consideration in solution due to the low barrier (C; ~2 kcal/mol) that divides it from the absolute minimum. Finally, a rotation barrier as high as 7 kcal/mol (E) corresponds to the conformation where two nitrogen atoms (one from Py and the other from **TT**) face one against the other.

The absolute minimum geometry (A conformation) simulated absorption spectrum has a good overlap with the experimental UV with mainly two bands, with $^1(\pi,\pi^*)$ character and intermediate weaker transition of $^1(\sigma,\pi^*)$,$^1(\sigma/\pi,\pi^*)$ and $^1(\pi,\pi^*)$ character, corresponding to S_0-$S_{1,A}$ and to S_0-$S_{7,A}$ (at 256 with f= 0.478 and at 207 with f= 0.428, respectively), where the σ contribution is mostly related to occupied MOs localized on one **TT** nitrogen atom. Even if the calculated maxima are blue-shifted with respect the experimental ones the calculated separation (1.16 eV) well matches the observed one (1.05 eV). Two triplet states, $T_{7,A}$ $^3(\sigma/\pi,\pi^*)$and $T_{6,A}$ $^3(\sigma,\pi^*)$, are computed closely to $S_{1,A}$ from where ISC can easily occurs. These triplets could be associated with the **HEP** observed in the emission spectrum.

A deeper investigation has revealed that another triplet state, $T_{9,A}$ at 254 nm, with $^3(\pi,\pi^*)$ character is closed to $S_{2,A}$ (241 nm, oscillator strength f = 0.021) of $^1(\sigma,\pi^*)$ character, this explains the slower **MEP** from $T_{1,A}$, having the same $^3(\pi,\pi^*)$ character as $T_{9,A}$, from which it is populated by internal conversion.

HEP is an anti-Kasha emission[14] from $T_{6,A}$ with $(\sigma/\pi,\pi^*)$ symmetry which is different from the (π,π^*) of the $T_{1,A}$. Compared to the **TTFPy**, for which **HEP** is not observed, the closest triplet states to S_1 have the same $(\sigma/\pi,\pi^*)$ symmetry as T_1 so the IC to this state produces only a low energy molecular phosphorescence.

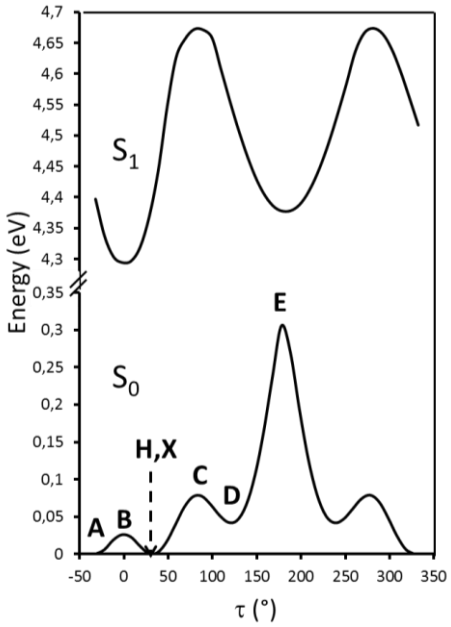

*Figure 11: Scan of the relaxed potential energy surface of the S_1 and S_0 states of **TT2Py** along the N7-C10-C2-C1 torsion angle, τ, at the (TD)-ωB97X/6-311++G(d,p) level of theory. Energies are relative to the S_0 state equilibrium geometry. A, H and X refer to the optimized molecular structures of **TT2Py-A**, **-H**, and **-X**, respectively. B, C, D and E denote the other stationary states. Reproduced from ref.[2] free of charge, https://pubs.rsc.org/en.*

The geometrical optimization of $S_{1,A}$ of (π,π*) with (π,π*) leads to a planar conformation which corresponds to the B geometry of the ground state at only slightly lower energy with respect to the Franck-Condon one. The **HEF** observed in solution, films and solid state at 350-370 nm when excited at 3700-300 nm can occur from this state. The excitation energies calculated in the local minimum's geometry D provide a $S_{0,D}$-$S_{1,D}$ transition, with mixed (σ/π,π*) character, at higher energy with respect to that computed for A, consequently, a molecule in this conformation cannot reach the $S_{1,D}$ using the same excitation energies (270-300nm). However, geometry optimization of $S_{1,D}$ leads to the planar conformation corresponding to the ground state's E geometry and associated with much lower energy than the Franck-Condon one. The **LEF** observed in films and in the solid state at 450 nm when exciting at 390 nm can be associated to this new $S_{1,E}$. The low excitation energy allows for population of a triplet state with proper (π,π*) symmetry which crosses $S_{1,E}$ and finally decays on the ground state. Such a complicated mechanism, $S_{0,D}\rightarrow T_{m,D}\rightarrow S_{1,E}\rightarrow S_{0,E}$, has to be invoked since no singlet states are computed at such low (390 nm) energy neither for the molecule nor for its dimeric aggregates (Figure 12). The pump-probe results support these conclusions. Upon pumping directly the $T_{m,D}$ triplet state (recognizable in the spectrum from the negative PIA band $T_{m,D}\rightarrow T_{n,D}$) the $S_{1,E}$ state responsible for the **LEF** emission is populated by intersystem crossing [4]. The same process could occur even from $S_{1,D}$ but it cannot be observed because obscured by the efficient **HEF**. Moreover, **LEF** can be observed only in a rigid environment, as films or crystals, but in the latter case, it arises from crystal defects where a portion of molecules, inside the crystals as well as on the surface, should be found in the D conformation. To completely understand the intricate behaviour of the **TT2PyH$^+$**, the PMMA film was exposed to acidic vapour in order to protonate the pyridinic nitrogen and consequently block the free rotation around the bond connecting the triimidazole and the pyridine. After 30 minutes of exposition the film is not fully protonated, in fact, steady state experiment revealed the high energy fluorescence of the **TT2Py** together with the additional red shifted fluorescence of the **TT2PyH$^+$** (412 nm, τ_{av}= 3.56 ns). After 45 minutes only the 412 nm fluorescence is visible. Exciting at 390 the protonated film, a phosphorescence at 425 nm (τ_{av}= 13.94 ms) is observed, while the 450 nm **LEF** is missing. The original spectrum is restored by exposing the film of **TT2PyH$^+$** to NH_3 vapors (Figure 4).

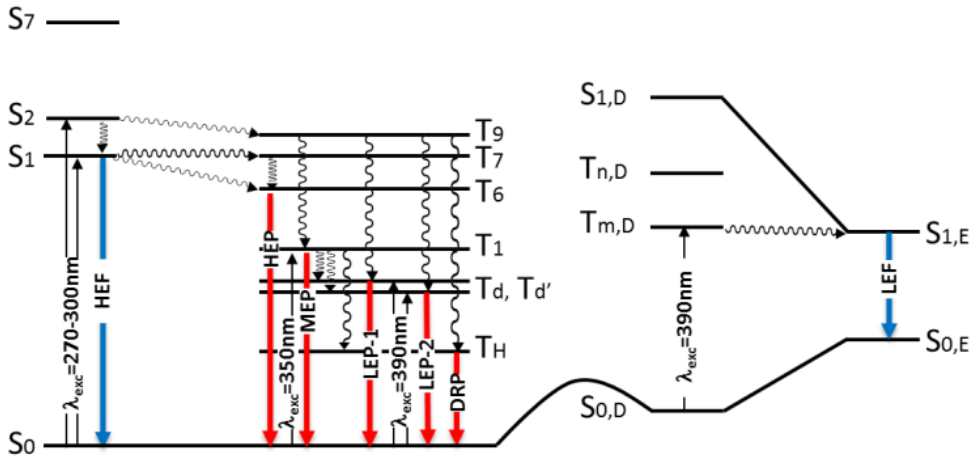

*Figure 12: Schematic photophysical processes of **TT2Py** (fluorescences and phosphorescences shown as blue and red arrows, respectively). Reproduced from ref.[2] free of charge, https://pubs.rsc.org/en.*

As revealed by the geometrical optimization, the simple addition of a proton on the basic nitrogen atom of the **TT2Py** generate a metastable conformation (Figure 13). The relaxed energy scan for **TT2PyH**$^+$shows a more stable conformation (>10 kcal/mol) where the pyridinic protonated nitrogen and one nitrogen of the triimidazole are facing each other, according to a geometry reminiscent of the proton sponges' one [15]. The small barrier (~2 kcal/mol) between these two states allows the quantitative transformation from the higher to the lower energy minimum at RT. In agreement, the TDDFT calculation has confirmed the origin of the red-shifted fluorescence observed and the stable conformation calculated. Importantly, the absence of the low energy fluorescence at 450 nm is predicted by the rigidity of the **TT2PyH**$^+$ scaffold.

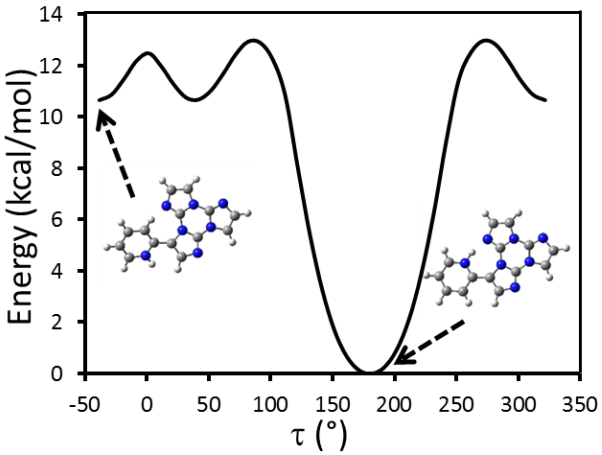

*Figure 13: Scan of the relaxed potential energy surface of **TT2PyH**$^+$ along the N7-C10-C2-C1 torsion angle, τ, at the (TD)-ωB97X/6-311++G(d,p) level of theory. Energies are relative to the minimum energy geometry. Reproduced from ref.[2] free of charge, https://pubs.rsc.org/en.*

9.4 Conclusions

In conclusion we can claim that **TT2Py** displays excitation-dependent emissions and in particular **HEF**, **HEP**, **MEP** and **LEF** emissions of molecular origin, together with **LEPs** and **DRP** aggregated RTPs. The tunable properties and the complex photophysic shown by this dye make **TT2PY** an elegible candidate for industrial application in the anticounterfieding area, in the displays fabrication and in sensoristic field.

9.5 References

[1] Lucenti, E.; Forni, A.; Botta, C.; Giannini, C.; Malpicci, D.; Marinotto, D.; Previtali, A.; Righetto, S.; Cariati, E., Intrinsic and Extrinsic Heavy-Atom Effects on the Multifaceted Emissive Behavior of Cyclic Triimidazole. *Chemistry – A European Journal* **2019,** *25* (10), 2452-2456.

[2] Lucenti, E.; Forni, A.; Previtali, A.; Marinotto, D.; Malpicci, D.; Righetto, S.; Giannini, C.; Virgili, T.; Kabacinski, P.; Ganzer, L.; Giovanella, U.; Botta, C.; Cariati, E., Unravelling the intricate photophysical behavior of 3-(pyridin-2-yl)triimidazotriazine AIE and RTP polymorphs. *Chemical Science* **2020,** *11* (29), 7599-7608.

[3] Cerullo, G.; Manzoni, C.; Lüer, L.; Polli, D., Time-resolved methods in biophysics. 4. Broadband pump–probe spectroscopy system with sub-20 fs temporal resolution for the study of energy transfer processes in photosynthesis. *Photochemical & Photobiological Sciences* **2007,** *6* (2), 135-144.

[4] Borrego-Varillas, R.; Ganzer, L.; Cerullo, G.; Manzoni, C., Ultraviolet Transient Absorption Spectrometer with Sub-20-fs Time Resolution. *Applied Sciences* **2018,** *8* (6), 989.

[5] Svelto O. (2010), Principles of Lasers. Springer, Boston, MA. https://doi.org/10.1007/978-1-4419-1302-9

[6] Portone, A.; Ganzer, L.; Branchi, F.; Ramos, R.; Caldas, M. J.; Pisignano, D.; Molinari, E.; Cerullo, G.; Persano, L.; Prezzi, D.; Virgili, T., Tailoring optical properties and stimulated emission in nanostructured polythiophene. *Scientific Reports* **2019,** *9* (1), 7370.

[7] Lucenti, E.; Forni, A.; Botta, C.; Carlucci, L.; Giannini, C.; Marinotto, D.; Previtali, A.; Righetto, S.; Cariati, E., H-Aggregates Granting Crystallization-Induced Emissive Behavior and Ultralong Phosphorescence from a Pure Organic Molecule. *The Journal of Physical Chemistry Letters* **2017,** *8* (8), 1894-1898.

[8] Lucenti, E.; Forni, A.; Botta, C.; Carlucci, L.; Giannini, C.; Marinotto, D.; Pavanello, A.; Previtali, A.; Righetto, S.; Cariati, E., Cyclic Triimidazole Derivatives: Intriguing Examples of Multiple Emissions and Ultralong Phosphorescence at Room Temperature. *Angewandte Chemie International Edition* **2017,** *56* (51), 16302-16307.

[9] Lucenti, E.; Forni, A.; Botta, C.; Carlucci, L.; Colombo, A.; Giannini, C.; Marinotto, D.; Previtali, A.; Righetto, S.; Cariati, E., The Effect of Bromo Substituents on the Multifaceted Emissive and Crystal-Packing Features of Cyclic Triimidazole Derivatives. *ChemPhotoChem* **2018,** *2* (9), 801-805.

[10] Lucenti, E.; Forni, A.; Botta, C.; Giannini, C.; Malpicci, D.; Marinotto, D.; Previtali, A.; Righetto, S.; Cariati, E., Intrinsic and Extrinsic Heavy-Atom Effects on the Multifaceted Emissive Behavior of Cyclic Triimidazole. *Chemistry – A European Journal* **2019,** *25* (10), 2452-2456.

[11] Kang, H.; Facchetti, A.; Zhu, P.; Jiang, H.; Yang, Y.; Cariati, E.; Righetto, S.; Ugo, R.; Zuccaccia, C.; Macchioni, A.; Stern, C. L.; Liu, Z.; Ho, S.-T.; Marks, T. J., Exceptional Molecular Hyperpolarizabilities in Twisted π-Electron System Chromophores. *Angewandte Chemie International Edition* **2005,** *44* (48), 7922-7925.

[12] Wang, Y.; Yang, J.; Tian, Y.; Fang, M.; Liao, Q.; Wang, L.; Hu, W.; Tang, B. Z.; Li, Z., Persistent organic room temperature phosphorescence: what is the role of molecular dimers? *Chemical Science* **2020,** *11* (3), 833-838.

[13] Bünzli, J.-C. G.; Piguet, C., Taking advantage of luminescent lanthanide ions. *Chemical Society Reviews* **2005,** *34* (12), 1048-1077.

[14] Wu, Y.-H.; Xiao, H.; Chen, B.; Weiss, R. G.; Chen, Y.-Z.; Tung, C.-H.; Wu, L.-Z., Multiple-State Emissions from Neat, Single-Component Molecular Solids: Suppression of Kasha's Rule. *Angewandte Chemie International Edition* **2020,** *59* (25), 10173-10178.

[15] Llamas-Saiz, A. L.; Foces-Foces, C.; Elguero, J., Proton sponges. *Journal of Molecular Structure* **1994,** *328*, 297-323.

10 TT-Pyrene derivative

10.1 Introduction

The appealing of purely organic dyes has suffered from their well-known Aggregation Caused Quenching (ACQ) behaviour especially in those fields requiring water as the main media since most of the more attractive organic luminophores are nonpolar polycyclic aromatic hydrocarbons[1]. However, the ever growing discovery of new, Aggregation Induced organic Emitters (AIE) with high quantum yields, has open up to the possibility of using very unsoluble molecules in the biological area as markers for specific organelles or as photodynamic therapy agents[2][3][4]. In this regard, the recently reported CIE (crystallization Induced emission) and RTUP (room temperature ultralong phosphorescent) properties of triimidazo[1,2-*a*:1',2'-*c*:1'',2''-*e*][1,3,5]triazine, **TT**[5][6], seem particularly intriguing from a biological point of view in which autofluorescence and background interference problems cannot be completely overcome in direct microscopy[7][8][9]. Experimentally, when using a strong intensity excitation source, dye photobleaching, background interference and autofluorescence, are important concerns[10]. In particular, autofluorescence is due to the fact that biological environment normally contains a large number of different chemicals some of which emissive themselves (NAD, FAD, riboflavin, porphyrins). Luckily, most of them show a low intensity signal which, however, becomes relevant with high intensity source. These interferences can be overcome either by using a low intensity source with a very highly efficient emitter or, even more interestingly, a stable phosphorescent dye whose signal is freed from prompt autofluorescence.

Unfortunately, being the emission intensity of **TT** strictly related to its crystallinity grade, the preparation of small aggregate dispersion through the direct addition of the dye in a non-solvent results in a very weak fluorescent signal due to the amorphous nature of the aggregates[11].

In order to solve this problem and obtain highly emissive aggregates we have decided, to couple **TT** with pyrene (**Pyr**), a traditional ACQ emitter suffering from excimer whose formation could be inhibited by the presence of the **TT** fragment[12][13].

10.2 Synthesis and Crystal Structure Analysis

TTPyr can be synthetized in high yields by Suzuki coupling reaction between mono-brominated **TT1Br** [14] and the corresponding boronic acid derivative (Scheme 1) and further purified by standard chromatography techniques and crystallization.

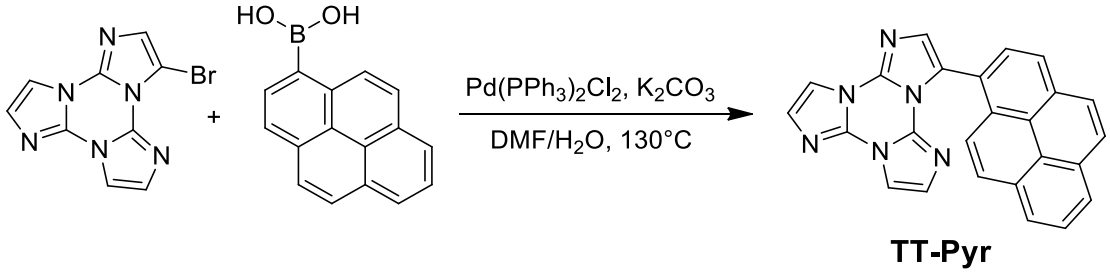

*Scheme 1: Syntethetic pathway for the preparation of **TTPyr**.*

TTPyr forms long needled shaped crystals suitable for single crystal X-ray diffraction analysis by slow diffusion of a non-solvent, such as HEX (**TTPyr(H)**), EtOH (**TTPyr(Et)**) or MeOH (**TTPyr(Me)**), in a DCM solution of the chromophore.

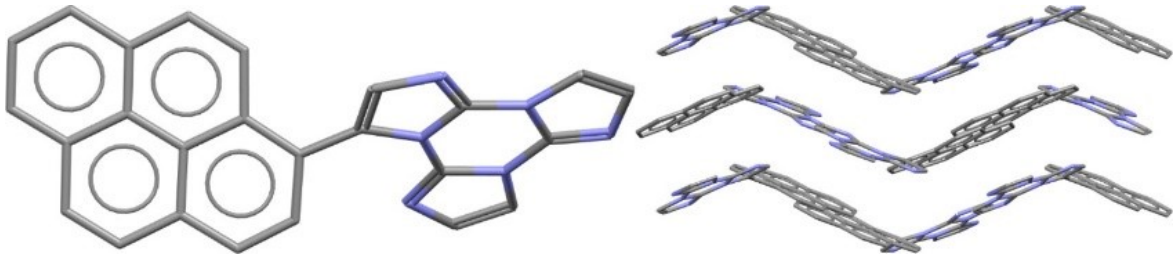

*Figure 1: X-ray structure of **TTPyr(H)** single crystal obtained from DCM/HEX.*

TTPyr(H), obtained from a DCM/HEX solution, crystallizes in the monoclinic P21/c space group with the asymmetric unit containing one molecule with Z=4. Molecules of **TTPyr** are characterized by a dihedral angle (θ) between **Pyr** and **TT** mean planes of 49.3°. The bond connecting the **TT** and **Pyr** units measures 1.470 Å. The triimidazole unit of one molecule stacks in between two **Pyr** units of neighbour molecules with distances of 3.78 and 4.04 Å between the **TT** and pyrene centroids forming infinite columns of H-aggregates. This arrangement is unusual for the reported members of the **TT**-family, all having stacking interactions between **TT**-units of adjacent molecules and represents an interesting case of study for the photophysical behaviour associated with the presence of H aggregates (Figure 1)[15][16].

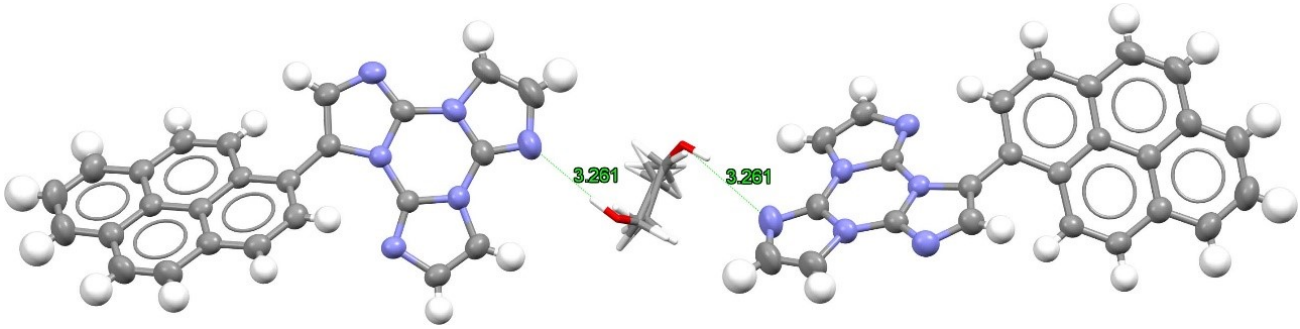

*Figure 2: X-ray structure of **TTPyr(Et)** single crystal obtained from DCM/EtOH.*

The ethanol solvated from, **TTPyr(Et)**, has been isolated from DCM solution with EtOH. This solvate derivative crystallize in the C2/c monoclic space group with the asymmetric unit containing one **TTPyr** molecule and half molecule of ethanol which is disordered over two positions (Figure 2). The dihedral angle between the mean planes of **TT** and pyrene fragments within a molecule is 46.8°. The ethanol molecule is disordered on two positions allowing it to interact one by one *via* hydrogen bond with two **TTPyr** molecules (O-H···N = 3.261 Å) (Figure 2). The packing show that **TTPyr** molecules align in antiparallel fashion along the crystallographic *b* direction giving rise to columns similar to that found in the crystal structure of **TTPyr(H)**. Along this columns **TT** and pyrene fragments are parallel disposed with alternating distances of 3.78 and 3.98 Å between their respective centroids.

Intriguingly, another conformationally stable structure was obtain. In fact, trying to prepare better shaped crystals we have thermally treated a semi-crystalline **TTPyr(Me)** sample few grades below its melting point (m.p.= 232°C). By slowly cooling (0.2 °/min) the sample to RT, crystals of a new phase, **TTPyr(HT)**, were formed.

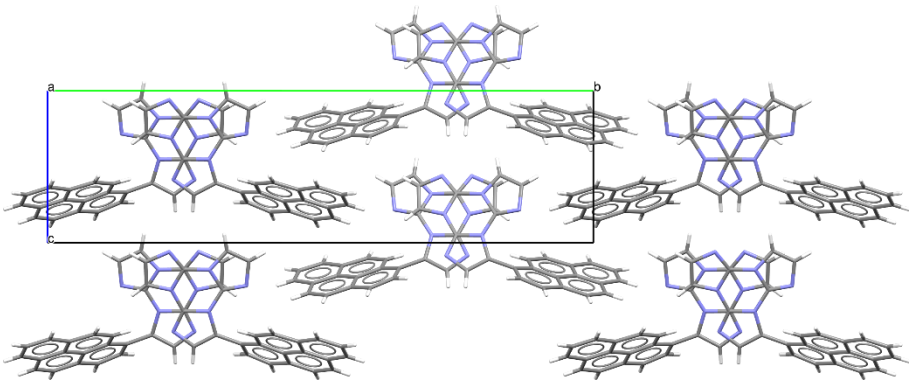

*Figure 3: X-ray structure of **TTPyr(HT)** single crystal obtained after thermal treatment of a crystalline sample obtained from DCM/MeOH.*

The anhydrous form obtained at high temperature, **TTPyr(HT)**, crystallizes in the orthorhombic Pna21 space group, the asymmetric unit contain one molecule with Z = 4. The dihedral angle between mean planes of **TT** and pyrene in a molecule is 52.8°, slightly larger with respect to that found for the low temperature polymorph (Figure 3). The packing here is completely different from that found for the LT form. The molecules form columns along the crystallographic *a* direction and only the **TT** fragments are facing each other while the pyrene units of adjacent molecules orient in opposite directions. Along the columns the mean planes of two adjacent **TT** units are not parallel showing a dihedral angle of 8.2°. The distance between centroids of adjacent **TT** fragments along the crystallographic a direction is 4.15 Å.

Thermal treatments have then been performed in order to prepare all the different phase/polymorphs starting from **TTPyr(Et)**. In particular, we have acquired the X-ray powders diffraction spectra of:

- Starting crystals

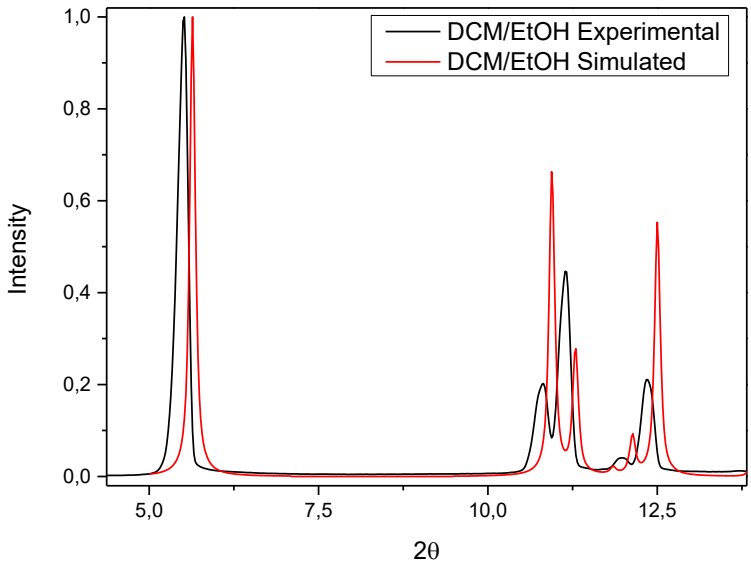

*Figure 4: XRPD of **TTPyr(Et)** (Black line) and its simulated pattern (Red line).*

TTPyr(Et) simulated spectra and the experimental one are identical except for a small shift, probably due to instrumental factors, and the relative intensity of the peaks that is distorted by the preferential orientation of the crystalline powders analysed (These considerations about the small discrepancy between simulated and experimental spectra are valid even for the following experiments) (Figure 4).

- Crystals after 1h at 110°C

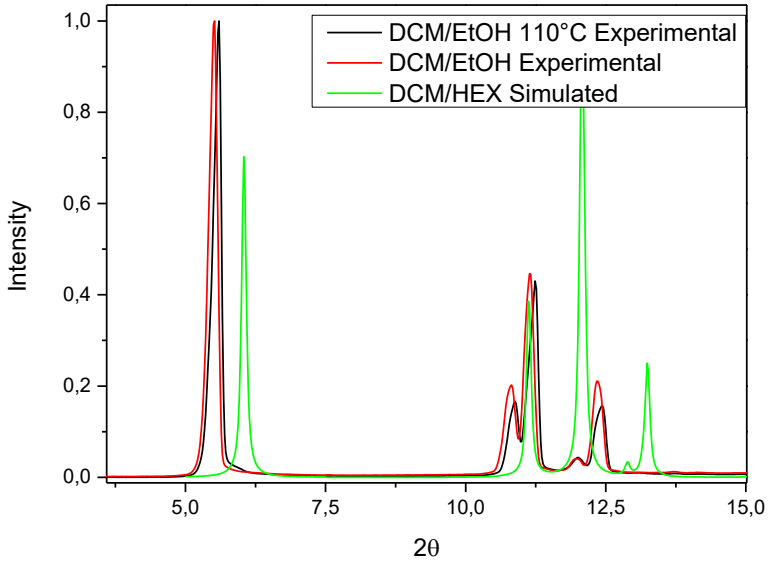

*Figure 5: XRPD of **TTPyr(Et)** before (Red line) and after(Black line) thermal treatment at 110°C and **TTPyr(H)** simulated pattern.*

The powders diffraction spectrum after the thermal treatment at 110°C perfectly matches with that of the starting material indicating that the solvent is strongly bonded in the structure and higher temperatures are needed for its removal (Figure 5).

- Crystals after 1h at 180°C

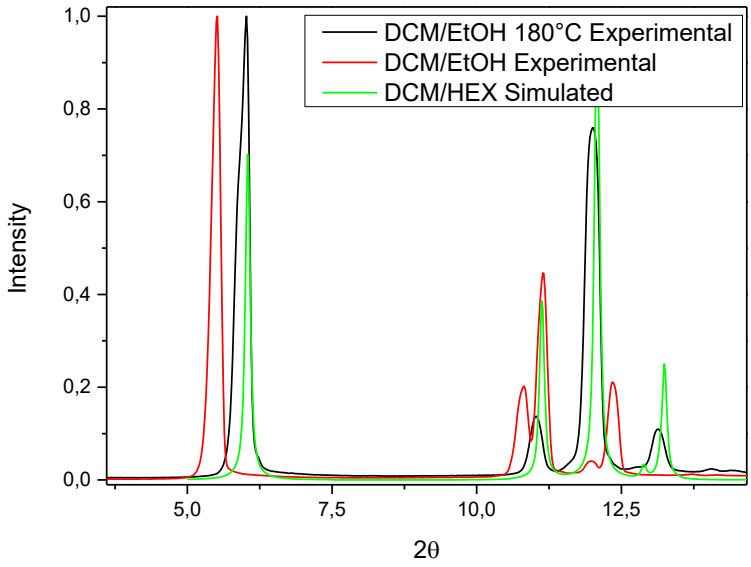

*Figure 6: XRPD of **TTPyr(Et)** before (Red line) and after(Black line) thermal treatment at 180°C and **TTPyr(H)** simulated pattern.*

The ethanol is efficiently removed when the sample is heated at 180°C resulting in the formation of **TTPyr(H)** (Figure 6) which is the same phase obtained from DCM/HEX.

- Crystals after 2h at 220°C and slowly cooled to RT

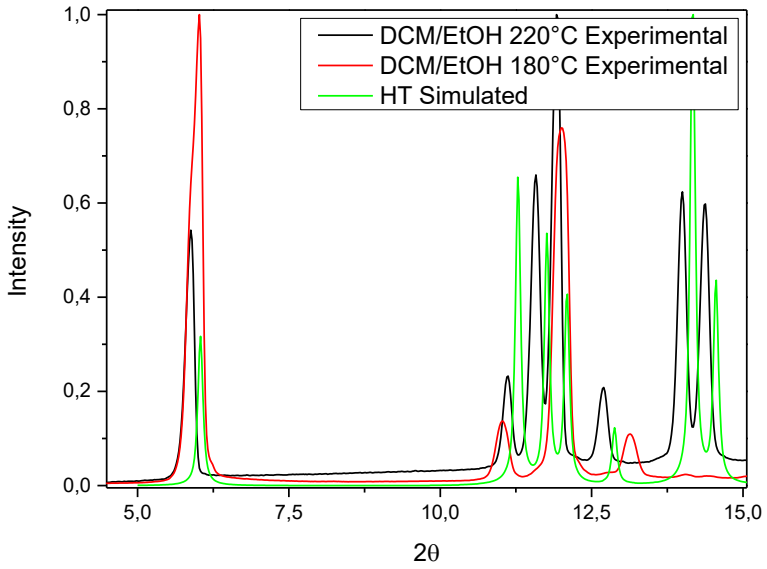

*Figure 7: XRPD of **TTPyr(Et)** after thermal treatment at 180°C (Red line) and after thermal treatment at 220°C (Black line), and **TTPyr(HT)** simulated pattern.*

Finally, the thermal treatment at 220°C allows to obtain the third phase **TTPyr(HT)** (Figure 7).

10.3 Photophysical characterization

10.3.1 DMSO Solutions

Diluted DMSO solutions of **TT-Pyr** (10^{-5} M) show two absorptions with replicas at 257, 268, 279 nm and 332, 347 nm respectively; only slightly red-shifted with respect to those of pyrene itself in the same condition (with peaks at 254, 264, 274 nm and 309, 322, 338 nm). At 298 K, the solution displays an intense fluorescent emission peaked at 420 nm (Φ = 92%, τ_{av}= 2.76 ns) ascribable to deactivation from an excited state (S_1) with main pyrene character as suggested by the similarity of the corresponding excitation spectrum (displaying components at 275 nm and 346 nm) with the absorption spectrum of pyrene itself (Figure 8).

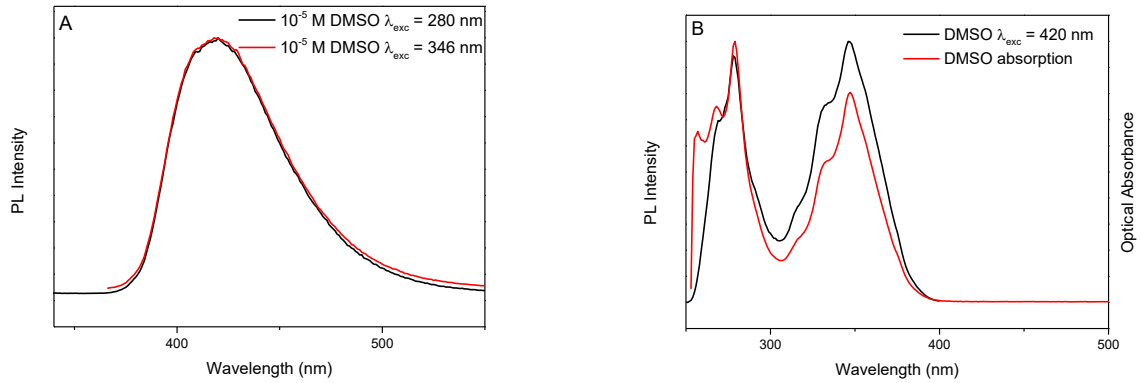

*Figure 8: A) Normalized emission spectra of **TTPyr** in DMSO 10^{-5}M. λ_{exc}= 280 nm (Black line); λ_{exc}= 346 nm (Red line); B) Normalized excitation spectra of **TTPyr.** DMSO 10^{-5}M. λ_{em}= 420 nm (Black line); DMSO 10^{-5} M Normalized absorbance (Red line).*

The nature of the low energy transition has been explored by DFT/TDDFT calculations, providing two close singlet states (S_1 at 304 nm with oscillator strength f=0.06 and S_2 at 302 nm, f=0.50), both involving molecular orbitals (HOMO-1, HOMO, LUMO and LUMO+1) localized on the pyrene moiety with only a small contribution (coming from HOMO-1) on **TT**. Optimization of the S_1 state converges on a less twisted conformation with respect to the ground state (θ varying from 67 to 31°) and shortening of the bond connecting the **TT** and **Pyr** units (from 1.478 to 1.425 Å), implying a greater conjugation between them. Emission from the relaxed S_1 state is computed at 384 nm (f=0.89) and involves HOMO and LUMO both delocalized on pyrene with a large tail on **TT**.

10.3.2 Nano-Aggreggates

Nano aggregation experiments performed through rapid injection of different water volumes to solutions of **TTPyr** in DMSO (keeping the concentration equal to 10^{-5} M; Figure 9), have revealed an aggregation and excitation dependent behaviour. In fact, by irradiation at 340 nm, a gradual increase and a concomitant blue shift of the emission at 420 nm is observed by increasing the water fraction up to 70%. Further water addition results in an attenuation of this emission. Moreover, the appearance of an additional low energy component at about 480 nm is observed for the 90 and 99% (water content in volume) suspension. At 405 nm excitation wavelength, the intensification of the low energy component can be monitored since freed from the more intense high energy one. It is thus evident that the 480 nm emission is already visible and actually more intense at 80% water content.

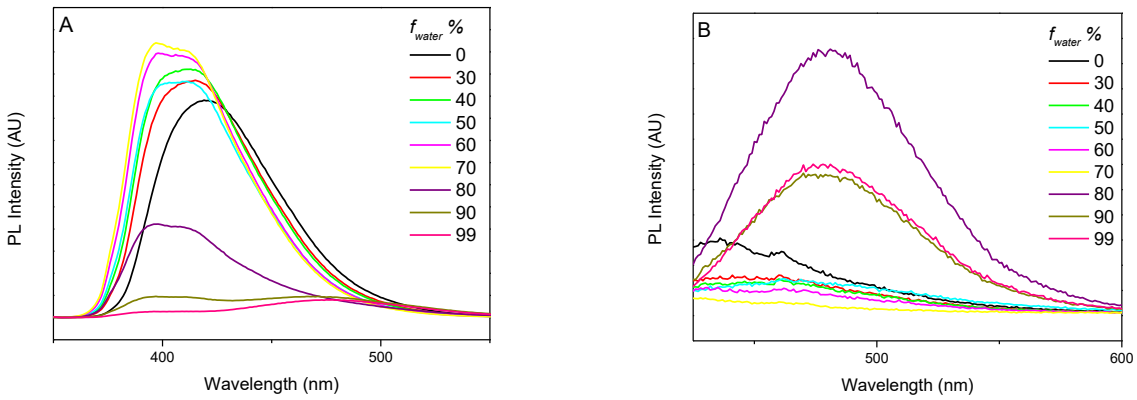

*Figure 9: PL spectra of **TTPyr** in DMSO/H_2O mixtures with different water fractions (f_w) 10^{-5} M. A) λ_{exc}= 340 nm. B) λ_{exc}= 405 nm*

A detailed analysis of the 90% water containing suspension has been performed (Figure 10). By exciting at 346 nm, a low energy band at about 480 nm (τ_{av} = 25.66 ns) is visible together with a stronger one at about 400 nm (τ_{av} = 12.32 ns). On the other side, by exciting at 405 nm, only the broad emission at 480 nm is observed. The excitation profiles are strictly related to the emission taken into account. When monitored at 400 nm emission, the excitation spectrum is superimposable to that of the diluted DMSO solution with two structured intense absorptions centred at about 280 nm and 346 nm. While at 480 nm, the excitation profile becomes broader with a tail in the visible range in agreement with the absorption spectrum of the solvent/non solvent suspension. It is thus conceivable that the low energy emission is associated to aggregated species with red shifted absorption component. The 400 nm emission, on the other side, is to be associated to the monomeric species still visible at 90% non-solvent volume due to its high quantum efficiency, much stronger than that of the aggregates. The formation of excimers in the nanoaggregated suspensions could be expected from pyrene containing species[17]. In the case of **TTPyr**, however, it seems that the **TT** moiety prevents excimers formation and favors ground state aggregates as indicated by the

excitation dependent emission and the presence of an aggregate fingerprint absorption in the excitation spectrum[18].

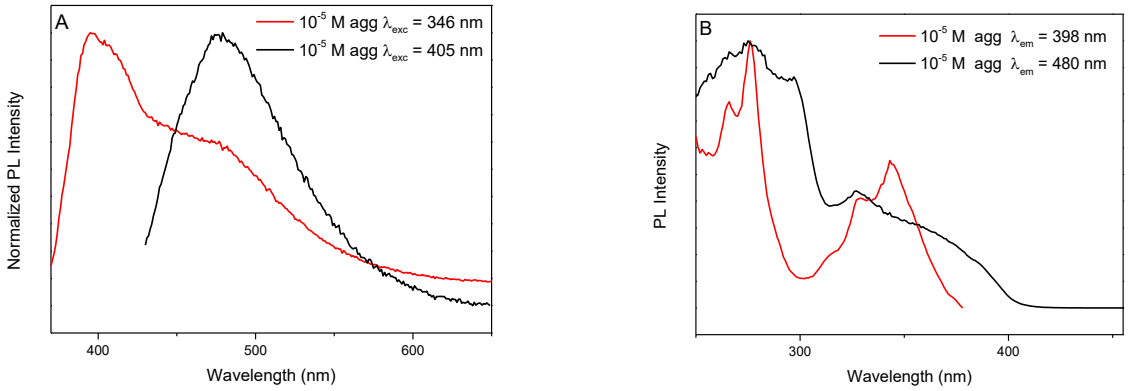

*Figure 10: A) Normalized Emission spectra of **TTPyr** aggregates in DMSO/H_2O (10/90 v/v) 10^{-5} M at 298 K λ_{exc}= 346 nm (Red line); λ_{exc}= 405 nm (Black line); B) Normalized Excitation spectra of **TTPyr** aggregates in DMSO/H_2O (10/90 v/v) 10^{-5} M at 298 K λ_{em}= 398 nm (Red line); λ_{em}= 480 nm (Black line).*

10.3.3Crystals

10.3.3.1 TTPyr(Et)

Crystals of **TTPyr(Et)** at RT display an intense fluorescence at 493 nm (Φ = 53.2%, τ_{av}= 2.97 ns) when excited in the 300-400 nm range. Through selective excitation at 495 nm a phosphorescent component appears at 555 nm (τ_{av}= 4.90 ms) (Figure 11). The excitation spectrum monitored at 610 nm clearly shows the presence of a direct triplet population at 525 nm which is furtherly intensify by lowering the temperature at 77K. At low temperature, the two emissions become more vibronically resolved as shown by the structure shoulder at 595 nm for the phosphorescence (τ_{av}= 5.37 ms) and at 460 and 520 nm for the fluorescence (τ_{av}= 4.17 ns) (Figure 12).

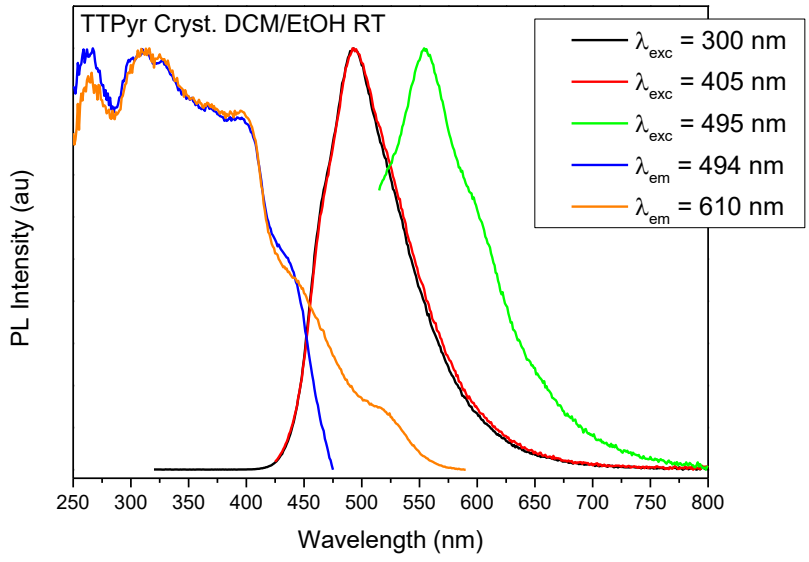

*Figure 11: Normalized PL spectra of **TTPyr(Et)** crystals at 298K. λ_{exc}= 300 nm (Black line); λ_{exc}= 405 nm (Red line); λ_{exc}= 495 nm (Green line);); λ_{em}= 494 nm (Blue line); λ_{em}= 610 nm (Orange line).*

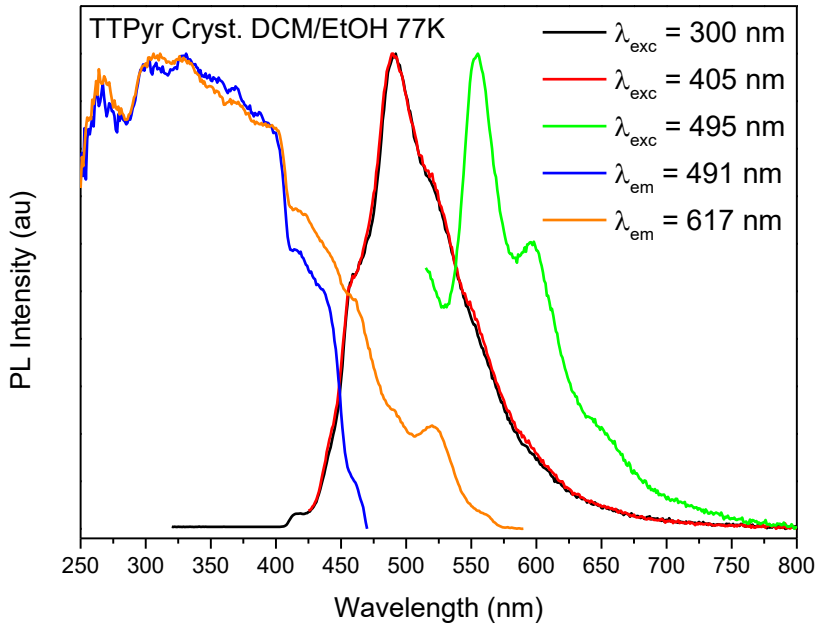

*Figure 12: Normalized PL spectra of **TTPyr(Et)** crystals at 77K. λ_{exc}= 300 nm (Black line); λ_{exc}= 405 nm (Red line); λ_{exc}= 495 nm (Green line);); λ_{em}= 491 nm (Blue line); λ_{em}= 617 nm (Orange line).*

10.3.3.2 TTPyr(Me)

TTPyr(Me) displays at RT a vibronically resolved fluorescent emission (470, 499 and 530 nm; Φ = 42.1 %; τ_{av}= 3.38 ns) and a phosphorescent component (τ_{av} = 5.18 ms) (Figure 13) as already observed for **TTPyr(Et)**.

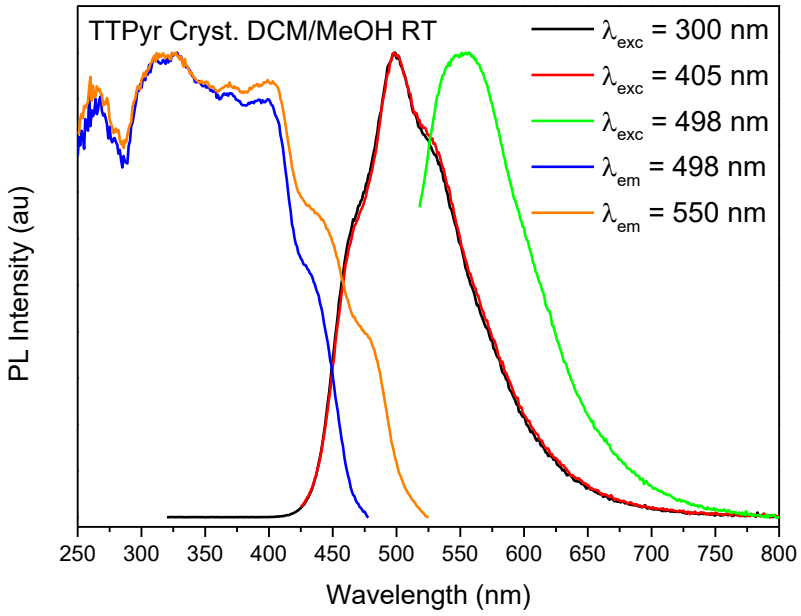

*Figure 13: Normalized PL spectra of **TTPyr(Me)** crystals at 298K. λ_{exc}= 300 nm (Black line); λ_{exc}= 405 nm (Red line); λ_{exc}= 498 nm (Green line);); λ_{em}= 498 nm (Blue line); λ_{em}= 550 nm (Orange line).*

10.3.3.3 TTPyr(H)

Some differences with respect to previous phases are observed for **TTPyr(H)**. In particular, a small blue shift and a lower vibronical resolution is measured for the fluorescent (491 nm; Φ = 38.2 %; τ_{av}= 3.03 ns) and the phosphorescent (549 nm; τ_{av} = 4.54 ms) emissions with respect to **TTPyr(Et)** (Figure 14).

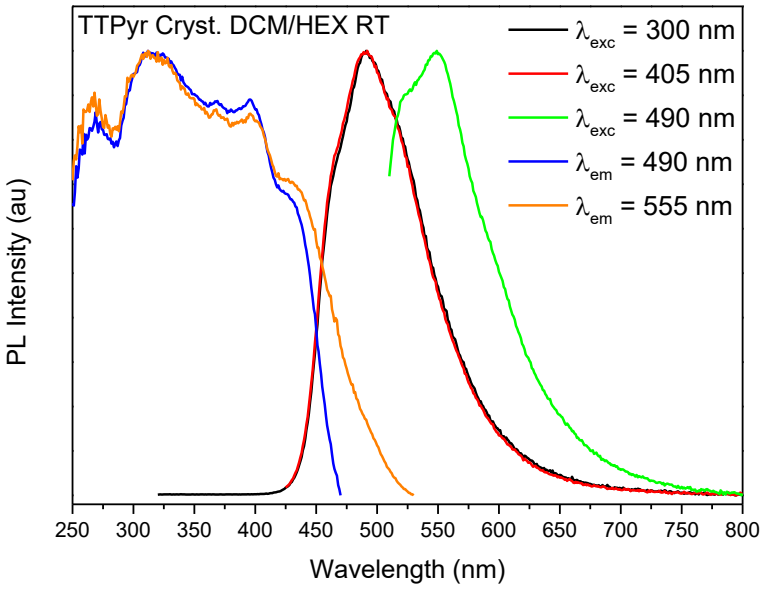

*Figure 14: Normalized PL spectra of **TTPyr(H)** crystals at 298K. λ_{exc}= 300 nm (Black line); λ_{exc}= 405 nm (Red line); λ_{exc}= 490 nm (Green line);); λ_{em}= 490 nm (Blue line); λ_{em}= 555 nm (Orange line).*

10.3.3.4 TTPyr(HT)

The high temperature polymorph, **TTPyr(HT)** (Φ = 43.0 %), displays an emissive behavior quite different from that of the other phases. In fact, at room temperature, this polymorph shows a fluorescence at 480 nm (τ_{av} = 2.28 ns) and a quite intense phosphorescence at 546 nm (τ_{av} = 6.08 ms) (Figure 15). An additional high energy fluorescence, which becomes better resolved lowering the temperature to 77K (Figure 16), is detected at 420 nm (τ_{av} = 1.01 ns). At 77 K all emissive components acquire a better vibronic resolution.

Moreover, the **TTPyr(HT)** phase crystallize in a non-centrosymmetric space group. This is a strict requirement to have non-zero second order non-linear optical properties (NLO). The second harmonic

generation (SHG) response of **TTPyr(HT)** powders, evaluated with a Kurtz-Perry setup at 1064 nm, results in 0.1 times that of the standard urea.

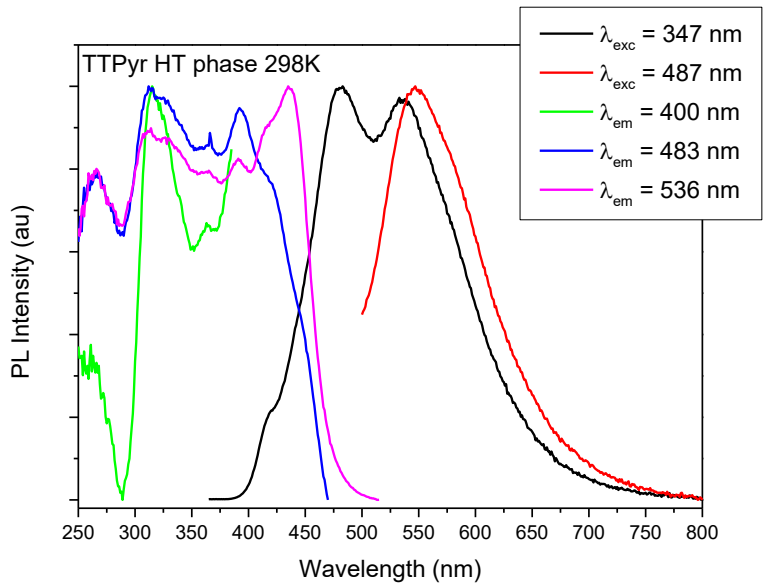

*Figure 15: Normalized PL spectra of **TTPyr(HT)** crystals at 298K. λ_{exc}= 347 nm (Black line); λ_{exc}= 487 nm (Red line); λ_{em}= 400 nm (Green line);); λ_{em}= 483 nm (Blue line); λ_{em}= 536 nm (Violet line).*

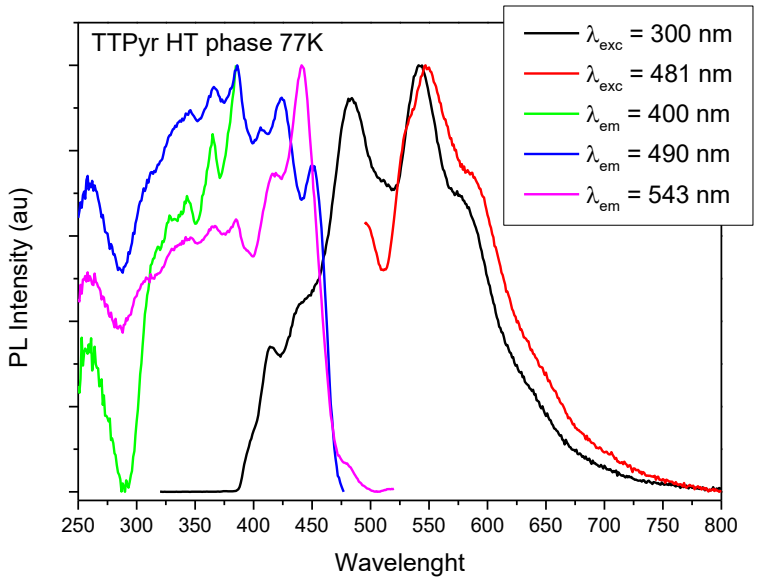

*Figure 16: Normalized PL spectra of **TTPyr(HT)** crystals at 77K. λ_{exc}= 300 nm (Black line); λ_{exc}= 481 nm (Red line); λ_{em}= 400 nm (Green line); λ_{em}= 490 nm (Blue line); λ_{em}= 543 nm (Violet line).*

10.3.4 Amorphous films

Amorphous films, prepared by melting (at 250°C) **TTPyr** powders and rapidly quenching the melt with liquid nitrogen, display an intense fluorescence at 465 nm (τ_{av} = 9.13 ns) resembling the 90/10 H_2O/DMSO one. The

excitation spectrum at 470 nm is characterized by peaks at 265, 310 and 390 nm which are ascribable to the pyrene moiety similarly to what observed for solutions and nano-aggregates (Figure 17).

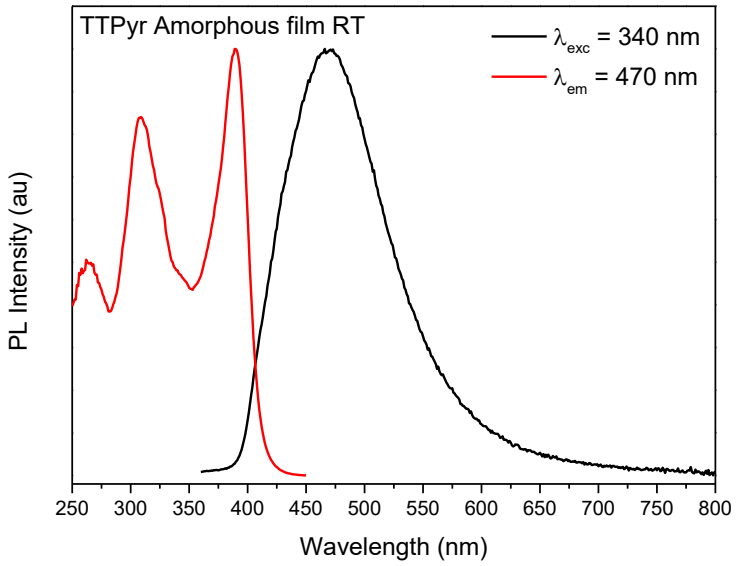

*Figure 17: Normalized PL spectra of **TTPyr** amorphous film at 298K. λ_{exc}= 340 nm (Black line); λ_{em}= 470 nm (Red line).*

10.3.5 Discussion

All **TTPyr** phases display both short and long-lived components whose origin is still under investigation since the isolation of all pure phases has revealed to be very time consuming. In particular, the effect of the different packing arrangements (**TTPyr(Et)**, **TTPyr(Me)** and **TTPyr(H)** display dual-component **TT**/pyrene H-aggregation while in **TTPyr(HT)** only the triimidazolic fragments are involved in the H-aggregates) on the emissive behavior of the different polymorphs require to be better and fully analyzed. From a preliminary analysis, it seems that fluorescent emission in the solid state is significantly red-shifted (by about 60 and 30 nm) with respect to what observed in solution. Such red shift could be explained by the effect of packing forces that impose a lower twisting of the two molecular moieties resulting in a higher conjugation. In fact, a prototype dimeric DFT model has shown that the dihedral angle θ decreases from 67 (isolated monomer) to 53°, approaching the X-ray value (46.8° for **TTPyr(H)** and 52.8 for **TTPyr(HT)**). The smaller red shift measured for aggregates and amorphous film may be due to the formation of small dimers or small aggregates that, as demonstrated by DFT calculations, can only partially force the planarization.

TTPyr(Et), **TTPyr(Me)** and **TTPyr(H)** share the same crystalline structure apart for the presence of disordered methanol or ethanol molecules and small differences in the intermolecular distances. These differences seem to have low impact on **TTPyr** photophysic, whose emissions appears only more vibronically structured when O-H···N bonds are formed with solvents molecules. In the same direction, the structural rigidification provided by the H-bonds formation seems to increase Φ, in particular $\Phi_{\mathbf{TTPyr(Et)}} > \Phi_{\mathbf{TTPyr(Me)}} > \Phi_{\mathbf{TTPyr(H)}}$ [19;20]. Such trend could be justified by the formation of better shaped crystals with EtOH with respect to MeOH for which no crystals suitable for X-diffraction analysis have been obtained.

Reasonably, the phosphorescence observed for every polymorph may be associated to the H-aggregates formation as for the previous cases described [11]. The high energy fluorescence detected at 420 nm for

TTPyr(HT) may be associated to an anti-Kasha emission form an S_2 level, which was already observed for pyrene and its derivatives [21][22].

10.4 Biological evaluation

Based on the observation that triazinic functionalities are frequently used in the biological field due to their ability to work as central scaffold for further modification or as mimetic of purine moieties, we assumed that the insertion of the **TT** moiety on pyrene dyes could, not only modify its photophysical properties, but also enhance the biological value acting as a carrier through the cell membrane. For this reason, we performed a detailed investigation of the performances of **TTPyr** in a biological context [23][24].

10.4.1 Bacteria imaging

TTPyr is a good candidate for bacterial imaging because of its balance of hydrophilicity and hydrophobicity. To verify the bacterial imaging ability of **TTPyr**, *S. aureus* and *E. coli* were chosen as bacterial models, which represent Gram-positive and Gram-negative bacteria respectively. As shown in Figure 18, **TTPyr** can stain both *S. aureus* and *E. coli* effectively within 60 min by entering the bacterial cells. In addition, **TTPyr** showed very high staining efficiency towards both Gram-positive and Gran-negative bacteria. A few *E. coli* cells showed weak emission compared to *S. aureus*, which is due to the outer membrane of E. coli that hampers the dyes penetration.

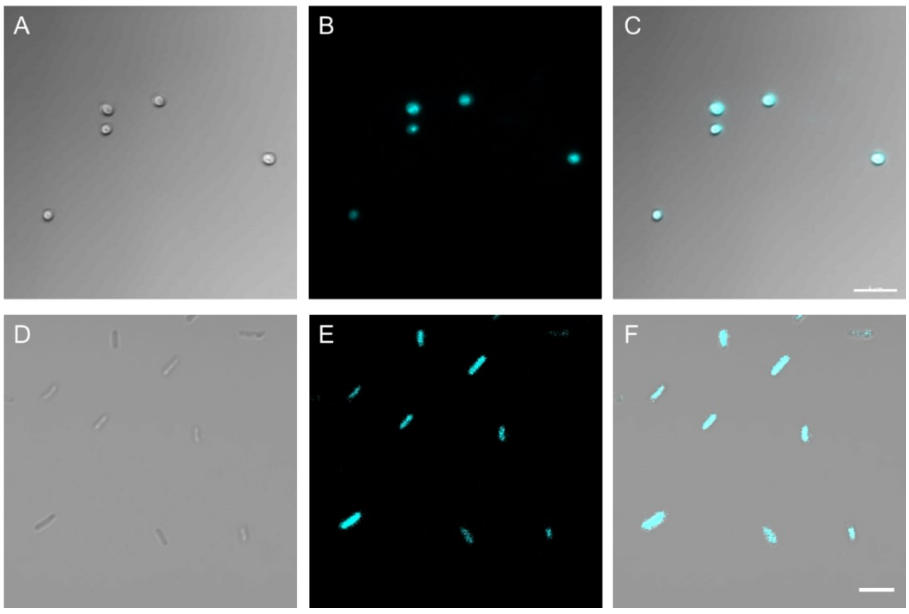

*Figure 18: Confocal Laser Scanning Microscope (CLSM) images of bacteria stained with 100 µM **TTPyr** for 60 min. (A-C) S. aureus. (D-F) E. coli. Scale bar: 5 µm.*

10.4.2 Cell imaging

Confocal microscope images indicate that **TTPyr** aggregates are detectable inside cells at concentration as low as 10 µM when they are added to the culture media of HeLa, HLF and cell lines.

From an accurate observation of the co-staining experiment pictures on HeLa (Figure 19-20) and HLF (Figure 21-22) it is evident a good overlap between the **TTPyr** aggregates signal and those of the Lysotracker, and

BODIPY 493/503, in particular in HLF cells. Only a partial overlap between **TTPyr** and Mitotracker signals is detected.

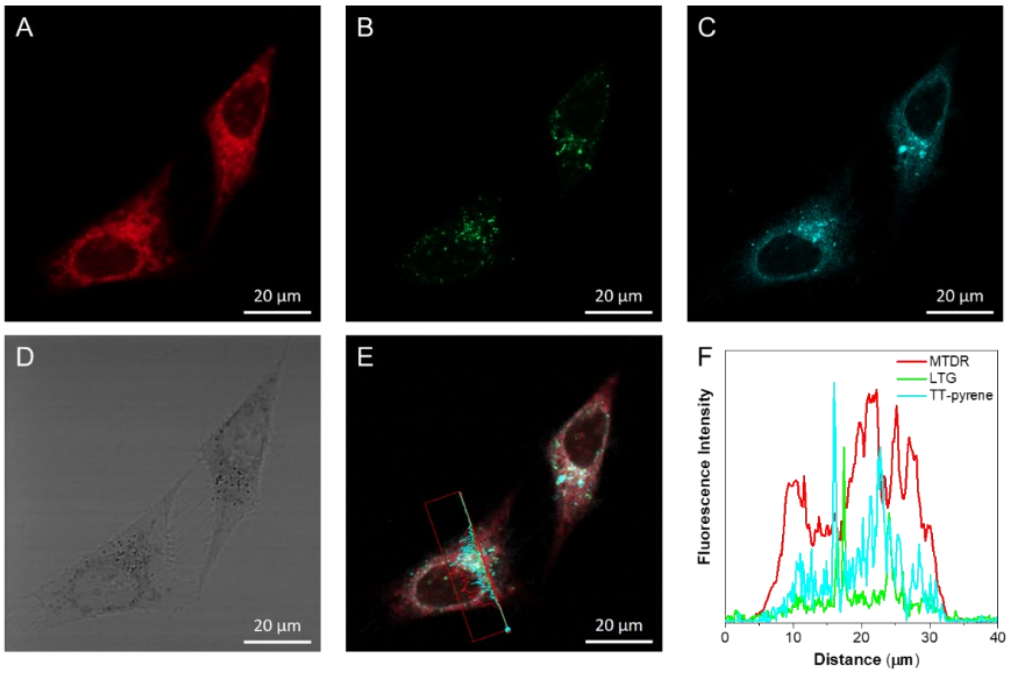

*Figure 19: HeLa cells co-staining experiment. A) MitoTracker Deep Red. B) LysoTracker Green DND 26. C) **TTPyr** 10 uM. D) Bright field. E) On screen axial fluorescent intensity of **TTPyr**, MitoTracker and LysoTracker. F) The fluorescence intensities of MTDR, LTG, **TTPyr** along the axis.*

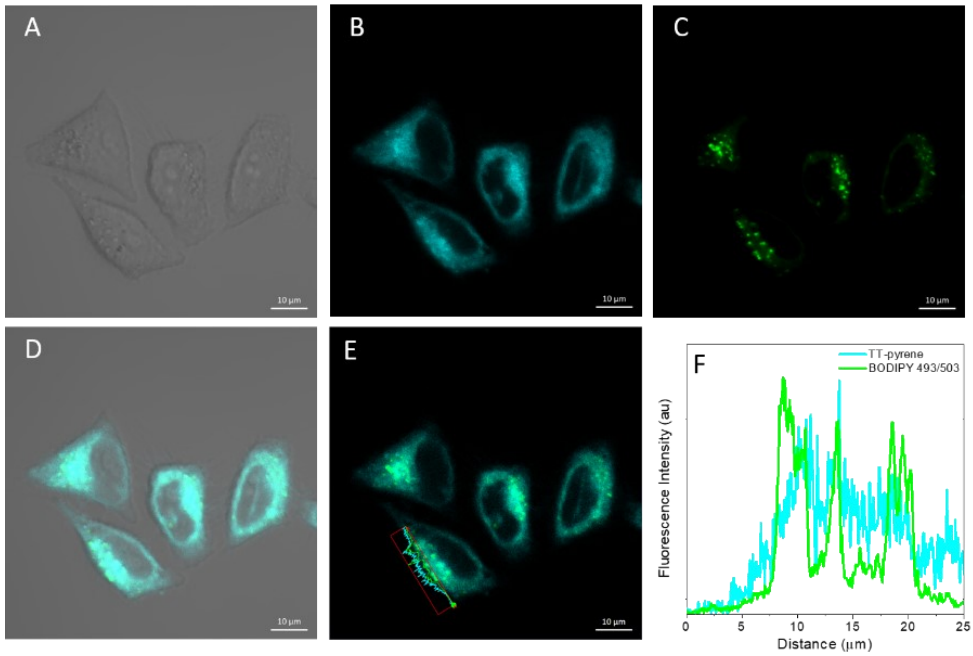

*Figure 20: HeLa cell co-staining experiment. A) Bright field. B) **TTPyr** 10 µM. C) BODIPY 493/503. D) Merged image of A-C. E) On screen axial fluorescent intensity of **TTPyr** and BODIPY 493/503. F) The fluorescence intensities of **TTPyr** and BODIPY 493/503 along the axis.*

Curiously, this means that the cells accumulate **TTPyr** aggregates in lysosomes and lipid droplets as if they were trying to degrade or at list contain the chromophore that, however, seems to be widespread throughout the cytoplasm. This attempt to eliminate the dye from the cells is a clear indication of **TTPyr** toxicity. In fact, after sufficiently long staining time, **TTPyr** seems to be not well metabolized by the cells as revealed by their round shape and the high number of vesicles which are indicative of a general unhealthy condition.

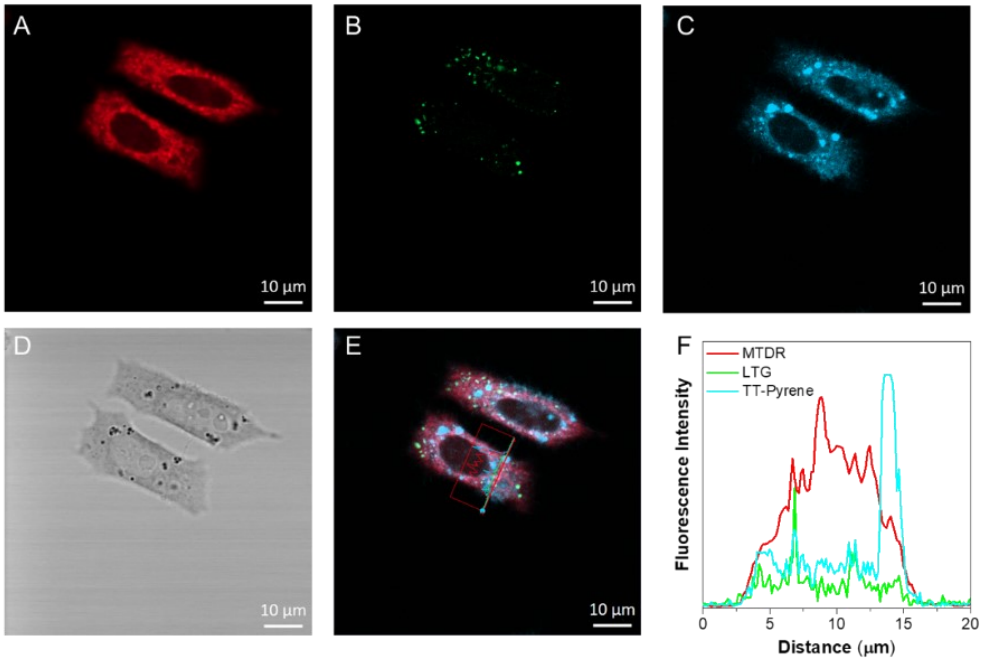

*Figure 21: HLF cell co-staining experiment. A) MitoTracker Deep Red. B) LysoTracker Green DND 26. C) **TTPyr** 10 uM. D) Bright field. E) On screen axial fluorescent intensity of **TTPyr**, MitoTracker and LysoTracker. F) Fluorescence intensities of MTDR, LTG, **TTPyr** along the axis.*

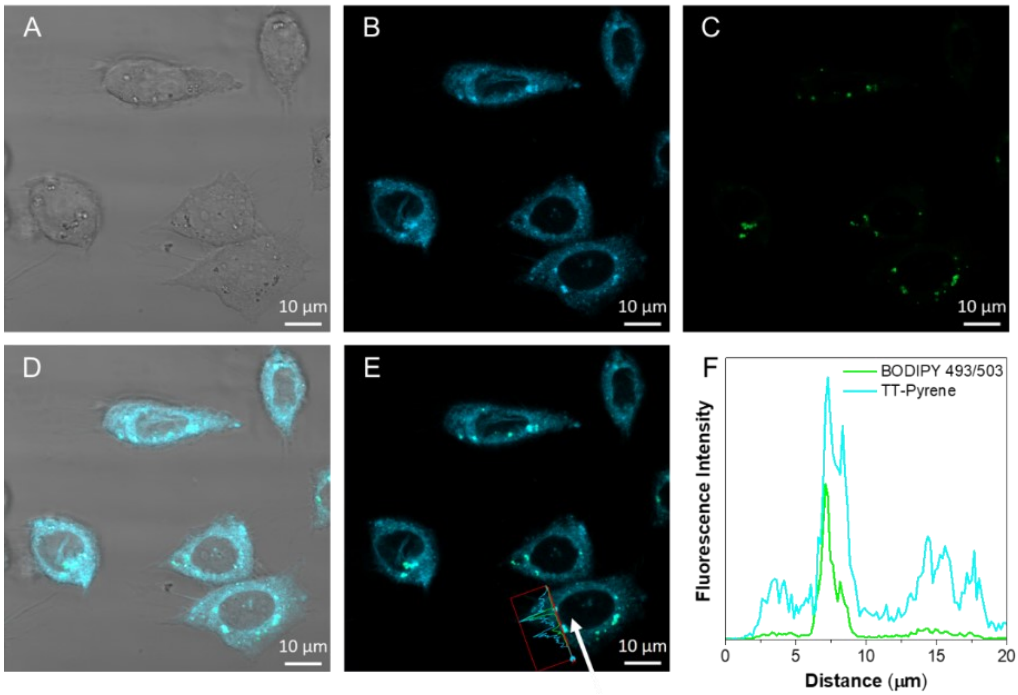

*Figure 22: HLF cell co-staining experiment. A) Bright field. B) **TTPyr** 10 µM. C) BODIPY 493/503. D) Merged image of A-C. E) On screen axial fluorescent intensity of **TTPyr** and BODIPY 493/503. F) The fluorescence intensities of **TTPyr** and BODIPY 493/503 along the axis.*

To certify the presence of **TTPyr** inside the cells, we have acquired the *in-situ* steady state spectra. As clearly visible in Figure 23, there is a perfect match between the *in-situ* spectra and the one obtained with the 90% non-solvent aggregate previously described.

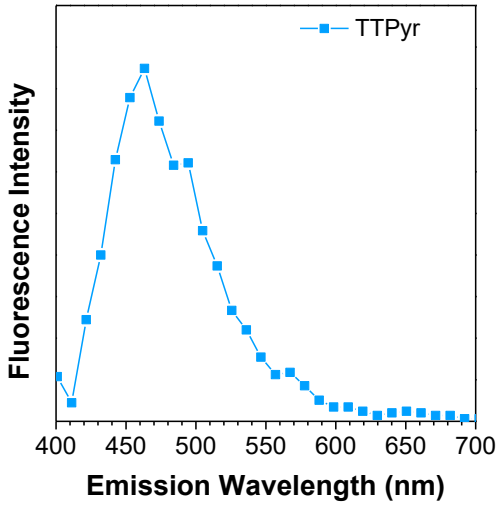

*Figure 23: In-situ emission spectra of 10 µM **TTPyr** (right) in HeLa cells obtained on CLSM. λ_{exc} = 405 nm.*

In agreement with staining experiments, the MTT test (Figure 24) points out a major cytotoxicity of **TTPyr**. It is expected, in fact, that the binding of **TTPyr** with the Mitocondria, as highlighted by the staining experiments, could lead to the invalidation of the ATP production process causing the death of the cells. Moreover, ***TTPyr** showed* more toxicity towards HeLa cells, which could attributed to the stronger metabolism of HeLa cells compared to HLF cells.

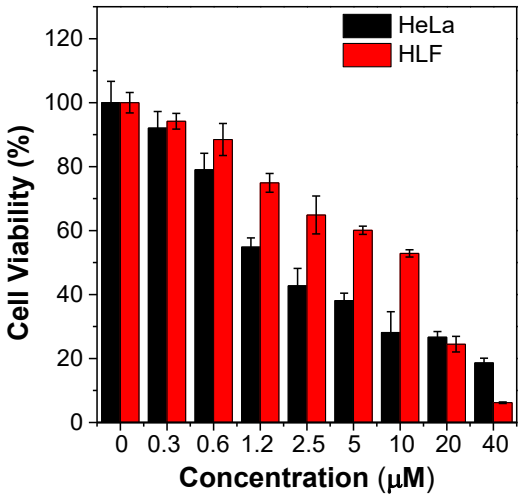

*Figure 24: Cell viability of HeLa cells and HLF cells treated with different concentrations of **TTPyr**.*

10.5 Conclusions

In conclusion, the high quantum efficiency shown by **TTPyr** solutions, aggregates and crystalline powders makes this material an appealing resource in view of further application. In addition to the great staining ability of this dye, its use as sensing fluorophore for the detection of explosives is ongoing and the preliminary data are promising. A detailed analysis of **TTPyr** behavior is still to be completed but from the results obtained so far some statements can be made. In particular, the conjugation of **TT** with pyrene does not prevent the H-aggregates formation and the arise of the associated phosphorescence. Moreover, the flat structure of pyrene allows to form mixed pyrene/**TT** H-aggregates in **TTPyr(H)**, -**(Me)** and -**(Et)** which, from a comparison

with the **TTPyr(HT)** one, seems to be as efficient as the “pure” **TT**/**TT** H-aggregates in the generation and stabilization of triplet excitons.

In view of the good results obtained with pyrene, triimidazole could be introduced as substituent on other flat scaffolds in order to switch on or to enhance phosphorescent emissions.

10.6 References

[1] Bandyopadhyay, D.; Sanchez, J. L.; Guerrero, A. M.; Chang, F.-M.; Granados, J. C.; Short, J. D.; Banik, B. K., Design, synthesis and biological evaluation of novel pyrenyl derivatives as anticancer agents. *European Journal of Medicinal Chemistry* **2015,** *89*, 851-862.

[2] Islam, M. M.; Hu, Z.; Wang, Q.; Redshaw, C.; Feng, X., Pyrene-based aggregation-induced emission luminogens and their applications. *Materials Chemistry Frontiers* **2019,** *3* (5), 762-781 .

[3] Schnermann, M. J., Organic dyes for deep bioimaging. *Nature* **2017,** *551* (7679), 176-177 .

[4] Banerji, B.; Chatterjee, S.; Chandrasekhar, K.; Ghosh, S.; Mukherjee, K.; Mandal, C., Detection of Lysosome by a Fluorescent Heterocycle: Development of Fused Pyrido–Imidazo–Indole Framework via Cu-Catalyzed Tandem N-Arylation. *The Journal of Organic Chemistry* **2018,** *83* (21), 13011-13018.

[5] Schubert, D. M.; Natan, D. T.; Wilson, D. C.; Hardcastle, K. I., Facile Synthesis and Structures of Cyclic Triimidazole and Its Boric Acid Adduct. *Crystal Growth & Design* **2011,** *11* (3), 843-850.

[6] Buck, D. M.; Kunz, D., Triazine Annelated NHC Featuring Unprecedented Coordination Versatility. *Organometallics* **2015,** *34* (21), 5335-5340.

[7] Chelushkin, P. S.; Tunik, S. P., Phosphorescence Lifetime Imaging (PLIM): State of the Art and Perspectives. **2019,** *119*, 109-128.

[8] Berezin, M. Y.; Achilefu, S., Fluorescence Lifetime Measurements and Biological Imaging. *Chemical Reviews* **2010,** *110* (5), 2641-2684 .

[9] Baggaley, E.; Sazanovich, I. V.; Williams, J. A. G.; Haycock, J. W.; Botchway, S. W.; Weinstein, J. A., Two-photon phosphorescence lifetime imaging of cells and tissues using a long-lived cyclometallated Npyridyl^Cphenyl^Npyridyl Pt(ii) complex. *RSC Advances* **2014,** *4* (66), 35003-35008 .

[10] Fu, Y.; Finney, N. S., Small-molecule fluorescent probes and their design. *RSC Advances* **2018,** *8* (51), 29051-29061.

[11] Lucenti, E.; Forni, A.; Botta, C.; Carlucci, L.; Giannini, C.; Marinotto, D.; Previtali, A.; Righetto, S.; Cariati, E., H-Aggregates Granting Crystallization-Induced Emissive Behavior and Ultralong Phosphorescence from a Pure Organic Molecule. *The Journal of Physical Chemistry Letters* **2017,** *8* (8), 1894-1898.

[12] Nie, H.; Liang, Y.; Han, C.; Zhang, R.; Zhang, X.; Yan, H., Rational design of cyanovinyl-pyrene dual-emission AIEgens for potential application in dual-channel imaging and ratiometric sensing in living cells. *Dyes and Pigments* **2019,** *168*, 42-48.

[13] Qian, J.; Tang, B. Z., AIE Luminogens for Bioimaging and Theranostics: From Organelles to Animals. *Chem* **2017,** *3* (1), 56-91 .

[14] Lucenti, E.; Forni, A.; Botta, C.; Carlucci, L.; Giannini, C.; Marinotto, D.; Pavanello, A.; Previtali, A.; Righetto, S.; Cariati, E., Cyclic Triimidazole Derivatives: Intriguing Examples of Multiple Emissions and Ultralong Phosphorescence at Room Temperature. *Angewandte Chemie International Edition* **2017,** *56* (51), 16302-16307.

[15] Yuan, J.; Wang, S.; Ji, Y.; Chen, R.; Zhu, Q.; Wang, Y.; Zheng, C.; Tao, Y.; Fan, Q.; Huang, W., Invoking ultralong room temperature phosphorescence of purely organic compounds through H-aggregation engineering. *Materials Horizons* **2019,** *6* (6), 1259-1264.

[16] Forni, A.; Lucenti, E.; Botta, C.; Cariati, E., Metal free room temperature phosphorescence from molecular self-interactions in the solid state. *Journal of Materials Chemistry C* **2018,** *6* (17), 4603-4626.

[17] Van Dyke, D. A.; Pryor, B. A.; Smith, P. G.; Topp, M. R., Nanosecond Time-Resolved Fluorescence Spectroscopy in the Physical Chemistry Laboratory: Formation of the Pyrene Excimer in Solution. *Journal of Chemical Education* **1998,** *75* (5), 615.

[18] Zhao, Z.; Chen, S.; Lam, J. W. Y.; Lu, P.; Zhong, Y.; Wong, K. S.; Kwok, H. S.; Tang, B. Z., Creation of highly efficient solid emitter by decorating pyrene core with AIE-active tetraphenylethene peripheries. *Chemical Communications* **2010,** *46* (13), 2221-2223.

[19] Yang, S.; Yin, P.-A.; Li, L.; Peng, Q.; Gu, X.; Gao, G.; You, J.; Tang, B. Z., Crystallization-Induced Reversal from Dark to Bright Excited States for Construction of Solid-Emission-Tunable Squaraines. *Angewandte Chemie International Edition* **2020,** *59* (25), 10136-10142.

[20] Ji, Y.; Peng, Z.; Tong, B.; Shi, J.; Zhi, J.; Dong, Y., Polymorphism-dependent aggregation-induced emission of pyrrolopyrrole-based derivative and its multi-stimuli response behaviors. *Dyes and Pigments* **2017,** *139*, 664-671.

[21] Baba, H.; Nakajima, A.; Aoi, M.; Chihara, K., Fluorescence from the Second Excited Singlet State and Radiationless Processes in Pyrene Vapor. *The Journal of Chemical Physics* **1971,** *55* (5), 2433-2438.

[21] Geldof, P. A.; Rettschnick, R. P. H.; Hoytink, G. J., Fluorescence from the second excited singlets of pyrene and 3,4-benzpyrene. *Chemical Physics Letters* **1969,** *4* (2), 59-61.

[23] Shah, D. R.; Modh, R. P.; Chikhalia, K. H., Privileged s-triazines: structure and pharmacological applications. *Future Medicinal Chemistry* **2014,** *6* (4), 463-477.

[24] Chauhan, K.; Sharma, M.; Shivahare, R.; Debnath, U.; Gupta, S.; Prabhakar, Y. S.; Chauhan, P. M. S., Discovery of Triazine Mimetics As Potent Antileishmanial Agents. *ACS Medicinal Chemistry Letters* **2013,** *4* (11), 1108-1113.

11 Ag(I) and Cu(I) cyclic-triimidazole coordination polymers

11.1Introduction

The fundamental properties of emissive coordination compounds of monovalent coinage d^{10} metals Cu(I) and Ag(I), have been the subject of extensive investigation in view of their possible applications in different fields spanning from OLEDs to biological sensors[1-6]. In particular, Cu(I) coordination compounds have received remarkable attention due to their usually high quantum efficiency, Cu low-cost and natural abundance. Silver(I) compounds, on the other hand, have received much less attention mainly due to their usually high light sensitivity.

d^{10} metal coordination polymers are known to display various structural formats characterized by strikingly different emissive behavior. Among them, the double-stranded stair-step polymeric structure, $\{MXL\}_\infty$ (with M = d^{10} metal, X = Br, I and L = organic ligand), is a quite common motif for Cu(I) compounds[7]. On the other side, very few Ag(I) double-stranded structures have been reported[8] and in only one study the photophysical characterization of the two investigated compounds have been reported[9].

Based on the presence at the vertex of a regular triangle of three nitrogen atoms available for coordination to metal ions, **TT** appears as a useful tecton to prepare coordination compounds and we have decided to test the coordination capability of **TT** in presence of Cu(I) and Ag(I) moieties. From this work, a quite interesting photophysical comparative analysis has been performed on two isostructural Cu(I) and Ag(I) double-stranded stair-step polymers as reported in the following.

11.2 Results and discussion

11.2.1 1D $[Ag(TT)I]_n$, 1-Ag

Crystals of the 1D coordination polymer $[Ag(TT)I]_n$, hereafter **1-Ag**, have been obtained by slow addition of an acetonitrile (CH_3CN) solution of **TT** to a saturated aqueous solution of AgI in KI or to a solution of AgI and KI in *N*,*N*-dimethylformamide (DMF).

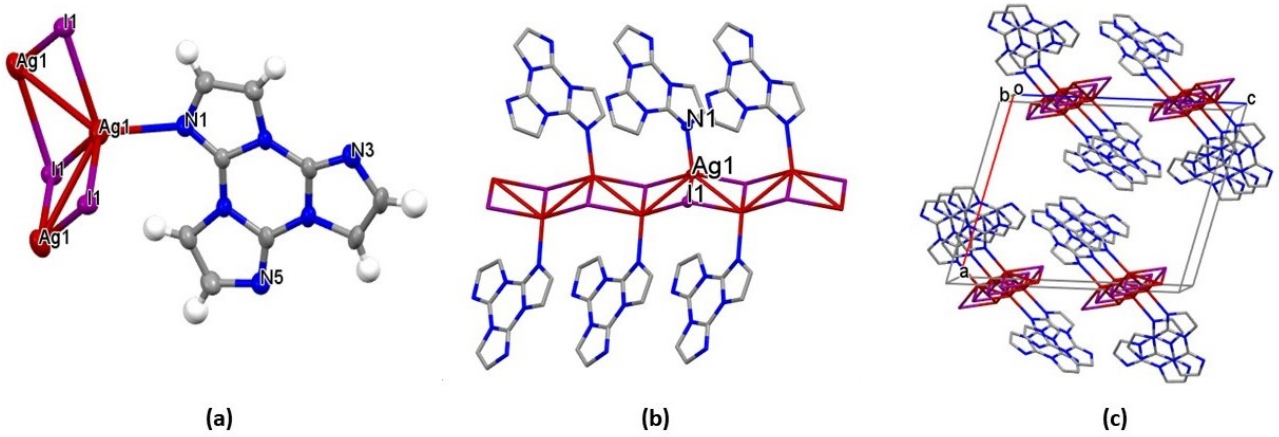

*Figure 1: Crystal structure of **1-Ag.** a)* Ag(I) coordination sphere. b) Stair motif. c) Crystal packing along b axis.

1-Ag crystallizes in the $P2_1/c$ monoclinic spatial group with an asymmetric unit containing one molecule of **TT**, one silver ion and one iodide ion. The silver ion displays a distorted tetrahedral geometry, AgI_3N-like, (Figure 1a) with a **TT** nitrogen and three μ_3-iodine ions which adopt a distorted trigonal pyramidal geometry (Ag-I distances equal to: 2.869, 2.812, 2.936 Å and Ag-N: 2.331 Å; the angles formed around the silver ion are included between 94.35 and 123.35°). The μ_3-iodine ions generate a 1D stair motif $[AgI]_n$ with decorative **TT**

molecules on both sides (Figure 1b). The Ag···Ag distance is 3.192 Å significantly shorter than the sum of the Van der Waals radii (3.44 Å). The **TT** ligand molecules on the two sides of the stairs form stack parallel with distances between the triazinic centroids equal to 4.737 Å (Figure 1c). Columns belonging to the same stairs are almost orthogonal with angles between the mean planes of adjacent ligands of different columns equal to 85.0°. In agreement with the presence of a twofold screw axis along the *b* direction the ligands disposition forms a helical stair motif but adjacent stairs have opposite handedness thus the packing is centrosymmetric (Figure 2).

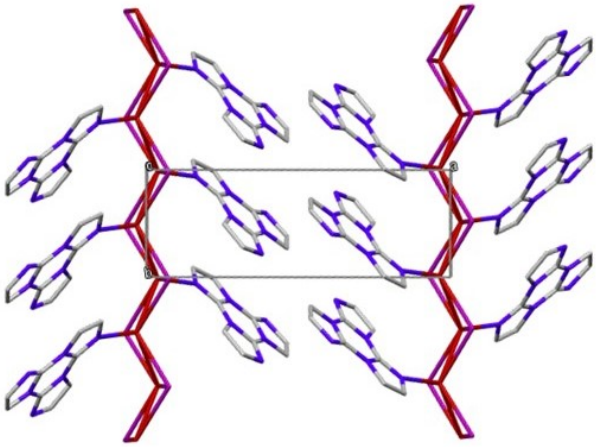

*Figure 2: Portion of the coordination polymer **[Ag(TT)I]**$_n$, the opposite helicity of antiguous stairs is evident.*

Crystals of **1-Ag** at 298 K display an intricate emissive behavior characterized by the concomitant presence of fast and long lived components (overall quantum efficiency, Φ, equal to 19%) with relative intensities varying according to the excitation energy and covering a large portion (from 385 to 700 nm) of the visible spectrum (see Figure 3).

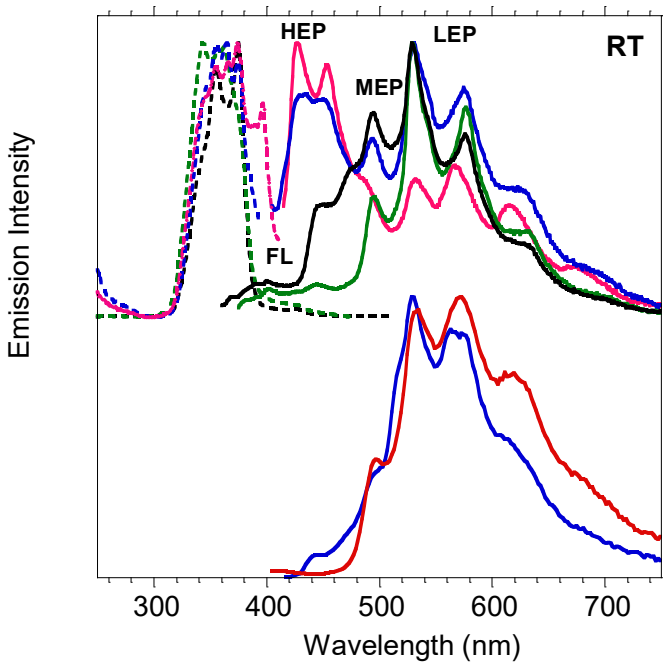

*Figure 3: Normalized emission end excitation spectra of crystals of **1-Ag** at 298 K. Top: PL spectra (solid line) at λ_{exc} = 397 nm (pink line), λ_{exc} = 390 nm (blue line), λ_{exc} = 355 nm (green line), λ_{exc} = 341 nm (black line) and PLE spectra (dotted line) at λ_{em} = 410 nm (blue line), λ_{em} = 430 nm (pink line), λ_{em} = 495 nm (green line), λ_{em} = 530 nm (black line). Bottom: phosphorescence spectra (blue line, delay 200 μs, window 500 μs, λ_{exc} = 360 nm; red line, delay 100 μs, window 500 μs, λ_{exc} = 397 nm).*

A weak high energy fluorescence is observed at about 385 and 400 nm together with three sets of vibrationally resolved long lived components by exciting in the 340-430 nm range: a high energy phosphorescence, HEP (411, 445 nm), in addition to two partially overlaid phosphorescent emissions at lower energy (medium energy phosphorescence, MEP at 446, 476 and 509 nm, and low energy phosphorescence LEP at 494, 530, 575, 620 and 680 nm, τ_{av} = 39.76 ms). The analysis of the emission and excitation spectra has revealed that LEP prevails when crystals are excited in the 350-370 nm range, while the MEP is intensified by exciting at 340 nm. Finally, exciting from 390 to 397 nm the HEP becomes visible and is gradually intensified.

MEP and LEP are visible in time delayed spectra independently by the excitation wavelength (lower panel of Figure 3) while HEP is hardly detectable due to its short lifetime which is too close to the instrument temporal resolution (50 μs).

To deepen the **1-Ag** photophisics additional measurements at 77 K were performed (see Figure 4). The four emissions detected at 298 K are still present though with longer lifetimes and higher vibrational resolution. In particular, the weak fluorescence at 386 and 395 nm is observed together with HEP at 425 and 446 nm, MEP at 440, 470 and 506 nm and LEP at 490, 528, 576, 631 and 701 nm. The relative emissions' intensities are again affected by the excitation wavelength. All components are visible in the spectrum at λ_{exc} =350 nm; MEP is intensified exciting at 340 nm and HEP can be selectively activated by exciting in the 390-397 nm range. In delayed spectra (bottom of Figure 4), HEP contribution is clearly visible thanks to its longer lifetime with respect to 298 K, while the evolution of the spectral shape, observed by recording the emission at different delays, evidences that emission lifetimes increase in the order HEP<MEP<LEP.

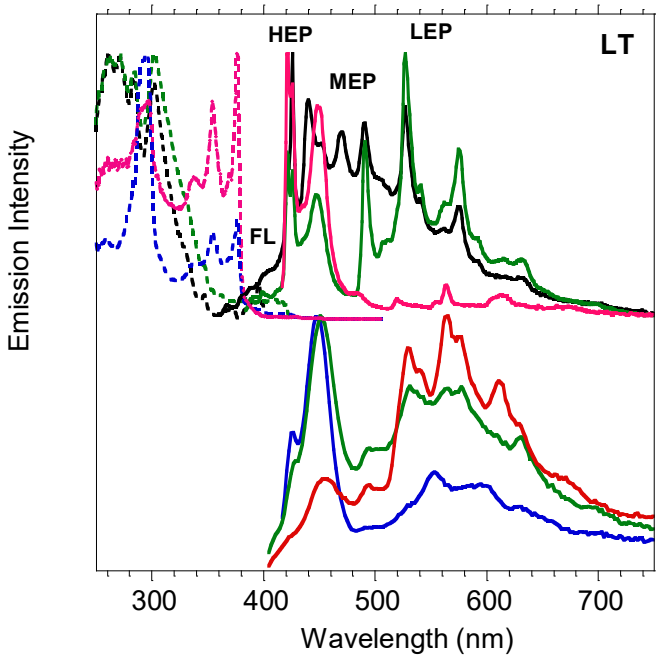

*Figure 4: Normalized emission end excitation spectra of crystals of **1-Ag** at 77 K. Top: PL spectra (solid line) at λ_{exc} = 397 nm (pink line), λ_{exc} = 364 nm (green line), λ_{exc} = 340 nm (black line), and PLE spectra (dotted line) at λ_{em} = 421 nm (black line), λ_{em} = 443 nm (green line), λ_{em} = 527 nm (pink line), λ_{em} = 630 nm (blue line). Bottom: phosphorescence spectra (λ_{exc} = 397 nm; blue line, delay 50 μs, window 100 μs; green line, delay 100 μs, window 500 μs; red line, delay 1 ms, window 5ms).*

Single crystal X-ray diffraction results indicate the arrangement of **TT** molecules into H-aggregates present in the free ligand is maintained in **1-Ag**. This packing motif has been suggested as responsible for the long lived, low energy emission of many members of the **TT**-family [10-15]. In particular, **1-Ag** LEP peaks show a remarkable similarity with the vibrational components of the T_H-S_0 emission of the mono-iodinated (**TTI**) and the co-crystal of **TT** with 1,4-diiodiotetrafluorobenzene (**TTCo**) derivatives at 77 K[12]. This observation is in agreement with the comparable interplanar distance of **TT** units in the three compounds (3.173 Å in **1-Ag,**

3.309 Å in **TTI** and 3.332, 3.488 Å in **TTCo**). Therefore, it is reasonable to assign LEP to deactivation from T_H. Impressively, close inspection of the 77 K emission spectra of **1-Ag**, **TTI** and **TTCo**, reveals the same pattern for the MEP of the former with emission from T_I of the two latter. Such phosphorescence was previously ascribed to the I···N halogen bonding interaction which is present in the structures of **TTI** and **TTCo**, but absent in **1-Ag**. However, based on the similarity in position and shape of the emissions of the three systems, all containing **TT** and I atoms, it seems possible a common origin (T_I-S_0) with a mechanism different from the one previously suggested. Looking at the shorter contacts between adjacent stairs (in **1-Ag**), helices (in **TTI**) and chains (in **TTCo**) involving iodine atom, it is found that the three structures share a comparable I···C distance of 3.664, 3.764 and 3.736 Å compatible with intermolecular electronic coupling of two units with partial orbital overlapping[16].

In agreement with previous findings[13][15] and theoretical calculation, HEP has to be assign to deactivation from a ligand centered triplet state (T_M-S_0, where M stands for "molecular" in order to distinguish its origin from the supramolecular one of LEP and MEP). Furtherly, the ligand centered nature of the T_M-S_0 phosphorescence is supported by the energy spacing (about 1300-1550 cm^{-1}) of its vibrational components which can be associated to a vibronic progression involving imidazole ring modes[17]. Similar values are calculated for the vibrational peaks of MEP and LEP, having themselves a negligible contribution from the metal.

11.2.2 1D $[Cu(TT)I]_n$, 1-Cu

Crystals of the 1D coordination polymer $[Cu(TT)I]_n$, hereafter **1-Cu**, have been obtained by addition of an acetonitrile (CH_3CN) solution of **TT** to a saturated aqueous solution of CuI in KI. After one night at room temperature colorless needle-shaped **1-Cu** crystals are filtered out from the solution. Single crystal X-ray diffraction analysis revealed that **1-Cu** and **1-Ag** are isostructural.

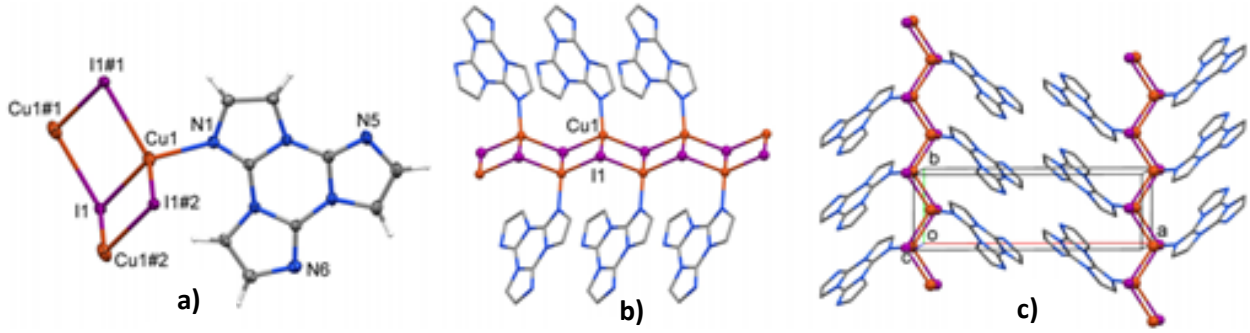

*Figure 5: Crystal structure of **1-Cu**: a) Ag(I) coordination sphere. b) Stair motif. c) Crystal packing along b axis. Reproduced with permission from ref.[1] © 2019, American Chemical Society.*

The 1D double-stranded stair motif of $[CuI]_n$ composition is quite commonly encountered for Cu(I) coordination polymers (Figure 5a). **1-Cu** crystallizes in the monoclinic $P2_1/c$ space group with an asymmetric unit containing one molecule of **TT**, one Cu(I) ion and one iodide ion. The copper ion displays a distorted tetrahedral geometry, CuI_3N-like, where the three μ_3-iodide form a distorted trigonal pyramid (Cu-I distances equal to: 2.611, 2.723, 2.772 Å and Cu-N: 2.028 Å; the angles formed around the copper ion are between 99.16−129.41°). As in the **1-Ag** case, the μ_3-iodine ions generate a 1D stair motif $[CuI]_n$ with decorative **TT** molecules on both sides (Figure 5b). Unlike **1-Ag**, the Cu···Cu distances (3.248 Å) are longer than the sum of the Cu(I) ions van der Waals radii and so no interaction between metal centres can be assumed. The **TT** ligand molecules on the two sides of the stair form stack parallel with a distance of 3.173 Å between their mean planes and a distance of 4.509 Å between triazinic centroids. Columns belonging to the same stairs are almost orthogonal with angles between the mean planes of adjacent ligands of different columns equal to 89.4°. In

agreement with the presence of a twofold screw axis along the *b* direction the ligands disposition forms a helical stair motif but adjacent stairs have opposite handedness thus the packing is centrosymmetric (Figure 5c).

By exciting **1-Cu** crystals in the 300-360 nm region, the emission spectrum is dominated by an intense ^{3}MLCT (T_M-S_0) phosphorescence (τ_{av} = 32 μs) (upper panel figure 6). However, by exciting the sample with longer wavelength (λ_{exc} >390 nm), two less intense vibronically resolved phosphorescences are detected (upper panel of Figure 6). Specifically, at room temperature a lower energy and longer lived (τ_{av} = 302 μs) component, LEP, peaked at 536, 582, 623 nm, impressively overlapped with the **1-Ag** analogue one (the two compounds sharing an identical interplanar **TT** distance equal to 3.173 Å) and a higher energy phosphorescence with peaks at 431, 460 and 487 nm, are collected for **1-Cu** (lower panel figure 6). This latter component in the **1-Ag** analogue lies in-between HEP and MEP. However, at 77 K it has revealed its close similarity with **1-Ag** MEP and since the I···C interstep distance, 3.721 Å, is compatible with intermolecular electronic coupling, it is reasonable to use the same acronym (MEP, T_I-S_0 emission) to refer also to it. Notably, the shorter I···C distance of **1-Ag**, 3.664 Å, can justify its MEP lower energy. In the delayed spectrum at room temperature, only the longer lived LEP is visible (lower panel figure 6).

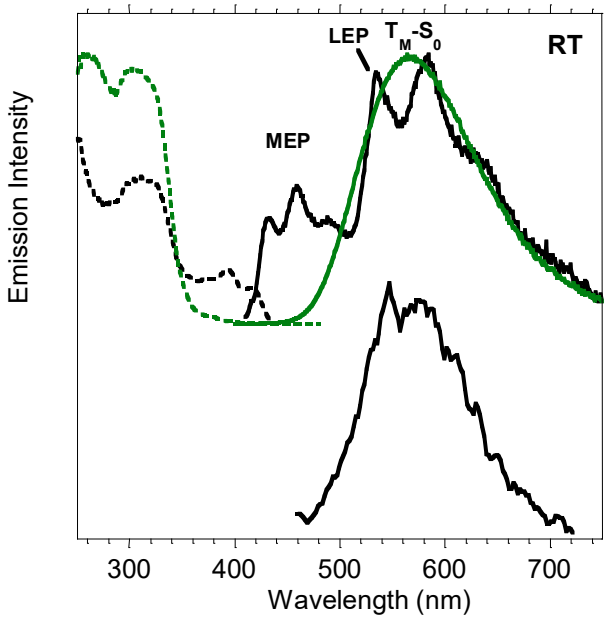

*Figure 6: Normalized emission and excitation spectra of crystals of **1-Cu** at 298 K. Top: PL spectra (solid line) at λ_{exc} = 300 nm (green line), λ_{exc} = 390 nm (black line) and PLE spectra (dotted line) at λ_{em} = 460 nm (black line), λ_{em} = 563 nm (green line). Bottom: phosphorescence spectrum (λ_{exc} = 420 nm; black line, delay 100 μs, window 500 μs).*

The similarity of LEP detected for **1-Cu**, **1-Ag**, **TTI** and **TTCo**, supports its ligand's H-aggregation origin (T_H-S_0) also for the copper derivative. From the comparison between the isostructural **1-Cu** and **1-Ag**, it is clear that the metal plays on LEP a secondary role and can be therefore referred to as an "external" perturber[13]. The same observation can be made for MEP of the two compounds, in agreement with its I···C intermolecular electronic coupling origin. The metal secondary effect results in shorter emission lifetimes for MEP and LEP of **1-Cu** having a lower atomic number.

In the emission spectra collected at 77 K (see Figure 7) the broad band at 568 nm with MLCT character excited at high energy (300-340 nm) is still present together with the structured LEP and MEP (better isolated when exciting between 390-420 nm) (upper panel figure 7). Time delayed experiments have revealed the overlap between the MEP and the LEP, with the latter displaying narrow peaks whose relative intensity varies with

the delay time (lower panel figure 7). The perfect agreement between Ag and Cu LEP and MEP supports their common origins.

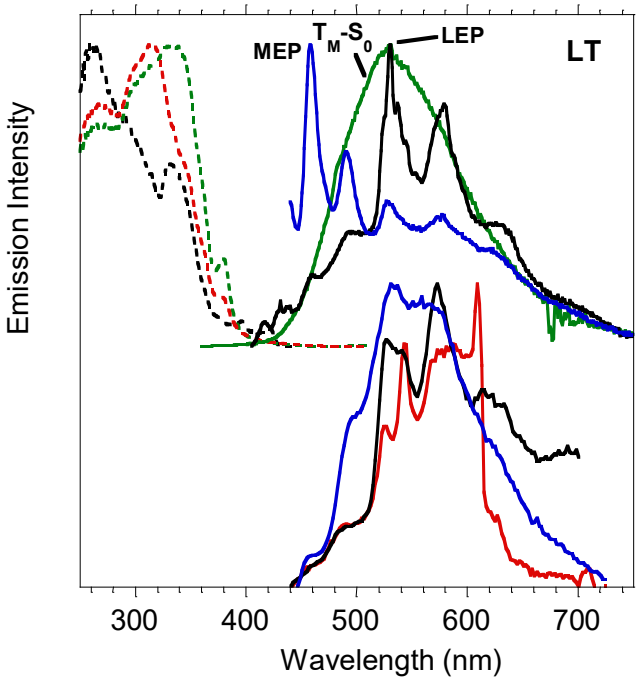

*Figure 7: Normalized emission and excitation spectra of crystals of **1-Cu** at 77 K. Top: PL spectra (solid line) at λ_{exc} = 340 nm (green line), λ_{exc} = 390 nm (black line), λ_{exc} = 420 nm (blue line) and PLE spectra at λ_{em} = 460 nm (black line), λ_{em} = 530 nm (green dashed line) and λ_{em} = 633 nm (red dashed line). Bottom: phosphorescence spectra (λ_{exc} = 420 nm; blue line, delay 100 μs, window 500 μs; black line, delay 1 ms, window 5ms; red line, delay 5 ms, window 10ms).*

DFT and TDDFT calculations have been performed on the $[M(TT)I]_4$ model compounds (M=Ag, Cu) in order to furtherly confirm the intramolecular origin of the emission bands in **1-Ag** and **1-Cu**. It is important to highlight that the geometry optimization of discrete models causes the loss of the symmetry characterizing the $[M(TT)I]_n$ polymeric structure owing to major boundary effects. This could generate an artificial splitting of the electronic excitation levels disallowing a close one-to-one correspondence between computed and observed states. The first singlet level (S_1, Figure 8) computed at 274 (Ag) and 307 nm (Cu), has ^{1}XMCT character with some ^{1}XMLCT contribution, much greater for the Cu compound with respect to the Ag one (Figure 8). According to this, the QTAIM analysis shows a higher covalence degree for the Cu–N bond with respect to the Ag–N one. This result perfectly agrees with the suppression of fluorescence through easy ISC to close triplets, the shorter lifetimes and the importance of the MLCT emission detected for **1-Cu** and that are symptoms of the greater metal contribution on the intramolecular emissive behavior respect to **1-Ag**.

DFT/TDDFT calculations also provide the first triplet levels ($T_1 \div T_4$ and $T_1 \div T_3$ for **1-Ag** and **1-Cu** compounds, respectively) at 324 (Ag) and 329 nm (Cu), with mixed ^{3}LC/^{3}XMLCT character. In addition, a low energy ^{3}XMCT/^{3}XMLCT triplet state (T_4, at about 0.01 eV from $T_1 \div T_3$) is calculated for Cu but it is absent in the Ag model compound. For this latter, pure ^{3}XMCT triplet states are computed at higher energy (T_9, T_{14}), where accessible singlet states are not present preventing the efficient triplets population by ISC.

Accordingly, the observed **1-Ag** HEP emission requires an alternative mechanism to be populated. In particular, it may be either the triplet direct population at low energy or the ISC from S_1. This latter process is facilitated by the presence of triplet states (T_{15} and T_{16}) close to S_1 and having partial σ character deriving from the coordinating nitrogen atoms.

Concerning the broad low energy phosphorescence observed at 568 nm for **1-Cu** when exciting at high energy (about 300 nm), it may be assigned to emission from T_4, which could relax to lower energy than that of $T_1 \div T_3$ states. T_4 can be populated either by IC from higher triplet states having the same character, that are populated by ISC from close high energy singlet states, or by ISC from S_1.

11.3 Conclusions

The detailed photophysical comparative study of **1-Ag** and **1-Cu** has revealed some interesting aspects. The two compounds display excitation dependent photoluminescence. For the Ag(I) derivative the decay paths, all of ligand-centered nature, are simultaneously activated but varied in intensity by changing the excitation energy. On the contrary, **1-Cu** shows non-thermally equilibrated XMLCT and Ligand-centered emissive states.

11.4 References

[1] Lucenti, E.; Cariati, E.; Previtali, A.; Marinotto, D.; Forni, A.; Bold, V.; Kravtsov, V. C.; Fonari, M. S.; Galli, S.; Carlucci, L., Versatility of Cyclic Triimidazole to Assemble 1D, 2D, and 3D Cu(I) Halide Coordination Networks. *Crystal Growth & Design* **2019,** *19* (3), 1567-1575.

[2] Leitl, M. J.; Zink, D. M.; Schinabeck, A.; Baumann, T.; Volz, D.; Yersin, H., Copper(I) Complexes for Thermally Activated Delayed Fluorescence: From Photophysical to Device Properties. *Topics in Current Chemistry* **2016,** *374* (3), 25.

[3] Katsuyuki, S.; Jiyoung, L.; Hiroyuki, T.; Hiroko, N.; Takuma, Y.; Hironori, K.; Chihaya, A., Highly efficient electroluminescence from purely organic donor–acceptor systems. *Pure and Applied Chemistry* **2015,** *87* (7), 627-638.

[4] Cariati, E.; Lucenti, E.; Botta, C.; Giovanella, U.; Marinotto, D.; Righetto, S., Cu(I) hybrid inorganic–organic materials with intriguing stimuli responsive and optoelectronic properties. *Coordination Chemistry Reviews* **2016,** *306*, 566-614.

[5] Kakizoe, D.; Nishikawa, M.; Degawa, T.; Tsubomura, T., Intense blue emission and a reversible hypsochromic shift of luminescence caused by grinding based on silver(i) complexes. *Inorganic Chemistry Frontiers* **2016,** *3* (11), 1381-1387.

[6] Xiang, H.; Cheng, J.; Ma, X.; Zhou, X.; Chruma, J. J., Near-infrared phosphorescence: materials and applications. *Chemical Society Reviews* **2013,** *42* (14), 6128-6185.

[7] Cariati, E.; Lucenti, E.; Botta, C.; Giovanella, U.; Marinotto, D.; Righetto, S., Cu(I) hybrid inorganic–organic materials with intriguing stimuli responsive and optoelectronic properties. *Coordination Chemistry Reviews* **2016,** *306*, 566-614.

[8] Christoph, W.; María Dolores Polo, B.; Ina, D.; Daniel, K.; Peter, G. J., Einfaches System, vielfältige Strukturen: Eine Neuuntersuchung der (Amin)halogenidosilber(I)-Komplexe/ A Simple System with many Structural Variants: A Reexamination of (Amine)halogenidosilver(I) Complexes. *Zeitschrift für Naturforschung B* **2010,** *65* (6), 647-673.

[9] Yang, D.; Xu, W.; Cao, X.; Zheng, S.; He, J.; Ju, Q.; Fang, Z.; Huang, W., Two Silver Coordination Network Compounds with Colorful Photoluminescence. *Inorganic Chemistry* **2016,** *55* (16), 7954-7961.

[10] Lucenti, E.; Forni, A.; Botta, C.; Carlucci, L.; Giannini, C.; Marinotto, D.; Pavanello, A.; Previtali, A.; Righetto, S.; Cariati, E., Cyclic Triimidazole Derivatives: Intriguing Examples of Multiple Emissions and Ultralong Phosphorescence at Room Temperature. *Angewandte Chemie International Edition* **2017,** *56* (51), 16302-16307.

[11] Lucenti, E.; Forni, A.; Botta, C.; Carlucci, L.; Giannini, C.; Marinotto, D.; Previtali, A.; Righetto, S.; Cariati, E., H-Aggregates Granting Crystallization-Induced Emissive Behavior and Ultralong Phosphorescence from a Pure Organic Molecule. *The Journal of Physical Chemistry Letters* **2017,** *8* (8), 1894-1898.

[12] Lucenti, E.; Forni, A.; Botta, C.; Giannini, C.; Malpicci, D.; Marinotto, D.; Previtali, A.; Righetto, S.; Cariati, E., Intrinsic and Extrinsic Heavy-Atom Effects on the Multifaceted Emissive Behavior of Cyclic Triimidazole. *Chemistry – A European Journal* **2019,** *25* (10), 2452-2456.

[13] Previtali, A.; Lucenti, E.; Forni, A.; Mauri, L.; Botta, C.; Giannini, C.; Malpicci, D.; Marinotto, D.; Righetto, S.; Cariati, E., Solid State Room Temperature Dual Phosphorescence from 3-(2-Fluoropyridin-4-yl)triimidazo[1,2-a:1′,2′-c:1″,2″-e][1,3,5]triazine. *Molecules* **2019,** *24* (14), 2552.

[14] Lucenti, E.; Forni, A.; Botta, C.; Carlucci, L.; Colombo, A.; Giannini, C.; Marinotto, D.; Previtali, A.; Righetto, S.; Cariati, E., The Effect of Bromo Substituents on the Multifaceted Emissive and Crystal-Packing Features of Cyclic Triimidazole Derivatives. *ChemPhotoChem* **2018,** *2* (9), 801-805.

[15] Lucenti, E.; Forni, A.; Previtali, A.; Marinotto, D.; Malpicci, D.; Righetto, S.; Giannini, C.; Virgili, T.; Kabacinski, P.; Ganzer, L.; Giovanella, U.; Botta, C.; Cariati, E., Unravelling the intricate photophysical behavior of 3-(pyridin-2-yl)triimidazotriazine AIE and RTP polymorphs. *Chemical Science* **2020,** *11* (29), 7599-7608

[16] Forni, A.; Lucenti, E.; Botta, C.; Cariati, E., Metal free room temperature phosphorescence from molecular self-interactions in the solid state. *Journal of Materials Chemistry C* **2018,** *6* (17), 4603-4626.

[17] Majoube, M.; Henry, M.; Chinsky, L.; Turpin, P. Y., Preresonance Raman spectra for imidazole and imidazolium ion: interpretation of the intensity enhancement from a precise assignment of normal modes. *Chemical Physics* **1993,** *169* (2), 231-241.

12 Procedures and methods.

12.1 General information

All reagents and model molecules were purchased from chemical suppliers and used without further purification unless otherwise stated.

^{1}H, ^{13}C and ^{15}N NMR spectra were recorded on a Bruker AVANCE-400 instrument (400 MHz). Chemical shifts are reported in parts per million (ppm) and are referenced to the residual solvent peak (DMSO, ^{1}H 2.50 ppm, ^{13}C 39.50 ppm) and to the NH_3 for ^{15}N resonances. Coupling constants (J) are given in hertz (Hz) and are quoted to the nearest 0.5 Hz. Peak multiplicities are described in the following way: s, singlet; d, doublet; t. triplet; m, multiplet.

Mass spectra were recorded on a Thermo Fisher LCQ Fleet Ion Trap Mass Spectrometer equipped with UltiMate™ 3000 HPLC system.

UV-Visible spectra were collected by a Shimadzu UV3600 spectrophotometer.

Photoluminescence quantum yields were measured using a C11347 Quantaurus–Absolute Photoluminescence Quantum Yield Spectrometer (Hamamatsu Photonics K.K), equipped with a 150 W Xenon lamp, an integrating sphere and a multichannel detector.

Steady state emission and excitation spectra and photoluminescence lifetimes were obtained using both a FLS 980 (Edinburg Instrument Ltd) and a Nanolog (Horiba Scientific) spectrofluorimeter composed of an iH320 spectrograph equipped with a Synapse QExtra charge-coupled device. The steady state measurements were recorded by excitation with a monochromated 450 W Xenon arc lamp and the spectra are corrected for the instrument response. Phosphorescence spectra are obtained with a PPD-850 single photon detector module with time-gated separation by exciting with a pulsed Xe lamp. Photoluminescence lifetime measurements were performed using: Edinburgh Picosecond Pulsed Diode Laser EPL-375, EPLED-300, (Edinburg Instrument Ltd) and microsecond flash Xe-lamp (60W, 0.1÷100 Hz) with data acquisition devices time correlated single-photon counting (TCSPC) and multi-channel scaling (MCS) methods, respectively. Nanolog TCSPC measurements are performed using DeltaTime series DD-300 DeltaDiode and a DD-405L DeltaDiode Laser, with a PPD-850 single photon detector module and are analysed with the instrument software DAS6. Average lifetimes are obtained as $\tau_{av} = \sum \frac{A_i \tau_i^2}{A_i \tau_i}$ from bi-exponential or three-exponential fits. Low temperature measurements are performed by immersion of the sample in a LN_2 quartz dewar or with a variable temperature liquid nitrogen cryostat Oxford DN1704.

Microscopy fluorescence images were collected with a Nikon Eclipse TE2000-U inverted confocal microscope by exciting with a 100 W Hg lamp with a 330–380 nm band-pass excitation filter.

X-ray data were collected on a Bruker Apex II diffractometer using MoKα radiation. The structures were solved using direct methods and refined using a full-matrix least squares procedure based on F^2 using all data. Hydrogen atoms were placed at geometrically estimated positions.

DFT and TDDFT calculations were performed with Gaussian 16 program (Revision A.03) using the 6-311++G(d,p) basis set. The geometries have been optimized starting from the experimental structures as derived from X-ray studies.

Ultrafast pump-probe measurements exciting at 290 nm were carried out on a pump-probe setup fed by a Ti:sapphire laser (780-nm central wavelength, 100-fs pulses, 1-kHz repetition rate; Libra, Coherent). A fraction of the fundamental wavelength (FW) pulse was used to seed a home-built visible non-collinear optical parametric amplifier (NOPA). The broadband output centered at 580 nm was up-converted by second-harmonic generation in a 20-µm-thick BBO crystal, providing sub-20-fs pump pulses in the UV range (290

nm). The fluence used was of ~ 0.7 mJ/cm^2 on the sample. The probe pulses were obtained by focusing a ~1µJ fraction of the FW onto a 3-mm-thick calcium fluoride plate. Through white-light continuum generation we obtained a broadband probe pulse in the range between 320 and 650 nm. The transmitted probe beam was dispersed in a spectrometer (SP2300 Acton, Princeton Instruments) and detected using a linear image sensor driven and read out by a custom-built board (Stresing Entwicklungsbüro, Berlin, Germany).

Ultrafast pump-probe measurements exciting at 390 nm were carried out on a pump-probe setup fed by a Ti:sapphire regenerative amplifier (780-nm central wavelength, 100-fs pulses, 2-kHz repetition rate; Libra, Coherent). As excitation pulses, the second harmonic of the FW has been used (λ = 390 nm). The excitation density was kept ~ 9 mJ/cm^2 on the sample. White light generated with a 2 mm-thick sapphire plate was used as a probe in the visible-near infrared range from 450 to 750 nm. For a spectrally-resolved detection of the probe light, spectrographs and CCD arrays were used. The chirp in the white light pulse was taken into account during the analysis and evaluation of the two-dimensional (wavelength and time) ΔT/T maps before extraction of the spectral and temporal data using homemade software. Overall, a temporal resolution of at least 100 fs was achieved for all excitation wavelengths.

12.2 Triimidazo[1,2-*a*:1',2'-*c*:1'',2''-*e*][1,3,5]triazine (Cyclic Triimidazole or TT)

12.2.1 Synthesis

Cyclic riimidazole (**TT**) is prepared starting from Copper(II) bisimidazolate by using the synthesis proposed by Schubert and coworkers [1]. In a 3 L two-necked flask equipped with a condenser, a solution of 70.23 g of imidazole (1.03 mol) and 180.15 g of NaHCO3 (2.14 mol) in 1L of H_2O was heated at reflux for 3 h. To this solution $CuSO_4 \cdot 5H_2O$ (61.23 g, 0.24 mol) dissolved in 200 mL of H_2O was added dropwise under vigorous stirring. The formation of a violet precipitate is immediately observed. By leaving the mixture under reaction conditions, the violet compound is gradually transformed into the blue polymorph of $Cu(im)_2$. After 5 h the blue compound is filtered off, washed with water, and dried at 110°C overnight in an oven[2].

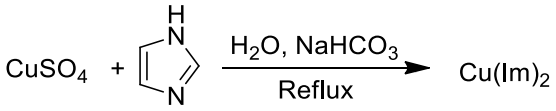

Figure 1: Synthetic pathway for Cu(im)$_2$.

A 1 L round-bottom flask was charged with the blue polymorph of Cu(im)$_2$ (100.61 g, 0.51 mol). The flask is then connected through an L-shaped glass connection, to a 50 cm long glass tube equipped with a vacuum adapter. The system under vacuum (10^{-2} Torr) was heated with a surrounding heating mantle to 200 °C. The temperature was then slowly increased to 300 °C over ca. 3 h and maintained in vacuo for another 4 h at 300 °C. A progressive formation of a white sublimate in the glass tube was observed along the reaction time. After cooling, 28.23 g of crude organic products containing **TT**, its isomer **ISO-A** which is the product showing a 1,5- instead of 1,2-annelation in one imidazole ring and imidazole, are collected by using a heat gun. The crude is than crystallized from hot toluene (150 mL) to separate the imidazole crystals from the desired product which remains in the toluene solution. After evaporation 6.87 g of crude triimidazole are obtained, after semiautomatic direct chromatography with DCM/MeOH mixture 4.32 g of pure **TT** are collected.

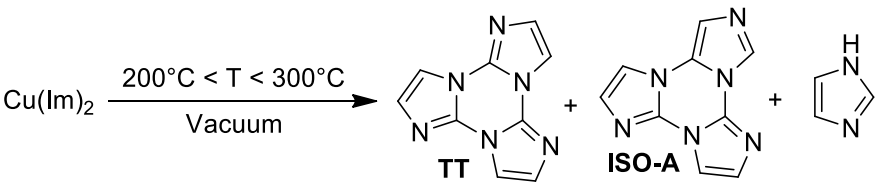

*Figure 2: Synthetic pathway for **TT**.*

^{13}C NMR (400 MHz, DMSO-d_6, 298 K, δ, ppm) 136.12, 129.61, 127.68, 113.04, 111.04.
^{1}H NMR (400 MHz, DMSO-d_6, 298 K, δ, ppm) 7.96 (3H, d, J= 1.6 Hz), 7.28 (3H, d, J= 1.6 Hz).

12.2.2 ^{1}H NMR

400 MHz, DMSO-d_6, 298 K

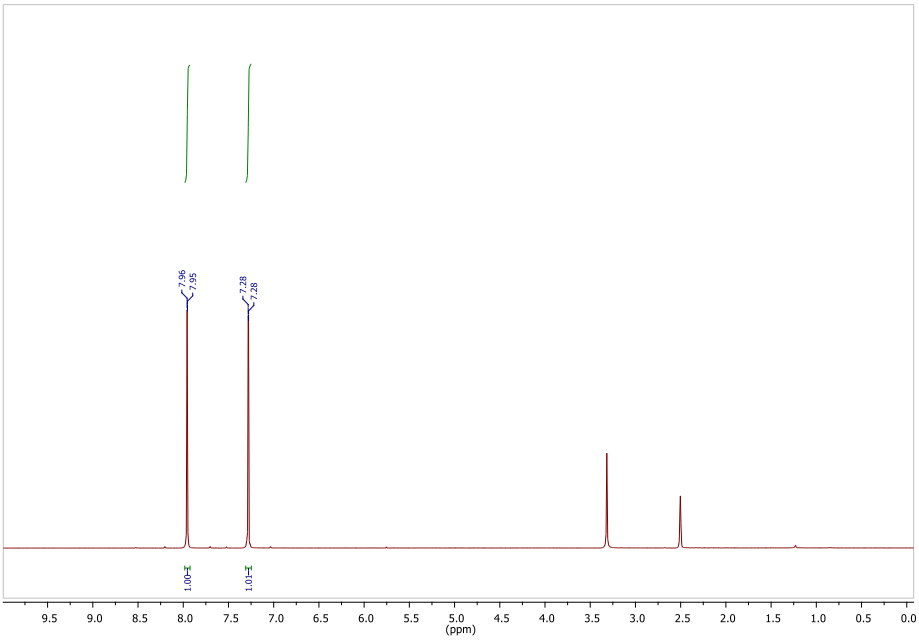

400 MHz, DMSO-d_6, 298 K, expanded region

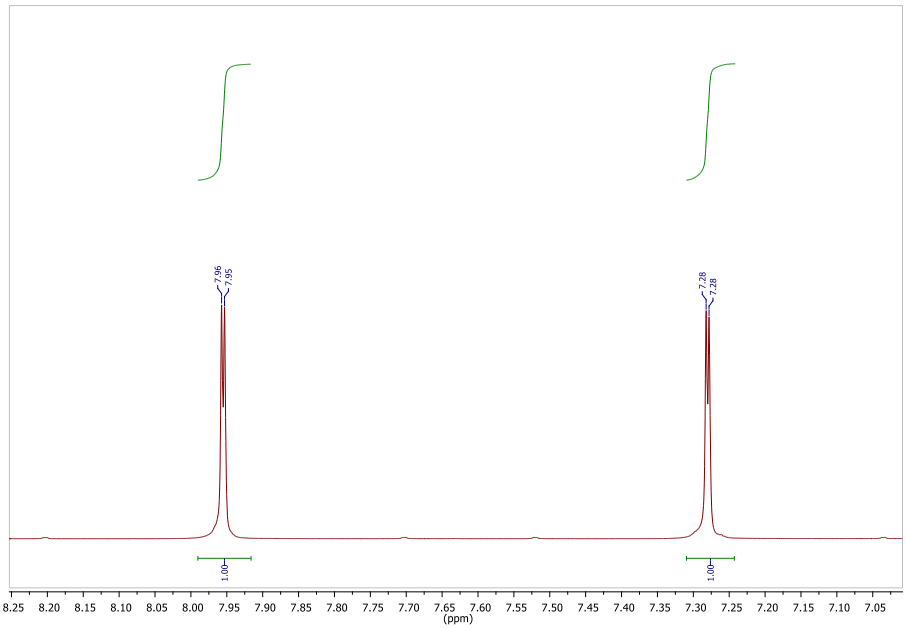

12.2.3 ^{13}C NMR

100 MHz, DMSO-d_6, 298 K

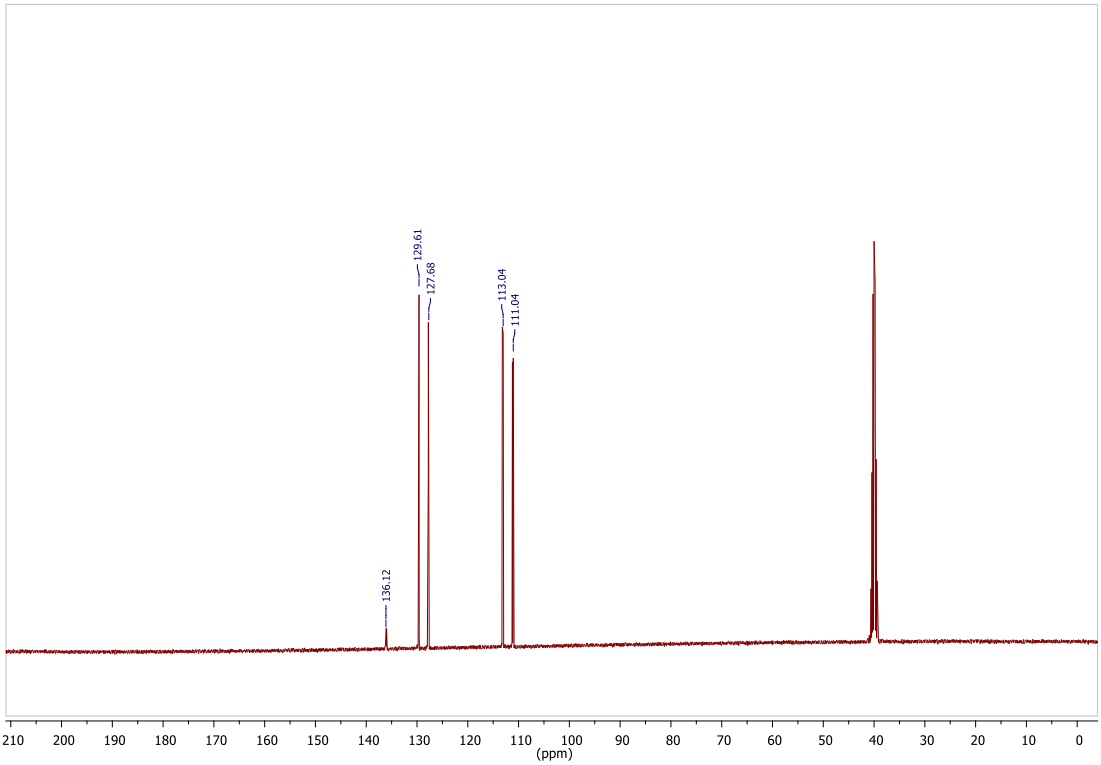

12.2.4 XRDP

TT simulated pattern calculated from crystal structure data (Refcode OSEXEQ) (black line); experimental collected on gently ground single crystals (red line).

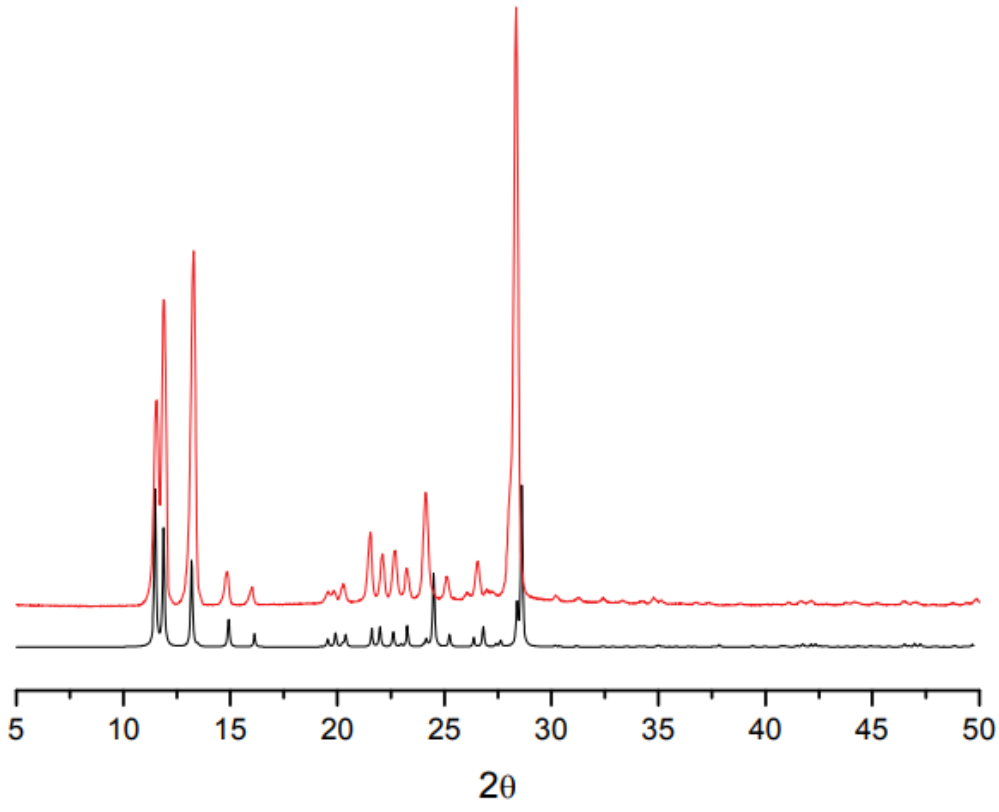

12.3 Brominated derivatives: 3-bromotriimidazo[1,2-*a*:1',2'-*c*:1'',2''-*e*][1,3,5]triazine or TT1Br, 3,7-dibromotriimidazo[1,2-*a*:1',2'-*c*:1'',2''-*e*][1,3,5]triazine or TT2Br, 3,7,11-tribromotriimidazo[1,2-*a*:1',2'-*c*:1'',2''-*e*][1,3,5]triazine or TT3Br

12.3.1 TT1Br and TT2Br Synthesis

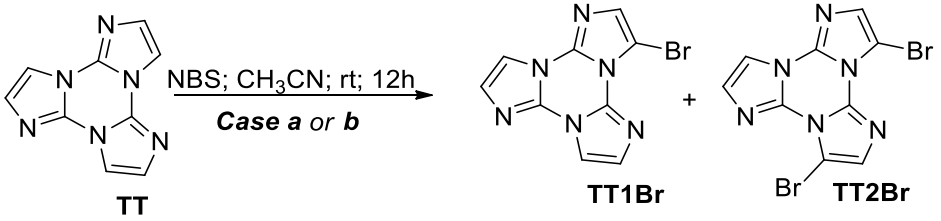

*Figure 3: Synthetic pathway for **TT1Br** and **TT2Br**.*

TT1Br and **TT2Br** are prepared by bromination of cyclic triimidazole with *N*-Bromosuccinimide (NBS) in acetonitrile [3]. In a typical reaction, in a one-necked flask with a magnetic stirrer 50 mg (0.252 mmol) of cyclic triimidazole are dissolved in CH_3CN (10mL) at room temperature. A solution of NBS in CH_3CN (10mg/mL) is then slowly added in 30 minutes (*case a*: 1 eq. of NBS, *case b*: 2 eq. of NBS). The reaction is stirred for 12 hours until all cyclic triimidazole reacted to form a mixture of products, as revealed by thin layer chromatography (CH_2Cl_2: MeOH=98:2; R_f = 0.22 for **TT1Br**; R_f = 0.50 for **TT2Br**). To facilitate the precipitation of the products and remove succinimide, 30 mL of water are added in the flask and the mixture is concentrated using a rotary evaporator system. The white precipitated is filtered on a Buchner and dried at 110°C for 1h.

The crude product is purified by gravimetric column chromatography on SiO_2 with gradient elution. *Case a*: gradient from CH_2Cl_2:MeOH = 99:1 to CH_2Cl_2:MeOH = 98:2; yield of **TT1Br** = 85%; yield of **TT2Br** = 5%. *Case b*: gradient from CH_2Cl_2:MeOH = 99.5:0.5 to CH_2Cl_2:MeOH = 98.5:1.5; yield of **TT1Br** = 57%; yield of **TT2Br** = 40%. Both **TT1Br** and **TT2Br** were crystallized from hot CH_3CN/H_2O solutions.

TT1Br ^{1}H NMR (400 MHz, DMSO-d_6, 298 K, δ, ppm): 7.99 (1H, d, J= 1.6 Hz), 7.93 (1H, d, J= 1.7 Hz), 7.37 (1H, s), 7.32 (1H, d, J= 1.6 Hz), 7.27 (1H, d, J= 1.7 Hz).

TT1Br ^{13}C NMR (100 MHz, DMSO-d_6, 298 K, δ, ppm): 136.8 (Cq), 136.1 (Cq), 135.7 (Cq), 129.5 (CH), 128.8 (CH), 128.6 (CH), 112.0 (CH), 111.9 (CH), 95.5 (CBr)

TT1Br MS (ESI-positive ion mode): m/z 277.1 $[M+H]^+$

TT2Br ^{1}H NMR (400 MHz, DMSO-d_6, 298 K, δ, ppm): 7.97 (1H, d, J= 1.6 Hz), 7.41(1H, s), 7.36 (1H, s), 7.31 (1H, d, J= 1.6 Hz).

TT2Br ^{13}C NMR (100 MHz, DMSO-d_6, 298 K, δ, ppm): 136.7 (Cq), 136.4 (Cq), 135.7 (Cq), 129.7 (CH), 129.4 (CH), 128.7 (CH), 111.7 (CH), 95.8 (CBr), 95.4 (CBr)

TT2Br MS (ESI-positive ion mode): m/z 357.1 $[M+H]^+$

12.3.2 ^{1}H NMR TT1Br

400 MHz, DMSO-d_6, 298 K

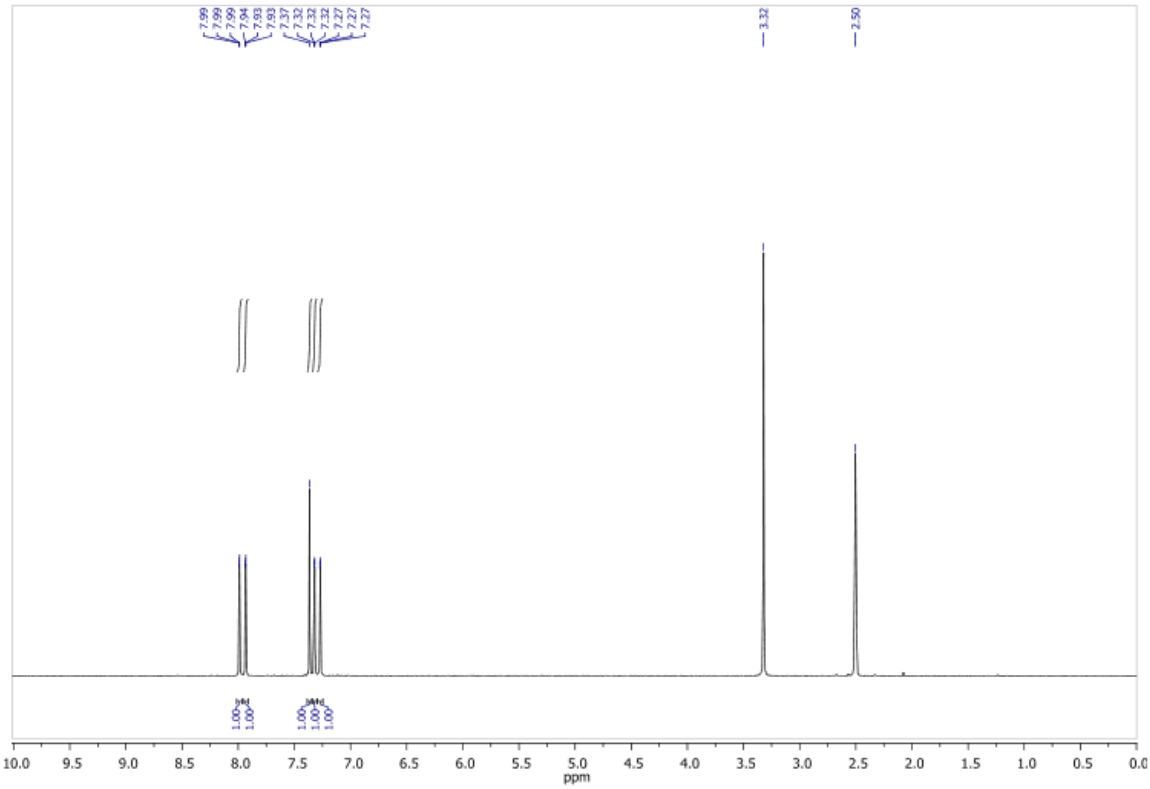

400 MHz, DMSO-d_6, 298 K, expanded region

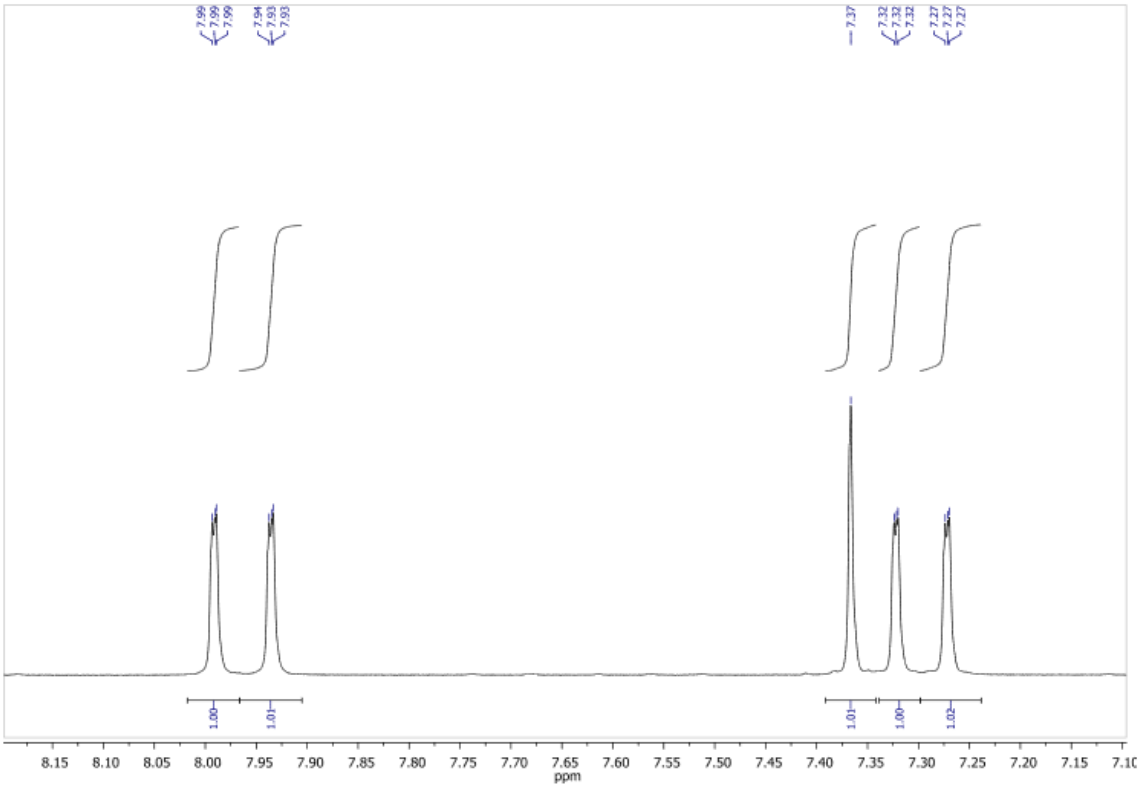

12.3.3 ^{1}H NMR TT2Br

400 MHz, DMSO-d_6, 298 K

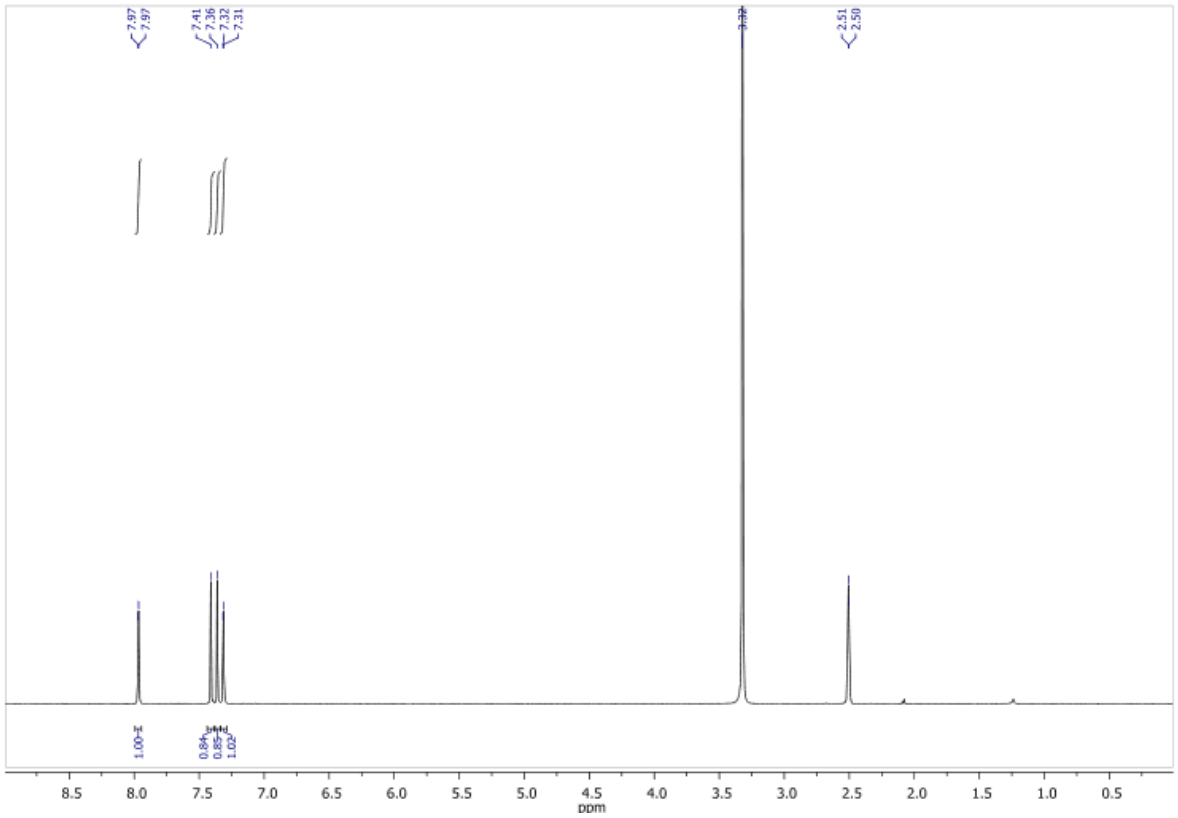

400 MHz, DMSO-d_6, 298 K, expanded region

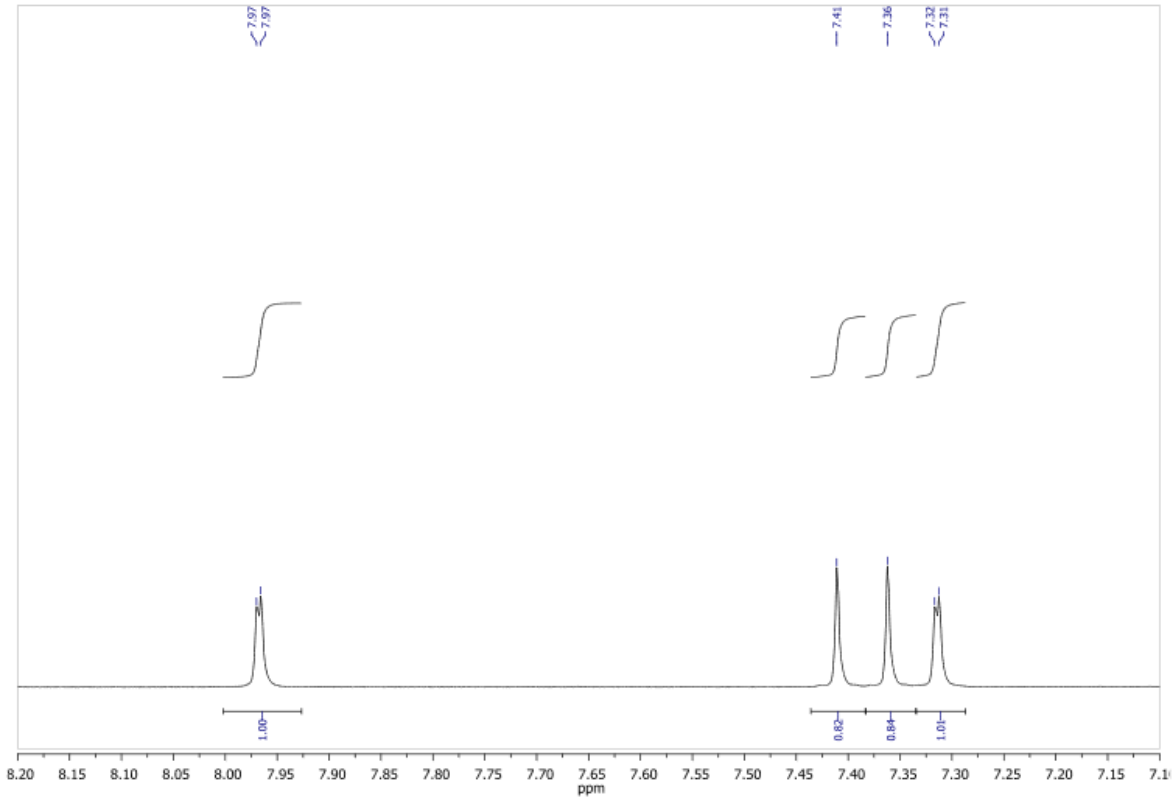

12.3.4 ^{13}C NMR TT1Br

100 MHz, DMSO-d_6, 298 K

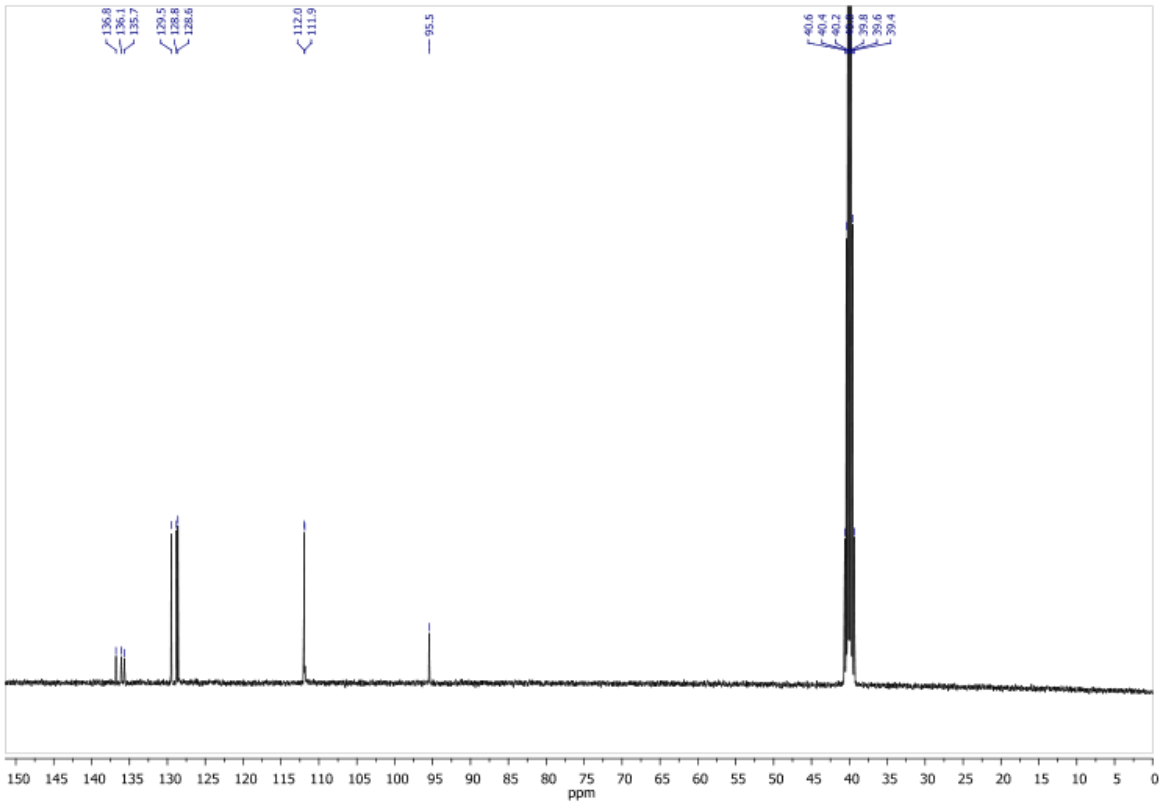

100 MHz, DMSO-d_6, 298 K, expanded region

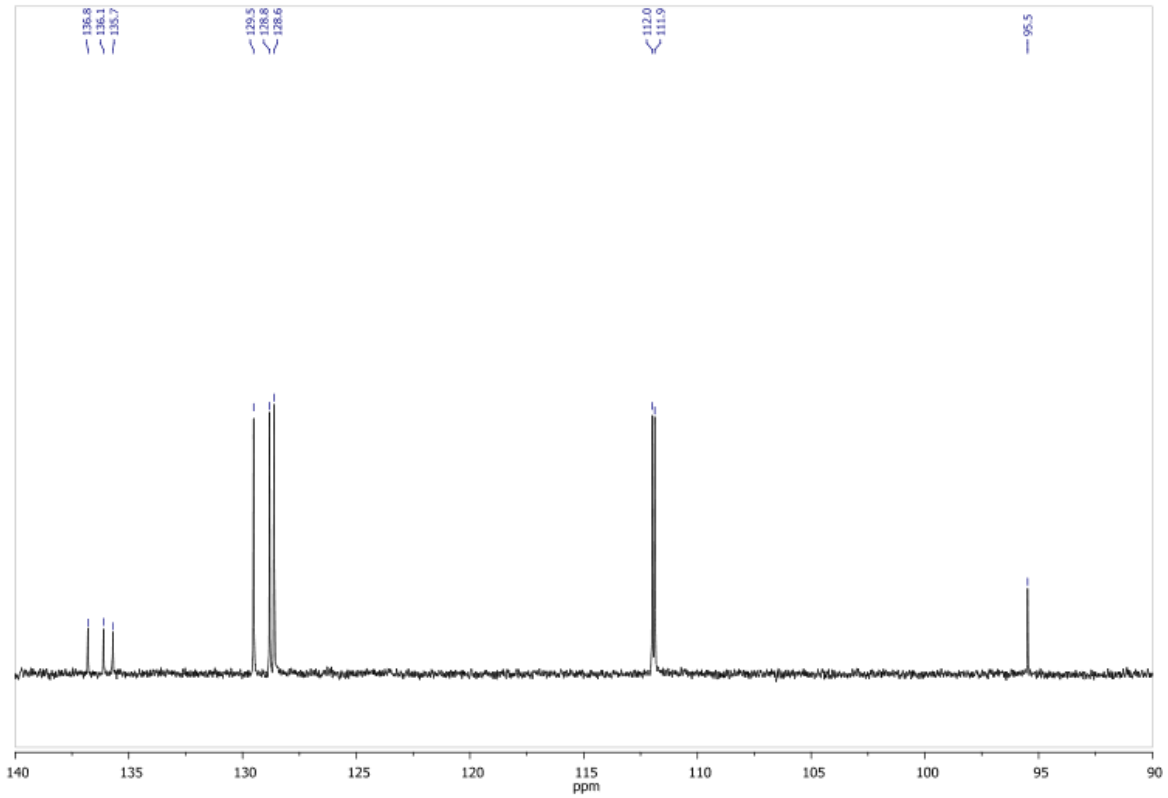

12.3.5 ^{13}C NMR TT2Br

100 MHz, DMSO-d_6, 298 K

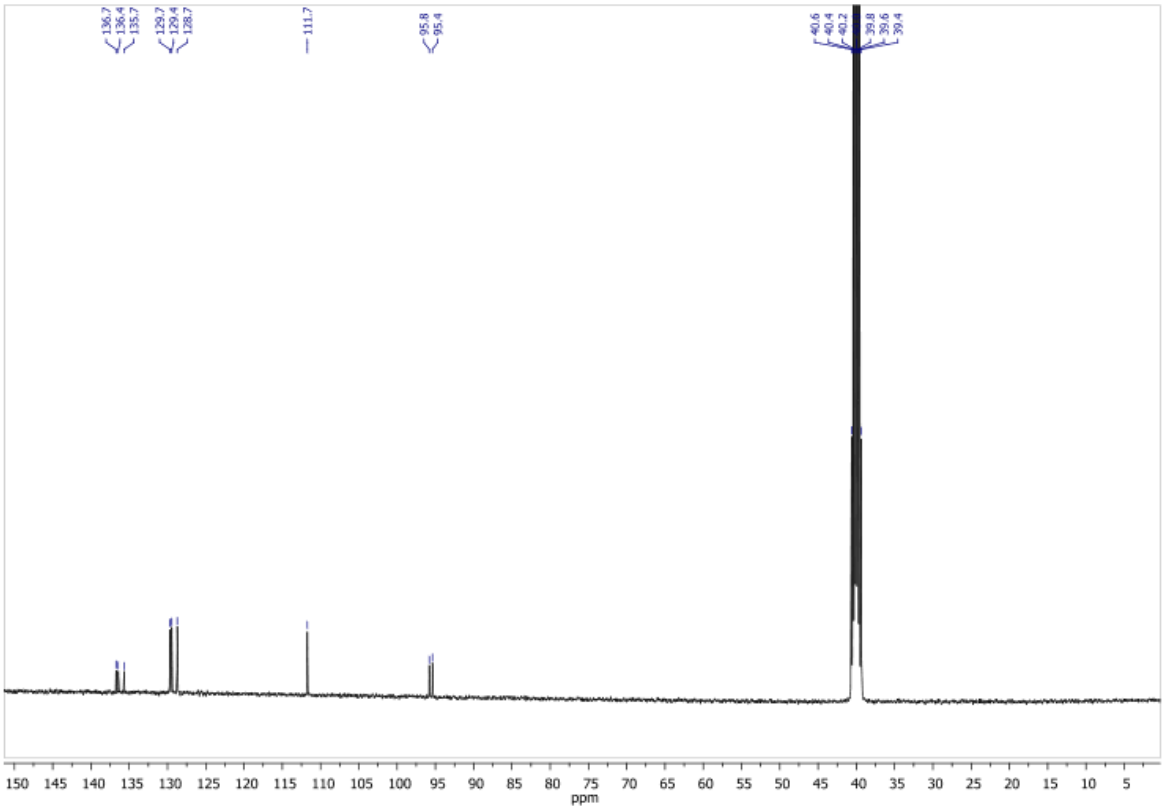

100 MHz, DMSO-d_6, 298 K, expanded region

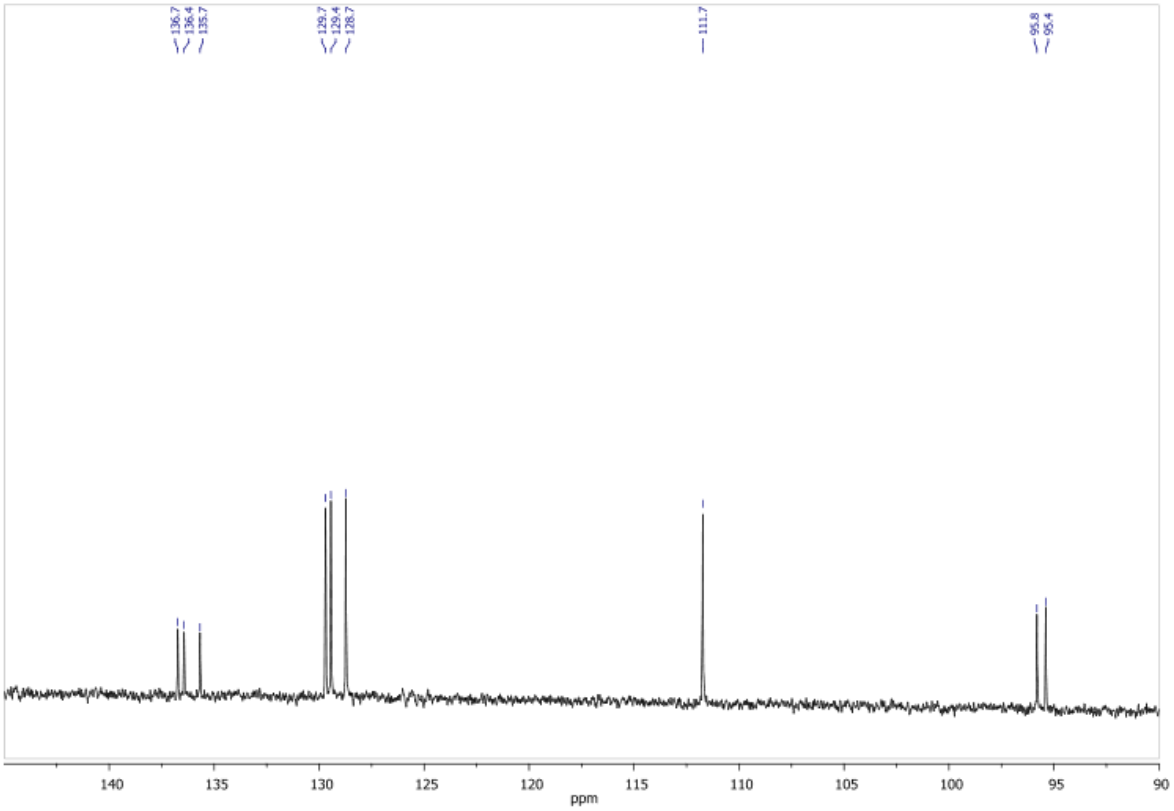

12.3.6TT3Br Synthesis

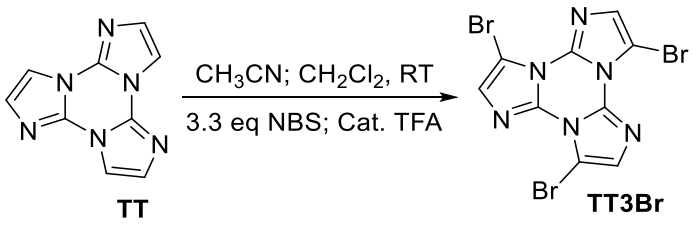

*Figure 4: Synthetic pathway for **TT3Br**.*

TT3Br is prepared by polybromination of cyclic triimidazole with *N*-Bromosuccinimide (NBS) in acetonitrile/dichloromethane mixture and acid condition [4]. In a 250mL one-necked flask with a magnetic stirrer, cyclic triimidazole (240 mg, 1.21 mmol, 1 eq) is dissolved in 30mL of CH_2Cl_2 and added with few drops of trifluoroacetic acid (TFA). To this flask, a solution of NBS (703 mg, 3.94 mmol, 3.3 eq) in CH_3CN (30 mL) is slowly added through a dropping funnel. The reaction is stirred overnight at room temperature and checked by TLC (2% MeOH in CH_2Cl_2 R_f = 0.70) to verify the complete disappearance of the starting material. The reaction is added with 10 mL of acetone and the solution was evaporated to obtain a white solid. The crude product was suspended in water and added with a dilute solution of NaOH up to neutrality. The white powder obtained was filtered on a Buchner and washed thoroughly with water to give 470 mg of pure product (yield 90%). The spectroscopical characterization was performed on samples which were further purified by column chromatography on silica gel (0.5% MeOH in CH_2Cl_2) and crystallization from hot CH_3CN.

^{1}H NMR (400 MHz, DMSO-d_6, 298 K, δ, ppm): 7.41 (3H, s).

^{13}C NMR (100 MHz, DMSO-d_6, 298 K, δ, ppm): 36.4 (Cq), 129.6 (CH), 95.7 (CBr)

TT3Br MS (ESI-positive ion mode): m/z 437.0 $[M+H]^+$

12.3.7 ^{1}H NMR TT3Br

400 MHz, DMSO-d_6, 298 K

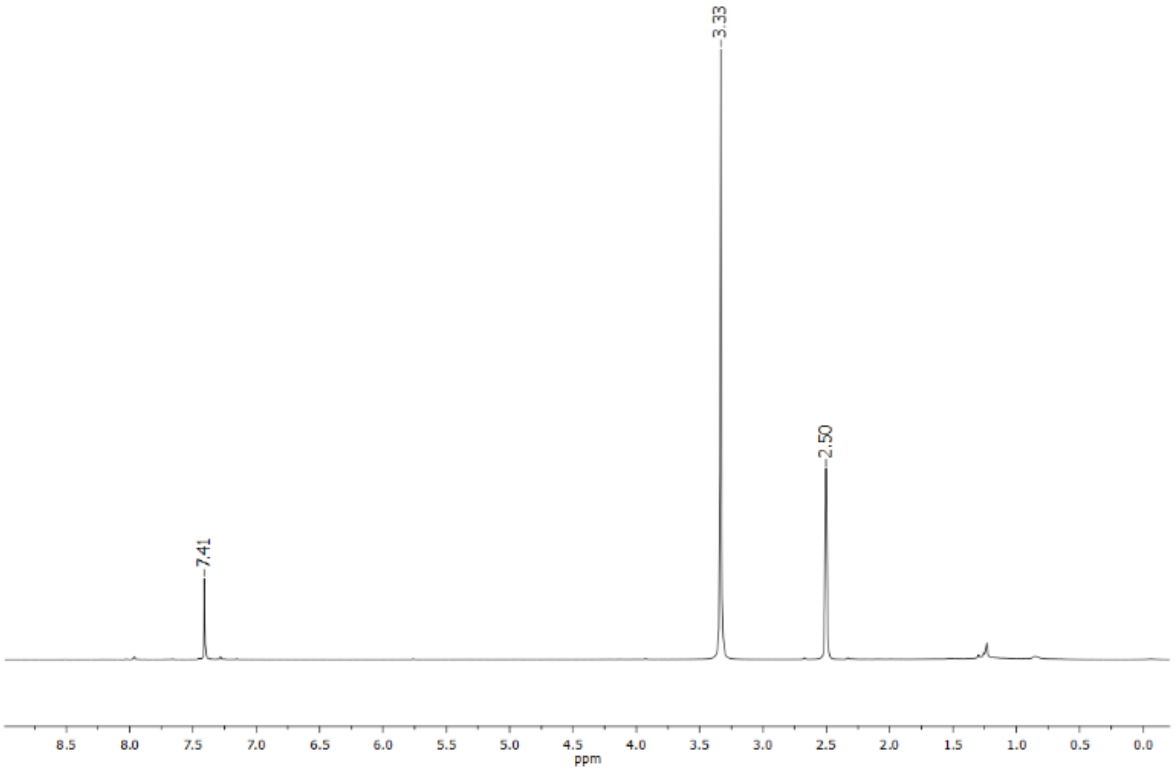

12.3.8 ^{13}C NMR TT3Br

100 MHz, DMSO-d_6, 298 K

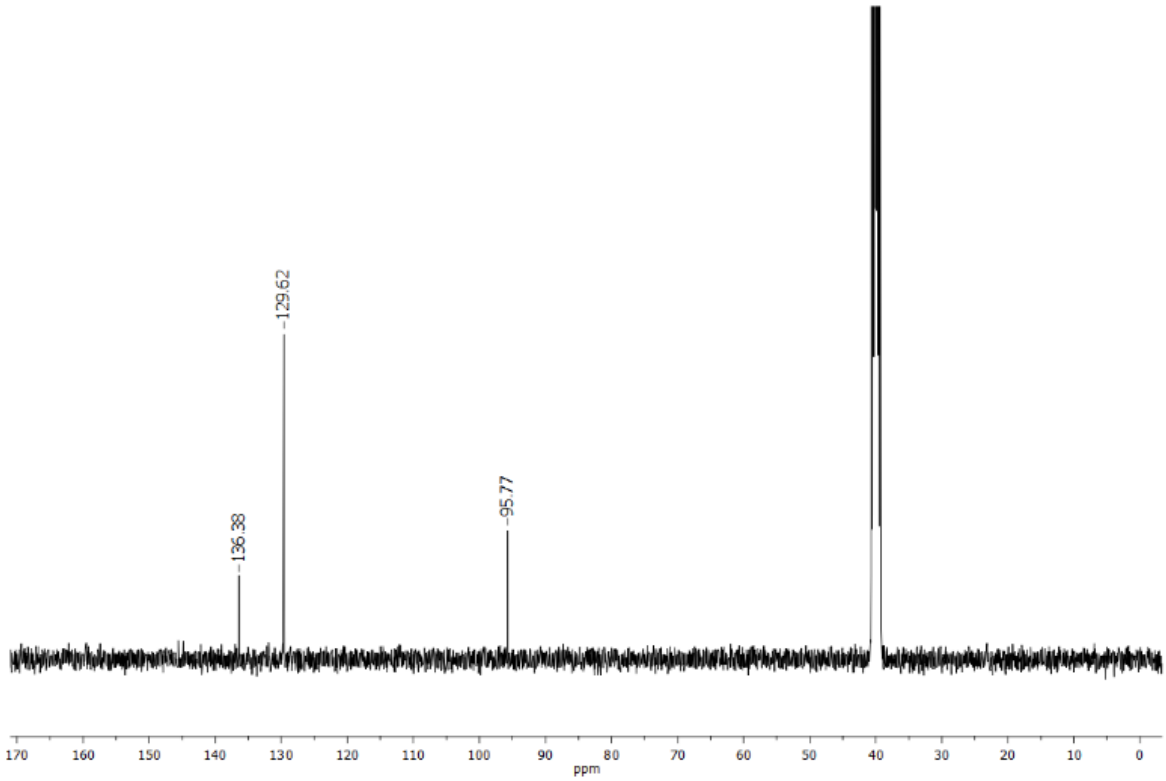

12.3.9 Crystallographic data

Compound	**TT1Br**	**TT2Br**	**TT3Br**
Chemical Formula	$C_9H_5BrN_6$	$2(C_9H_4Br_2N_6)$	$C_9H_3Br_3N_6$
Molecular weight	227.1	712.00	434.9
T(K)	293	293	293
Crystal system	Monoclinic	Triclinic	Monoclinic
Space group	$P2_1/c$	P-1	$P2_1/c$
a(Å)	12.1058	4.0675	7.6660
b(Å)	4.8458	15.7518	15.8580
c(Å)	16.6537	16.4084	19.1990
α(°)	90	99.9610	90
β(°)	101.264	94.4490	90.400
γ(°)	90	91.4050	90
V(Å^3)	985.13	1 029.87	2333.9
Z	4	2	8
Dcalcd (g cm^{-3})	1.921	2.296	2.475
μ (mm^{-1})	4.268	7.855	10.360
Crystal size (mm)	0.55 x 0.02 x 0.02	0.5 x 0.08 x 0.06	0.40 x 0.24 x0.04
2θmax (°)	63.8	63.2	63.5

No. of measured, independent and observed [I >2σ(I)] reflections	18528/3145/2231	24402/6440/2231	51490/7358/5522
(R_{int})/ (R_σ)	0.0466/0.0372	0.0236/0.0228	0.0494/0.0347
data/restraints/params	3145/0/145	6440/0/307	7358/0/325
R[F^2> 2σ(F^2)], wR(F^2), S	0.0375, 0.0899, 1.015	0.0283, 0.0701, 1.032	0.0690, 0.1695, 1.183
Δρmax, Δρmin (e Å^{-3})	0.79, -0.33	0.64, -0.46	1.987, -1.033

12.4 3-iodotriimidazo[1,2-*a*:1',2'-*c*:1'',2''-*e*][1,3,5]triazine or TT1I, 3,7-diiodotriimidazo[1,2-*a*:1',2'-*c*:1'',2''-*e*][1,3,5]triazine or TT2I and Triimidazale/Diiodotetrafluorobenzene or TTCo.

12.4.1 TT1I synthesis

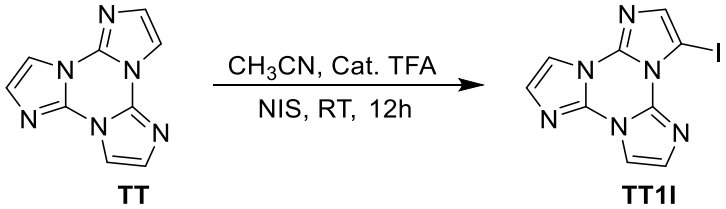

*Figure 5: Synthetic pathway for **TT1I.***

TT1I was prepared by iodination of cyclic triimidazole with *N*-Iodosuccinimide (NIS) and catalytic trifluoroacetic acid (TFA) in acetonitrile [5]. In a typical reaction, in a 100 mL one-necked flask with a magnetic stirrer, 100 mg (0.505 mmol) of **TT** were dissolved in CH_3CN (30 mL) at room temperature and few drops of TFA were added to the solution. A solution of NIS (116 mg, 0.515 mmol) in CH_3CN (30 mL) was then slowly added through a dropping funnel in 15 minutes. The reaction was stirred at room temperature for 12 hours and checked by TLC (CH_2Cl_2:MeOH = 98:2; R_f= 0.33 for **TT1I**). Then the reaction mixture was quenched with 10 mL of acetone and the solvent was evaporated to dryness. The crude product was purified by gravimetric column chromatography on SiO_2 with CH_2Cl_2 and MeOH as eluent. After crystallization from H_2O/CH_3CN (1:1) pure **TT1I** was isolated in 55% yield (90 mg, 0.278 mmol).

^{1}H NMR (400 MHz, DMSO-d_6, 298 K, δ, ppm): 7.94 (1H, d, J= 1.5 Hz), 7.89 (1H, d, J= 1.5 Hz), 7.34 (1H, s), 7.32 (1H, d, J= 1.5 Hz), 7.24 (1H, d, J= 1.5 Hz).

^{13}C NMR (100 MHz, DMSO-d_6, 298 K, δ, ppm): 137.5 (Cq), 135.9 (CH), 135.6 (Cq), 135.5 (Cq), 128.1 (CH), 128.0 (CH), 111.5 (CH), 111.4 (CH), 60.9 (CI).

MS (ESI-positive ion mode): m/z 325.1 $[M+H]^+$

12.4.2 TT2I synthesis

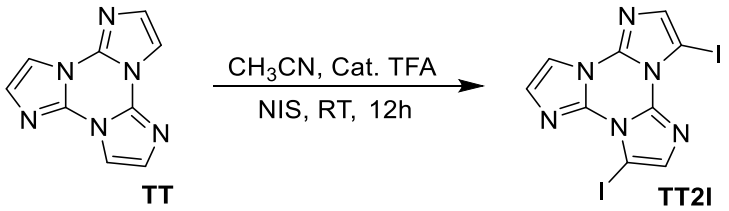

*Figure 6: Synthetic pathway for **TT2I.***

TT2I is prepared by iodination of cyclic triimidazole with N-Iodosuccinimide (NIS) and catalytic trifluoroacetic acid (TFA)in acetonitrile [5]. In a typical reaction, in a 250 mL one-necked flask with a magnetic stirrer, 300 mg (1.514 mmol) of **TT** is dissolved in CH_3CN (60 mL) at room temperature and few drops of TFA are added to the solution. A solution of NIS (760 mg, 2.206 mmol) in CH_3CN (60mL) is then slowly added through a dropping funnel in 30 minutes. The reaction was stirred at room temperature for 3.5 hours and checked by TLC (CH_2Cl_2:MeOH = 98:2; R_f= 0.62 for **TT2I**). Then the reaction mixture is added with 15 mL of acetone and the solvent is evaporated to dryness. The crude product is washed with 2 x 40 mL of water (stirred for 1 hour) and the precipitate filtered on büchner. The precipitate is purified by gravimetric column chromatography on SiO_2 with $CH_2Cl_2$and MeOH as eluent, crystallized from CH_3CN and water (2:1 ratio) and washed with hexane. Pure **TT2I** is isolated in 25% yield (166 mg, 0.37mmol).

^{1}H NMR (400 MHz, DMSO-d_6, 298 K, δ, ppm): 7.91(1H, d, J= 1.7Hz), 7.39(1H, s), 7.31(1H, s), 7.28(1H, d, J= 1.7 Hz).

^{13}C NMR (100 MHz, DMSO-d_6, 298 K, δ, ppm): 137.6 (Cq),137.4 (Cq), 136.0 (CH), 135.8(CH), 135.6 (Cq), 127.9(CH), 111.2(CH), 61.2(CI), 60.7(CI).

MS (ESI-positive ion mode): m/z 450.74$[M+H]^+$

12.4.3 TTCo cocrystallization

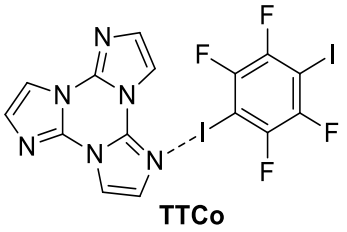

*Figure 7: **TTCo** chemical structure*

In the same 50 mL one-necked flask, **TT** (15 mg, 0.076 mmol) and 1,4-diiodotetrafluorobenzene (30 mg, 0.076 mmol) are dissolved in CH_2Cl_2 10 mL. The flask is left open at room temperature and the solvent slowly evaporates to give cocrystals of **TTCo** suitable for X-ray diffraction [5].

12.4.4 ^{1}H NMR TT1I

400 MHz, DMSO-d_6, 298 K

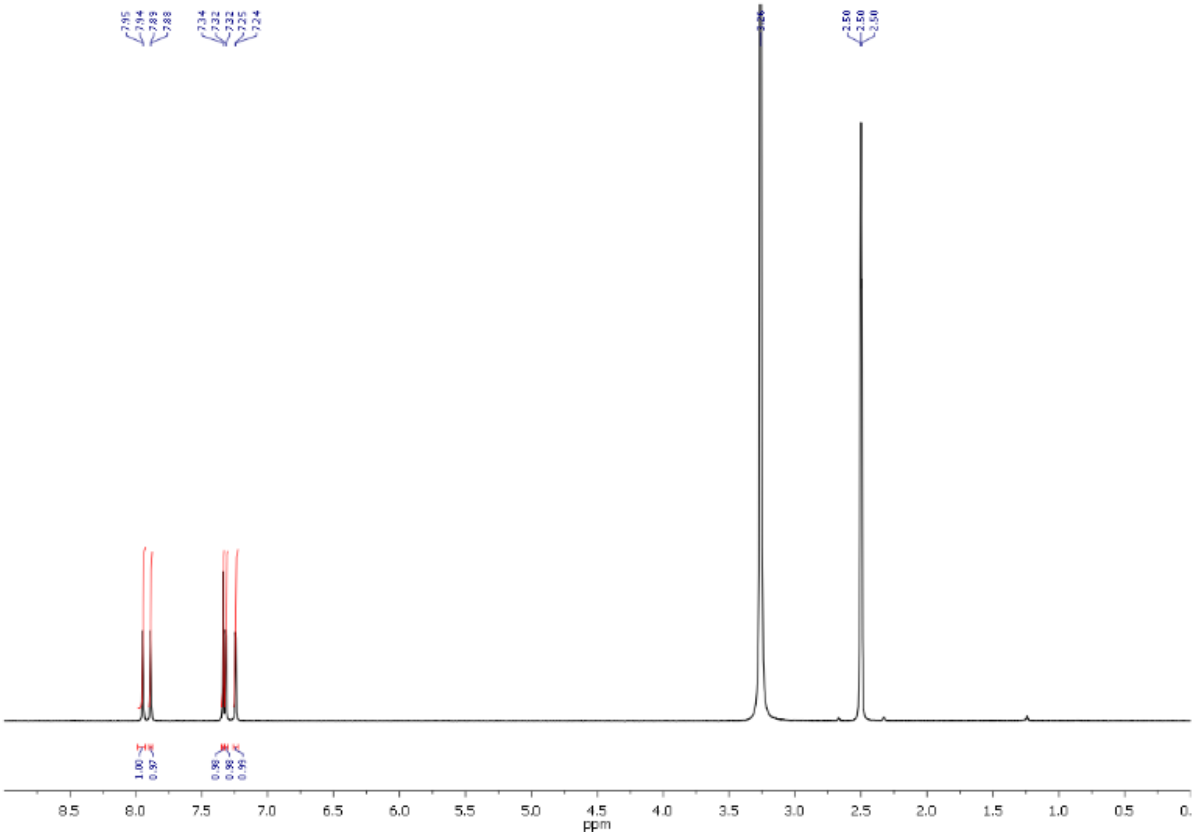

400 MHz, DMSO-d_6, 298 K, expanded region

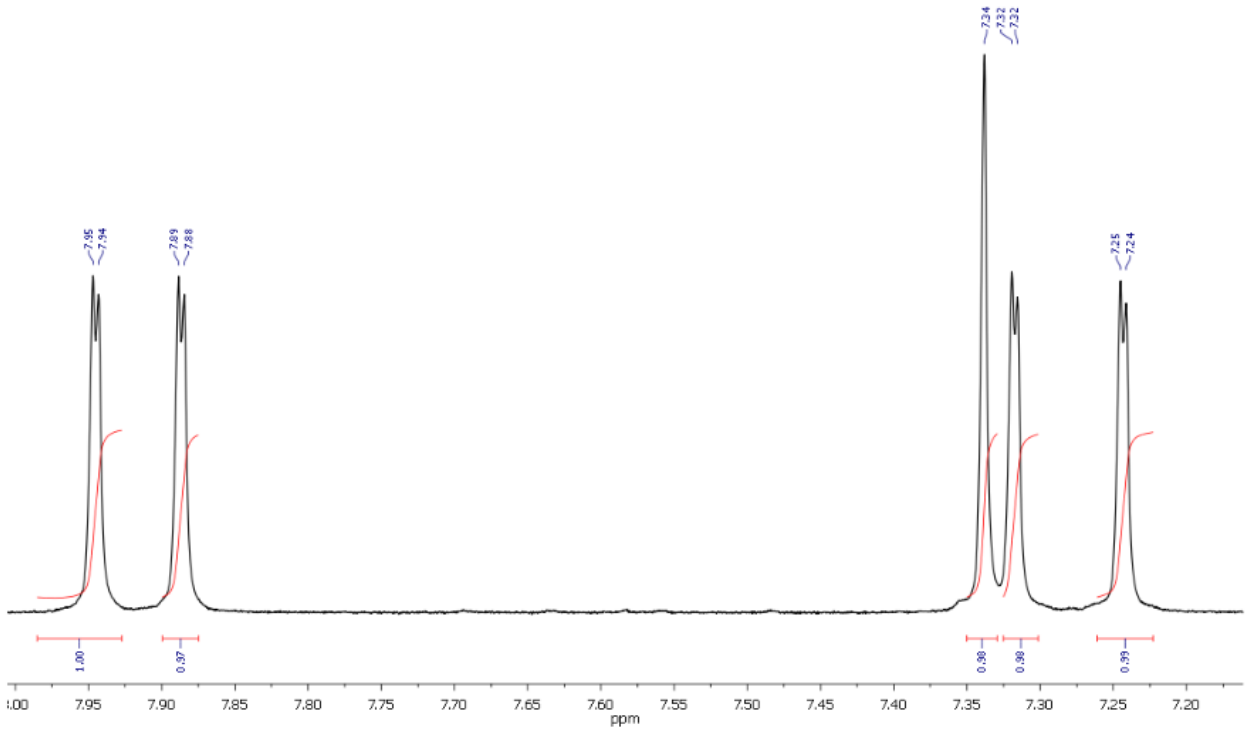

12.4.5 ^{1}H NMR TT2I

400 MHz, DMSO-d_6, 298 K

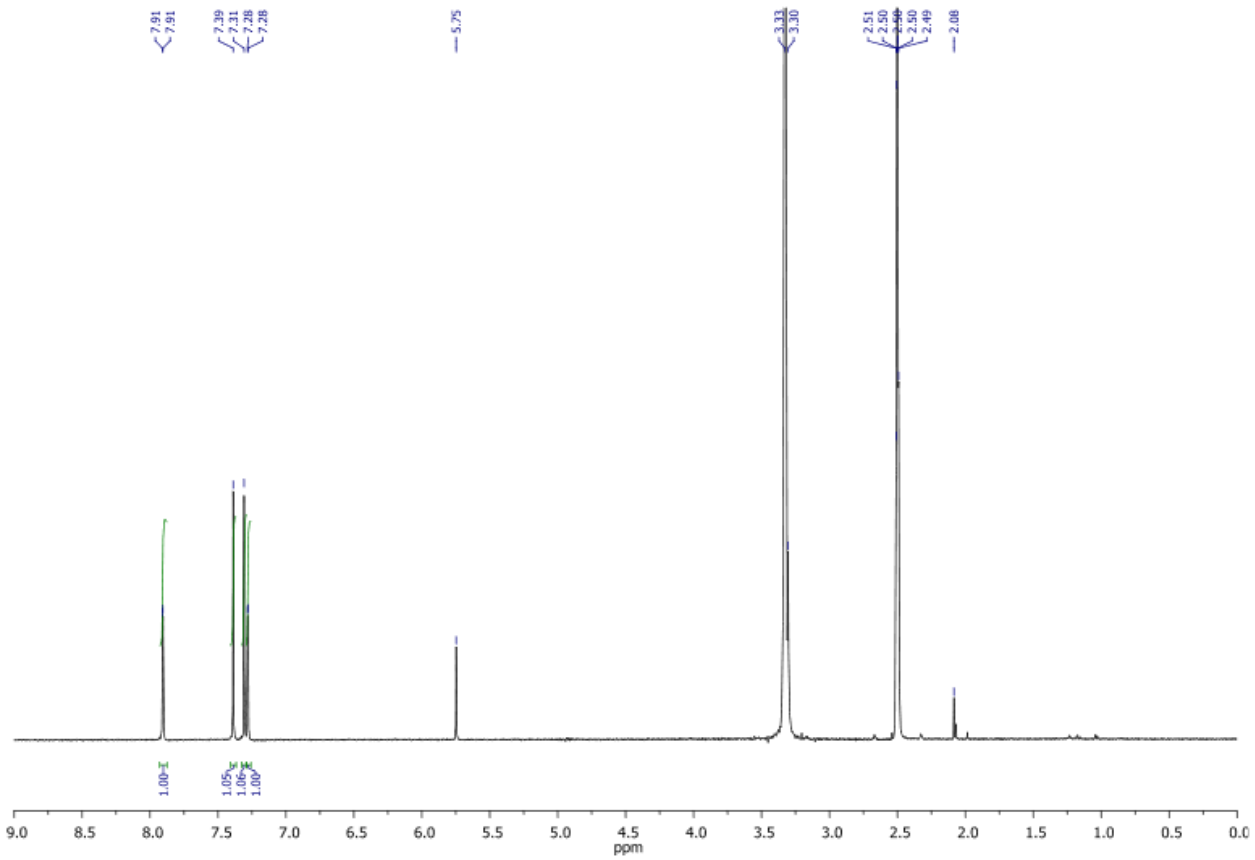

400 MHz, DMSO-d_6, 298 K, expanded region

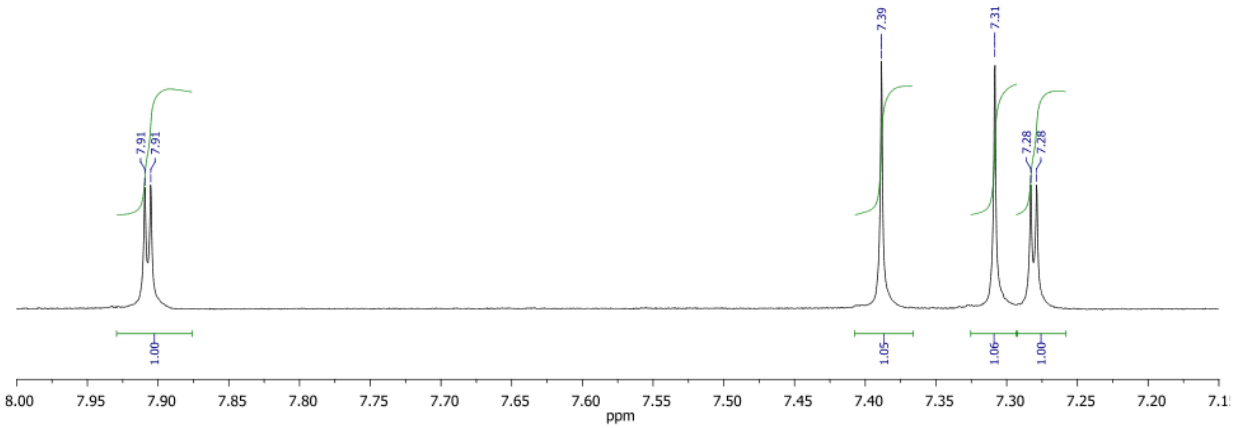

12.4.6 ^{13}C NMR TT1I

100 MHz, DMSO-d_6, 298 K

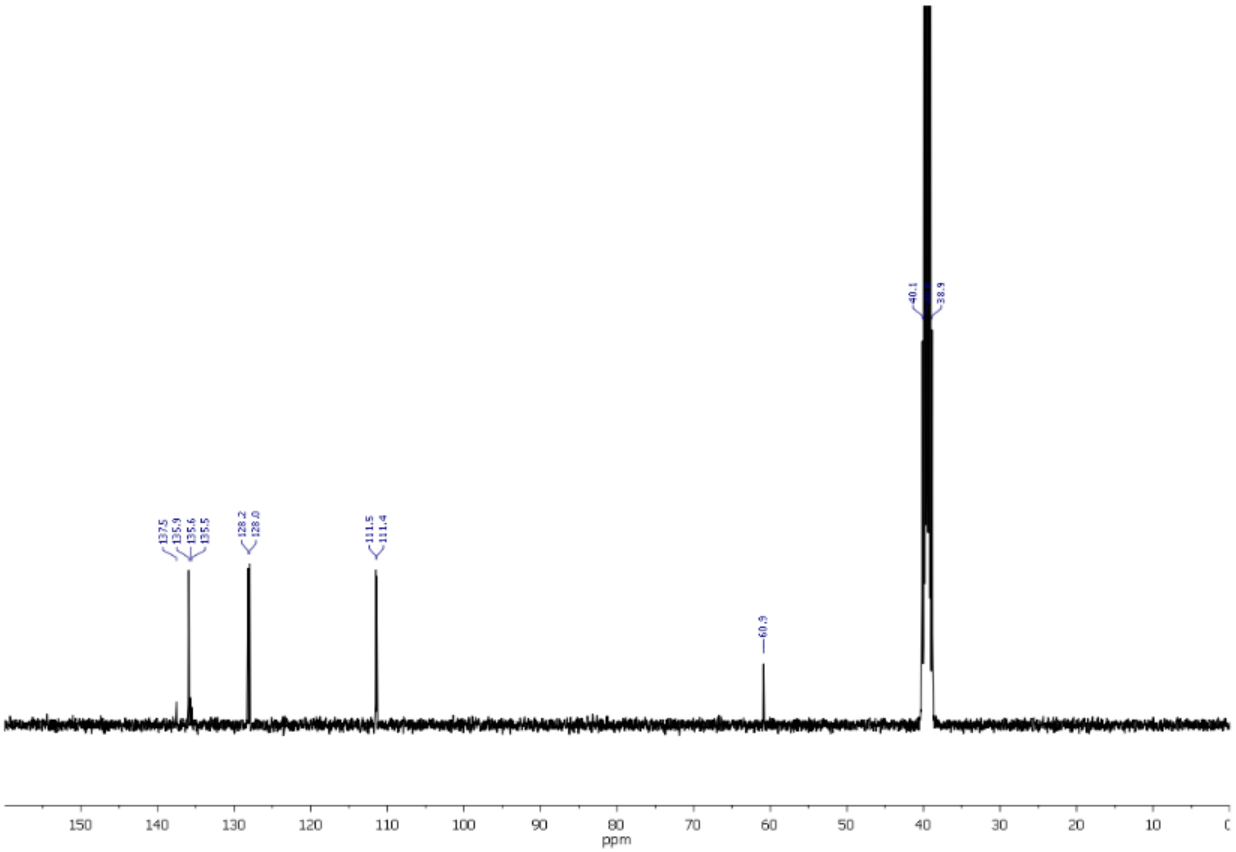

100 MHz, DMSO-d_6, 298 K, expanded region

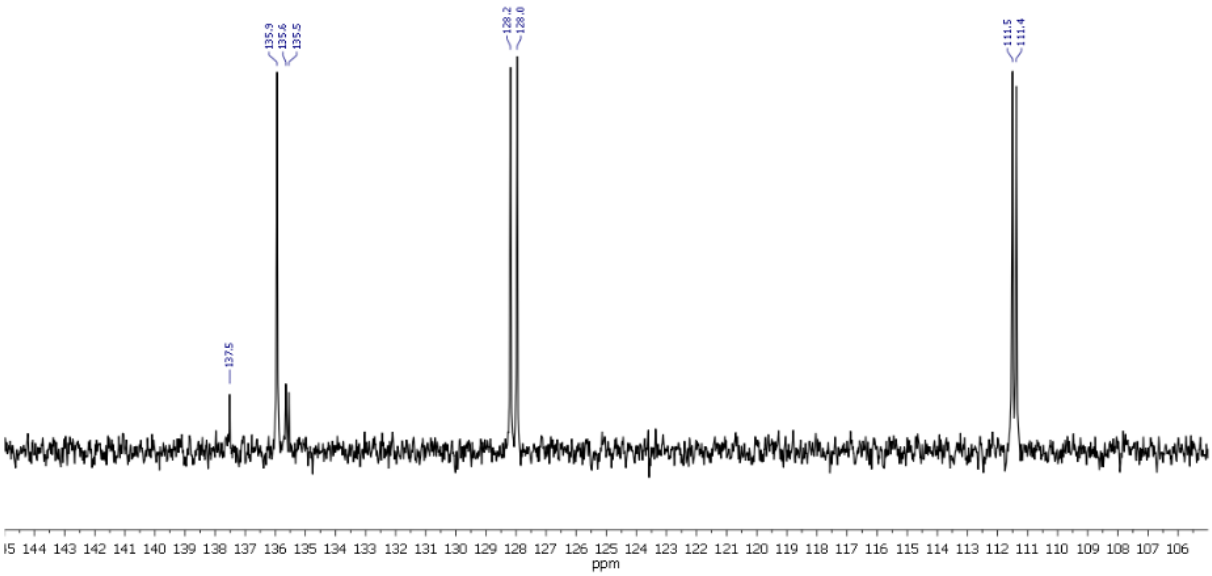

12.4.7 ^{13}C NMR TT2I

100 MHz, DMSO-d_6, 298 K

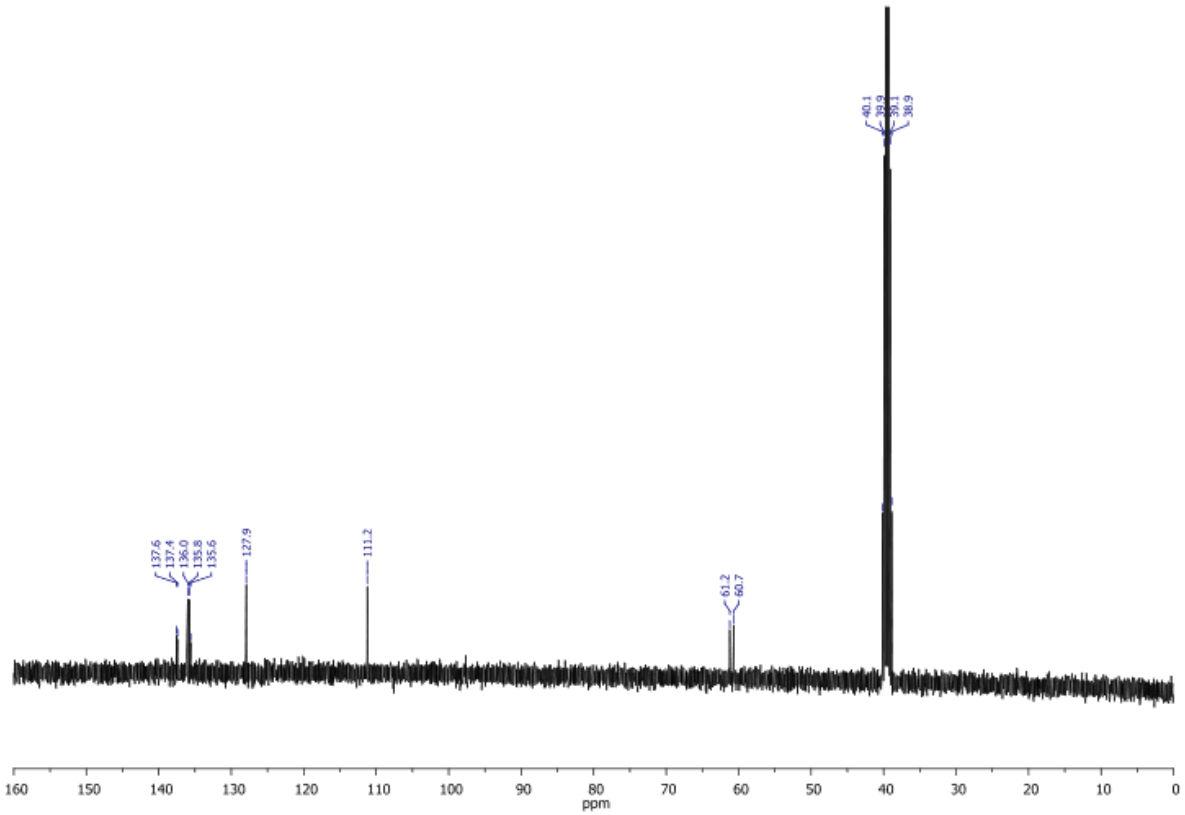

100 MHz, DMSO-d_6, 298 K, expanded region

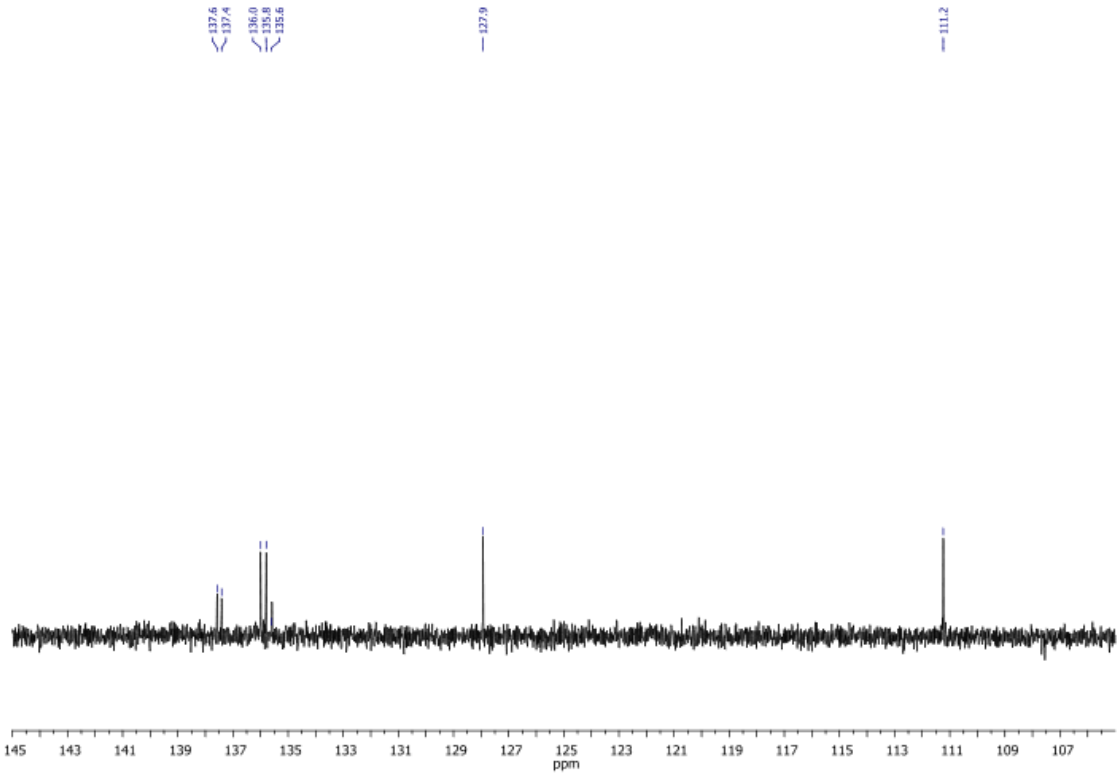

12.4.8 Crystallographic data

Compound	**TT1I**	**TT2I**	**TTCo**
Chemical Formula	$C_9H_5IN_6$	$C_9H_4I_2N_6$	$C_9H_6N_6{\cdot}C_6F_4I_2$
Molecular weight	324.09	449.98	600.06
T(K)	120	293	293
Crystal system	Monoclinic	Triclinic	Monoclinic
Space group	*C*2/*c*	*P*-1	$P2_1/n$
a(Å)	34.18	4.3042	4.3699
b(Å)	4.097	16.0441	29.647
c(Å)	31.19	16.6604	13.3748
α(°)	90	101.7635	90
β(°)	117.37	94.5898	97.63
γ(°)	90	91.492	90
V(Å^3)	3880	1121.68	1717.4
Z	16	4	4
*D*calc (g cm^{-3})	2.22	2.665	2.321
μ (mm^{-1})	3.281	5.593	3.717
Crystal size (mm)	0.46 x 0.01 x 0.01	0.45 x 0.10 x 0.03	0.50 x 0.12 x 0.02
2θmax (°)	41.2	63.7	58.2
No. of measured, independent and observed [I >2σ(I)] reflections	13464/1934/1500	22743/7190/6497	30115/4580/3725
(R_{int})/ ($R_σ$)	0.1258/0.0841	0.0204/0.0188	0.0431/0.0295
data/restraints/params	1934/60/289	7190/0/307	4580/0/244
R[F^2> 2σ(F^2)], wR(F^2), S	0.0451, 0.0670, 1.002	0.0202, 0.0500, 1.055	0.0463, 0.0590, 1.230
Δρmax, Δρmin (e Å^{-3})	1.1163, -0.688	0.684, -0.0889	1.328, -0.573

12.5 3-(2-fluoropyridin-4-yl)triimidazo[1,2-*a*:1',2'-*c*:1'',2''-*e*][1,3,5]triazine or TTFPy

12.5.1 Synthesis

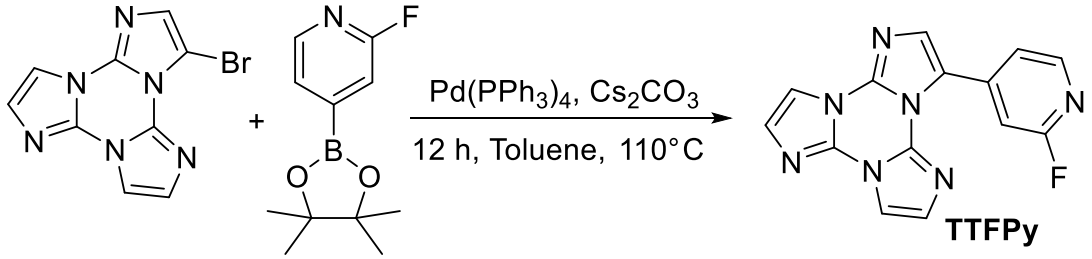

*Figure 8: Synthetic pathway for **TTFPy***

TTFPy is obtained by Suzuki-Miyaura coupling between **TT1Br** and 2-fluoropyridine-4-boronic acid pinacol ester[6]. The reaction is performed under nitrogen in a Schlenk flask. **TT1Br** (300 mg, 1.08 mmol), 2-fluoropyridine-4-boronic acid pinacol ester (340 mg, 1.52 mmol), cesium carbonate (1.76 g, 5.40 mmol), $Pd(PPh_3)_4$ (120 mg, 0.10 mmol) and anhydrous toluene (10 mL) are transferred inside the Schlenk flask. The mixture is heated at 110◦C under static nitrogen for 12 h. The reaction is then cooled to room temperature, diluted with CH_2Cl_2 (80 mL), filtered on buchner and evaporated to dryness. The crude product is washed with hexane to remove Ph_3PO and then purified by column chromatography with AcOEt on silica gel (R_f = 0.23) to give pure **TTFPy** (190 mg, yield 60%). Crystals suitable for X-ray diffraction studies are obtained by layering a CH_2Cl_2 solution of **TTFPy** with hexane.

^{1}H NMR (400 MHz, DMSO-d_6, 298 K, δ, ppm): 8.32 (1H, d, J = 5.3 Hz), 8.02 (2H, m), 7.82 (1H, m), 7.75 (1H, s), 7.71 (1H, m), 7.33 (1H, d, J = 1.7 Hz), 7.29 (1H, d, J = 1.6 Hz).

^{13}C NMR (100 MHz, DMSO-d_6, 298 K, δ, ppm): 163.0 CF, (1C, d, J= 233.3 Hz), 147.1 CH (1C, d, J = 14.7 Hz), 141.2 C (1C, d, J = 8.8 Hz), 138.1 C (1C, s), 135.9 C (1C, s), 135.6 C (1C, s), 130.8 CH, (1C, s), 128.8 CH (1C, s), 127.9 CH (1C, s), 124.6 C (1C, d, J = 4.4 Hz), 121.4 CH (1C, d, J = 2.9 Hz), 111.9 CH (1C, s), 111.5 CH (1C, s), 108.5 CH (1C, d, J = 39.6 Hz).

MS (ESI-positive ion mode): m/z 294.0 $[M+H]^+$.

12.5.2 ^{1}H NMR TTFPy

400 MHz, DMSO-d_6, 298 K

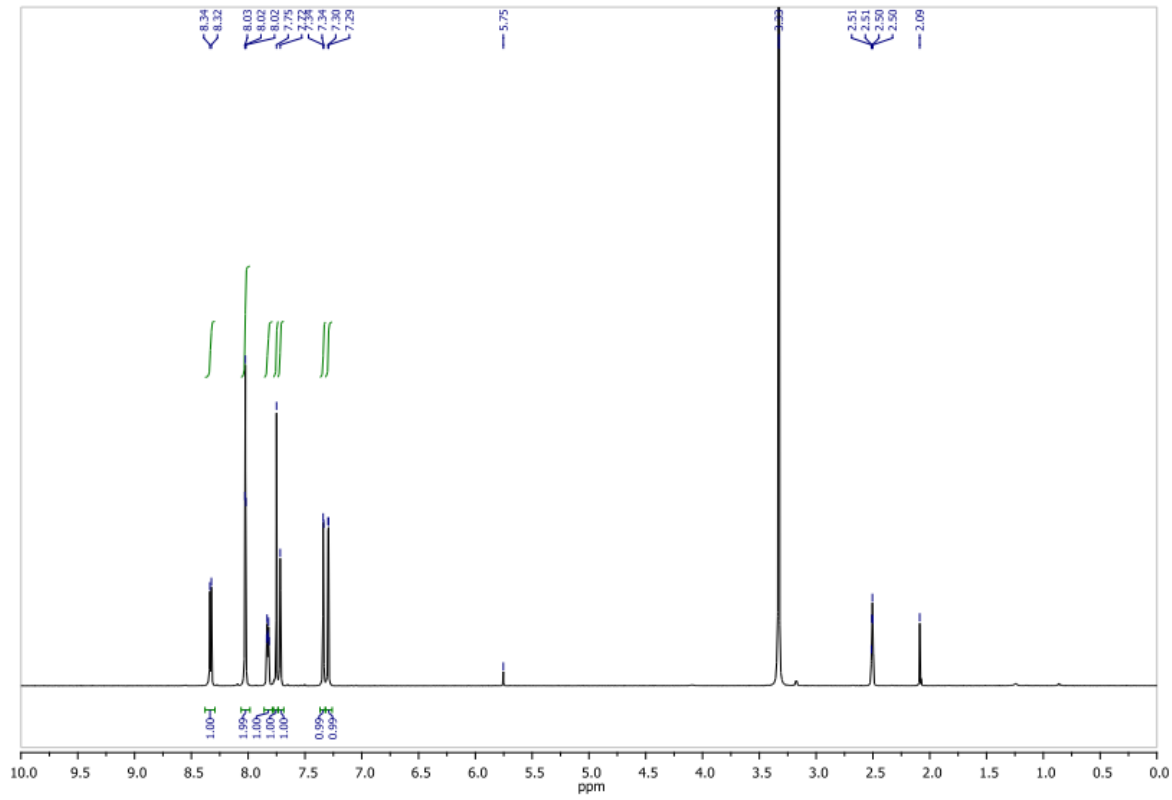

400 MHz, DMSO-d_6, 298 K, expanded region

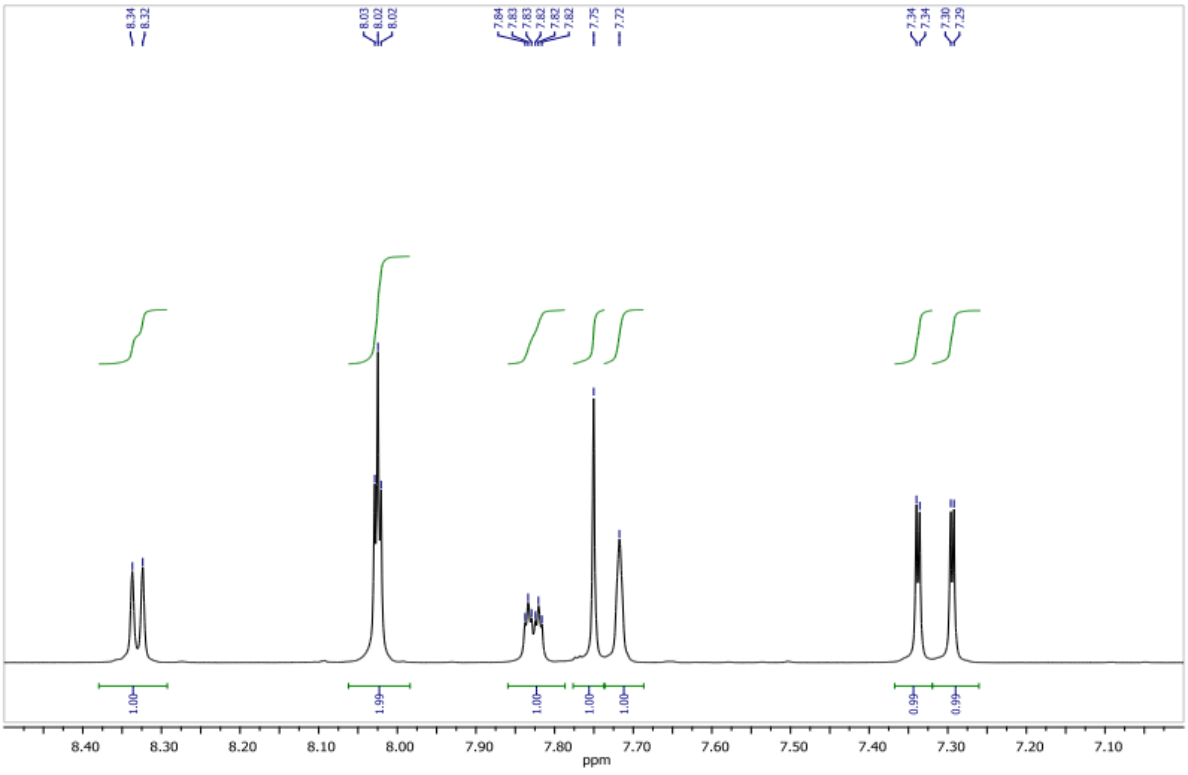

12.5.3 ^{13}C NMR TTFPy

100 MHz, DMSO-d_6, 298 K

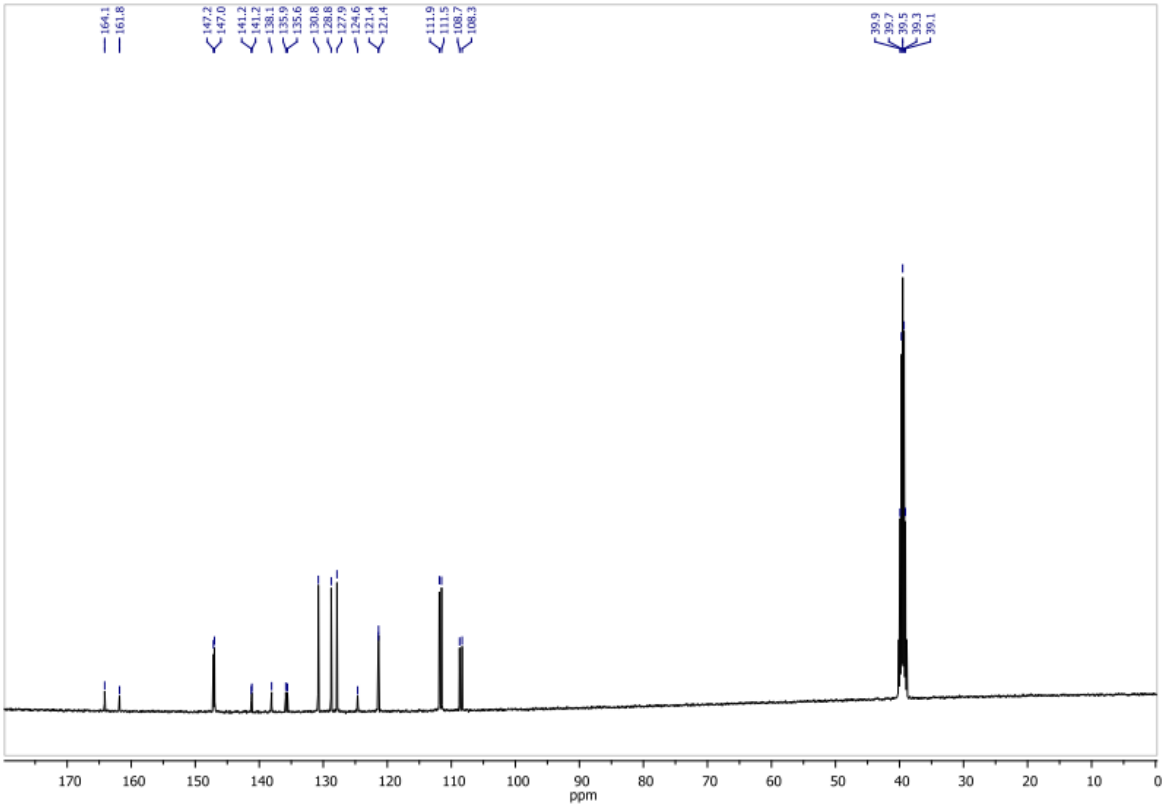

100 MHz, DMSO-d_6, 298 K, expanded region

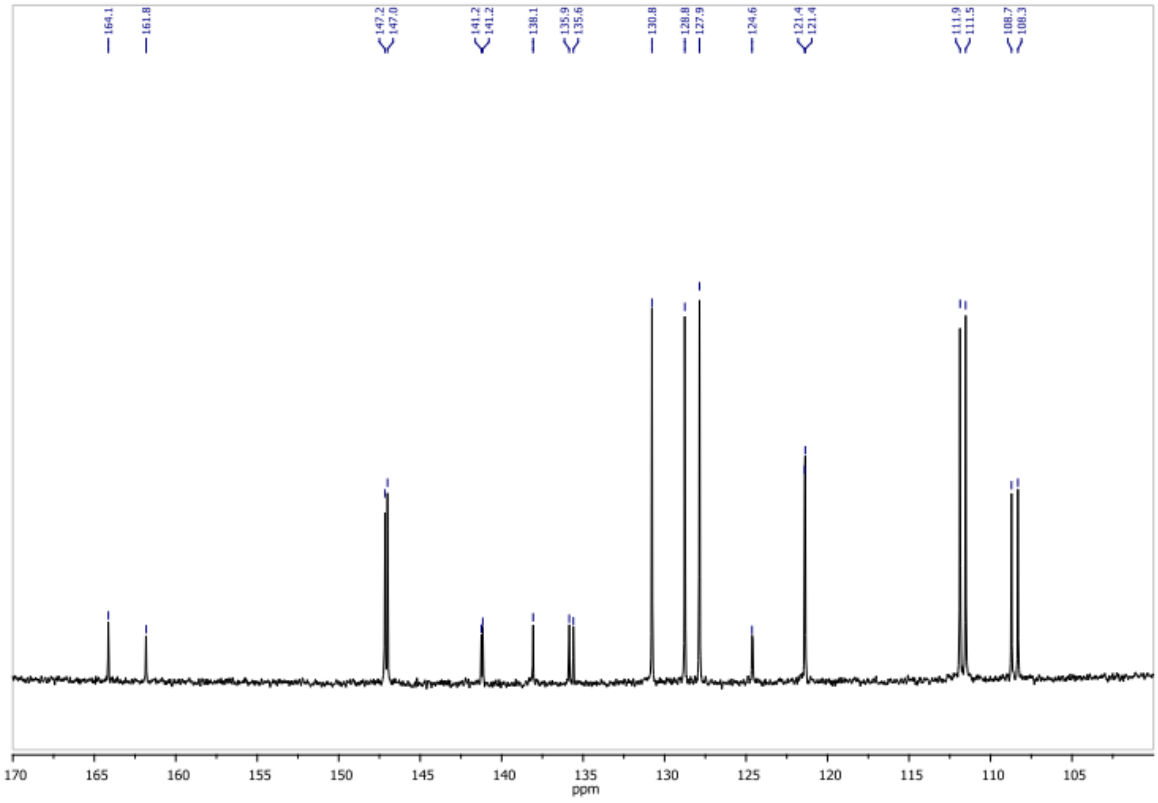

12.5.4 Crystallographic data

Compound	**TTFPy**
Chemical Formula	$C_{14}H_9FN_7$
Molecular weight	293.27
T(K)	291
Crystal system	Triclinic
Space group	*P*-1
a(Å)	3.8305
b(Å)	11.9825
c(Å)	13.8072
α(°)	78.411
β(°)	89.735
γ(°)	87.962
V(Å^3)	620.42
Z	2
*D*calc (g cm^{-3})	1.57
μ (mm^{-1})	0.114
Crystal size (mm)	0.52 x 0.10 x 0.05
2θmax (°)	61.0
No. of measured, independent and observed [I >2σ(I)] reflections	12492/3780/2772
(R_{int})/ ($R_σ$)	0.0251/0.0255
data/restraints/params	3780/0/199
R[F^2> 2σ(F^2)], wR(F^2), S	0.0484, 0.0655, 1.051
Δρmax, Δρmin (e Å^{-3})	0.341, -0.210

12.6 3-(pyridin-2-yl)triimidazo[1,2-*a*:1',2'-*c*:1'',2''-*e*][1,3,5]triazine or TT2Py

12.6.1 Synthesis

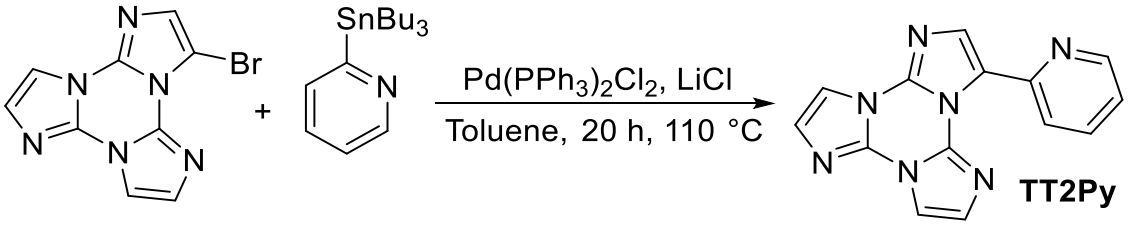

*Figure 9: Synthetic pathway for **TT2Py***

TT2Py is obtained by Stille coupling between **TT1Br** and 2-(tributylstannyl)pyridine[7]. The reaction is performed in a closed cylindrical Pyrex flask (diameter 30 mm, length 300 mm) fitted with a central neck bearing a side neck equipped with a Rotaflo stopcock. **TT1Br** (500mg, 1.80mmol), LiCl (685mg, 16.16mmol) and $Pd(PPh_3)_2Cl_2$ (38mg, 0.054 mmol) are transferred inside the cylindrical flask, to this mixture 2-(tributylstannyl)pyridine (assay 85%, 1mL, 2.70 mmol) and anhydrous toluene (15mL) are added and three freeze-pump-thaw cycles are performed. The mixture is heated at 110*C under static nitrogen for 20 hours. After cooling to room temperature, the reaction mixture is added with NaOH 1M (20mL) and stirred for 15 minutes. The biphasic solution is diluted with AcOEt (60mL) and H_2O (40mL) and separated. The aqueous phase is extracted with an additional 3×10 mL of AcOEt, and the combined organic phases are dried over Na_2SO_4, filtered and evaporated to dryness. The crude product is purified by column chromatography on silica gel (CH_2Cl_2:MeOH = 95:5; Rf = 0.38) to give **TT2Py** (370mg, yield 75%). Single crystals of the three different polymorphs are obtained as laminae (**TT2Py-A**), needles (**TT2Py-H**) and rectangular blocks (**TT2Py-X**) by slow evaporation of CH_2Cl_2/CH_3OH, CH_3CN/H_2O and CH_3CN solutions, respectively.

^{1}H NMR (400 MHz, DMSO-d_6, 298 K, δ, ppm): 8.65 (ddd, J=4.8, 1.7, 0.9 Hz, 1H), 8.10 (dt, J=8.0, 0.9 Hz, 1H), 8.0 (d, J=1.7 Hz, 1H), 7.98 (d, J=1.6 Hz, 1H), 7.9 (tt, J=5.6, 2.8 Hz, 1H), 7.54 (s, 1H), 7.41 (m, 1H), 7.31 (d, J=1.7 Hz, 1H), 7.22 (d, J=1.6 Hz, 1H).

^{13}C NMR (100 MHz, DMSO-d_6, 298 K, δ, ppm): 149.1 (CH), 147.4 (Cq), 136.8 (Cq), 135.9(CH), 135.6 (Cq), 129.4 (CH), 128.6 (CH), 127.9 (Cq), 127.8 (CH), 124.8 (CH), 122.9 (CH), 111.8 (CH), 111.4(CH).

MS (ESI-positive ion mode) : m/z 276.2 $[M+H]^+$.

12.6.2 ^{1}H NMR TT2Py

400 MHz, DMSO-d_6, 298 K

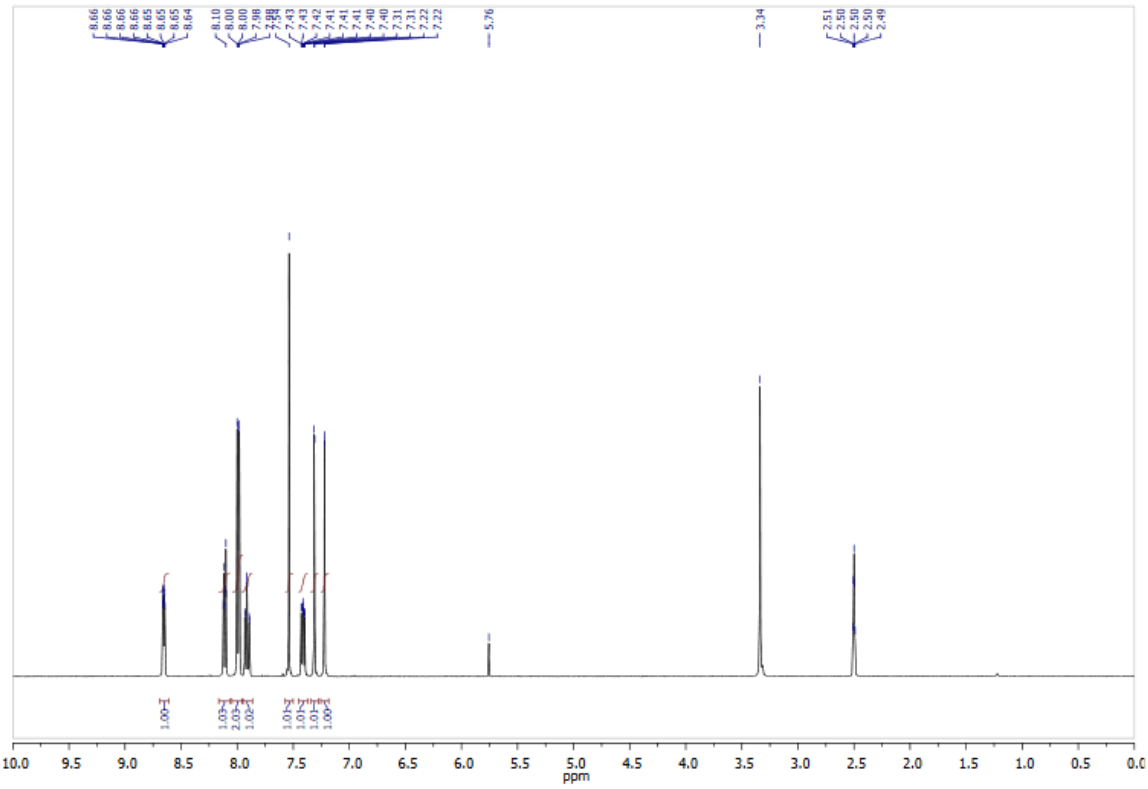

400 MHz, DMSO-d_6, 298 K, expanded region

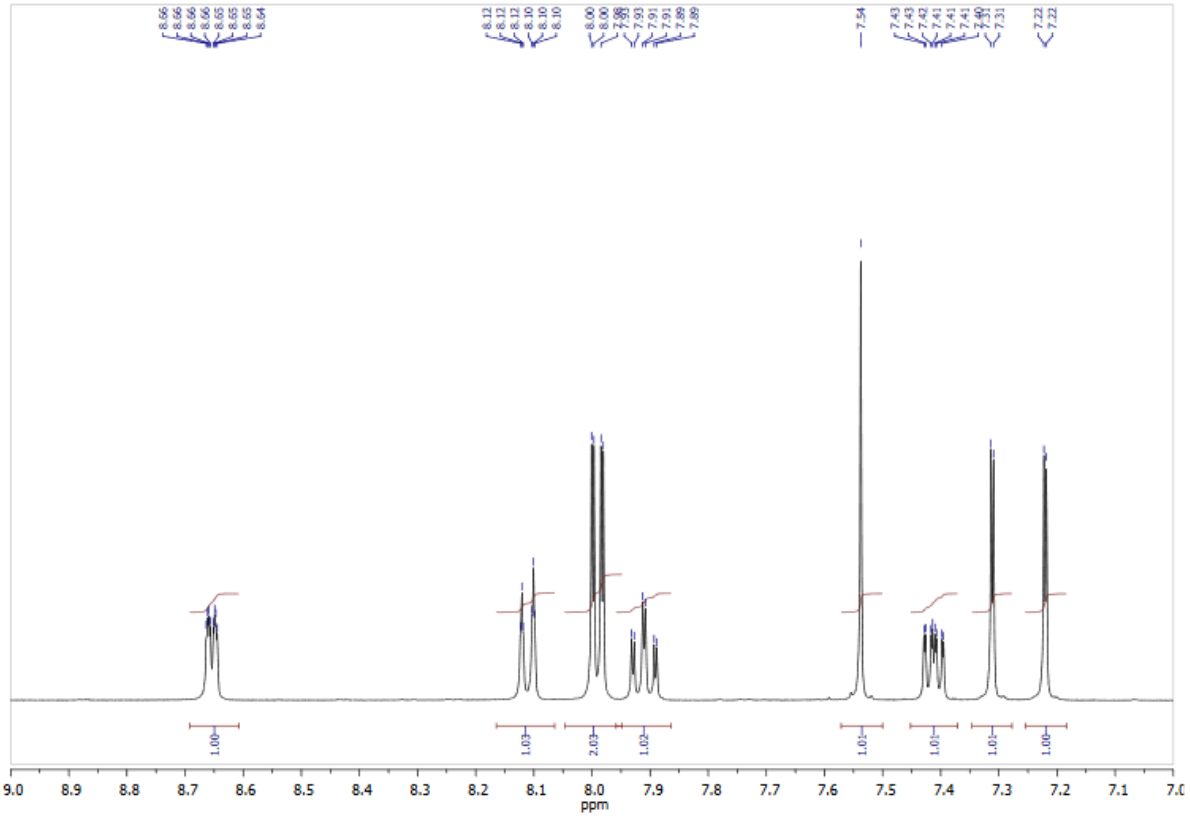

12.6.3 ^{13}C NMR TT2Py

100 MHz, DMSO-d_6, 298 K

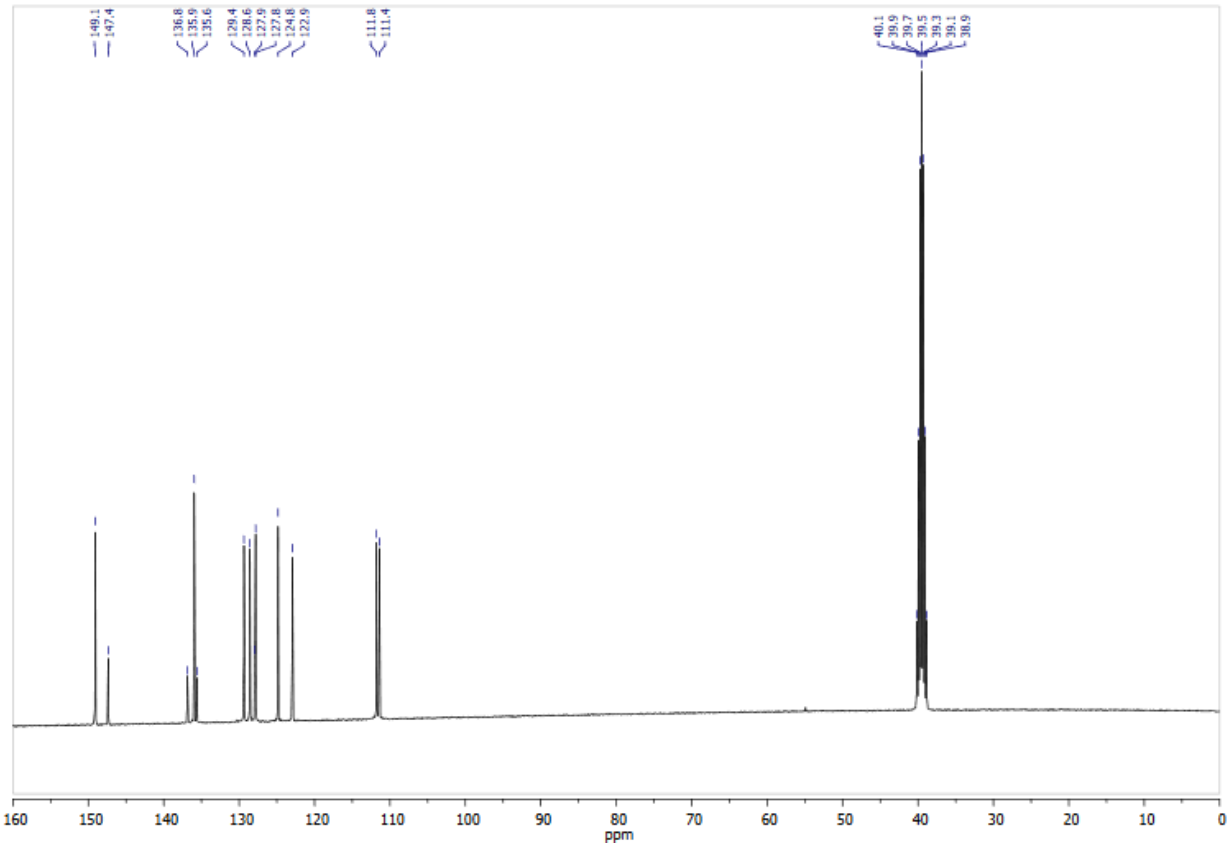

100 MHz, DMSO-d_6, 298 K, expanded region

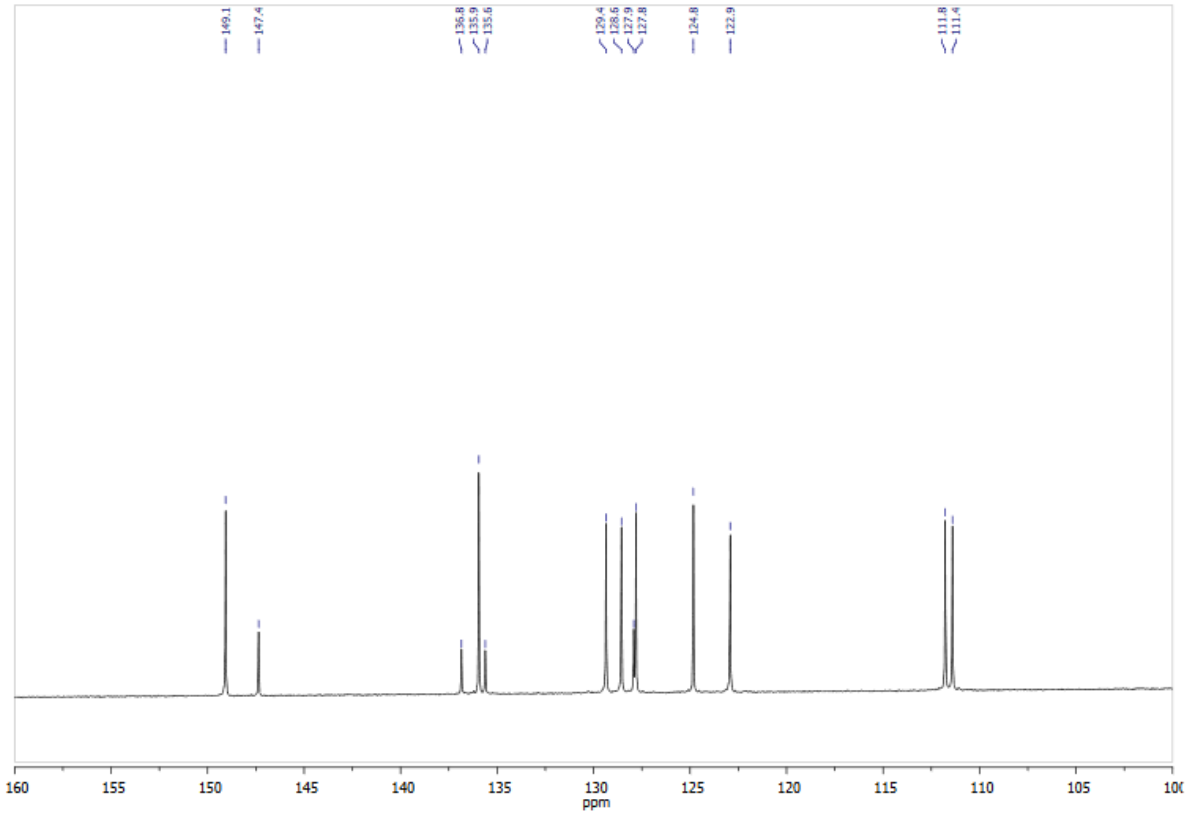

12.6.4Crystallographic data

Compound	**TT2Py(A)**	**TT2Py(H)**	**TT2Py(X)**
Chemical Formula	$C_{14}H_9N_7$	$C_{14}H_9N_7 \cdot 1.7H_2O$	$C_{14}H_9N_7$
Molecular weight	275.28	307.28	275.28
T(K)	293	120	293
Crystal system	Orthorhombic	Monoclinic	Monoclinic
Space group	*Pbcn*	$P2_1/c$	$P2_1/c$
a(Å)	33.189	3.7357	18.0949
b(Å)	10.162	14.805	8.8509
c(Å)	7.2434	23.784	17.3684
α(°)	90	90	90
β(°)	90	90.284	117.796
γ(°)	90	90	90
V(Å^3)	2443	1315.4	2460.69
Z	8	4	8
Dcalc (g cm^{-3})	1.497	1.552	1.486
μ (mm^{-1})	0.099	0.112	0.099
Crystal size (mm)	0.55 x 0.07 x 0.01	0.45 x 0.04 x 0.04	0.35 x 0.27 x 0.18
2θmax (°)	55	55.32	61
No. of measured, independent and observed [I >2σ(I)] reflections	66937/2803/1742	19094/3031/1577	47901/7501/5146
(R_{int})/ (R_σ)	0.1067/0.0384	0.1709/0.1332	0.0285/0.0201
data/restraints/params	2803/0/190	3031/6/220	7501/0/379
R[F^2> 2σ(F^2)], wR(F^2), S	0.0497, 0.112, 1.059	0.0665, 0.1518, 1.000	0.0468, 0.1245, 1.028
Δρmax, Δρmin (e Å^{-3})	0.185, -0.204	0.303, -0.349	0.166, -0.220

12.7 3-(pyren-1-yl)triimidazo[1,2-*a*:1',2'-*c*:1'',2''-*e*][1,3,5]triazine or TTPyr

12.7.1 Synthesis

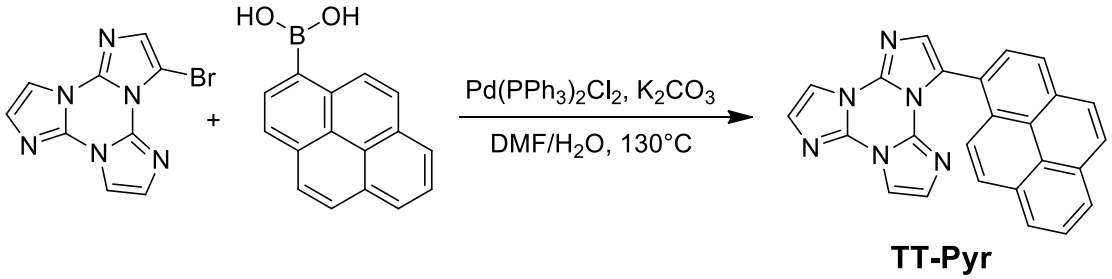

*Figure 10: Synthetic pathway for **TTPyr***

TTPyr is obtained by Suzuki-Miyaura coupling between **TT1Br** and pyren-1-ylboronic acid. The reaction is performed under nitrogen in a Schlenk flask. **TT1Br** (200 mg; 0.72 mmol), pyren-1-ylboronic acid (246 mg, 1.01 mmol), potassium carbonate (400 mg, 2.88 mmol), $Pd(PPh_3)_2Cl_2$ (25 mg, 0.03 mmol), water (2mL) and DMF (10 mL) are transferred inside the Schlenk flask. The mixture is heated at 130◦C under static nitrogen for 12 h. The reaction is then cooled to room temperature, precipitated with water (100 mL) and filtered on buchner. The crude product is purified by column chromatography with CH_2Cl_2 and MeOH as eluent on silica gel to give pure **TTPyr** (258 mg, yield 90%) as a pale yellow solid.

^{1}H NMR (400 MHz, DMSO-d_6, 298 K, δ, ppm): 8.38 (m; 2H), 8.30 (m; 3H), 8.18 (m; 1H), 8.12 (m; 4H), 7.88 (d; 1H, J= 1.4 Hz), 7.46 (s; 1H), 7.36 (d; 1H, J= 1.4 Hz), 6.81(d; 1H, J= 1.4 Hz).

^{13}C NMR (100 MHz, DMSO-d_6, 298 K, δ, ppm): 136.97, 136.26, 131.91, 131.30, 131.20, 130.85, 130.14, 128.97, 128.90, 128.57, 128.48, 128.10, 127.79, 126.91, 126.19, 126.05, 125.92, 125.60, 124.65, 124.14, 123.95, 112.22, 111.36.

12.7.2 ^{1}H NMR TTPyr

400 MHz, DMSO-d_6, 298 K

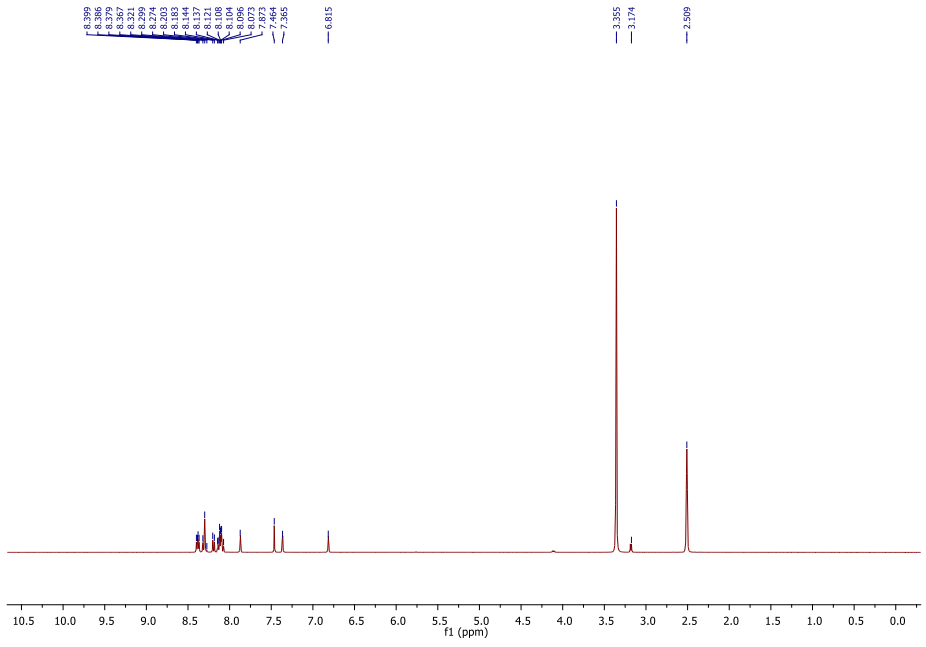

400 MHz, DMSO-d_6, 298 K, expanded region

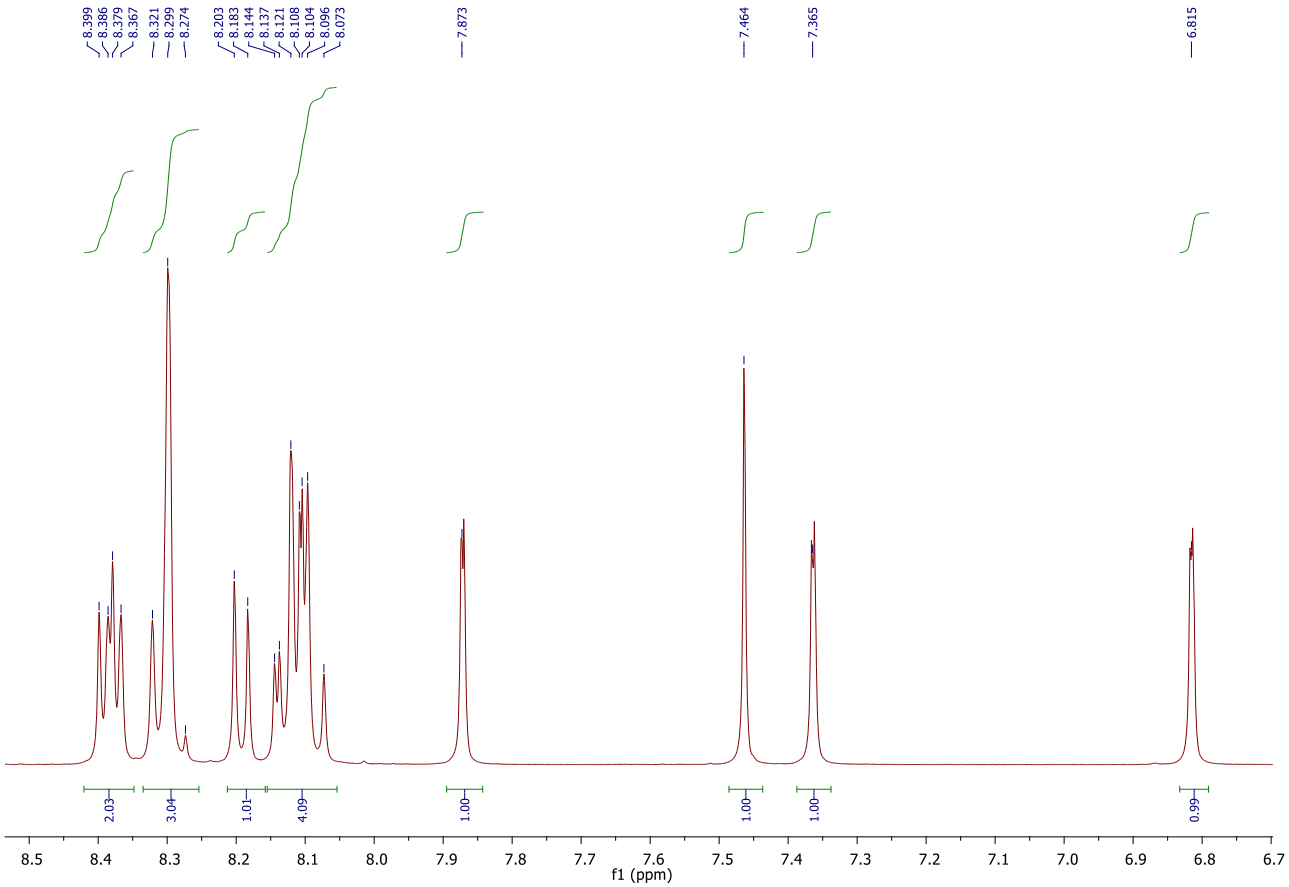

12.7.3 ^{13}C NMR TTPyr

APT; 100 MHz, DMSO-d_6, 298 K

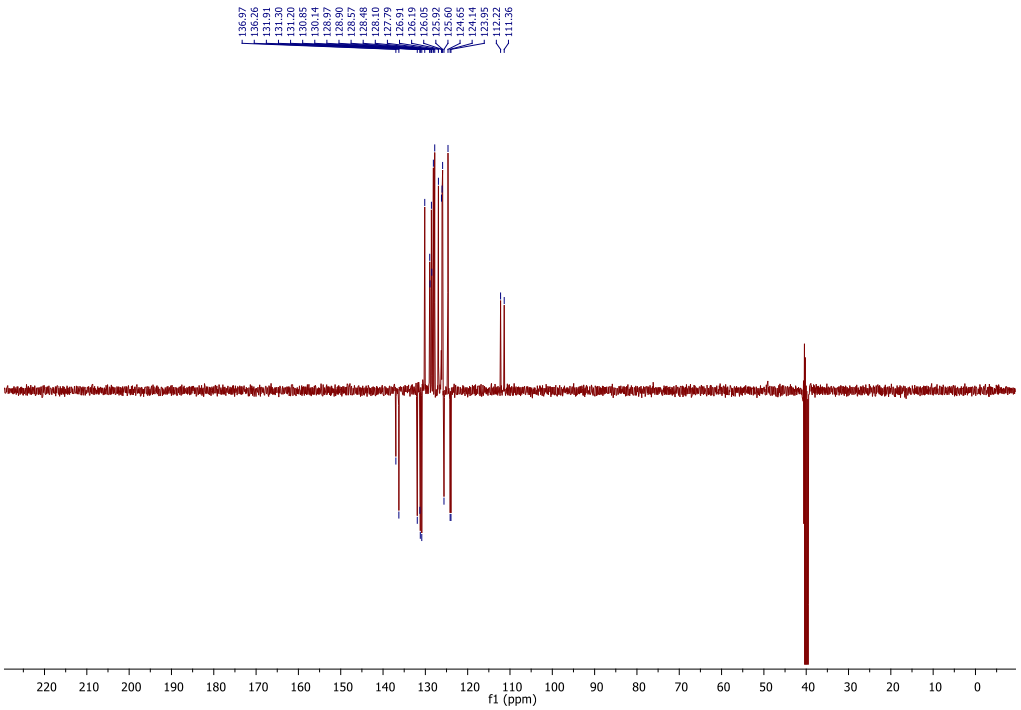

APT; 100 MHz, DMSO-d_6, 298 K, expanded region

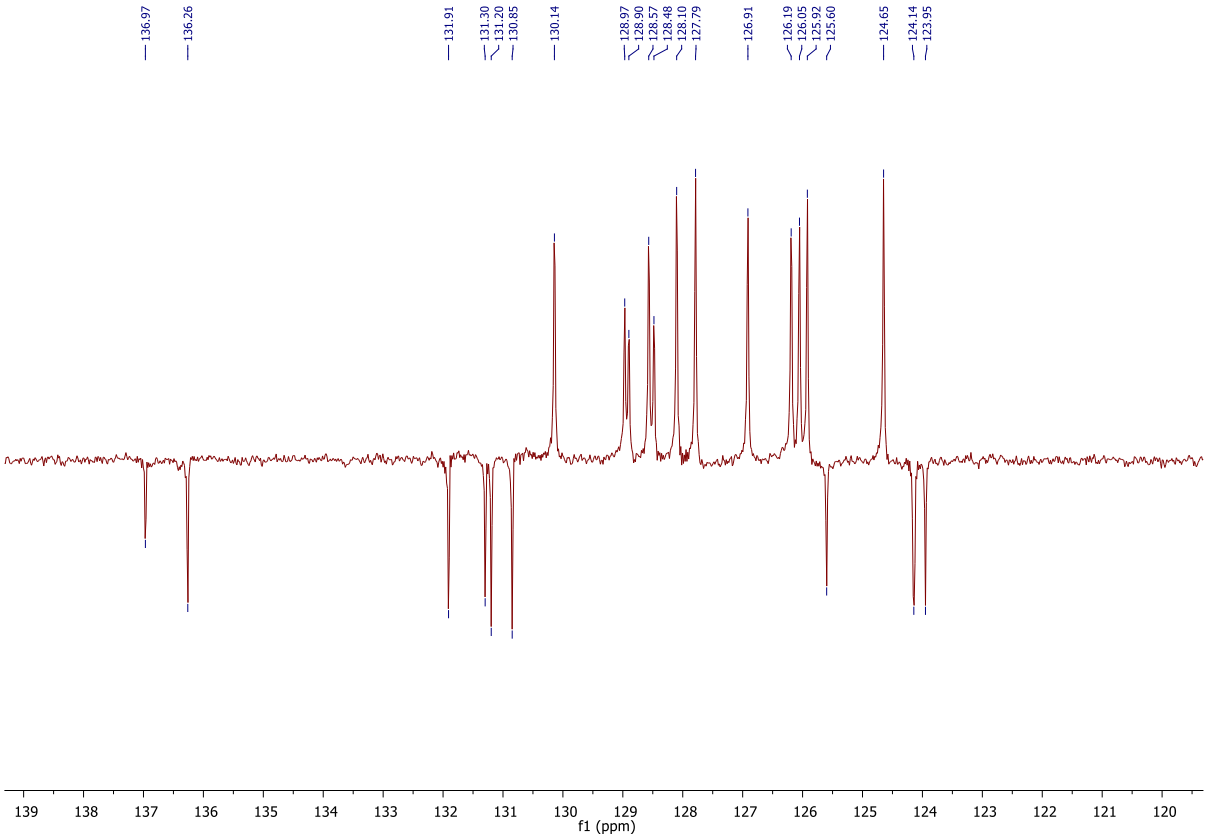

12.8 Cu(I) and Ag(I) coordination polymers

12.8.1 Synthesis of $[Cu(TT)I]_n$ (1-Cu)

Solid CuI is suspended in a saturated aqueous solution of KI. After vigorous stirring the suspension is filtered and 4 mL of the resulting solution is transferred in a vial. **TT** (15 mg, 0.076 mmol) is dissolved in CH_3CN (2 mL) and added to the aqueous solution. After 18h at room temperature, colorless needle-shaped **1-Cu** crystals are recovered from the solution through filtration on a Buchner[8].

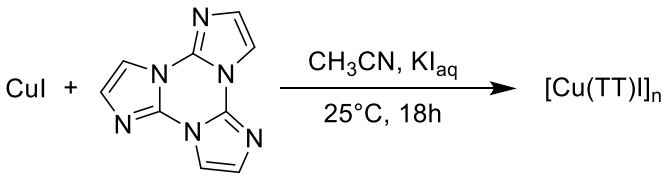

*Figure 11: Synthetic pathway for $[Cu(TT)I]_n$, **1-Cu***

Anal. Calcd. for $C_9H_6CuIN_6$ (%): C, 27.81; H, 1.56; N, 21.62. Found: C, 27.63; H, 1.61; N, 21.82.

12.8.2 Synthesis of $[Ag(TT)I]_n$ (1-Ag)

AgI (55 mg, 0.234 mmol) is added to a solution of *N*,*N*-dimethylformamide (DMF, 5 mL) and KI (20 mg, 0.4 wt%) at 25 °C in the dark. After 15 minutes the resulting transparent solution is transferred into a vial. **TT** (47 mg, 0.238 mmol) dissolved in acetonitrile (CH_3CN, 3 mL) is added to this solution. The vial is kept closed at 25 °C in the dark producing after few days a white powder which is filtered and dried over filter paper.

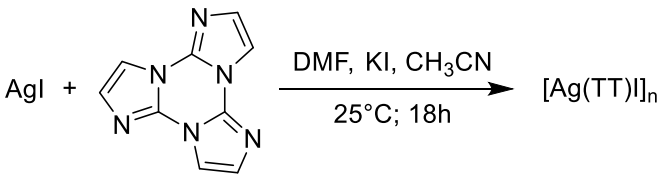

Figure 12: Synthetic pathway for $[Ag(TT)I]_n$, ***1-Ag.***

Alternatively, **TT** (11 mg, 0.056 mmol) dissolved in CH_3CN (2 mL) is added to a vial containing 4 mL of a saturated aqueous solution of AgI in KI. The vial is kept closed at 25 °C in the dark producing after few days needle-shaped crystals suitable for X-ray diffraction analysis.

Anal. Calcd. for $C_9H_6AgIN_6$ (%): C, 25.03; H, 1.17; N, 19.46. Found: C, 25.39; H, 1.29; N, 19.63.

12.8.3 Crystallographic data

Compound	**1-Cu**	**1-Ag**
Chemical Formula	$C_9H_6CuIN_6$	$C_9H_6AgIN_6$
Molecular weight	388.64	432.97
T(K)	150	150
Crystal system	Monoclinic	Monoclinic
Space group	$P2_1/c$	$P2_1/c$
a(Å)	14.117	13.858
b(Å)	4.509	4.7312
c(Å)	17.113	17.303
α(°)	90	90
β(°)	105.6	105.388
γ(°)	90	90
V(Å^3)	1049.2	1093.8
Z	4	4
Dcalc (g cm^{-3})	2.46	
μ (mm^{-1})	5.008	4.65
Crystal size (mm)	0.60 x 0.04 x 0.02	0.305 × 0.045 × 0.030
2θmax (°)		
No. of measured, independent and observed [I >2σ(I)] reflections	19478/2585	12349/3516/2515
(R_{int})/ ($R_σ$)	0.0316	0.0478/0.0456
data/restraints/params	2585/0/154	3516/0/154
R[F^2> 2σ(F^2)], wR(F^2), S	0.019, 0.041, 1.160	0.0343, 0.0692, 0.962
Δρmax, Δρmin (e Å^{-3})	0.875, -0.835	2.145, -1.211

12.9 References

[1] Lucenti, E.; Forni, A.; Botta, C.; Carlucci, L.; Giannini, C.; Marinotto, D.; Previtali, A.; Righetto, S.; Cariati, E., H-Aggregates Granting Crystallization-Induced Emissive Behavior and Ultralong Phosphorescence from a Pure Organic Molecule. *The Journal of Physical Chemistry Letters* **2017,** *8* (8), 1894-1898.

[2] Masciocchi, N.; Bruni, S.; Cariati, E.; Cariati, F.; Galli, S.; Sironi, A., Extended Polymorphism in Copper(II) Imidazolate Polymers: A Spectroscopic and XRPD Structural Study. *Inorganic Chemistry* **2001,** *40* (23), 5897-5905.

[3] Lucenti, E.; Forni, A.; Botta, C.; Carlucci, L.; Giannini, C.; Marinotto, D.; Pavanello, A.; Previtali, A.; Righetto, S.; Cariati, E., Cyclic Triimidazole Derivatives: Intriguing Examples of Multiple Emissions and Ultralong Phosphorescence at Room Temperature. *Angewandte Chemie International Edition* **2017,** *56* (51), 16302-16307.

[4] Lucenti, E.; Forni, A.; Botta, C.; Carlucci, L.; Colombo, A.; Giannini, C.; Marinotto, D.; Previtali, A.; Righetto, S.; Cariati, E., The Effect of Bromo Substituents on the Multifaceted Emissive and Crystal-Packing Features of Cyclic Triimidazole Derivatives. *ChemPhotoChem* **2018,** *2* (9), 801-805.

[5] Lucenti, E.; Forni, A.; Botta, C.; Giannini, C.; Malpicci, D.; Marinotto, D.; Previtali, A.; Righetto, S.; Cariati, E., Intrinsic and Extrinsic Heavy-Atom Effects on the Multifaceted Emissive Behavior of Cyclic Triimidazole. *Chemistry – A European Journal* **2019,** *25* (10), 2452-2456.

[6] Previtali, A.; Lucenti, E.; Forni, A.; Mauri, L.; Botta, C.; Giannini, C.; Malpicci, D.; Marinotto, D.; Righetto, S.; Cariati, E., Solid State Room Temperature Dual Phosphorescence from 3-(2-Fluoropyridin-4-yl)triimidazo[1,2-a:1′,2′-c:1″,2″-e][1,3,5]triazine. *Molecules* **2019,** *24* (14), 2552.

[7] Lucenti, E.; Forni, A.; Previtali, A.; Marinotto, D.; Malpicci, D.; Righetto, S.; Giannini, C.; Virgili, T.; Kabacinski, P.; Ganzer, L.; Giovanella, U.; Botta, C.; Cariati, E., Unravelling the intricate photophysical behavior of 3-(pyridin-2-yl)triimidazotriazine AIE and RTP polymorphs. *Chemical Science* **2020,** *11* (29), 7599-7608.

[8] Lucenti, E.; Cariati, E.; Previtali, A.; Marinotto, D.; Forni, A.; Bold, V.; Kravtsov, V. C.; Fonari, M. S.; Galli, S.; Carlucci, L., Versatility of Cyclic Triimidazole to Assemble 1D, 2D, and 3D Cu(I) Halide Coordination Networks. *Crystal Growth & Design* **2019,** *19* (3), 1567-1575.

13 Conclusion

This work is aimed at the development of new materials with enhanced emissive properties in the solid state. These materials are particularly appealing in view of possible application in different fields spanning from OLED fabrication to the biological area. Research in these contexts was historically limited by the observation that luminogens possess better properties in dispersed system than in the condensed phase due to the well-known Aggregation Caused Quenching (ACQ) phenomenon. However, in 2001 Tang and co-workers reported some pioneering works on luminogens displaying opposite properties, being highly emissive in the condensed phase but not in diluted solution, a behaviour named Aggregation Induced Emission (AIE)[1]. Different mechanisms may explain the AIE phenomenon, the most frequent one being the inhibition of molecular motions (vibrations and rotations) which works as non-radiative deactivation channels for the molecule but is somehow locked in the aggregated state.

In parallel, great efforts have been devoted to the search of organic molecules with long-lived excited states that enable exciton migration over long distances for increased production of free charges. Usually, transitions from singlet (short-lived) to triplet (long-lived) states are facilitated by the presence of metals or specific organic moieties (i.e. aromatic aldehyde, heavy halogen atoms, heteroatoms with lone pairs). In addition, since triplet excitons generated in organic molecules are highly sensitive to oxygen and temperature, stringent conditions are required to observe long-lived phosphorescence from purely organic molecules. However, very recently, An et al. reported ultralong phosphorescent emission features in structures of planar organic molecules coupled in H-aggregates, which provide an effective means of stabilizing and protecting triplet excitons formed through intersystem crossing (ISC)[2]. The stabilized excited state, which functions as an energy trap at a lower energy level, may delocalize on several neighbouring molecules, offering suppressed radiative and nonradiative deactivation decay rates in favour of long-lived excited states and room temperature ultralong phosphorescence (RTUP).

In this regard, my research work was focused on the synthesis and characterization of triimidazo[1,2-*a*:1',2'-*c*:1'',2''-*e*][1,3,5]triazine (**TT** or cyclic triimidazole) and of its derivatives. In fact, **TT** has shown intriguing solid state AIE and RTUP properties. Diluted solutions of **TT** in DCM display weak emission (Φ = 2%) even under inert atmosphere, while crystalline powders (Φ = 30%) show an intense fluorescent emission at 425 nm and an ultralong emission at 520 nm with decay time close to 1 s. This behaviour, in agreement with works by An et al. [2] arises from the formation of H-aggregates in the crystal structure of the compound as revealed by XRD studies [3].

The main goal of my project has been the synthesis and characterization of organic and hybrid inorganic-organic **TT**-derivatives in order to expand both the photophysical features of the triimidazole family and our comprehension of the mechanisms involved in view of future applications. In hybrid materials, **TT** and its derivatives have been used as ligands thanks to the presence of the three different nitrogen atoms prone to metal coordination.

At the early stage of my research, my efforts were devoted to the preparation and characterization of the halogenated **TT**-derivatives. 3-bromotriimidazo[1,2-*a*:1',2'-*c*:1'',2''-*e*][1,3,5]triazine, **TT1Br**, 3,7-dibromotriimidazo[1,2-*a*:1',2'-*c*:1'',2''-*e*][1,3,5]triazine, **TT2Br**, 3,7,11-tribromotriimidazo[1,2-*a*:1',2'-*c*:1'',2''-*e*][1,3,5], **TT3Br** and 3-iodotriimidazo[1,2-*a*:1',2'-*c*:1'',2''-*e*][1,3,5]triazine, **TT1I**, 3,7-diiodotriimidazo[1,2-*a*:1',2'-*c*:1'',2''-*e*][1,3,5]triazine, **TT2I**, were easily prepared by reaction of **TT** with different amounts of N-bromosuccinimmide (NBS) or N-iodosuccinimmide (NIS). In addition, cocrystallization of **TT** with 1,4-diiodotetrafluorobenzene resulted in the isolation of **TTCo**[4-6].

The presence of halogens strongly affects the **TT** photophysic leading to the generation of new deactivation channels. In fact, the heavy halogen atoms allow efficient ISC to populate high energy triplet levels resulting in molecular phosphorescence (MP) both in the solid state and in diluted solution at 77 K. Besides MP, an

additional long lived emission in the solid state is observed for **TT2Br**, **TT3Br, TT1I** and **TTCo**, due to supramolecular interactions through Br···Br or N···I halogen bonds. Moreover, since H-aggregation is preserved in crystalline **TT2Br**, **TT3Br, TT1I**, **TT2I** and **TTCo**, these compounds manifest also RTUP features. Importantly, evaluation of the extrinsic *vs* intrinsic heavy-atom effect on the photophysics of **TT** was performed by comparing results obtained for **TTCo** and **TT1I**. Specifically, a more efficient ISC is observed when the iodine plays the role of an intrinsic perturber, in fact, while **TT1I** displays MP already at 298 K, it is visible only at 77 K for **TTCo**.

The halo-derivatization of the **TT** scaffold opens to a greater reactivity towards coupling reaction and to the functionalization with different chromophoric fragments which are expected to modify the emissive properties at both molecular and, through different packing arrangement, solid-state levels.

In particular, pyrenyl and pyridinyl fragments were conjugate to **TT** through coupling reaction.

3-(pyren-1-yl)triimidazo[1,2-*a*:1',2'-*c*:1'',2''-*e*][1,3,5]triazine, **TTPyr**, was easily prepared by Suzuki-Miyaura coupling reaction between **TT1Br** and pyren-1-ylboronic acid. The full explanation of the photophysical phenomena observed for **TTPyr** is still ongoing due the difficulties associated to the concomitant formation of at least three different crystalline phases. However, during the five months spent in Prof. Tang's laboratories at the Hong Kong university of Science and technology, the possibility to use **TTPyr** as a dye for cellular staining was investigated. Nano-aggregates of **TTPyr** are characterized by a high emission quantum efficiency (Φ = 67% for DMSO/water 90/10; prepared through rapid injection of water in a **TTPyr** DMSO solution).

The preliminary staining experiments on **TTPyr** have revealed that the dye diffusion starts immediately after the addition of 10^{-5}M **TTPyr** (99% water) aggregates to the culture media of HeLa, COS-7 or HLF cells as revealed by confocal microscope images. After few hours of staining, the cells display a round shape indicative of unhealthy conditions, confirming the cytotoxicity of this molecules as highlighted by the MTT assay.

For what concern the pyridinyl derivatization, 3-(2-fluoropyridin-4-yl)triimidazo[1,2-*a*:1',2'-*c*:1'',2''-*e*][1,3,5]triazine, **TTFPy**, containing the 2-fluoropyridine moiety, was synthetized by Suzuki-Miyaura coupling between **TT1Br** and 2-fluoropyridine-4-boronic acid pinacol ester. The compound's photophysical behavior is markedly different from that of the parent **TT** being, already as a molecule, quite fluorescent at room temperature (Φ = 50 %, 10^{-5} M in CH_3CN). In addition, crystals of **TTFPy** are characterized by multiple emissions comprising one fluorescence and two phosphorescences, with overall quantum efficiency equal to 25%. Through experimental, theoretical and X-ray diffraction studies, the fluorescence and the high energy phosphorescence were assigned to radiative deactivation from molecular S_1 and T_1 while the low energy, long lived (up to 0.1 s) phosphorescence was ascribed to the formation of H-aggregates in the compound's crystal structure[7].

Moreover, even a different pyridinyl fragment was used to modified the triimidazole structure. **TT2Py** (3-(pyridin-2-yl)triimidazo[1,2-*a*:1',2'-*c*:1'',2''-*e*][1,3,5]triazine) was prepared by Stille coupling between **TT1Br** and 2-(tributylstannyl)pyridine. The compounds crystallizes in three different polymorphic forms (**TT2Py-A, TT2Py-H** and **TT2Py-X**) all characterized by the $\pi\cdots\pi$ stacking already observed in **TT** and its derivatives.

Crystals of the three phases are characterized by a very complex emissive behaviour comprising two fluorescent and three phosphorescent components which, through detailed experimental and theoretical investigations, were selectively assigned to molecular and supramolecular effects[8].

Besides its intriguing photophysical behaviour, **TT2Py**, can be identified as an interesting ligand due to presence of multiple nitrogen atoms available for coordination to different metal atoms.

Positive results on the use of **TT** itself as ligand have been obtained by its reaction with Cu(I) or Ag(I) halides. In fact, the preparation of the isostructural $[M(TT)I]_n$ coordination polymers (with M = Ag; Cu) has allow to compare their photophysics[9].

In conclusion, these studies have allowed to deepen the knowledge of the effects played by molecular and supramolecular features on **TT** emissive properties. In particular, the role played by halogen atoms, metals and aromatic substituents have been deeply investigated. New and intriguing properties have emerged that will be further exploited in various application fields.

13.1 References

[1] Luo, J.; Xie, Z.; Lam, J. W. Y.; Cheng, L.; Chen, H.; Qiu, C.; Kwok, H. S.; Zhan, X.; Liu, Y.; Zhu, D.; Tang, B. Z., Aggregation-induced emission of 1-methyl-1,2,3,4,5-pentaphenylsilole. *Chemical Communications* **2001,** (18), 1740-1741.

[2] An, Z.; Zheng, C.; Tao, Y.; Chen, R.; Shi, H.; Chen, T.; Wang, Z.; Li, H.; Deng, R.; Liu, X.; Huang, W., Stabilizing triplet excited states for ultralong organic phosphorescence. *Nature Materials* **2015,** *14* (7), 685-690.

[3] Lucenti, E.; Forni, A.; Botta, C.; Carlucci, L.; Giannini, C.; Marinotto, D.; Previtali, A.; Righetto, S.; Cariati, E., H-Aggregates Granting Crystallization-Induced Emissive Behavior and Ultralong Phosphorescence from a Pure Organic Molecule. *The Journal of Physical Chemistry Letters* **2017,** *8* (8), 1894-1898.

[4] Lucenti, E.; Forni, A.; Botta, C.; Carlucci, L.; Giannini, C.; Marinotto, D.; Pavanello, A.; Previtali, A.; Righetto, S.; Cariati, E., Cyclic Triimidazole Derivatives: Intriguing Examples of Multiple Emissions and Ultralong Phosphorescence at Room Temperature. *Angewandte Chemie International Edition* **2017,** *56* (51), 16302-16307.

[5] Lucenti, E.; Forni, A.; Botta, C.; Carlucci, L.; Colombo, A.; Giannini, C.; Marinotto, D.; Previtali, A.; Righetto, S.; Cariati, E., The Effect of Bromo Substituents on the Multifaceted Emissive and Crystal-Packing Features of Cyclic Triimidazole Derivatives. *ChemPhotoChem* **2018,** *2* (9), 801-805.

[6] Lucenti, E.; Forni, A.; Botta, C.; Giannini, C.; Malpicci, D.; Marinotto, D.; Previtali, A.; Righetto, S.; Cariati, E., Intrinsic and Extrinsic Heavy-Atom Effects on the Multifaceted Emissive Behavior of Cyclic Triimidazole. *Chemistry – A European Journal* **2019,** *25* (10), 2452-2456.

[7] Previtali, A.; Lucenti, E.; Forni, A.; Mauri, L.; Botta, C.; Giannini, C.; Malpicci, D.; Marinotto, D.; Righetto, S.; Cariati, E., Solid State Room Temperature Dual Phosphorescence from 3-(2-Fluoropyridin-4-yl)triimidazo[1,2-a:1′,2′-c:1″,2″-e][1,3,5]triazine. *Molecules* **2019,** *24* (14), 2552.

[8] Lucenti, E.; Forni, A.; Previtali, A.; Marinotto, D.; Malpicci, D.; Righetto, S.; Giannini, C.; Virgili, T.; Kabacinski, P.; Ganzer, L.; Giovanella, U.; Botta, C.; Cariati, E., Unravelling the intricate photophysical behavior of 3-(pyridin-2-yl)triimidazotriazine AIE and RTP polymorphs. *Chemical Science* **2020,** *11* (29), 7599-7608.

[9] Lucenti, E.; Cariati, E.; Previtali, A.; Marinotto, D.; Forni, A.; Bold, V.; Kravtsov, V. C.; Fonari, M. S.; Galli, S.; Carlucci, L., Versatility of Cyclic Triimidazole to Assemble 1D, 2D, and 3D Cu(I) Halide Coordination Networks. *Crystal Growth & Design* **2019,** *19* (3), 1567-1575.